
Three-Dimensional, Time-Dependent Radiative Transfer for H II Regions, the Diffuse Ionized Gas, and the Reionization of the Universe

Johann Andreas Weber



München 2018

Three-Dimensional, Time-Dependent Radiative Transfer for H II Regions, the Diffuse Ionized Gas, and the Reionization of the Universe

Johann Andreas Weber

Dissertation
an der Fakultät für Physik
der Ludwig–Maximilians–Universität
München

vorgelegt von
Johann Andreas Weber
aus Rosenheim

München, den 30. Mai 2018

Erstgutachter: Prof. Dr. A. W. A Pauldrach
Zweitgutachter: PD Dr. Klaus Dolag
Tag der mündlichen Prüfung: 17. Juli 2018

Zusammenfassung

Die Wechselwirkung der ionisierenden Strahlung von Sternen oder anderen Strahlungsquellen mit dem umgebenden Gas spielt bei vielfältigen astrophysikalischen Fragestellungen eine entscheidende Rolle. So erlaubt beispielsweise die Untersuchung des Verlaufs der Reionisation von Wasserstoff und Helium im Universum Rückschlüsse auf die Entwicklung früher Sternpopulationen und aktiver galaktischer Kerne. Bei der Untersuchung der chemischen Zusammensetzung von Sternentstehungsgebieten – und damit zusammenhängend der Evolution von Galaxien – sind Analysen des Spektrums der damit assoziierten H II-Regionen von zentraler Bedeutung. Dies erfordert zum einen ein Verständnis der mikrophysikalischen Zusammenhänge, auf welchen die Ionisations- und Rekombinationsvorgänge sowie die Heiz- und Kühlprozesse im ionisierten Gas basieren, zum anderen die Berücksichtigung der makroskopischen Dichtestruktur des interstellaren Gases.

In der vorliegenden Arbeit wird ein Verfahren zur dreidimensionalen Simulation der Wechselwirkung von ionisierender Strahlung mit atomarem Gas vorgestellt und auf Fragestellungen im Zusammenhang mit photoionisiertem Gas auf unterschiedlichen Skalen angewendet.

Die verwendete Methode beinhaltet ein numerisch stabiles Verfahren zur Berechnung der zeitlichen Veränderung der Ionisations- und Temperaturstruktur in Abhängigkeit von der Dichte und der Zusammensetzung des Gases sowie der spektralen Energieverteilungen der ionisierenden Quellen. Sie berücksichtigt dabei die Ionen und Atome des Wasserstoffs, des Heliums und der häufigsten Metalle.

Zuerst untersuchen wir, inwieweit unterschiedliche Sternpopulationen zur Reionisation des Universums beitragen haben können (Wasserstoff: Reionisation abgeschlossen bei einer Rotverschiebung von $z \sim 6$; Helium: bei $z \sim 2.8$). Eine der hierfür in Frage kommenden stellaren Populationen besteht aus massereichen, aus primordiales Material zusammengesetzten Sternen der Population III, welche aber zum Ende der Reionisationsphase bereits durch Sterne späterer Populationen ersetzt worden ist. Wir simulieren deshalb auch Reionisationsszenarien durch entwickeltere stellare Populationen. Dies ist zum einen eine Population, deren Anfangsmassenverteilung derjenigen im gegenwärtigen Universum entspricht, zum anderen eine, deren ionisierende Strahlung im Wesentlichen durch sehr massereiche, durch stellare Verschmelzungsprozesse entstandene Sterne erzeugt wird. Das Hauptergebnis dieser Untersuchung ist, dass in letzterem Fall die Beteiligung von nur ca. 1 % der neu gebildeten stellaren Masse an Verschmelzungsprozessen ausreichend ist, um den Großteil der für die Helium II-Reionisation erforderlichen Photonen bereitzustellen, sofern die Effektivtemperaturen der so entstandenen Sterne bei mindestens 65 000 K liegen, wohingegen eine He II-Reionisation mit einer der heutigen entsprechenden Anfangsmassenverteilung nicht möglich ist.

Anschließend analysieren wir den Zusammenhang zwischen den temperatur- und metallizitätsabhängigen spektralen Energieverteilungen von O-Sternen und den Eigenschaften der umliegenden H II-Regionen. Dafür wird ein Gitter von Sternmodellen erstellt, die den Temperatur- und Metallizitätsbereich von O-Sternen in Sternentstehungsgebieten des heutigen Universums abdecken. Die Auswirkungen der stellaren Eigenschaften auf die Temperatur- und Ionisationsstruktur des umliegenden Gases werden dabei zuerst mittels sphärisch-symmetrischer Rechnungen untersucht. Anschließend werden für eine Auswahl dieser Sternspektren zusätzliche Effekte untersucht, die sich aus der dreidimensionalen Dichtestruktur des Gases und der unterschiedlichen räumlichen Verteilung der Quellen auf das Emissionsspektrum der umgebenden H II-Regionen ergeben. Dabei zeigt sich, dass unterschiedliche Dichtestrukturen sich zwar auf die Intensitätsverteilung der einzelnen Linien auswirken, die Gesamtemission der jeweiligen Linien jedoch weitgehend unverändert bleibt und analoges für die unterschiedliche räumliche Verteilung von Strahlungsquellen innerhalb einer H II Region gilt.

Schließlich befassen wir uns mit der Frage, inwieweit reine Photoionisationsmodelle, die davon ausgehen, dass die gesamte Strahlung von heißen, massereichen Sternen in der galaktischen Scheibe stammt, ausreichend sind, um die Ionisationsstruktur und Linienemission des diffusen ionisierten Gases (DIG) zu erklären, welches zwar über geringere Teilchendichten verfügt als „klassische“ H II-Regionen, das allerdings durch seine räumliche Ausdehnung den Großteil der Masse des ionisierten interstellaren Gases enthält. Einen Schwerpunkt bildet hierbei die Untersuchung, in welchem Ausmaß die H II-Regionen in der Umgebung der ionisierenden Quellen deren spektrale Energieverteilung verändern. Zur Bestimmung der Eigenschaften des DIG werden sowohl sphärisch-symmetrische als auch 3D-Simulationen durchgeführt, wobei in letzteren die Eigenschaften des DIG in der Umgebung eines Spiralarmes nachgebildet werden. Dabei zeigt sich eine starke Abhängigkeit der Ionisationsstruktur von der räumlichen Struktur des Gases. So führt die erhöhte Rekombinationsrate in überdichten Bereichen zu verstärkter Absorption, andererseits entstehen im Falle großräumiger Dichtehomogenitäten aber auch „Kanäle“ niedriger Dichte, durch die die ionisierende Strahlung den scheinbaren Bereich der Galaxie verlassen kann. Unsere Photoionisationsmodelle legen nahe, dass die Ionisation des DIGs überwiegend durch relativ kühle O-Sterne ($T_{\text{eff}} \lesssim 35\,000\text{ K}$) erfolgt, oder zusätzlich zur Photoionisation weitere Energiequellen vorliegen.

Abstract

The interaction between the ionizing radiation of stars and other sources of radiation with the surrounding gas is of key importance for a variety of astronomical problems. For instance, an examination of the cosmological reionization history of hydrogen and helium provides information about the evolution of early stellar populations and active galactic nuclei. Studies of the emission spectra of H II regions surrounding newly formed hot stars are essential for the analysis of the chemical composition of the star formation regions, which in turn is an important tool for reconstructing the evolution of galaxies. Performing such analyses requires an accurate understanding of the micro-physical processes which determine the thermal balance, the ionization, and the recombination processes within the ionized gas. It is also necessary to consider the complex macroscopic structure of the interstellar gas, especially inhomogeneities in the density structure of the interstellar medium.

In this work we present a method for three-dimensional simulations of the effects of the radiation from the sources of ionization on the (atomic) gas in their environment and apply it to several astronomical problems involving gas at different scales. The method includes a numerically stable approach for computing the temporal evolution of the ionization and the temperature structure in dependence of the density and the composition of the gas as well as the distribution of the embedded sources. It considers the atoms and ions of hydrogen, helium, and the most abundant metals.

First, we examine to what extent stars may have contributed to the hydrogen reionization of the universe completed at $z \sim 6$, and the reionization of He II, which was complete at $z \sim 2.8$. One type of stellar population that may have contributed to the reionization process are massive primordial population III stars. As these have been replaced by later stellar populations towards the end of the reionization period, we additionally simulate reionization scenarios by more evolved stellar populations: one with an initial mass function (IMF) that corresponds to the mass distribution in the present universe and a population whose ionizing radiation originates primarily from very massive stars formed by stellar collisions in dense clusters. The main result of the study is that a fraction of only about 1 % of the newly formed stellar matter to contribute in such mergers is sufficient to provide the dominant fraction of the photons required to ionize He II, if the effective temperature of the merger products is at least 65000 K. By contrast a stellar population with the current IMF, whose ionizing spectrum is dominated by “normal” O-stars, is not able to provide a similar number of He II ionizing photons.

Next, we study the relation between the temperatures and metallicities of O-type stars and the line emission of the surrounding H II regions. To realize this aim, we create a grid of stellar models that covers the temperature and metallicity range of O-stars found in star-formation regions in the present universe. The effects of the stellar metallicities and temperatures on the surrounding gas are first studied using spherically symmetric models. In a second approach the effects of a three-dimensional density structure of the gas and different distributions of the ionizing stars on the emission line spectrum are studied for a subset of the stellar models. Hereby we show that different density structures lead to different intensity distributions in synthetic narrow-band images, but the total emission of the corresponding lines is only weakly affected. The same applies to different spatial distributions of the same set of stars.

As a last study in this work we examine whether pure photoionization models that assume hot massive stars close to the galactic disk as the only sources of ionization are able to explain the ionization structure and emission line ratios found in the diffuse ionized gas (DIG), which is characterized by considerably lower mass densities than the H II regions in the immediate surrounding of hot stars, but which due to its large spatial extent still contributes most to the total mass of the ionized gas in disk galaxies. The focus of our study lies on the modification of the stellar spectra of the ionizing sources by the H II regions in their environment. The examination is performed for the spherically symmetric case as well as for the 3D case, where we study the properties of the diffuse ionized gas in the surroundings of a spiral arm. The results of the 3D simulations show a strong dependence of the ionization structure on the distribution and the degree of inhomogeneity of the gas. On the one hand, the increased recombination rates in the overdense regions result in increased absorption. On the other hand, large-scale inhomogeneities lead to the formation of “channels” of low density through which the ionizing radiation is able to leave the regions of the galaxy close to the galactic disk. The higher O III/H β emission line ratios predicted by the simulations compared to the observations indicate that the photoionization is dominated by relatively cool O stars ($T_{\text{eff}} \lesssim 35\,000$ K), or additional energy sources are present.

Contents

Contents	v
1 Introduction	1
1.1 Motivation	1
1.2 Outline of the thesis	3
1.3 Photoionized gas at different scales	4
1.4 Observational methods to study the properties of ionized gas	15
1.5 The physics of photoionized gas	23
1.6 Numerical approaches to solve the equation of radiative transfer in three dimensions	45
2 Did very massive stars of different metallicities drive the second cosmic reionization?	51
2.1 Introduction	52
2.2 Three-dimensional radiative transfer as a tool for the description of the epochs of reionization	55
2.3 Implementation and optimization details of the algorithm	65
2.4 Photoionization models for H II regions around luminous stars in the early universe	72
2.5 Summary, conclusions, and outlook	89
3 SEDs of massive stars and time-dependent modelling of metals in H II regions	93
3.1 Introduction	94
3.2 Stellar wind models for O-type dwarfs and supergiants at different metallicities	96
3.3 Influence of stellar SEDs on the emission line intensities of H II regions	103
3.4 Summary and conclusions	129
3.5 Figures and model data	131
4 Numerical Models for the Diffuse Ionized Gas in Galaxies	143
4.1 Introduction	144
4.2 Spherically symmetric simulations of dilute ionized gas surrounding leaky H II regions	146
4.3 Simulations of the diffuse ionized gas in 3D	158
4.4 Summary and outlook	168
5 Summary and conclusions	171
A Computational aspects of our 3D radiative transfer approach	179
A.1 The iteration scheme of the simulation runs	179
A.2 Input to and output from the simulations	179
A.3 Performance aspects	182
A.4 Outlook and future work	189

1 Introduction

1.1 Motivation

The interaction between the ionizing radiation of stars and other sources of radiation with the surrounding gas is of key importance for a variety of astronomical problems. While the typical size scales of objects that consist of photoionized interstellar or intergalactic gas vary by many orders of magnitude, from below one parsec in the case of planetary nebulae up to the entire reionized universe, the common property of all these objects is that they consist of dilute gas that is ionized by one or several emitters of photons in the energy range of the extreme ultraviolet (EUV) above the ionization threshold of atomic hydrogen ($h\nu_{\text{ion}} \geq 13.6 \text{ eV}$, corresponding to a wavelength of 911 \AA). In the ionized gas a considerable fraction of the energy of these photons is then converted into line radiation, which can often be observed even at large distances. This line radiation is either emitted during the recombination process and the subsequent cascade of transitions to lower excitation stages, finally ending in the ground state of the recombined atom, or emitted by the radiative relaxation of collisionally excited states. A part of these lines are in the non-ionizing UV, the visible, or the infrared wavelength range, which can thus escape the photoionized region and penetrate the interstellar medium unabsorbed. These lines can therefore be observed by ground-based instruments (visible light, a part of the near-infrared radiation) or at least by satellite missions (near to mid ultraviolet, mid and far infrared wavelength range). In contrast, the original ionizing radiation from the sources can usually not be observed directly due to the large opacity of the interstellar gas in that energy range. The emission spectrum of the ionized nebulae thus does not only provide information about the properties of the gas itself (for example, the temperature and density structure, and the chemical composition), but also about the spectral energy distributions (SEDs) of the respective sources of ionization.

This allows observations of the photoionized gas to be used as a tool to study a large variety of astronomical problems.

For example, while the spectral energy distribution of the sources in the extreme ultraviolet can usually not be observed directly, it can be estimated from the emission spectrum of the H II regions ionized by that radiation. Based on this the luminosity and effective temperature of the ionizing sources can be determined. This approach has first been proposed by Zanstra (1931). In **Chapter 3** we study emission line ratios of H II regions in dependence of the effective temperature and metallicity of the ionizing stars.

The approach to infer the spectral energy distribution of the sources by the ionization structure of the gas has also been applied to reconstruct the properties of the first stars and active galactic nuclei from the reionization history of the universe, which has been completed at $z \sim 6$ (White et al. 2003, Fan et al. 2006a, Kashikawa 2007) for hydrogen and $z \sim 2.8$ for the ionization of He II to He III (Reimers et al. 1997, Kriss et al. 2001). Plausible scenarios for the age, the abundance, and the spectral energy distributions – and thus the physical nature – of the first generations of stars and active galactic nuclei therefore have to be consistent with the observed reionization history (**Chapter 2**).

Since the primordial first stars, the gas in galaxies has been enriched with metals generated by nuclear processes in stellar cores and distributed into the surrounding space via stellar winds and supernovae. Thus, the metallicity of gas results from the extent and nature of its reprocessing in pre-

vious generations of stars. Variations in the metallicity of H II regions depending on the redshift (e.g., Pilyugin et al. 2013), the mass of the host galaxy (e.g., Kewley & Ellison 2008), or on the distance from the galactic center (e.g., Rosolowsky & Simon 2008) therefore provides evidence about the star formation history and the recycling of matter in galaxies.

The current star formation rate can be determined by measuring the emission from H II regions as a proxy for the current star formation rate. This is possible due to the close connection of photoionized gas with recent star formation, which is a result of the short lifetimes of the hot massive stars emitting the ionizing radiation field. This method can be used even for high redshifts (e.g., Smit et al. 2016, who used (inferred) H α fluxes as a star formation indicator in the wavelength range of $z = 3.8 \dots 5.0$).

The formation of hot massive stars takes place in the disks of star-forming galaxies. However, there also exists a dilute, but wide-spread component of ionized interstellar medium that can be detected at distances of up to a few kiloparsecs above the central plane of galaxies, called warm ionized medium (WIM) or diffuse ionized gas (DIG). Its emission spectrum provides information about the porosity of the interstellar gas that allows ionizing radiation from hot massive stars close to the galactic disk to leak out to larger distances, as well as about the possible presence of sources of ionization at high galactic altitudes (**Chapter 4**, for a review see Haffner et al. 2009).

The interpretation of the observations of photoionized regions requires an accurate quantitative understanding of the interaction of their matter with the radiation field of the sources of ionization, and of the microphysical processes that are responsible for the ionization and temperature equilibrium in the gas. As we will show in Sect. 1.5, there is a large variety of processes that influence the physical parameters of the gas and the emitted spectrum. On the other hand, the efficiency of these processes reacts strongly on changes of these parameters of the gas. On the other hand, the efficiency of these processes reacts strongly to changes of these parameters of the gas. As a result, the modelling of photoionized gas requires the solution of systems of differential and integro-differential equations for each considered volume element and – depending on the considered problem – for multiple time steps. Simulations of photoionized gas thus require the application of sophisticated numerical approaches.

Concerning the macroscopic structure of gas, it also has to be taken into account that H II regions often show strong deviations from a spherically or otherwise symmetric structure. Furthermore, in H II regions associated with large star formation regions, the diffuse ionized gas, and the reionized universe there are multiple sources of ionization that may have considerably different spectral energy distributions. Thus, while one-dimensional (typically spherically symmetric) simulations of the gas around a source of ionization may be fast, which allows covering a large parameter space in the simulations, they have to assume a strongly simplified geometry compared to the real structure of the gas.

To account for the inhomogeneous density structure of ionized gas and the presence of multiple sources we have developed a numerically stable, three-dimensional method for a time-dependent simulation of the ionization and the temperature structure of photoionized gas and its line emission. It considers the density structure and the composition of the gas as well as the spatial distribution of the embedded sources.

In this work we apply this methodology to study problems involving H II regions around hot stars, the diffuse ionized gas, and the reionized universe. In each of the cases we take into account, in particular, the effect of the spectral energy distributions of the ionizing sources on the ionized gas. An overview of our work will be given below.

1.2 Outline of the thesis

In this Section we give a brief description of our work.

In the remainder of this chapter (**Chapter 1**) we first give a short description of the most important types of photoionized gas – planetary nebulae, “classical” H II regions surrounding hot massive stars, the diffuse ionized gas in galaxies, active galactic nuclei, and the reionized universe. Then we provide an overview of observational approaches to gain information about the properties of the ionized gas (density and temperature structure, chemical composition). This is followed by a quantitative description of the physical processes that define these properties and that we have used in modelling the gas in the different scenarios studied here. For this description, we first derive the equation of radiative transfer as a special case of the more general Boltzmann equation and define the quantities used to describe the radiation field. The computation of the radiative transfer is a computationally expensive process (especially if the condition of spherical symmetry is dropped), requiring the use of approximations in the description of the radiation field. Thus we continue our introduction with a discussion of the advantages and drawbacks of different numerical approaches to solving the radiation transfer, where our focus lies on methods that are able to consider three-dimensional density structures of the gas and multiple ionizing sources.

In **Chapter 2 (published as Weber et al. 2013)** we present a study of possible scenarios for the reionization of the universe using 3D radiative transfer simulations. We first introduce the theoretical basis of our simulations covering the concept of 3D radiative transfer and the physical mechanisms that influence the ionization structure of the gas surrounding the sources of ionization. We further present a numerical method to describe the temporal expansion of the ionization fronts that considers multiple ionization sources. Next we discuss important details of our numerical approach and present tests comparing our 3d results with those of analytical solutions, a radially symmetric radiative transfer code, and results from a comparison project initiated by Iliev et al. (2006). Then we present first applications of our 3D radiative transfer on showcase simulations of the reionization scenario. Although using simplified initial conditions, we demonstrate the influence of realistic stellar spectra of massive stars at different metallicities on the ionization structure of the surrounding gas under conditions which correspond to those of the early universe, and we focus on the different behavior of the expansion of the ionization fronts with respect to a homogeneous gas density and an inhomogeneous cosmological density structure. With regard to the He II reionization problem we further investigate the influence of different input spectra on the ionization structure of He III by performing a series of multi-source simulations. We finally interpret and summarize our results along with an outlook.

In **Chapter 3 (published as Weber et al. 2015)** we study the temperature and ionization structure of H II regions as well as their emission spectrum in dependence of the properties of their ionization sources. To realize this, we first set up a grid of O star models in the temperature range between 30 000 K and 55 000 K and for metallicities from $0.1 Z_{\odot}$ to $2.0 Z_{\odot}$, covering the parameter range of stars of the spectral type O in the present-day universe. We discuss the spectral energy distributions of these stars with regard to the ionizing fluxes that determine the abundances of the ionic species that are important for the energy balance and emission line spectrum of H II regions. We then apply our computed stellar energy distributions to a series of sample H II regions. First we perform spherically symmetric simulations where we assume the gas to be homogeneous and irradiated by a single star, where we show that the ionizing spectra can, even for the same effective temperature of the stars, strongly depend on their metallicity and their mass-loss rates. Having described extensions to the existing 3D radiative transfer method with respect to a consistent calculation of the temperature structure and the consideration of the ionization structure of the most abundant metals, we then abandon the restrictions of spherical symmetry and simulate inhomogeneous H II regions that partly include multiple

ionizing stars. Here, we find that the intensity pattern in synthetic images of the line emission varies strongly between homogeneous and inhomogeneous model regions while the integrated line emission is not strongly affected.

In **Chapter 4 (submitted to A&A)** we study to what extent hot O stars close to the galactic plane are able to ionize the diffuse ionized gas (DIG) in star-forming galaxies, a dilute but extended component of the interstellar medium in galaxies that can be detected up to several kiloparsecs above the galactic plane. To do so we first simulate the properties of the DIG as a function of both the temperature- and metallicity-dependent spectral energy distributions of the ionizing sources – based on the model stars presented in the previous chapter – and the escape fractions from the H II regions surrounding the ionizing stars, using the spherically symmetric method described above. Together, our study comprises emission line ratios for a grid of 60 spherically symmetric DIG models. In the second part of our study of the DIG we present a set of three-dimensional simulations of diffuse ionized gas where the distribution of the ionizing sources resembles a spiral arm in a star-forming galaxy. Here we show how, even for the same mean density and average filling factor, the ionization structure of the DIG is affected by its porosity, which is a function of the size and the spatial distribution of the overdense “clumps”. Our results of both the spherically symmetric and the three-dimensional simulations show that the line ratios found in H II regions indicate a strong contribution of relatively cool O stars ($T_{\text{eff}} \leq 35\,000\text{ K}$) to the radiation field that keep the DIG ionized.

After these studies we summarize our most important results in **Chapter 5**.

In an appendix we finally describe technical aspects of the code we have developed for this work. As simulations of three-dimensional radiative transfer require a large computational effort that may limit the achievable spatial and temporal resolution it is essential to use the available computational resources in an efficient way by parallelizing the numerical method. Thus the appendix also contains a description of our approach to distribute computations among multiple tasks and discuss its scaling behavior. We also show how the change of simulation parameters like size of the simulation grid and the number of considered sources affects the time required for a simulation run.

Finally we give an outlook on future extensions our methodology.

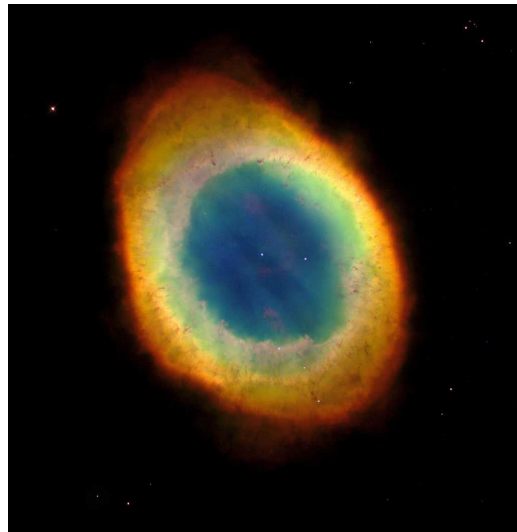
1.3 Photoionized gas at different scales

Below we will describe the key properties of the most important types of photoionized gas: planetary nebulae, “classical” H II regions around hot massive stars, the diffuse ionized gas (DIG), active galactic nuclei, and the reionized universe. We will also discuss to what extent the analysis of the properties of these objects can be used as tool for studying the evolution of galaxies and the universe. This section will be summarized with a tabular comparison of the different types of photoionized gas.

Planetary Nebulae. Planetary nebulae¹ are formed from the shells of low- and intermediate-mass stars (with initial masses below approximately $8 M_{\odot}$) that are ejected during the asymptotic giant branch (AGB) phase of the stellar development, which is reached after the end of the helium burning in the core. After the outer shells are detached from the central star (see below), the remnant shrinks and its effective temperature increases. As a result, the emission maximum of the star moves bluewards to the extreme UV radiation and the stellar radiation becomes able to ionize the previously ejected matter. The details of the mechanisms that lead to the mass loss are still not fully understood, but are

¹Our description of processes in AGB and post-AGB stars that lead to the formation of planetary nebulae follows Carroll & Ostlie (2006).

Figure 1.1: The ionization source of the planetary nebula M57 is a central star with an effective temperature of approximately 120 000 K (e.g., O’Dell et al. 2007). *Image credit: NASA, ESA and The Hubble Heritage Team (STScI/AURA)*



likely to be related to instabilities in the helium and the hydrogen-burning shells in the inner regions of AGB stars:

The interior of AGB stars consists of several layers which differ in their chemical composition and the type of nuclear reactions occurring there. In the center of AGB stars there is an inactive, degenerate core that consists predominantly of carbon and oxygen, the main products of helium burning. Above the core there is a thin helium-burning shell followed by an inert layer of helium that does not undergo nuclear fusion, a hydrogen-burning shell, and an outer layer of unburned material. During the early AGB phase both the helium-burning shell and the hydrogen-depleted layer above the helium-burning shell expand. As a result, the hydrogen-burning shell is pushed outwards where it is extinguished due to the lower temperatures occurring there. When the helium-burning shell moves towards the region that still contains hydrogen, the hydrogen-burning shell is reactivated and becomes the most important contributor to the total stellar luminosity. (At that point, the star is near the tip of the asymptotic giant branch in the Hertzsprung-Russell-Diagram). The thin helium-burning shell becomes unstable, which leads to nearly periodical episodes of activity and inactivity. The hydrogen-burning shell increases the amount of helium in the layer below. The increasing mass of that helium layer causes the region between the helium-burning shell and the inactive helium region to become partially degenerate. When the temperature in this layer has reached a critical temperature, an episode of helium burning occurs, which pushes the hydrogen-burning shell outwards. The hydrogen-burning shell consequently cools down until the helium production is interrupted. When the degeneracy of the helium-burning shell is lifted, the luminosity of the helium-burning shell decreases so that the hydrogen-burning shell is reactivated. As most of the luminosity of AGB stars is provided by the hydrogen burning shell, the episodes of *increased* helium burning lead to an *decreased* overall luminosity of the star.

As a result of these instabilities, pulsations occur and material is expelled from the envelope of the stars, where it cools down. At temperatures below 1000 K...1500 K, dust particles can form (e.g., Nanni et al. 2013, the exact value for the temperature that allows dust formation depends on the chemical composition of the dust particles), which are then accelerated outward by the stellar radiation field; a *dust-driven wind* forms. The mass-loss rate in the AGB phase can reach up to $10^{-4} M_{\odot}/\text{yr}$. At the end of the AGB phase most of the stellar envelope has been detached from the star and the effective temperature of the remaining star increases, but simultaneously the star shrinks, so that the overall luminosity remains nearly constant (in this phase of stellar evolution, the luminosity

of a star is a function of the mass of the degenerate stellar core, which remains almost constant, as the mass of the remaining hydrogen-burning shell is small compared to the mass of the degenerate inert core (the relationship between the mass of that core and the luminosity of a CSPN is described by the core-mass-luminosity relation, cf. Paczyński 1970, Kippenhahn 1981, Iben & Tutukov 1989, and Pauldrach et al. 2004). When the effective temperature of the post-AGB star has reached a temperature of approximately $T_{\text{eff}} = 30\,000\text{ K}$, its radiation becomes able to ionize the material expelled in the AGB phase. The line-emitting ionized gas is called a “planetary nebula”². Having reached higher effective temperatures, the stars develop a line-driven wind, which accelerates the detached outer layers from the AGB phase further outwards (Osterbrock & Ferland 2006). After that, the increase of the stellar temperature continues until shortly before the hydrogen-burning shell vanishes because the nuclear fuel has been used up. At that point the effective temperature of the central star reaches approximately $100\,000\text{ K}$. With the rise of the stellar temperature, the ionization structure of the nebula changes such that the abundances of higher ionization stages, like He III, rise. When the nuclear processes have halted, the core cools down and the star transforms into a white dwarf. The ionizing flux emitted from the central star consequently decreases. The dilution of the matter of the gaseous nebula and the decrease of the ionizing flux from the central star finally lead to the fading of the planetary nebula. The typical lifetime of a planetary nebula is on the order of a few times 10^4 yr (Gurzadyan 1997). Because of that short lifetime (compared to the lifetime of the progenitor stars on the main sequence which is on the order of 10^8 to 10^{10} yrs) the number of planetary nebulae that simultaneously exist in a galaxy is rather low (by 2012, approximately 2800 planetary nebulae in the galaxy were known, cf. Miszalski et al. 2012), in spite of the large number of stars in the mass range required for the formation of planetary nebulae.

The line emission of planetary nebulae can be detected at distances of up to approximately 20 Mpc. As their occurrence is connected with intermediate and old stars, they can be used to trace the dynamical and chemical properties of that part of the stellar population (Ford et al. 2002, Coccato et al. 2009). These observations are thus complementary to observations of classical H II regions connected to recent star formation (see below).

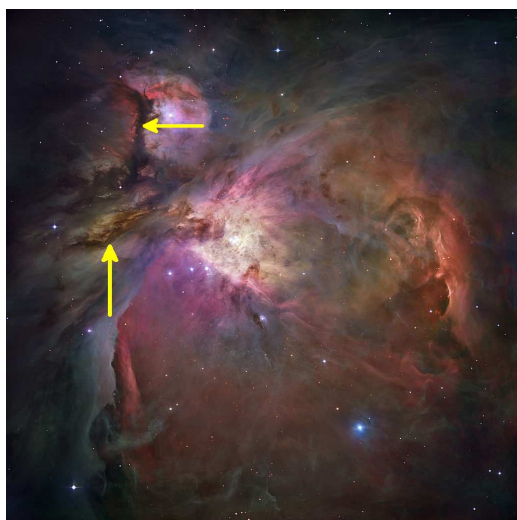


Figure 1.2: The Orion nebula (M 42), an H II region ionized by massive stars of the spectral types O and B. Not the entire gas in the environment is ionized and the host cloud still partly consists of cool molecular gas that contains dust and is able to form new stars. In the optical wavelength range, this component absorbs the light from the background and therefore appear dark (yellow arrows). *Image credit: NASA, ESA, M. Robberto (Space Telescope Science Institute/ESA) and the Hubble Space Telescope Orion Treasury Project Team.*

²The name refers to its optical appearance when observed with small instruments. Otherwise there is no connection between planetary nebulae and planets.

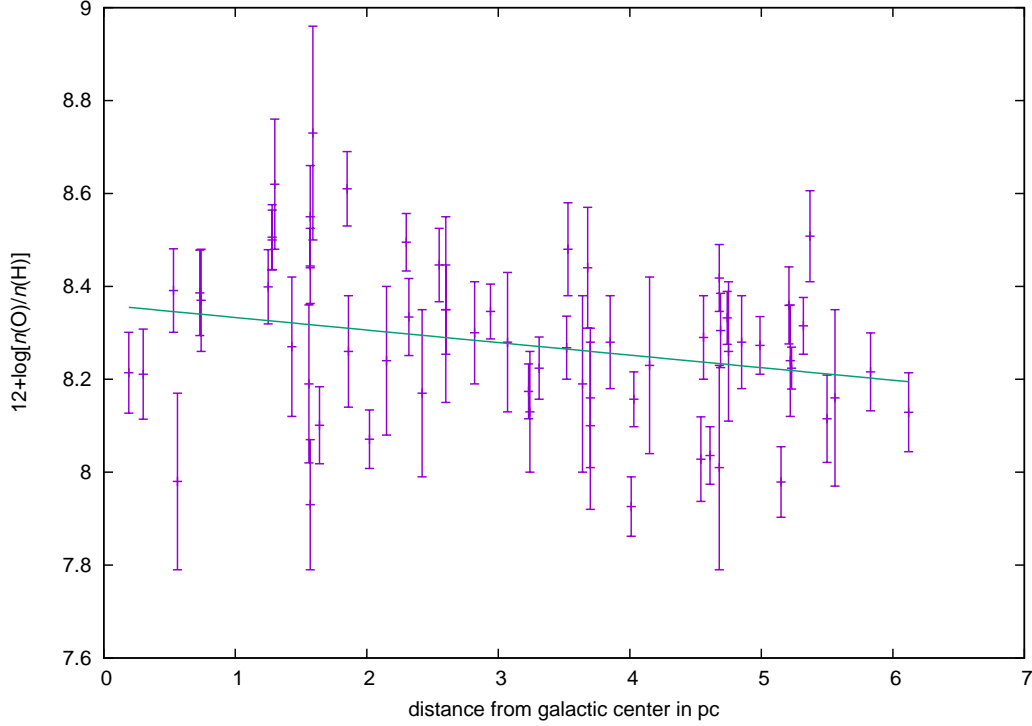


Figure 1.3: Oxygen abundances for H II regions in M33 as a function of their distance from the galactic center based on data from Rosolowsky & Simon (2008). While the oxygen abundance tends to decrease with larger distances from the galactic center, and can be fitted by $12 + \log(n(\text{O})/n(\text{H})) = 8.36 \pm 0.04 - (0.027 \pm 0.012) \frac{r_G}{\text{kpc}}$, where r_G is the distance from the galactic center of M33, there is also a considerable scatter of the oxygen abundances of the individual H II regions for any given galactocentric radius.

“Classical” H II regions around hot massive stars. “Classical” H II regions consist of gas ionized by hot massive stars of the spectral classes O and (to a lesser extent) B. These regions are associated with current or recent star formation for two reasons. First, both star formation and the development of a bright line-emitting region require the presence of relatively dense interstellar gas. Second, due to the short lifetime of such stars, they often remain in the stellar environment where they have formed during a large part of their existence. For instance, a star with $25 M_{\odot}$ remains on the main sequence for 6 Myr. (Schaller et al. 1992), which is less than one thousandth of the corresponding value for the Sun and one thirtieth of the time an object with the same galactocentric distance as the sun requires for one orbit around the galactic center. Hence the lifetime of O stars is in the same order or shorter than the lifetime of the stellar associations or clusters they are formed in, which depending on the initial mass and density of these associations can be some millions to some hundred millions of years³ (see, for example, Brown et al. 1997, Lada & Lada 2003 and Converse & Stahler 2010). In spiral galaxies the connection between H II regions and star formation also leads to a strong correlation between the spiral arms and the H II regions contained in these objects.

The chemical composition of H II regions is a result of the previous creation of metals in stellar cores and their redistribution by stellar winds and supernovae. Analyses of the chemical composition

³O stars also influence the dispersal of their host clusters by removing the gas content of these clusters by radiation pressure and wind or supernova feedback.

of H II regions in spiral galaxies have found that the metallicity tends to be anticorrelated with the distances from the galactic cores (e.g., Shaver et al. 1983, Rubin et al. 2007, 2008, Rosolowsky & Simon 2008, see also Fig. 1.3) and massive galaxies tend to have a larger metallicity than low-mass galaxies (Tremonti et al. 2004, Kewley & Ellison 2008). For instance, the metallicity of the star-forming regions in the Small Magellanic Cloud is only roughly one sixth of the solar metallicity (Dufour 1984), whereas it is approximately solar for the Milky Way (Balsler et al. 2011). This indicates that more metals have been produced and returned to the interstellar medium via supernova explosions and stellar winds in the denser inner regions of spiral galaxies than in the outer parts and that the reprocessing of stellar material is more efficient for more massive galaxies. Analyzing the element abundances of H II regions in different galaxies or as a function of their position within a galaxy hence provides an important tool for studies of the galactic evolution. We will discuss the spectral energy distributions of hot stars as a function of their effective temperature and chemical composition in Section 2.4.1 (published in Weber et al. 2013) and – in more detail – in Chapter 3 (published in Weber et al. 2015).

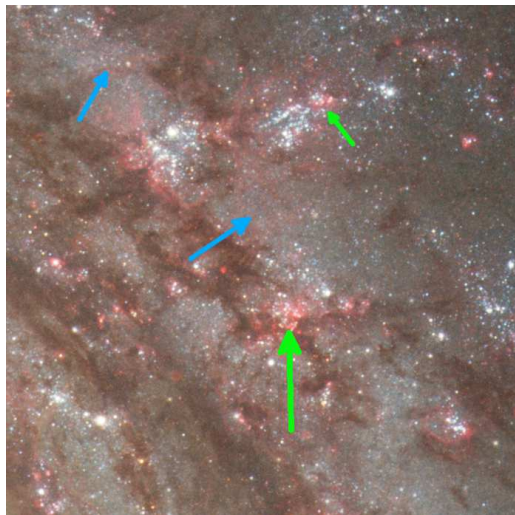


Figure 1.4: A part of a spiral arm in the star-forming galaxy M51. The size of the shown region is approximately 1.5 kpc. H α emitting regions of ionized gas appear in red. The image shows that besides H II regions around star-forming clusters (marked by green arrows) there is also a more diffuse component of ionized gas (blue arrows). *Image credit: NASA, ESA, S. Beckwith (STScI), and The Hubble Heritage Team STScI/AURA.*

The Diffuse Ionized Gas. Besides discrete H II regions in the environment of hot stars, recombination lines of hydrogen and collisionally excited emission lines can be also detected from up to distances of several kpc above the galactic disks⁴. This component is called the *diffuse ionized gas* (*DIG*; this term is usually used in an extragalactic context) or *warm ionized medium* (*WIM*; this expression is mainly used for gas within the Milky Way). First evidence for the existence of DIG has been discovered by Struve & Elvey (1938), who found H α emission in areas of the sky devoid bright nebulae. The first quantitative description of the DIG has been obtained by observations of the radio continuum of the ionized gas performed by Hoyle & Ellis (1963).

Although its hydrogen number density is only on the order of 0.1 cm^{-3} , it still contributes to a similar extent to the total line emission of galaxies as “classical” H II regions (cf. Zurita et al. 2000).

The mechanisms that keep the DIG ionized are still not entirely clear. While ionizing radiation from hot massive stars near the galactic plane seems to be important (cf. Haffner et al. 1999), observational results concerning the ionization and temperature structure suggest that there might exist additional sources of ionization. For example it has been observed that found that the [O III]/H α ratio is increased in the high altitude DIG for several edge-on galaxies (Tüllmann & Dettmar 2000,

⁴A smaller amount of line-emitting gas has can also be found in elliptical and S0 galaxies (Lacerda et al. 2018).

Collins & Rand 2001a), which is hard to explain by ionization from the galactic plane. Among these, evolved low-mass stars with high temperatures such as central stars of planetary nebulae or white dwarfs (Sokolowski & Bland-Hawthorn 1991, Flores-Fajardo et al. 2011). Unlike to the short-lived hot massive stars, which are strongly concentrated near the galactic disks, older evolved stars can occur in larger galactic heights, furthermore the effective temperature of these objects can exceed the temperature of normal O stars. Another explanation for the rising $[\text{O III}]/\text{H}\alpha$ ratio for large galactic heights has been presented by Collins & Rand (2001b), who discussed the possibility that shocks, induced by supernova explosions or stellar winds from OB associations, may provide a secondary source of ionization that becomes more important at larger distances from the galactic plane.

On the other hand, observations of the WIM in the solar environment of the Milky Way (Madsen et al. 2006) or M 31 (Greenawalt et al. 1997), show low emission from doubly ionized oxygen, indicating a softer ionizing spectrum than found in typical H II regions. There exist several approaches to explain that deviation, for example higher escape fractions of ionizing radiation from H II regions around relatively cool ionizing sources (as discussed by Reynolds & Tufté 1995). Hoffmann et al. (2012) has proposed a scenario, where both photoionization and the reconnection of magnetic field lines in the interstellar space contribute to the energy supply of the DIG.

Overall, it appears to be likely that several mechanisms for the energy supply of the DIG may coexist, with varying importance among different regions. We will discuss the ionization structure of the DIG in dependence of the density structure of the gas and the escape fractions of the ionizing radiation from the H II regions that surround the hot massive stars near in galactic disk in Chapter 4.

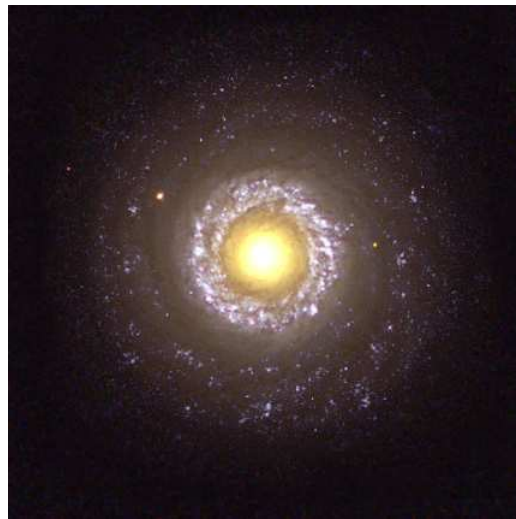


Figure 1.5: NGC 7742 hosts an active galactic nucleus. *Image credit: Hubble Heritage Team (AURA/STScI/NASA/ESA)*

Active Galactic Nuclei. The most important non-stellar sources of ionizing radiation are active galactic nuclei⁵ (AGNs), where the energy source is not driven by nuclear reactions as it is the case for stars, but by the release of gravitational energy by matter accreting onto a black hole. The term “active galactic nuclei” refers to objects whose luminosities differ by several orders of magnitude and can, in the case of most luminous quasars, reach up to approximately $10^{48} \text{ erg s}^{-1}$ (Khangulyan et al. 2013, Wu et al. 2015), i.e., more than $10^{14} L_{\odot}$. Emission regions related to AGNs can be subdivided into two regimes based on the width of the emission lines that results from the Doppler broadening caused by their motion around the central black hole: *narrow-line regions*, and *broad-line emission regions*

⁵Our description of Active Galactic Nuclei follows Osterbrock & Ferland (2006).

(with orbital velocities of up to $5\,000\text{ km s}^{-1}$ around the centers).

There is a larger range of ionization stages found in narrow-line AGN regions compared to “classical” H II regions. Both lines of neutral stages like O I and N I and of high ionization stages like Ne v and Fe VII are found in their emission spectra, whereas the abundance of such high stages in H II regions is low. The reason is that the coexistence of such a variety of ionic species requires a considerably harder ionizing spectrum than can be provided by O-stars. While photons with energies of $h\nu > 100\text{ eV}$ are able to generate the above mentioned high ionization stages, they are also able to penetrate deeper into the neutral gas than photons that are just slightly above the ionization edge of hydrogen or neutral or singly ionized helium as the ionization cross-sections of hydrogen and helium decrease for higher photon energies. Consequently, photons with energies considerably above the corresponding ionization edges tend to be absorbed at larger distances from their sources than lower-energetic photons. This effect, the “radiation hardening”, is quantitatively discussed in Sect. 2.2.2.4. The result is a more gradual transition between the ionized and the neutral gas than it would be the case for nebulae ionized by stellar radiation fields with – compared to AGNs – softer ionizing radiation.

Models show that the observed line ratios can be best explained with an ionizing SED that is described by a power-law spectrum $L_\nu = C\nu^{-\alpha}$, where $\alpha = 1 \dots 2$ (we compare the SEDs of different types of sources of ionizing radiation in Fig. 1.8). The emission spectra of active galactic nuclei with a steep slope of the power law spectrum and a low emissivity are dominated by the emission lines of neutral atoms like O I or low ionization stages like S II. Such objects are called *LINERS* (low-ionization nuclear emission-line regions).

Broad-line emission is created in the immediate environment of the central black hole of luminous AGNs⁶. The large speed of the emitting material orbiting the black hole causes the broad line profiles due to the Doppler effect. In this environment the number densities are larger ($n_e \sim 10^{10}\text{ cm}^{-3}$) than in the other types of emission regions described above. Thus the emission of forbidden lines (relative to the emission of allowed lines like the recombination lines of hydrogen) is considerably weaker than, for example, in the narrow line region⁷, as the upper states are more likely to be collisionally de-excited than to decay spontaneously into the ground state (cf. Sect. 1.5.5 and 1.4.2).

As observations of broad line emission regions have shown changes of the luminosity on timescales of a few weeks, the volume from which most of the line radiation is emitted must be considerably smaller than one parsec.

The amount of radiation emitted by AGNs emitted per unit time and volume can not be explained by thermonuclear reactions in the centers of stars within that volume, where only about 1 % of the rest energy of the matter involved in the nuclear reactions is converted into heat and finally electromagnetic radiation during the stellar lifetime. A much larger amount of energy can be released when material is accreted onto a supermassive black hole and friction in the accretion disk causes the material to heat up and consequently to emit photons. The achievable efficiency of this process is 5.72 % for a non-rotating black hole and 42.3 % for a black hole with maximal rotation. These values are computed from the absolute value of the gravitational energy of a particle at the lowest stable orbit around a black hole, which is approximately 3 times the Schwarzschild radius in the case of a non-rotating black hole. The maximal value for the efficiency of energy release (Carroll & Ostlie 2006) increases

⁶By contrast, measurements of narrow-line emission regions in active galaxies by Bennert et al. (2006) showed sizes in the order of one kiloparsec

⁷Galaxies whose emission line spectra are characterized by broad-line emission of the allowed transitions of H I, He I, and He II and narrower forbidden lines, e.g., of O III, are classified as *Seyfert 1* galaxies, the emission of mainly narrow (both allowed and forbidden) lines characterizes *Seyfert 2* galaxies. The reason for the absence of the broad emission lines in *Seyfert 2* galaxies is the occultation of radiation from the corresponding emission region by optically thick gas in its environment.

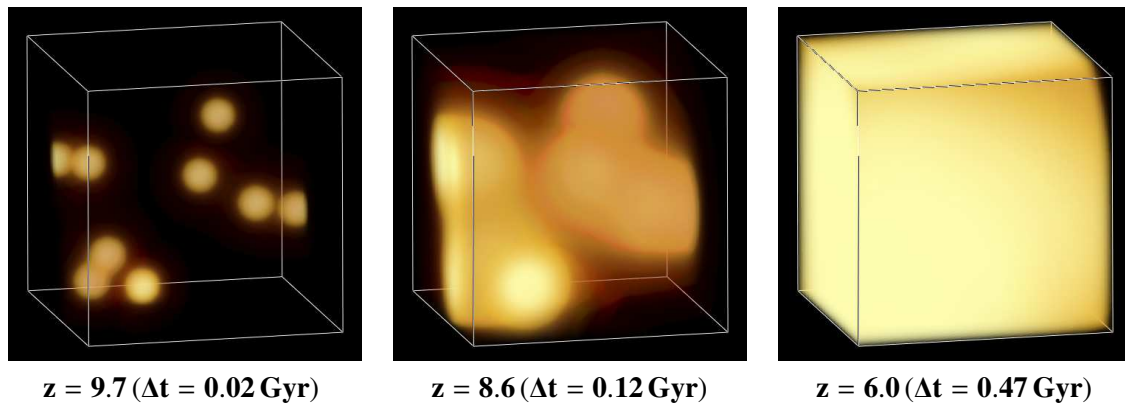


Figure 1.6: Simulation representing the second stage of the cosmic reionization, driven by massive population II/I stars following a Kroupa IMF. The radiation of the clusters is able to reionize the hydrogen content of the simulation volume within the redshift interval from $z \sim 10$ to $z \sim 5.8$. (Δt is the time interval since the beginning of the simulation at $z = 10$.)

for rotating black holes because the radius of the lowest stable orbit for accreted matter shrinks.

The reionized universe. At a redshift of $z \sim 1100$ (corresponding to a world age of approx. 380 000 yrs), protons and electrons recombined to neutral hydrogen when the hot plasma that existed after the Big Bang had cooled down to temperatures of a few thousand Kelvins. If the interstellar medium were still neutral, the intergalactic space would have remained opaque for hydrogen-ionizing radiation and the Lyman line radiation of hydrogen, so that no radiation with wavelengths below the redshifted Lyman- α line would be detected. For low redshifts, such complete absorption (“Gunn-Peterson trough”) was not observed (Gunn & Peterson 1965).

Absorption of wavelengths below the Lyman alpha line could, however, be observed for quasars with redshifts $z \gtrsim 6$ (Becker et al. 2001, White et al. 2003, Kashikawa 2007). This indicates that at a redshift of $z \sim 6$ the intergalactic hydrogen of the universe has for the most part become re-ionized. At approximately the same time most of the neutral helium has been turned into singly ionized helium. By contrast, the full ionization of helium into He III has not been completed until $z \sim 2.8$ (Reimers et al. 1997, Kriss et al. 2001 Syphers et al. 2012). The nature of the sources providing the photons for the reionization process is not yet fully determined. The most likely sources that provide the energy required for the reionization process are hot stars and active galactic nuclei (e.g., quasars). For the first phase of the reionization process, when hydrogen is ionized, several studies claim that this phase has been mainly driven by hot stars (e.g., Willott et al. 2005, Mahabal et al. 2005). It is, however, not clear whether the first generation of stars (“population III stars”) had a similar initial mass function (and consequently a similar emission of ionizing photons per unit stellar mass) as the present generation of stars or whether more massive stars are formed at the onset of star formation: due to the absence of metals, their initial mass function had possibly been shifted towards higher stellar masses. The reason is that primordial gas clouds, which contain no metals and are therefore also devoid of dust, can not cool efficiently. As a consequence of the larger gas temperatures the Jeans mass, i.e., the mass a protostellar cloud must reach until it collapses under its own gravity, is increased, which may also lead to higher masses of the formed stars (Bromm et al. 2002, Abel & Wandelt 2002) and higher effective temperatures of up to approximately 10^5 K (cf. Schaerer 2002), leading to an increased emission of ionizing photons.

However, fragmentation processes could still lead to the formation of low-mass primordial stars (see, for example, Stacy et al. 2016). Furthermore, it is likely that the stellar population changed significantly during the epoch of re-ionization as the clouds and stars formed in the late phase of this period already contained a significant amount of metals produced by the earlier stellar populations (Maio et al. 2010). Cen (2003) suggests that there have been two separate epochs of reionization, a first one driven by population III stars at $z \sim 15$ followed by a phase of partial recombination and a second phase of reionization completed at $z \sim 6$.

The most commonly assumed ionization source for the ionization of helium to He III (Miralda-Escudé et al. 2000, Furlanetto 2009) are AGN. However, stellar sources could have been important if there had been a larger fraction of the stars with effective temperatures considerably above 50 000 K than in the present-day universe. This could, for example, be the case if during that time period very hot and massive stars formed by merging processes in dense clusters. The conditions for such a reionization scenario are examined in Section 2.4 (published as Weber et al. 2013).

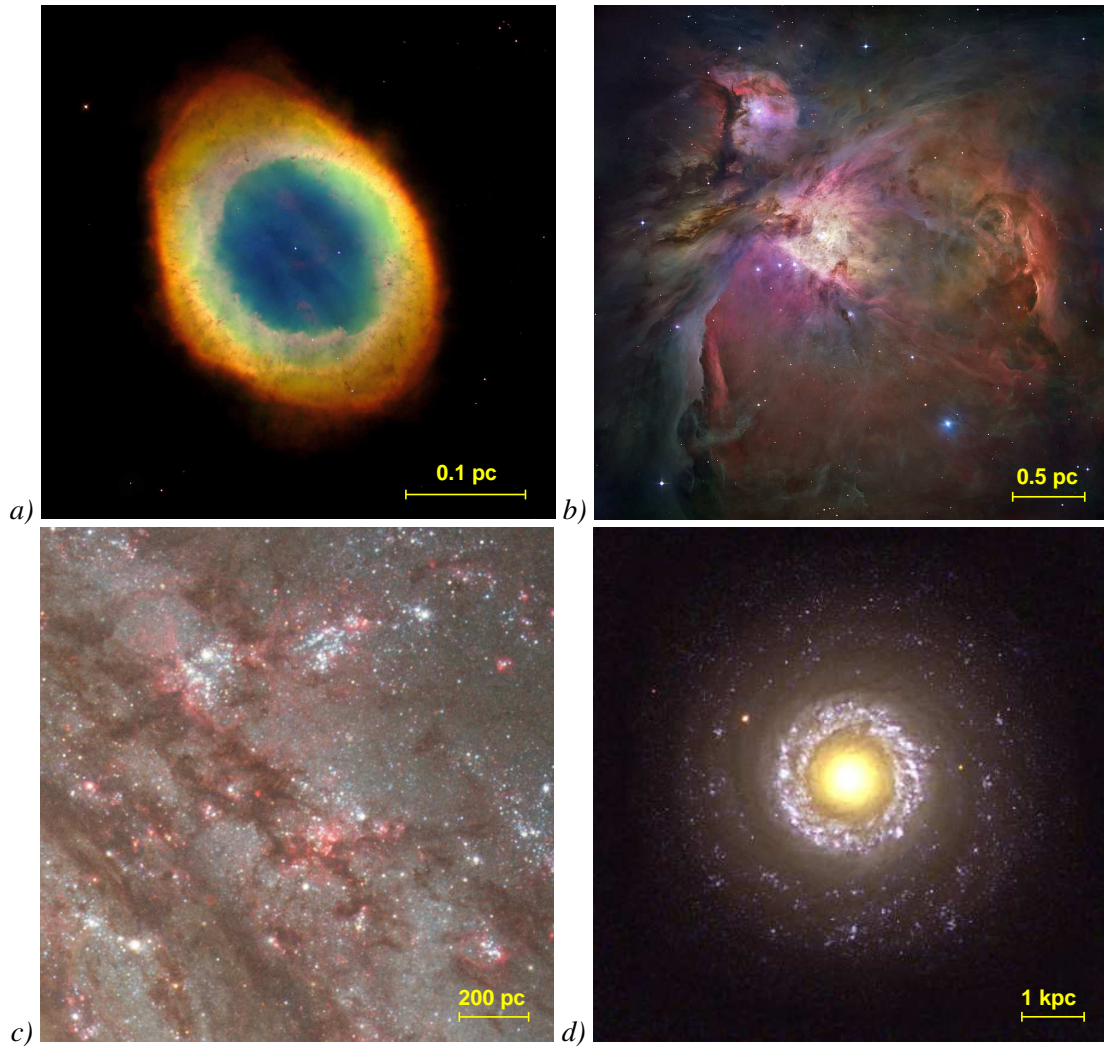


Figure 1.7: Comparison of the sizes of objects that represent the different types of line-emitting photoionized gas: planetary nebulae, “classical” H II regions, the diffuse ionized gas, and galaxies with active galactic nuclei. The depicted objects correspond to objects shown in Figs. 1.1 through 1.5. The length of the scales has been computed based on distance measurements by Harris et al. (1997) (distance of the ring nebula: 700 pc), Menten et al. (2007) (distance of the Orion Nebula: 414 ± 7 pc), Takáts & Vinkó (2006) (distance of M51: 7.1 ± 1.2 Mpc), Tully (1988) (distance of NGC 7742: 22 Mpc), and the information pages to the corresponding images at <http://www.hubblesite.org> for the angular extents of the objects on the sky.

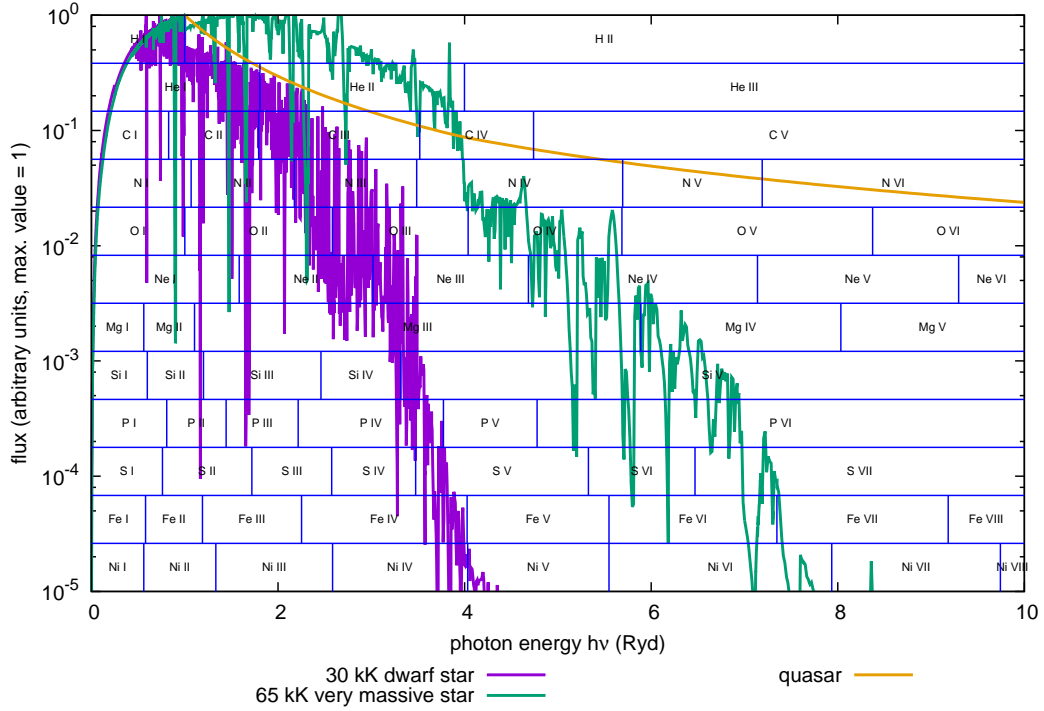


Figure 1.8: Comparison of spectral energy distributions of the sources of ionization for several types of photoionized gas with the ionization edges of the most abundant elements. The violet line shows the spectrum of a dwarf (i.e., main sequence) star with an effective temperature of $T = 30\,000$ K and solar metallicity (model from Sect. 3.2.2), which among the stars of the spectral type O has a relatively soft ionizing spectrum. The green line shows the SED of a very massive 65 000 K model star, which might have formed by stellar collisions in dense clusters in the early universe and belongs to a stellar population that could have contributed to the reionization of the universe (Pauldrach et al. 2012). The orange line represents the EUV part of quasar continua approximated by power laws following Shull et al. (2012) using data from Telfer et al. (2002), Hasinger et al. (1993), and Hasinger (1994). The fluxes were scaled such that the maximal value of the continuum for all plots is set to unity. The plot shows that in active galactic nuclei higher ionization stages can be generated by photoionization than in “normal” H II regions.

Table 1.1: Overview of the properties of the various types of photoionized gas. Note that for each type of photoionized region there is a considerable variation in size and number density.

Type	ionizing sources	typical size	typical hydrogen number density n_H
planetary nebulae	post-AGB stars	~ 1 pc	$\sim 10^3 - 10^5 \text{ cm}^{-3}$ (Zhang et al. 2004)
“classical” H II regions	hot massive stars ($T_{eff} \gtrsim 30\,000$ K)	$\sim 1 - 500$ pc	$\lesssim 10^4 \text{ cm}^{-3}$
diffuse ionized gas (DIG)/ warm ionized medium (WIM)	not fully clear, likely hot massive stars with possible additional contributions from hot evolved stars, shocks, or magnetic reconnection	some kpc	$\sim 0.1 \text{ cm}^{-3}$
active galactic nuclei	accretion onto supermassive black holes in the centers of galaxies	< 1 pc (accreting regions) ~ 1 kpc (narrow-line regions)	$\sim 10^9 \text{ cm}^{-3}$ (broad line regions) $\lesssim 10^4 \text{ cm}^{-3}$ (narrow line regions)
the reionized universe	early stars (POP III stars, early POP II stars), AGN	28.5 Gpc (Wright 2006) (comoving diameter of the observable universe)	$\sim 70 \text{ m}^{-3}$ ($z = 6$) $\sim 0.2 \text{ m}^{-3}$ ($z = 0$) (mean hydrogen density in universe)

1.4 Observational methods to study the properties of ionized gas

In this section we will discuss how to deduce its properties from observational results. Hereby, a large variety of different approaches using data obtained in all accessible wavelength ranges is applied. In this section we will outline the most important observational techniques to study the properties of the gas – temperature, electron density, and element abundances. Most of these methods are based on the analysis of emission line ratios, but some also utilize the (radio) continuum. If not noted otherwise, our description follows Osterbrock & Ferland (2006).

1.4.1 Methods to determine the temperature structure of the ionized gas

1.4.1.1 Comparison of nebular and auroral lines

The collisional excitation rate (in s^{-1}) of an ion from the lower state l to the upper state u is

$$C_{lu} = n_e \frac{8.629 \cdot 10^{-6} \Omega_{lu}(T)}{T^{1/2}} \frac{\Omega_{lu}(T)}{g_l} e^{-h\nu_{lu}/kT}, \quad (1.1)$$

where n_e is the electron number density in cm^{-3} , T the temperature in K, Ω_{lu} the quantum-mechanical collision strength of the transition, g_l the statistical weight of the lower state and $h\nu_{lu}$ the excitation energy. For processes, where the excitation energy corresponds to the energy of photons in the visible or UV spectral range there is a strong dependence on the temperature because of the $e^{-h\nu_{lu}/kT}$ -term, where $h\nu > kT$ for typical temperatures of H II regions. This dependence is reflected in the emission of the corresponding emission lines. Therefore these collisionally excited lines can be used to measure the temperature within the gas. However, the emission of the collisionally excited lines additionally

depends on the chemical composition and the ionization structure of the considered H II region. These ambiguities can be avoided if several lines *of the same ion* are compared. The most notable examples are the nebular and auroral lines of N II and O III (see Figure 1.9). While the excitation energy of an ion in the ground state to the 1D_2 state corresponds to the energy of a photon in the visible wavelength range for both ions – the lines emitted by the corresponding de-excitation processes are called the *nebular lines* – the excitation into the 1S_0 state requires approximately 2.1 times higher energies for both N II and O III. Therefore direct transitions from the 1S_0 state into the 3P states lead to the emission of photons in the UV wavelength range which can not be observed by ground-based instruments. Instead, the excitation of the 1S_0 state is determined by observations of the *auroral lines* emitted by transitions from the 1S_0 states of the corresponding ions into the 1D_2 states. For N II and O III these lines lie in the visible wavelength range. We plot the intensity ratios between the nebular and auroral lines of N II and O III in Figure 1.10, based on data by Lennon & Burke (1994) and retrieved from Osterbrock & Ferland (2006). The plot shows that for typical temperatures of H II regions auroral lines are by two to three orders of magnitude weaker than the nebular lines. Therefore the main difficulty of the comparison approach is the faintness of the auroral lines. The comparison of nebular and auroral lines has been suggested by Menzel et al. (1941) and is widely used. Such measurements have, for example, been performed by Osterbrock et al. (1992) for the Orion Nebula, Garnett et al. (1997) for H II regions in NGC 2403, Kennicutt et al. (2003) for H II regions in M 101, and Ly et al. (2014) for emission-line galaxies with redshifts of up to $z \sim 0.9$.

A more general discussion of collisional excitation processes will follow in Sect. 1.5.5.

1.4.1.2 Comparison of optical and infrared lines

For lines in the mid to far infrared like the ones caused by transitions within the split “ground-levels” of, for instance oxygen, which lead to the emission of line radiation at $51.8\ \mu\text{m}$ and $88.3\ \mu\text{m}$ the exponential term in Eq. 1.1 is close to unity. Due to the resulting different energy dependence of these lines and lines in the optical wavelength range – both types of transitions are, for example, present in the emission spectra of N II, O III and S III – a comparison between the lines of such ions in the optical and far-IR wavelength ranges allows for the determination of the electron temperature in the parts of H II regions where the corresponding ions prevail. A problematic aspect of this method is, however, that Earth’s atmosphere is opaque to the mid- and far infrared, so that observations in this wavelength band require space or at least airborne observatories. On the other hand, the mid-IR lines are less affected by the absorption due to interstellar dust than visible light.

Such comparisons have, for example, been performed for the visible and far-IR emission lines of O III from planetary nebulae by Dinerstein et al. (1985), who used ground based observations in the optical wavelength range and IR observations with the Kuiper Airborne Observatory (KAO) and by Luridiana et al. (2003) who used data from the Infrared Space Observatory (ISO) for the infrared and from the Hubble Space telescope for the visible wavelength range.

1.4.1.3 Determining the gas temperature in different parts of the H II regions

The measurement of the gas temperature by applying the methods described above to emission lines of different ions will usually not lead to the same results, because the abundance of these ions depends on the position within the H II region. For example, N II is more abundant in the outer parts of the ionized volume, while O III is more abundant in the inner parts of H II regions. For intermediate and large metallicities ($Z \gtrsim 0.4 Z_\odot$) the temperatures in the outer parts of H II regions are typically larger as a result of the radiation hardening and the lack of the efficient cooling by O III lines (cf. Section 3.3.1.2).

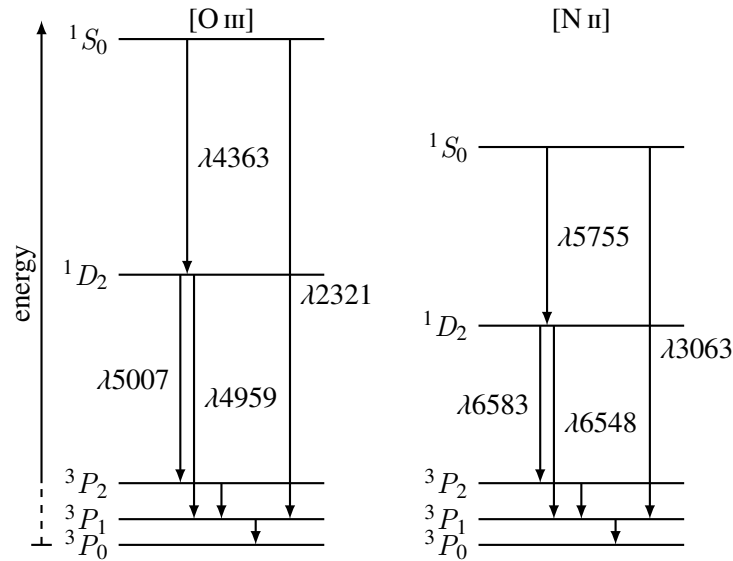


Figure 1.9: Energy level diagram showing the 3P levels, the 1D_2 level, and the 1S_0 level of the isoelectronic ions N II and O III. De-excitation processes from the 1D_2 level to the split 3P “ground level” lead to the emission of a photon in the visible wavelength range (“nebular lines”). The energy required to excite a N II or O III ion into the 1S_0 state, exceeds the excitation energy for the 1D_2 state by a factor of approximately 2.1. Therefore, the photons emitted by the transitions from the 1S_0 level to one of the 3P levels are in the UV wavelength range and can thus not be accessed by ground-based observations, whereas the transitions from the 1S_0 level to the 1D_2 level lead to the emission of photons in the visible range (“auroral lines”) and are therefore used for the comparison of the excitation rates. Due to the $\exp(-E_{lu}/kT)$ -dependence of the collisional excitation rate (where E_{lu} is the energy difference between the ground level and the excited level and T is the electron temperature of the ionized gas), the ratios between the nebular and the auroral lines are strongly temperature-dependent and can therefore be used to determine the temperature in the gas.

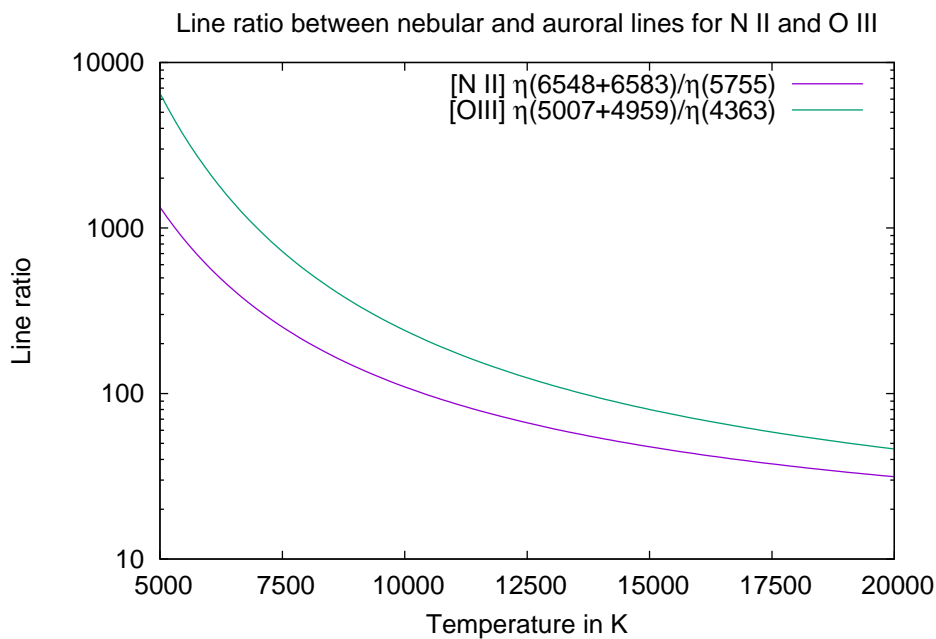


Figure 1.10: Ratio of nebular to auroral line emissivities of N II and O III as a function of the electron temperature in the range typically found in H II regions

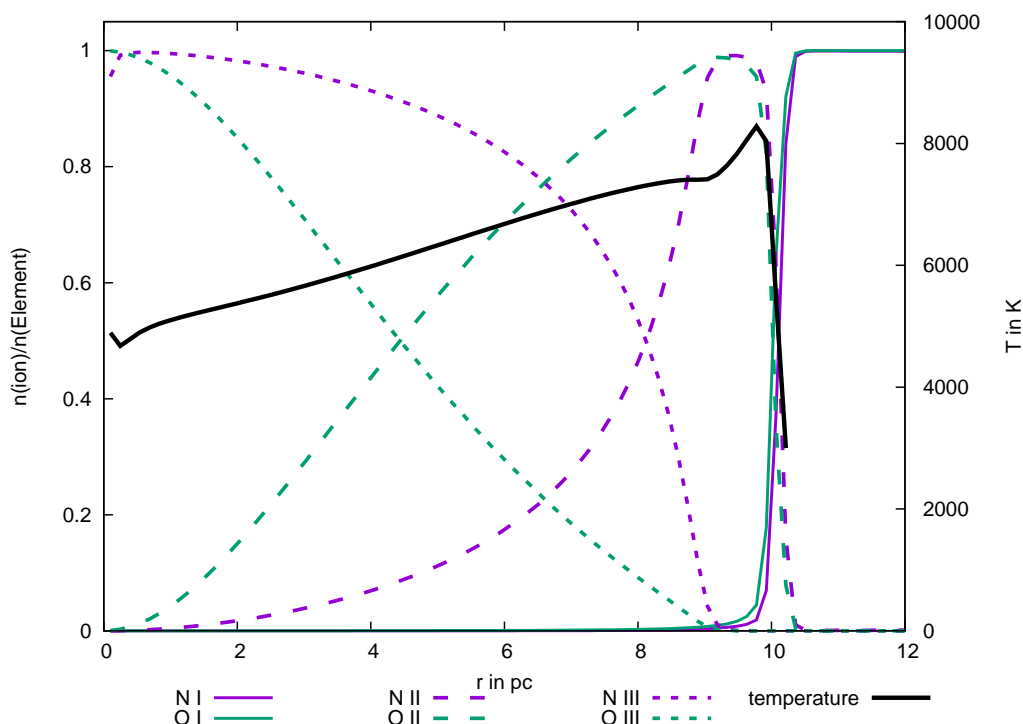


Figure 1.11: A comparison of the ionization structures of nitrogen and oxygen and the gas temperature in an H II region ($n_{\text{H}} = 10 \text{ cm}^{-3}$) around a 35 kK main-sequence star, where the metallicity of both the star and the gas in the H II region is solar. The temperature of the gas rises for larger distances from the source due to radiation hardening and the less effective cooling by transitions of the O III ion, which is less abundant in the outer parts of the H II region. As a result, an analysis based on the comparison of nebular and auroral emission lines of O III would result in a lower value for the temperature than an analogous analysis based on the emission lines of N II.

Thus an analysis of the auroral and nebular lines of N II will show larger temperatures than an analysis using the corresponding lines of O III. By contrast, for very metal poor gas with inefficient O III cooling and decreasing temperatures for larger distances from the sources (due to the cooling by the collisionally excited lines of neutral hydrogen), the temperature obtained from the N II lines is lower. This effect has, for example, been discussed by Ercolano et al. (2007).

1.4.1.4 Determining the temperature by measurements of the radio continuum

As shown in the last paragraph of Section 1.5.5, ionized nebulae become opaque for continuum radiation in the radio wavelength range so that their spectral energy distribution in that wavelength range can be described by a black body with a temperature that corresponds to the electron temperature of the gas. The main drawback of this method is that at radio frequencies, the minimum angle that can be resolved by single telescopes is larger or on the same order of magnitude as the apparent sizes of most H II regions. For example, an H II region with an electron number density of $n_e = 100 \text{ cm}^{-3}$, a temperature of 10 000 K, and a diameter of 10 pc reaches an optical depth (for a path through the center of the volume) of $\tau = 1$ for frequencies of $\nu \sim 200 \text{ MHz}$ ($\lambda \gtrsim 1.5 \text{ m}$) (Osterbrock & Ferland 2006). For this frequency, the angular resolution of a radio telescope with an aperture of 100 m is approximately 50 arc minutes (in a distance of 1 kpc this corresponds to a spatial extent of 15 pc).

Thus, either corrections have to account for the fact that the H II regions may not completely fill the beam of the telescope, or the resolution has to be increased using interferometric methods. Results of such investigations have, for instance, been presented by Shaver (1970), Subrahmanyam (1992), and Subrahmanyam et al. (2001).

1.4.2 Measurements of the electron density

1.4.2.1 Derivation of the electron density from emission line ratios

A collisionally excited state can be de-excited by radiative processes (where a photon is released) as well as by collisional processes (where the energy is transferred to a free electron involved in the collision process, cf. Section 1.5.5). For a very low electron number density $n_e \rightarrow 0$, the probability that an excited state will decay radiatively will approach unity, whereas it will be close to zero for very large number densities. The density where the probability of a collisional and a radiative de-excitation process are equal is called the *critical density*. For measurements of the electron density independently of other properties of the gas, the considered pair of lines should fulfill the following criteria: *a)* To avoid the effects of uncertainties concerning the chemical composition of the gas and its ionization structure both lines should be connected to the collisionally excited states of the same ion. *b)* To minimize the influence of the electron temperature of the gas, the energies required to reach the considered upper levels should be very similar. *c)* The critical densities of the de-excitation processes connected to the lines should be different and for at least one of the lines the critical density should be similar to the density of the observed object. These criteria are fulfilled, for example, by the transitions between the $^4S_{3/2}^o$ state and the $^2D^o$ states of O II and S II. The collisional excitation rate towards the $^2D_{5/2}^o$ and the $^2D_{3/2}^o$ levels is proportional to the statistical weights of the excited states, which is

$$C_{^4S_{3/2}^o, ^2D_{5/2}^o} / C_{^4S_{3/2}^o, ^2D_{3/2}^o} \approx \left(2 \cdot \frac{5}{2} + 1\right) / \left(2 \cdot \frac{3}{2} + 1\right) = 6/4 = 1.5 . \quad (1.2)$$

Below we will discuss the line ratios for the example of the [O II] doublet line. The computation of the [S II] line ratio is analogous. For an electron density of $n_e \rightarrow 0$ almost every excitation process is followed by a radiative transition to the ground state. Thus, the number of de-excitation processes equals the number of the corresponding excitation processes⁸ and the ratio between the two near-UV lines of O II is

$$\frac{\eta_{\lambda 3729}}{\eta_{\lambda 3726}} \approx \frac{C_{^4S_{3/2}^o, ^3D_{5/2}^o}}{C_{^4S_{3/2}^o, ^3D_{3/2}^o}} = 1.5. \quad (1.3)$$

If the electron density is large ($n_e \rightarrow \infty$), most transitions occur due to collisional processes, so that the ratios between the occupation numbers of the different excitation states are described by Boltzmann statistics. In the case of the O II and the S II ions this means that the occupation numbers of the $^2D^o$ levels of the O II or the S II ion are proportional to their statistical weights as the energy difference between the two levels is small compared to the mean thermal energy of the electrons. The ratio of the emissivities of the components of the O II doublet can be computed by multiplying the occupation numbers of the upper states with the corresponding Einstein coefficients for the transition into the ground state (the wavelengths and the values for the Einstein coefficients refer to the O II ion):

⁸This argument is only valid since the Einstein coefficient for the radiative transition between the $^2D_{3/2}^o$ level and the $^2D_{5/2}^o$ level is

$A(^2D_{3/2}^o, ^2D_{5/2}^o) = 1.3 \cdot 10^{-7} \text{ s}^{-1}$, i.e., much smaller than the Einstein coefficient of the corresponding transition into the ground state,

$A(^2D_{3/2}^o, ^4S_{3/2}^o) = A_{\lambda 3726} = 1.6 \cdot 10^{-4} \text{ s}^{-1}$.

$$\frac{\eta_{\lambda 3729}}{\eta_{\lambda 3726}} \approx \frac{n(^2D_{5/2}^o)}{n(^2D_{3/2}^o)} \cdot \frac{A_{\lambda 3729}}{A_{\lambda 3726}} = \frac{6}{4} \cdot \frac{3.6 \cdot 10^{-5} \text{ s}^{-1}}{1.6 \cdot 10^{-4} \text{ s}^{-1}} \approx 0.34. \quad (1.4)$$

We note that there is no simple analytic expression for the interpolation between the two extreme cases because the ratio between the lines is not only influenced by the critical densities concerning the recombination into the ground state, but also the collisional excitation and de-excitation rates between the two $^4S^o$ states. The line ratios for the electron densities between the extreme cases have to be computed numerically based on the transition rates defined by the atomic parameters (see Fig. 1.12), the electron density, and the temperature of the gas. The results of such a numerical computation are presented in Fig. 1.13.

The described technique for the determination of the electron density has been proposed first by Aller et al. (1949) and applied, for instance, by Seaton & Osterbrock (1957), Osterbrock & Flather (1959), Weedman (1968), Meatheringham et al. (1988), and Kingsburgh & Barlow (1992). Its main application is the study of planetary nebulae with electron densities of $n_e \sim 10^3 \text{ cm}^{-3} \dots 10^5 \text{ cm}^{-3}$, i.e., in the same order as the critical densities for the collisional de-excitation of $^2D_{5/2}^o$ ($n_{\text{crit}} \approx 3 \cdot 10^3 \text{ cm}^{-3}$) and $^2D_{3/2}^o$ ($n_{\text{crit}} \approx 1.6 \cdot 10^3 \text{ cm}^{-3}$). It is not suited to determine the electron structure in dilute gas like the DIG.

1.4.2.2 Measuring the dispersion of pulsar signals to study the clumpiness of the gas

Our discussion of the method to gain information about the density distribution of the ionized interstellar gas by measuring of the dispersion of pulsar signals follows Spitzer (1978).

When an electromagnetic wave traverses a plasma, its phase velocity is

$$v_{\text{phase}} = \frac{c}{\sqrt{1 - \frac{v_p^2}{v^2}}}, \quad (1.5)$$

where ν is the frequency of the considered electromagnetic radiation and ν_p is the plasma frequency given by

$$\nu_p = \sqrt{\frac{n_e e^2}{\pi m_e}}. \quad (1.6)$$

n_e is the number density of the electrons, e is the elementary charge and m_e is the mass of an electron. The group velocity v_{group} can be computed from the phase velocity by

$$v_{\text{group}} = \left[\frac{d}{d\nu} \left(\frac{\nu}{v_{\text{phase}}} \right) \right]^{-1} = c \sqrt{1 - \frac{v_p^2}{\nu^2}}. \quad (1.7)$$

If an electromagnetic pulse crosses a distance of s , the travel time therefore is

$$t = \frac{s}{c} + \frac{e^2}{2\pi m_e c} \int_0^s \frac{n_e ds}{\nu^2}. \quad (1.8)$$

The integral $DM = \int_0^s n_e ds$, which is performed along the line of sight, is called the *dispersion measure*. By observing pulsars at different frequencies and determining the differences of the arrival times the dispersion measure DM can be computed as

$$DM = \frac{2\pi m_e c (t_1 - t_2)}{e^2 \left(\frac{1}{\nu_1^2} - \frac{1}{\nu_2^2} \right)}, \quad (1.9)$$

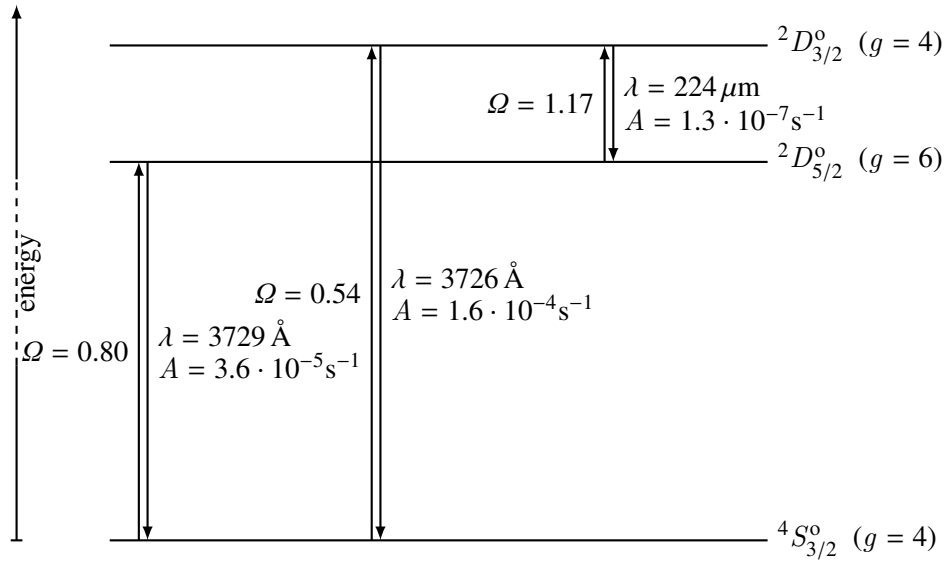


Figure 1.12: Diagram of the levels and transitions that are involved in the formation of the [O II] line doublet at $\lambda = 3726 \text{ \AA}$ and $\lambda = 3729 \text{ \AA}$. Shown are the term symbols and the statistical weights of the levels, the strengths Ω of collisional transitions between these levels, the Einstein coefficients A for the radiative transition as well as the wavelengths λ of the photons emitted by these radiative processes.

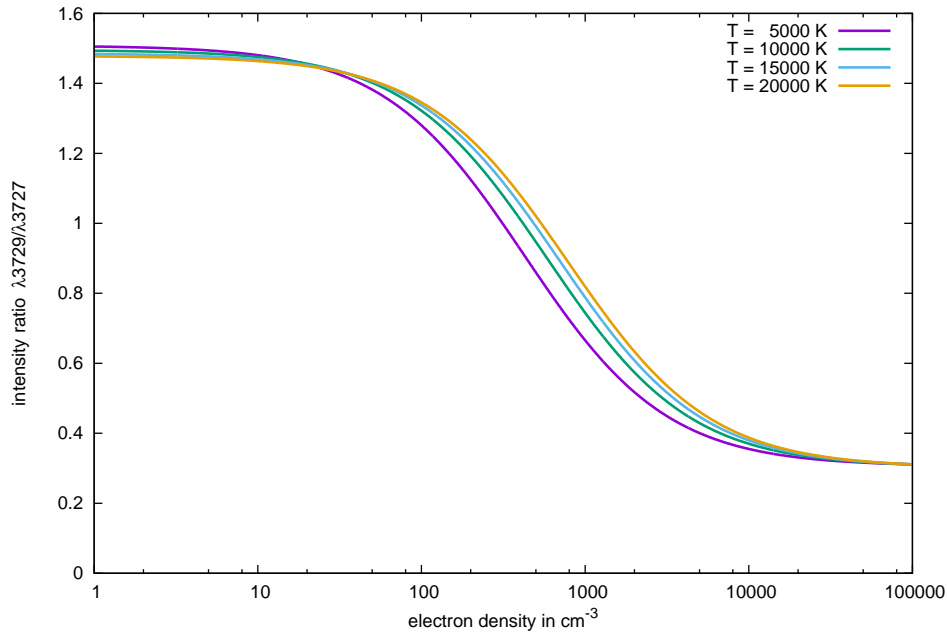


Figure 1.13: Emissivity ratio between the [O II] line emitted by the $2D_{5/2}^o - 4S^o$ transition at $\lambda = 3729 \text{ \AA}$, and the line emitted by the $2D_{3/2}^o - 4S^o$ transition at $\lambda = 3726 \text{ \AA}$ as a function of the electron density for different gas temperatures. In the low density limit almost each excitation process is followed by the inverse de-excitation process so that the emissivity ratio corresponds to the statistical weights. In the high-density limit the ratio of the occupation numbers of the $2D^o$ levels corresponds to their statistical weights and the emissivity ratio is therefore the ratio of the statistical weights multiplied by the corresponding Einstein coefficients of the radiative de-excitation process into the ground level. The plot shows that the intensity ratios do not depend strongly on the temperature of the gas. An analysis of this O II line ratio therefore is a robust method to determine the electron density. The ratios have been computed based on atomic data published by Pradhan (1976) and Zeippen (1987).

where t_1 and t_2 are the arrival times of the signals at the frequencies ν_1 and ν_2 .

The comparison of the dispersion measure with the emission measure $EM = \int_0^\infty n_e^2 ds$, which can be obtained by emission line diagnostics, provides information about the extent of inhomogeneity in the medium. While for a homogeneous medium $\langle n_e^2 \rangle = \langle n_e \rangle^2$, inhomogeneities will lead to an increased clumping factor $f_{cl} \langle n_e^2 \rangle / \langle n_e \rangle^2$. An obvious disadvantage of the pulsar method is the poor coverage of the sky due to the limited number of observable pulsars, so that measurements of the dispersion are predominantly used for large-scale structures like the warm ionized medium in the Milky Way.

Reynolds 1991 observed pulsars in globular clusters at heights of up to 1.2 kpc above the plane of the Milky Way. He found a clumped structure of the high-altitude gas between the Earth and the pulsars, where the mean density of the clumps was 0.08 cm^{-3} , and these clumps occupied about one fifth of the line of sight.

1.4.3 Determination of the element abundances in ionized gas

The chemical composition of ionized gas can in principle be determined by comparing the emission from the recombination lines of hydrogen with the line emission from the heavier elements, most importantly the collisionally excited lines. An important problem concerning the determination of the composition of ionized gas is that in many cases several ionization stages of an element contribute significantly to the total abundance of an element.

For example, in H II regions around intermediate-temperature O stars ($T_{\text{eff}} \sim 35\,000 \text{ K}$), O III is the dominant ionization stage in the inner regions while O II is the most abundant ionization stage in the outer regions. To study the chemical composition of an H II region it is therefore required to account for all of these ionization stages. By contrast, the emission of the hydrogen recombination lines occurs in the entire ionized volume. Consequently it is required to compare the hydrogen recombination lines with lines from all ionization stages present in significant amounts in the observed H II region. In the case of oxygen around O-type stars, there exist strong emission lines of both O II and O III in the optical wavelength range observable with ground-based instruments, which is why the abundance of oxygen is often used to represent the total metallicity of the gas.

However, as explained in Sect. 1.5.5, the collisionally excited optical emission lines are, unlike the emission lines in the far-infrared like the [O III] lines at $51.8 \mu\text{m}$ and $88.4 \mu\text{m}$, strongly temperature-dependent. At the same time the emission by collisionally excited metal ions is the most important cooling process in photoionized gas⁹. Thus, an increase of the metallicity has two opposing effects on the emission of these lines: On the one hand, a higher metallicity increases the number density of ions that are potential line emitters. On the other hand, the lower temperature of the gas decreases the probability of a collisional excitation process, which finally leads to the emission of optical line radiation. This can lead to a non-monotonic behavior of the optical line emission of metals, where for low metallicities there is an increase of the emission until a maximum is reached. If the metallicity is further increased, the effect of the cooler temperatures, which are also a result of the emission of infrared metal lines, that show only a weak dependence on temperature, leads to a decrease of the visible emission. This non-monotonic behavior can cause measurements based purely on the oxygen emission and hydrogen recombination lines to have two solutions where one represents a lower metallicity and the other one a higher metallicity (Kewley & Ellison 2008). To lift this degeneracy, further information is required. For instance, the different excitation energies of the optical lines of N II and O II lead to a temperature dependence of the corresponding line ratios that allows to decide whether the ionized gas

⁹With the exception of extremely metal-poor gas with metallicities of $Z \leq 0.1Z_\odot$, where the collisional excitation of hydrogen becomes dominant

is in the high-temperature or low-temperature regime. Still there is a considerable variation between different calibrations of the observations. For example, the analysis by Kewley & Ellison (2008), who have computed the mass-metallicity relation for $\sim 27\,000$ galaxies of the Sloan Digital Sky Survey (SDSS) using 10 different metallicity calibrations based on emission line ratios from H II regions, has shown a variation of up to 0.7 dex with respect to the absolute metallicity scale.

These problems can be partly overcome by observations in the infrared wavelength range, where the emissivity due to de-excitation of collisionally excited states is less dependent on an accurate knowledge of the temperature structure. Furthermore, in the mid-IR the effects caused by the absorption by the interstellar gas and dust are considerably less pronounced than in the visible range, which on the one hand allows the observations of nebulae that could otherwise not be detected and on the other hand reduces the uncertainties induced by a not fully understood absorption behavior of the interstellar dust. For example, the most abundant ionization stages of neon and sulfur emit de-excitation lines within a relatively narrow wavelength band (Ne II: $12.81\ \mu\text{m}$, Ne III: $15.656\ \mu\text{m}$, S III: $15.56\ \mu\text{m}$, S IV: $10.51\ \mu\text{m}$). Additionally, the above mentioned wavelength range contains the transition between the 7th and the 6th level of hydrogen, which allows to determine the emission measure along the corresponding line of sights. These properties of the emission spectrum in the corresponding wavelength range have been utilized by Rubin et al. (2006), Rubin et al. (2008) and Rubin et al. (2016), who have used observations with the Spitzer space telescope to determine the abundances of Ne and S in three galaxies with different metallicities.

1.5 The physics of photoionized gas

The nature of the sources of ionization described above varies considerably, but the various regimes of photoionized gas share the same basic types of physical processes that define their ionization and temperature structure as well as their line emission. These processes will be quantitatively described in this section.

First we will derive the equation of radiative transfer from the Boltzmann equation and introduce the quantities used to describe the radiation field (based on Pauldrach 2016). Subsequently we will show the structure of the rate equations for the ionization and recombination rates and explain the computation of the required rate coefficients. Finally, we will discuss the transfer of line radiation involved in bound-bound transitions, the interaction between ions in the gas, and provide a short overview about the role of dust in H II regions. The observational techniques to study the properties of the gas resulting from these processes will be explained in the next section.

1.5.1 The equation of radiative transfer derived from the Boltzmann equation

The temporal evolution of particle distributions by means of their phase-space densities, i.e., the number of particles per phase-space volume,

$$f(\mathbf{x}, \mathbf{p}, t) = \frac{dN}{d^3x d^3p} \quad (1.10)$$

is described by the Boltzmann equation:

$$\frac{\partial f}{\partial t} + \frac{\partial \mathbf{x}}{\partial t} \nabla_{\mathbf{x}} f + \frac{\partial \mathbf{p}}{\partial t} \nabla_{\mathbf{p}} f = \left[\frac{\partial f}{\partial t} \right]_{\text{ic}}, \quad (1.11)$$

where the vector \mathbf{x} is the location of the particles and \mathbf{p} their momentum. $\nabla_{\mathbf{x}}$ and $\nabla_{\mathbf{p}}$ are the respective gradients of the phase-space density, and $\left[\frac{\partial f}{\partial t}\right]_{\text{ic}}$ is the internal change of the phase-space density due to the generation (emission) or destruction (absorption) of particles or due to scattering processes.

In the case of photons, the momentum can be rewritten as

$$\mathbf{p} = \frac{h\nu}{c}\hat{\mathbf{n}}, \quad (1.12)$$

where h is Planck's constant, ν the frequency of the photons, c the speed of light, and $\hat{\mathbf{n}}$ the directional unit vector. Accordingly, the velocity \mathbf{v} of the photons can be expressed as

$$\mathbf{v} = \frac{\partial \mathbf{x}}{\partial t} = c\hat{\mathbf{n}}. \quad (1.13)$$

The integral form of Eq. 1.10 is

$$\begin{aligned} N &= \int f(\mathbf{x}, \mathbf{p}, t) d^3x d^3p = \\ &\oint f(\mathbf{x}, \hat{\mathbf{n}}, p, t) d^3x p^2 dp d\Omega, \end{aligned} \quad (1.14)$$

where the first line describes the momentum space in Cartesian coordinates, the second line in spherical coordinates, where the integration is performed over the absolute value of p and the solid angle Ω .

For calculations concerning the radiative transfer it is often useful to replace the momentum-space by the frequency-space of the photons using Eq. 1.12 (N_{γ} is the number of photons within the considered phase space):

$$N_{\gamma} = \int \tilde{f}(\mathbf{x}, \hat{\mathbf{n}}, \nu, t) d^3x d\Omega d\nu \quad (1.15)$$

where from Eq. 1.14 follows

$$\tilde{f}(\mathbf{x}, \hat{\mathbf{n}}, \nu, t) = \frac{h^3 \nu^2}{c^3} f(\mathbf{x}, \mathbf{p}(\hat{\mathbf{n}}, \nu), t). \quad (1.16)$$

When neglecting the expansion of space or relativistic effects, the temporal derivative of the momentum of the photons, i.e., the force acting upon them is zero, such that the Boltzmann equation can be simplified to

$$\frac{\partial \tilde{f}}{\partial t} + c\hat{\mathbf{n}}\nabla_{\mathbf{x}}\tilde{f} = \left[\frac{\partial \tilde{f}}{\partial t}\right]_{\text{ic}}, \quad (1.17)$$

To relate the phase space density of the photons to the commonly used measures of radiation, flux and (specific) intensity, we now consider the transport of photons, whose phase-space density is described by \tilde{f} through an infinitesimal surface element $d\mathbf{A}$, where the direction of the surface normal vector corresponds to the ‘‘outward direction’’. The net number of photons that is transported through an infinitesimal spatial surface element $d\mathbf{A}$ per time unit is related to the phase space density by

$$\begin{aligned} \frac{dN}{dt} &= f(\mathbf{x}, \mathbf{p}, t)\mathbf{v}(\mathbf{p}) \cdot d\mathbf{A} d^3p = \\ &\underbrace{\int_{\mathbf{v}\cdot d\mathbf{A}>0} f(\mathbf{x}, \mathbf{p}, t) \cdot |c\hat{\mathbf{n}} \cdot d\mathbf{A}| d^3p^3}_{\text{outward flowing particles}} - \underbrace{\int_{\mathbf{v}\cdot d\mathbf{A}<0} f(\mathbf{x}, \mathbf{p}, t) \cdot |c\hat{\mathbf{n}} \cdot d\mathbf{A}| d^3p}_{\text{inward flowing particles}} \end{aligned} \quad (1.18)$$

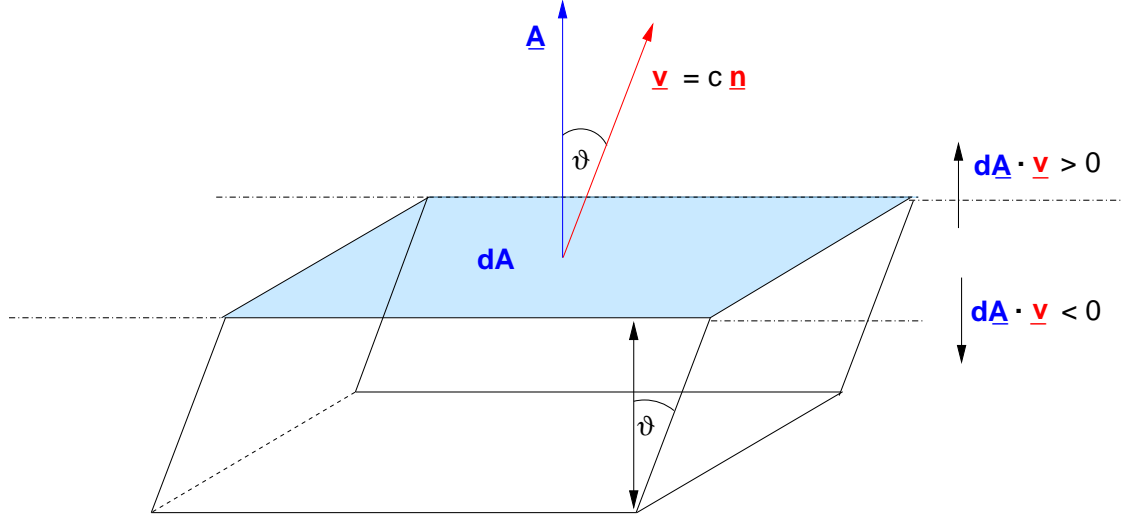


Figure 1.14: The net number flux of photons per a frequency interval $d\nu$ corresponds to the phase-space density $\tilde{f}(\mathbf{x}, \hat{\mathbf{n}}, \nu, t)$ multiplied with the scalar product of the particle velocity $c\hat{\mathbf{n}}$ and the surface vector $d\mathbf{A}$ integrated over the sphere. The energy flux is then obtained by multiplying the number flux with the photon energy $h\nu$.

The flux of an advected quantity $K(\mathbf{x}, \mathbf{p}, t)$ through the surface element results from Eq. 1.18 as

$$F_{\mathbf{A}} = \int f(\mathbf{x}, \mathbf{p}, t) \cdot K(\mathbf{x}, \mathbf{p}, t) \mathbf{v}(\mathbf{p}) \cdot d\mathbf{A} d^3p = \int_{\mathbf{v} \cdot d\mathbf{A} > 0} f(\mathbf{x}, \mathbf{p}, t) \cdot K(\mathbf{x}, \mathbf{p}, t) \cdot |\mathbf{v} \cdot d\mathbf{A}| d^3p - \int_{\mathbf{v} \cdot d\mathbf{A} < 0} f(\mathbf{x}, \mathbf{p}, t) \cdot K(\mathbf{x}, \mathbf{p}, t) \cdot |\mathbf{v} \cdot d\mathbf{A}| d^3p \quad (1.19)$$

The special case of Eq. 1.19 that is important in the context of radiative transfer is the energy flux of photons (c.f., Eq. 1.14), where the advected quantity is the energy $E_\gamma = h\nu$ of the photons:

$$F_{\mathbf{A}} = \frac{dE}{dt} = \int f(\mathbf{x}, \mathbf{p}, t) \cdot h\nu c \mathbf{n} \cdot d\mathbf{A} dp^3 = \oint \underbrace{\tilde{f}(\mathbf{x}, \hat{\mathbf{n}}, \nu, t) \cdot h\nu c}_{I_\nu} \cos \vartheta dA d\Omega d\nu \quad (1.20)$$

Here ϑ is the angle between the direction of the radiation and the outward normal of the surface element and the cosine follows from the scalar product $\hat{\mathbf{n}} \cdot d\mathbf{A} = \cos \vartheta dA$. The expression

$$I_\nu = \tilde{f}(\mathbf{x}, \mathbf{p}, t) \cdot h\nu c = \frac{dE}{\cos \vartheta dA d\Omega dt}, \quad (1.21)$$

i.e., the radiative energy passing through an infinitesimal surface element dA per time, solid angle, and frequency (as sketched in Fig. 1.15) is called the *specific intensity*. In the cgs system the unit of the intensity is $[I_\nu] = \text{erg cm}^{-2} \text{sr}^{-1} \text{Hz}^{-1} \text{s}^{-1}$.¹⁰ Eq. 1.21 can be solved for \tilde{f}

$$\tilde{f}(\mathbf{x}, \hat{\mathbf{n}}, \nu) = \frac{1}{h\nu c} I_\nu(\mathbf{x}, \hat{\mathbf{n}}, \nu) \quad (1.22)$$

¹⁰Alternatively, the intensity can also be defined per wavelength interval:

$I_\lambda(\mathbf{r}, \hat{\mathbf{n}}, t) = \frac{dE}{dA d\Omega d\lambda dt} = \frac{dE}{dA d\Omega d\nu dt} \cdot \left| \frac{d\nu}{d\lambda} \right| = I_\nu \cdot \frac{c}{\lambda^2} = I_\nu \cdot \frac{\nu^2}{c}$, where the unit of the specific intensity is $[I_\lambda] = \text{erg cm}^{-2} \text{sr}^{-1} \text{cm}^{-1} \text{s}^{-1}$

In this text, we will generally describe the quantities that characterize the radiation field as a function of frequency.

and the result inserted into the Boltzmann equation (Eq. 1.17), which leads to

$$\frac{1}{ch\nu} \left[\frac{\partial}{\partial t} + c\hat{\mathbf{n}}\nabla_x \right] I_\nu = \frac{1}{h\nu} \left[\frac{\partial I_\nu}{c\partial t} \right]_{ic}. \quad (1.23)$$

The right-hand side of Eq. 1.23 contains in its denominator the product of the infinitesimal time interval with the speed of light which corresponds to the distance ds traveled by the photons within that time interval such that Eq. 1.23 can be written as

$$\frac{1}{ch\nu} \left[\frac{\partial}{\partial t} + c\hat{\mathbf{n}}\nabla_x \right] I_\nu = \frac{1}{h\nu} \left[\frac{dI_\nu^{em} - dI_\nu^{abs}}{ds} \right]_{ic}, \quad (1.24)$$

where dI_ν^{em}/ds is the increase of the intensity per distance element due to emission processes and dI_ν^{abs}/ds is the corresponding reduction of intensity due to absorption processes. It can be assumed that for infinitesimal path elements ds the emission properties of the material do not change so that the contribution to the intensity due to (spontaneous) emission processes per length of a path element remains constant, i.e.,

$$dI_\nu^{em}/ds = \eta_\nu, \quad (1.25)$$

where η_ν is called the *emissivity* of the medium. If the properties of the absorbing medium do not change, the probability for all photons of the same direction and frequency to be absorbed within the path element ds is the same. Consequently, the change of the intensity is proportional to the intensity itself:

$$dI_\nu^{em}/ds = \chi_\nu I_\nu \quad (1.26)$$

where the proportionality factor χ_ν is called *opacity*. Like the absorption, the change of intensity due to stimulated emission (see Sect. 1.5.2.3 and Sect. 1.5.3) is proportional to the incoming intensity and can therefore be interpreted as “negative opacity”. So the general form of the equation of radiative transfer (in absence of relativistic effects) is:

$$\frac{1}{h\nu} \left[\frac{1}{c} \frac{\partial}{\partial t} + \hat{\mathbf{n}} \cdot \nabla_x \right] I_\nu(\mathbf{r}, \hat{\mathbf{n}}, \nu, t) = \frac{1}{h\nu} [\eta(\mathbf{r}, \hat{\mathbf{n}}, \nu, t) - \chi(\mathbf{r}, \hat{\mathbf{n}}, \nu, t) I_\nu] \quad (1.27)$$

which can be simplified to

$$\frac{1}{c} \frac{\partial}{\partial t} + \hat{\mathbf{n}}\nabla_x I_\nu = \eta_\nu - \chi_\nu I_\nu. \quad (1.28)$$

The moments of the specific intensity. For computations of the interaction between the radiation field and matter, often the moments of the intensity are used instead of the specific intensity itself. In the general case, the k -th moment of the intensity is defined as a tensor whose components are

$$M_{k,\nu}^{i_1, i_2, \dots, i_k}(\mathbf{r}, t) = \frac{1}{4\pi} \oint I_\nu(\mathbf{r}, \hat{\mathbf{n}}, \nu, t) \prod_{\ell=1, k} n^{i_\ell} d\Omega, \quad (1.29)$$

where $i_\ell \in \{1, 2, 3\}$ and n^{i_ℓ} is one of the components of the directional unit vector¹¹. The integration is performed over the unit sphere. The first three moments of the intensity are the scalar *mean intensity*

$$J_\nu(\mathbf{r}, t) = \frac{1}{4\pi} \oint I_\nu(\mathbf{r}, t) d\Omega = \frac{1}{4\pi} \int_0^\pi \int_0^{2\pi} I_\nu(r, \vartheta, \phi, t) \sin \vartheta d\phi d\vartheta, \quad (1.30)$$

¹¹In the spherically symmetric case, Eq. 1.29 simplifies to $M_{k,\nu} = \frac{1}{2} \int_0^\pi I_\nu(r, \mu, \nu, t) \mu^k d\mu$, where r is the distance from the center and μ the cosine of the angle between the ray direction and the outward normal on the spherical surface element.

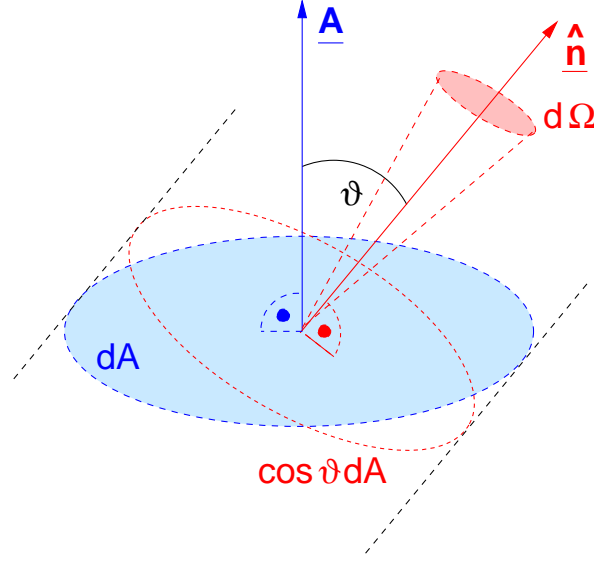


Figure 1.15: The (specific) intensity I_ν is defined as the amount of energy dE passing through a surface element dA into a solid angle $d\Omega$ around the direction $\hat{\mathbf{n}}$, divided by the cosine of the angle ϑ between the surface normal \mathbf{A} and the direction $\hat{\mathbf{n}}$.

the *Eddington flux*¹², a vector, for which the i -th entry is

$$H_\nu^i(\mathbf{r}, t) = \frac{1}{4\pi} \oint I_\nu(\mathbf{r}, \hat{\mathbf{n}}, t) n^i d\Omega, \quad (1.31)$$

and the *K-integral*, a matrix where the entry in the i -th line and j -th column is defined as

$$K_\nu^{ij}(\mathbf{r}, t) = \frac{1}{4\pi} \oint I_\nu(\mathbf{r}, \hat{\mathbf{n}}, t) n^i n^j d\Omega. \quad (1.32)$$

1.5.2 The ionization balance in H II regions

As mentioned above, the defining property of H II regions is the presence of (photo-)ionized hydrogen gas. Although hydrogen is by far the most abundant element in the interstellar medium, the temperature and the emission spectrum of H II regions are also strongly affected by the ionization structure of helium and the most abundant metals like carbon, nitrogen, oxygen, neon, and sulfur. Below we will discuss the main processes that establish the ionization balance in H II regions.

1.5.2.1 The general structure of the rate equations.

In principle, the mathematical formalism described in this section can be applied both to different ionization stages and to different excitation states within an ionization stage. In the limit case of the dilute gas in H II regions (“nebular approximation”), it can, however, be assumed that all ionization and recombination processes occur from the ground state of the corresponding ions, which allows the

¹²By multiplying the *Eddington flux* by 4π the *energy flux* F_ν (often simply called *flux*) is obtained. In some texts also the *astrophysical flux* F_ν^* is used, which is related to the energy flux F and the Eddington flux H_ν via $F_\nu^* = F_\nu/\pi = 4H_\nu$. For black body radiators the value of the astrophysical flux corresponds to Planck’s function, i.e., $F_\nu^* = B_\nu = \frac{2h\nu^3}{c^2} \frac{1}{e^{h\nu/kT} - 1}$.

use of a considerably simplified equation systems to compute the ionization state of the gas as will be quantitatively explained below in our discussion of the recombination and ionization processes.

The temporal change of the number density n_i of a particle in the state i can be described as the difference of the rates populating the i -th stage and the sum of all processes depopulating that stage. In a linear approximation the rates, i.e., the number of processes per time and volume unit, for a given transition can be expressed as the products of the number densities of the original states and the corresponding rate coefficients. The change of the number density n_i can therefore be expressed as

$$\frac{d}{dt}n_i = \sum_{j \neq i} \mathcal{P}_{ji}n_j - \sum_{j \neq i} \mathcal{P}_{ij}n_i, \quad (1.33)$$

where \mathcal{P}_{ij} is the rate coefficient for a transition from the state i to the state j .

The rate equations that contain all relevant transitions between the states of a particle can be summarized in matrix-vector form,

$$\frac{d}{dt}\mathbf{n} = \mathbf{G} \cdot \mathbf{n}, \quad (1.34)$$

where the entries of the column vector \mathbf{n} are the occupation numbers of the states and the matrix \mathbf{G} contains on its diagonal the negative of the sum of all rate coefficients for processes depopulating the corresponding states, whereas in the case non-diagonal elements of the matrix, the element in the i -th line and the j -th column contains the rate coefficients for the transition between the j -th and the i -th state:

$$g_{ii} = - \sum_{j \neq i} \mathcal{P}_{i,j} \quad (1.35)$$

$$g_{ij} = \mathcal{P}_{ji} \quad \text{for } i \neq j. \quad (1.36)$$

The stationary case. The stationary case is reached if for each point in the considered space, the sum of the rates of processes populating a state equals the sum of the rates of all processes depopulating that state, such that the occupation numbers of the involved states remain constant¹³:

$$\sum_{i \neq j} \mathcal{P}_{i,j}n_i = \sum_{i \neq j} \mathcal{P}_{j,i}n_j. \quad (1.37)$$

In this case the matrix equation Eq. 1.34 becomes

$$\mathbf{G} \cdot \mathbf{n} = \mathbf{0}. \quad (1.38)$$

The condition of particle conservation can be enforced by replacing the entries of one line of \mathbf{G} with 1 and the corresponding entry of the vector on the left-hand side by the total abundance of all states belonging to the same element.

It should be noted that the stationary case is an idealization, as the properties of the ionizing sources change over time and their feedback by radiation pressure and outflows like stellar winds modifies the density structure of the surrounding matter which in turn leads to changed properties of the gas with respect to its interaction with radiation, e.g., by a modified opacity.

¹³In contrast to the stationary case the condition of *local thermal equilibrium (LTE)* requires that the number of transitions from a state i into a state j is equal to the number of transitions from state j into state i for all states i and j , i.e., $\mathcal{P}_{i,j}n_i = \mathcal{P}_{j,i}n_j \quad \forall i, j$ (detailed balance).

1.5.2.2 Ionization processes

Photoionization. Using Eq. 1.15, and Eq. 1.30 the photoionization rate from the state l of a lower ionization stage i into the state u of an upper ionization stage j is computed as

$$R_{lu} = \int_{\nu_{lu}}^{\infty} n_{\gamma,\nu} c a_{lu}(\nu) d\nu = \int_{\nu_{lu}}^{\infty} \oint \tilde{f} c d\Omega a_{lu}(\nu) d\nu = \int_{\nu_{lu}}^{\infty} \oint \frac{I_{\nu}}{ch\nu} c d\Omega a_{lu}(\nu) d\nu = \int_{\nu_{lu}}^{\infty} \frac{4\pi J_{\nu}}{h\nu} a_{lu}(\nu) d\nu, \quad (1.39)$$

where $n_{\gamma,\nu}$ is the spatial density of photons within a frequency interval of $[\nu, \nu + d\nu]$, ν_{lu} is the threshold frequency for the transition that corresponds to the energy difference between the involved stages, $a_{lu}(\nu)$ is the frequency-dependent photoionization cross-section¹⁴ and J_{ν} the mean intensity of the radiation field.

In the nebular approximation, it can be assumed that the timescales of the radiative relaxation of an excited state are much shorter than the timescales for ionization and recombination processes even for forbidden transitions. As a result, almost every ionization process takes place from the ground state of the lower ionization stage. However, the ionization process may lead to different electronic states of the higher ionization stage. The total ionization rate coefficient \mathcal{R}_{ij} of an ion i into an ion j is thus:

$$\mathcal{R}_{ij} \approx \sum_{u=u_0}^{\infty} R_{l_0 u}, \quad (1.40)$$

where l_0 and u_0 are the ground states of the lower and upper ionization stages i and j , respectively, and the summation is performed over the relevant excitation stage immediately after the ionization.

Collisional ionization. Besides photoionization, there exist also ionization processes caused by collisions between ions and electrons. Like the photoionization cross-sections, the accurate cross-sections for ionization by collisions with free electrons have to be computed quantum-mechanically. In an approximation (Seaton 1962) the collisional ionization rates can be computed as

$$C_{lu} = n_e \frac{1.55 \cdot 10^{13}}{\left[\frac{T}{K}\right]^{1/2}} \bar{g} a_{lu}(\nu_0) \frac{e^{-h\nu_{lu}/kT}}{h\nu_{lu}/kT}, \quad (1.41)$$

where T is the temperature and $h\nu_{lu}$ the energy required for the ionization of an atom or ion in the state l into an ion of the state u . $a_{lu}(\nu_0)$ is the photoionization cross-section at the ionization threshold. The gaunt factor \bar{g} can be approximated as 0.1 for neutral atoms, 0.2 for singly ionized ions, and 0.3 for higher ionization stages (Seaton 1962). For dilute gas in H II regions the contribution of the collisional ionization to the total ionization rates is small compared to photoionization.¹⁵

¹⁴The photoionization cross-section $a_{lu}(\nu)$ has to be computed quantum-mechanically. A common approach to parameterize these results is to apply Seaton's approximation (Seaton 1959, cf. Figs. 1.16 and 1.17):

$$a_{lu}(\nu) = a_{lu} \left(\beta_{lu} \left(\frac{\nu}{\nu_{lu}} \right)^{-s_{lu}} + (1 - \beta_{lu}) \left(\frac{\nu}{\nu_{lu}} \right)^{-s_{lu}-1} \right),$$

where a_{lu} , β_{lu} , and s_{lu} are fit parameters that have to be determined for each ionization process.

¹⁵Let us, for example, assume a homogeneous H II region with an electron number density of $n_e = 200 \text{ cm}^{-3}$ and uniform temperature of $T = 10\,000 \text{ K}$ that is ionized by a star with 9 solar radii and an effective temperature of $T_{\text{eff}} = 40\,000 \text{ K}$ (here approximated by a black-body radiator). For simplicity we furthermore assume the Strömgren approximation, i.e., assume the gas within the ionized volume to be almost completely ionized and consequently optically thin. In this case the photoionization rate coefficient at a distance of 90% of the radius of the ionized sphere from the source exceeds the collisional ionization rate coefficient by a factor of approximately $2 \cdot 10^5$. However, this factor is strongly temperature dependent and is reduced to approximately 25 for a gas temperature of 20 000 K.

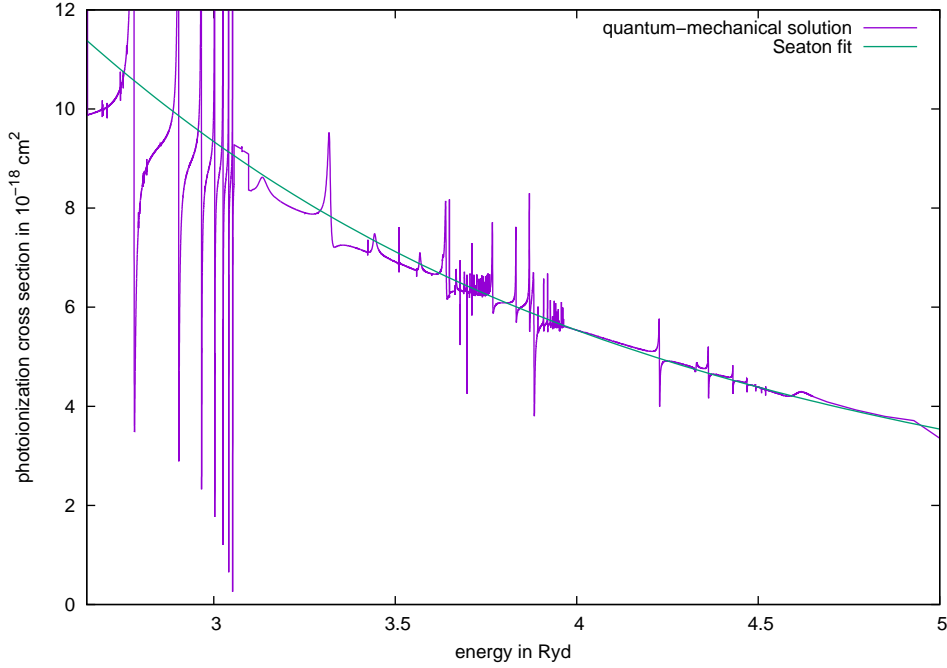


Figure 1.16: Comparison between a quantum-mechanical computation of the energy-dependent photoionization cross-section of the O^+ ion with Seaton's fit formula for the corresponding data. The peaks of the cross sections are related to discrete states which can decay via auto-ionization of the corresponding ion. The quantum-mechanical data have been provided by K. Butler.

1.5.2.3 Recombination processes

The recombination rates. The radiative recombination rate coefficient from a state u in the higher ionization stage to the state l of a lower ionization stage can be computed as

$$R_{ul} = \left(\frac{n_l}{n_u}\right)^* \int_{\nu_{lu}}^{\infty} \frac{4\pi a_{lu}(\nu)}{h\nu} \left(\frac{2h\nu^3}{c^2} + J_\nu\right) e^{-\frac{h\nu}{kT}} d\nu, \quad (1.42)$$

where the integration is performed between the threshold frequency ν_{lu} of the corresponding ionization process, which is equal to the energy difference between the stages, and infinity. n_e is the electron number density and

$$\left(\frac{n_l}{n_u}\right)^* = n_e \frac{g_l}{g_u} e^{h\nu_{lu}/kT} \frac{1}{2} \left(\frac{h^2}{2\pi m_e kT}\right)^{3/2} \quad (1.43)$$

is the Saha-Boltzmann factor, i.e., the ratio between the number densities of ion the states l and u that would prevail in thermodynamic equilibrium¹⁶. The J_ν term in Eq. 1.42 accounts for the stimulated

¹⁶The Saha-Boltzmann factor can be derived as follows (Mihalas1970):

The energy difference of the ionized system u with respect to the energy of the non-ionized state l is the sum of the ionization energy of the previous state and the kinetic energy of the free electron, i.e.,

$$\Delta E = h\nu_{lu} + \frac{1}{2} m_e v^2.$$

If the considered gas is in thermodynamic equilibrium, the number ratio of ions in the upper state where the velocity of the electron emitted by the ionization process lies between v and $v + dv$ to the ions in the lower ionization stage is

$$\frac{dn_u(v)/dv}{n_l} = \frac{g_{total}}{g_l} e^{-(h\nu_{lu} - \frac{1}{2} m_e v^2)/(kT)},$$

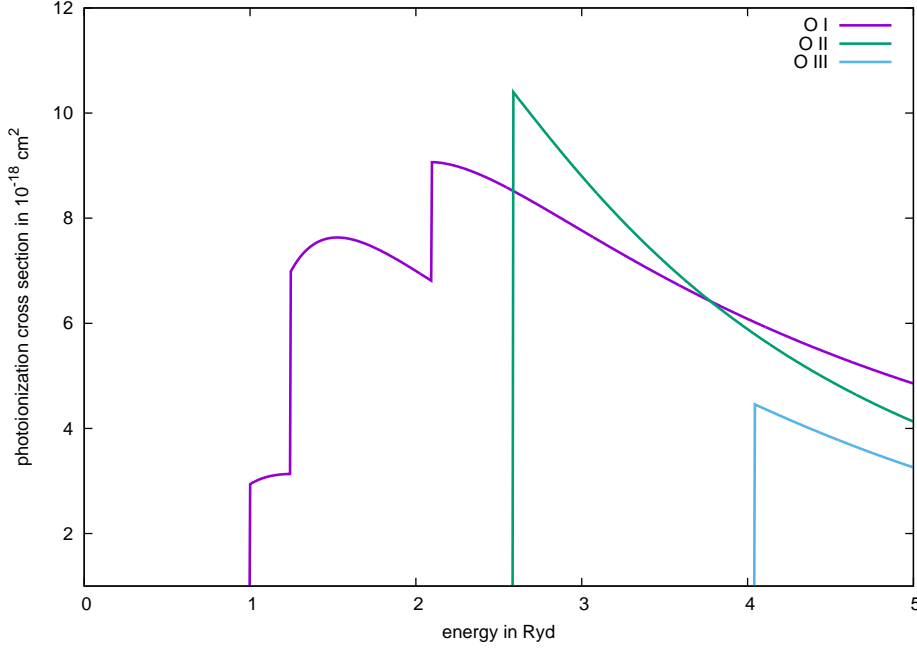


Figure 1.17: Energy-dependent ionization cross sections of neutral, singly ionized, and doubly ionized oxygen (in the Seaton approximation). Each of these ions emits collisionally excited lines in the optical or near-UV wavelength range. Thus, ground-based instruments can be used to determine the ionization structure of oxygen which in turn provides information about the properties of the ionizing radiation field. Furthermore, O II and O III are among the strongest coolants in H II regions. Therefore an accurate knowledge of the ionization structure of oxygen is also crucial for determining the temperature structure of ionized gaseous nebulae. For the ionization of neutral oxygen there exist three ionization processes (one to the ground state and two into excited states of O II) that – depending on the photon energy – contribute significantly to the total ionization cross section, which results in the non-monotonic behavior of the ionization cross-section as a function of energy.

emission, which can, however, be neglected in the ionized interstellar gas¹⁷.

where $g_{\text{total}} = g_u \times g_e$ is the product of the statistical weights of the ion in state u and the free electron. The statistical weight of a free electron within the infinitesimal volume $d^3\mathbf{x}$ and momentum range $d^3\mathbf{p}$ is

$$g_e = \frac{2d^3\mathbf{x}d^3\mathbf{p}}{h^3},$$

where the factor 2 results from two the possible two spin states of the free electron and the infinitesimal volume can be set to the volume available per electron, which equals the inverse of the electron number density: $d^3\mathbf{x} = n_e^{-1}$. Concerning the momentum space we can assume an isotropic movement of the electrons in the comoving system of the considered gas. The momentum space can therefore be expressed in spherical coordinates as

$$d^3\mathbf{p} = 4\pi p^2 dp = 4\pi m_e^3 v^2 dv.$$

The number of particles in the upper state for a given velocity interval of the free electron can be calculated by inserting the results for the statistical weights of the free electron in the Boltzmann distribution and is

$$\frac{dn_u}{n_l} = \frac{8\pi m_e^3}{h^3} \frac{g_u}{n_e g_l} e^{-\frac{h\nu_{lu} + \frac{1}{2}m_e v^2}{kT}} v^2 dv.$$

Substituting $\xi := \sqrt{\frac{1}{2}m_e v^2}$ leads to the equation

$$\frac{n_u n_e}{n_l} = \frac{8\pi m_e^3}{h^3} \frac{g_u}{g_l} e^{-\frac{h\nu_{lu}}{kT}} \left(\frac{2kT}{m_e}\right)^{3/2} \int_0^\infty e^{-\xi^2} \xi^2 d\xi.$$

By performing the integral ($\int_0^\infty e^{-\xi^2} \xi^2 d\xi = \sqrt{\pi}/4$) and dividing n_e by the result of the entire expression Eq. 1.43 is obtained.

¹⁷For instance, at a distance of 1 pc from a star with 9 solar radii and an effective temperature of 40 000 K, which we approximate by a black-body radiator, and a gas temperature of 10 000 K and an electron number density of $n_e = 10 \text{ cm}^{-3}$

In the nebular approximation, it can be assumed that all recombination processes occur from the ground level u_0 of the ion j . Still, the recombination may lead into the ground state l_0 or different excited stages of the lower ionization stage i . The total recombination rate coefficient therefore is

$$\mathcal{R}_{ji} \approx \sum_{l=l_0}^{\infty} R_{u_0 l}. \quad (1.44)$$

Derivation of the relation between ionization and recombination rates. It is clear from Eq. 1.42, that there is a close connection between wavelength-dependent ionization cross-sections and the corresponding temperature-dependent recombination rates. This follows from the Milne relation (Milne 1924, the derivation in this text is based on Mihalas & Mihalas 1984 and Osterbrock & Ferland 2006) that connects the cross-section of an ionization process for a given photon energy with the recombination-cross section of the corresponding inverse process. To derive the Milne equation we first consider the case of thermodynamic equilibrium, where each microphysical process occurs as often as the exactly inverse process (detailed balance). Concerning the ionization equilibrium this means that the rate of capture processes of electrons with a velocity of v , where the capturing ions change from the upper state u into the lower state l , equals the rate of ionization processes where electrons with the velocity v are emitted and the atoms or ions from which the electrons are removed undergo a transition from state l into state u .

There exist two types of radiative recombination processes, spontaneous and induced recombination. While the spontaneous recombination rate is independent of the radiation field, the induced contribution is proportional to the mean intensity of the radiation at photon energies equal to the sum of the ionization energy and the kinetic energy of the emitted photon. Thus the recombination rate for an electron with velocity v can be expressed as

$$n_l B_{lu} J_\nu dv = n_e f(v) v (A_{ul}(v) + B_{ul}(v) J_\nu) dv, \quad (1.45)$$

where $f(v)$ is the velocity distribution of the electrons, which in the case of thermodynamic equilibrium is the Maxwellian distribution,

$$f(v)dv = \left(\frac{m_e}{2\pi kT}\right)^{3/2} \exp\left(-\frac{mv^2}{2kT}\right) 4\pi v^2 dv. \quad (1.46)$$

With $h\nu = \frac{1}{2}m_e v^2 + h\nu_{lu}$ the relationship between the differential terms dv and $d\nu$ is

$$dv = \frac{h}{m_e v} d\nu \quad (1.47)$$

In the equilibrium case, the spectral energy distribution of the radiation field is described by Planck's law, i.e.,

$$J_\nu = B_\nu = \frac{2h\nu^3}{c^2} \frac{1}{e^{\frac{h\nu}{kT}} - 1}. \quad (1.48)$$

Using the identity $J_\nu = B_\nu$, Eq. 1.45 can be solved for B_ν :

$$B_\nu = \frac{A_{ul}/B_{ul}}{\frac{n_l^* B_{lu} m_e}{n_u^* n_e f(v) h B_{ul}} - 1}, \quad (1.49)$$

the contribution of the induced recombination to the total recombination rate is only $5 \cdot 10^{-25}$ for recombinations into the ground state of hydrogen and a similar value for recombination processes into the 10th excited state.

where the asterisk marks number densities thermodynamic equilibrium. A comparison of the expressions for B_ν in Eq. 1.48 and Eq. 1.49 shows the following relations between the coefficients in the equilibrium case:

$$A_{ul}(v) = \frac{2h\nu^3}{c^2} B_{ul}(v) \quad (1.50)$$

and

$$\frac{B_{lu}(v)}{B_{ul}(v)} = \frac{h}{m_e} n_e f(v) \left(\frac{n_u}{n_l} \right)^* e^{\frac{h\nu}{kT}}. \quad (1.51)$$

The ratio between the induced radiative downward rates and the radiative upward rates can be obtained from Eq. 1.51 as

$$\frac{n_e f(v) v n_u^* B_{ul}(v) B_\nu dv}{n_l^* B_{lu}(v) B_\nu dv} = n_e f(v) v \left(\frac{n_u}{n_l} \right)^* \frac{m_e v}{h} \frac{1}{n_e f(v)} \left(\frac{n_l}{n_u} \right)^* e^{-\frac{h\nu}{kT}} \frac{h}{m_e v} = e^{-\frac{h\nu}{kT}}. \quad (1.52)$$

The number of spontaneous recombination processes for a given electron velocity can be obtained by subtracting the induced recombination rates from the total number of radiative recombination processes, which in the case of thermodynamic equilibrium, equals the radiative ionization rate by photons with a frequency equal to the frequency of the photons emitted in the recombination process:

$$\frac{n_e(v) f(v) v n_u^* B_{ul}(v) dv}{n_l^* B_{lu}(v) J_\nu dv} = 1 - e^{-\frac{h\nu}{kT}}. \quad (1.53)$$

The coefficient $A_{ul}(v)$ can be interpreted as the cross-section for the spontaneous recombination process:

$$A_{ul} = \sigma_{ul}(v). \quad (1.54)$$

The relation between the coefficient B_{lu} and frequency-dependent ionization cross-section a_ν follows from Eq. 1.39

$$B_{lu} = a_{lu}(v). \quad (1.55)$$

Using the identities from Eq. 1.54 and Eq. 1.55 and inserting the expressions for the Saha-Boltzmann ratio (Eq. 1.43), the Maxwellian velocity distribution (Eq. 1.46) and Planck's Radiation law (Eq. 1.48) into the ratio between the photoionization and the spontaneous recombination (Eq. 1.53) leads to

$$\frac{4}{\sqrt{\pi}} \left(\frac{m_e}{2kT} \right)^{3/2} v^3 e^{-\frac{m_e v^2}{2kt}} \frac{2g_u}{g_l} \left(\frac{2\pi m_e T}{h^2} \right)^{3/2} e^{-\frac{h\nu_{lu}}{kT}} \frac{1}{\frac{4\pi}{h\nu} \frac{2h\nu^3}{c^2} \frac{1}{e^{\frac{h\nu}{kT}} - 1}} \frac{1}{vm_e} \frac{\sigma_{ul}(v)}{a_{lu}(v)} = 1 - e^{-\frac{h\nu}{kT}}. \quad (1.56)$$

Simplifying Eq. 1.56 and solving for the recombination cross-section finally leads to the Milne relation:

$$\sigma_{ul}(v) = \frac{g_l}{g_u} \frac{h^2 v^2}{m_e^2 c^2 v^2} a_{lu}(v). \quad (1.57)$$

The Milne relation depends only on the relative velocity between the electron and the ion and the frequency of the ionizing photon. Both are microphysical values and do not depend on the macroscopic state, e.g., the velocity distribution or number density of the electrons in the ionized gas, although the derivation of the Milne equation has been performed under the prerequisite of its validity in the case of thermodynamic equilibrium.

The spontaneous recombination coefficient of the upper state u for a given temperature can be obtained by integrating the product of the velocity distribution function, the velocity itself and the velocity-dependent ionization cross section over the entire velocity range:

$$\alpha_{\text{spont},ul}(T) = \int_0^{\infty} f(v)v\sigma(v)dv. \quad (1.58)$$

As each electron velocity corresponds to a frequency of an ionizing photon by $v(\nu) = \sqrt{\frac{2h(\nu-\nu_{lu})}{m_e}}$, the integral in Eq. 1.58 can be rewritten as integral of frequency from the ionization threshold ν_{lu} to infinity

$$\begin{aligned} \alpha_{\text{spont},ul}(T) &= \int_{\nu_{lu}}^{\infty} f(v(\nu))v(\nu)\sigma(v(\nu))\frac{dv}{d\nu}d\nu = \\ &= \int_{\nu_{lu}}^{\infty} \left(\frac{m_e}{2\pi kT}\right)^{3/2} \exp\left(-\frac{m\left(\frac{2h(\nu-\nu_{lu})}{m_e}\right)}{2kT}\right) 4\pi \sqrt{\frac{2h(\nu-\nu_{lu})}{m_e}} \frac{2h(\nu-\nu_{lu})}{m_e} \frac{g_l}{g_u} \frac{h^2\nu^2}{m_e^2 c^2} \frac{m_e}{2h(\nu-\nu_{lu})} a_\nu \frac{\frac{2h}{m_e}}{\sqrt{\frac{2h(\nu-\nu_{lu})}{m_e}}} d\nu = \\ &= \frac{g_l}{g_u} \exp\left(\frac{h\nu_{lu}}{kT}\right) \int_{\nu_{lu}}^{\infty} \frac{8\pi\nu^2}{c^2} a_{lu} e^{-\frac{h\nu_{lu}}{kT}} d\nu = \left(\frac{n_l}{n_u}\right)^* \int_{\nu_{lu}}^{\infty} \frac{4\pi a_{lu}(\nu)}{h\nu} \frac{2h\nu^3}{c^2} e^{-h\nu/kT} d\nu. \end{aligned} \quad (1.59)$$

The coefficient for the induced recombination is obtained by applying Eq. 1.50¹⁸, i.e. it is obtained by multiplying the integrand of Eq. 1.59 with $\frac{c^2}{2h\nu^3} J_\nu$:

$$\alpha_{\text{ind},ul}(T) = \left(\frac{n_l}{n_u}\right)^* \int_{\nu_{lu}}^{\infty} \frac{4\pi a_{lu}(\nu)}{h\nu} \frac{2h\nu^3}{c^2} e^{-h\nu/kT} \frac{c^2}{2h\nu^3} J_\nu d\nu = \left(\frac{n_l}{n_u}\right)^* \int_{\nu_{lu}}^{\infty} \frac{4\pi a_{lu}(\nu)}{h\nu} J_\nu e^{-\frac{h\nu_{lu}}{kT}} d\nu. \quad (1.60)$$

By summing up the spontaneous and the induced contribution to the recombination we obtain the total recombination coefficient as shown in Eq. 1.42.

Direct and dielectronic recombination processes. Radiative recombination processes can either occur via *direct radiative recombination* or *dielectronic recombination*. In direct radiative recombination processes a free electron is captured by an ion and its kinetic and potential energy (relative to the bound state immediately after the recombination) is converted directly into the energy of the emitted photon. In dielectronic processes the energy of the captured electron leads to the formation of a doubly excited intermediate state, which then relaxes via the emission of a photon. Dielectronic recombinations can only occur for discrete electron energies because of the additional bound-bound process. The direct radiative recombination processes are dominant for hydrogen and helium in the temperature range typically found in H II regions ($T \sim 5\,000\text{ K} \dots 20\,000\text{ K}$), but the dielectronic recombination rates are more important for metal ions and higher gas temperatures. A comparison of the direct radiative and dielectronic recombination rates as functions of temperature is shown for the example of the recombination $\text{O III} \rightarrow \text{O II}$ in Fig. 1.18.

Eq. 1.42 considers the radiative and dielectronic recombination processes¹⁹. To reduce the computational effort, in many applications performing the integral in Eq. 1.42 explicitly for each of the relevant recombination channels is avoided. Instead, fit formulae are used to compute the radiative and dielectronic recombination rates. Details can be found in Section 2.2.1.

¹⁸Note that Eq. 1.50 only contains microphysical quantities that do not depend on the macroscopic state of the gas. The validity of the relation is therefore independent of the condition of thermodynamic equilibrium.

¹⁹The discrete energies for the dielectronic rates corresponds to the peaks of the absorption cross section in Fig. 1.16.

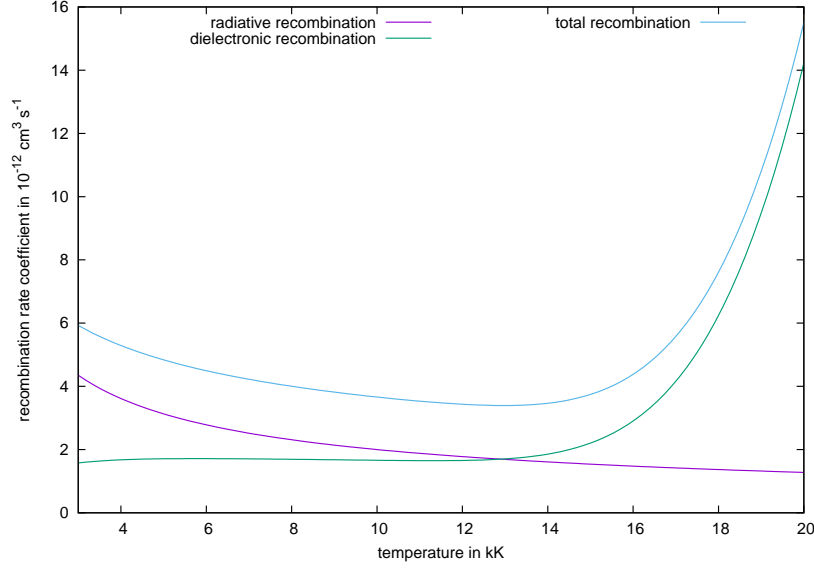


Figure 1.18: The direct radiative, dielectronic, and total recombination coefficients of O III as a function of the gas temperature. The plot is based on fit formulae and parameters given by Aldrovandi & Pequignot (1973) and Nussbaumer & Storey (1983) (cf. also Section 3.3.2.1) and covers the temperature range typically found in H II regions.

For the typical gas densities of H II regions, the *collisional recombination*, where the energy released by the recombination process is transferred to the kinetic energy of a third electron, can be neglected²⁰

1.5.2.4 The origin and the spectrum of the diffuse ionizing radiation field

A recombination process of a free electron that leads directly into the ground state of an atom or an ion releases a photon that is able to ionize another one of these atoms or ions. The energy of the emitted photon corresponds to the sum of the binding energy and the kinetic energy of the free electron before the recombination process. The most important recombination process where ionizing photons are emitted is the recombination of free electrons into the ground state of hydrogen which occurs in approximately one third to one half of all hydrogen recombination processes. As the emitted photons are likely to ionize another neutral hydrogen atom, the total amount of ionized hydrogen does not change. Therefore, in many cases the effect of the diffuse radiation field can be approximated by reducing the recombination rates of hydrogen by the rates for recombinations directly into the ground state (“case-B” recombination rates). This approximation does, however, assume that the emitted photons are locally re-absorbed, which does not accurately describe the situation in the optically thin ionized gas close to the ionizing sources (cf. Sect. 1.6.1 and Sect. 2.3.3.3).

²⁰The rate coefficients for the collisional recombination are the products of the rate coefficients for the corresponding collisional ionization process and the Saha-Boltzmann factor:

$$C_{ul} = \left(\frac{n_u}{n_l}\right)^* C_{lu}.$$

As these rate coefficients scale with the third power of the particle density (the reaction requires one ion and two electrons), the product is negligible for low-density gas. For example, for hydrogen, $\left(\frac{n_u}{n_l}\right)^* \sim 2 \cdot 10^{-10}$ for the ground state and $\left(\frac{n_u}{n_l}\right)^* \sim 8 \cdot 10^{-17}$ for the 10th energy level if the temperature of the gas is 10⁴ K and the electron density $n_e = 10 \text{ cm}^{-3}$.

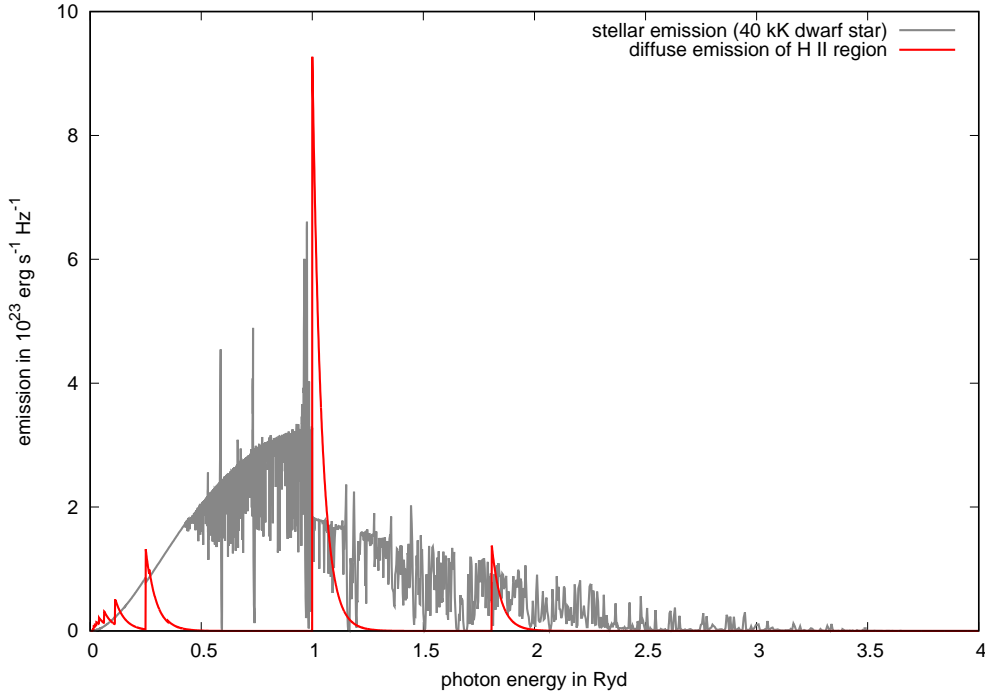


Figure 1.19: Comparison of the spectral energy distribution of a 40 000 K O star (based on the dwarf star model with solar metallicity described in Sect. 3.2.2) with the recombination continua of hydrogen and helium in the surrounding radiation-bounded H II region as described in Sect. 3.3.1. The emission of the recombination radiation peaks immediately above the respective recombination edges, but decreases quickly for higher energies. This plot does not account for the absorption processes within the H II region. In Fig. 1.22 we will additionally show the emissivity of ionized hydrogen gas in the non-ionizing frequency-range for different gas temperatures.

The energy of the lowest excited state of He I with respect to the corresponding ground state is approximately 19.8 eV (Kramida et al. 2018), i.e., it lies above the ionization threshold of each neutral atom with the exception of helium and neon atoms. Thus, each recombination process of helium leads to the emission of photon that – for radiation bounded H II regions – will cause a further photoionization process.

In Fig. 1.19 we show a comparison between radiation the emitted by a 40 kK dwarf star with solar metallicity²¹ and the recombination continuum of hydrogen and helium in a surrounding radiation-bounded H II region²².

1.5.2.5 The Strömgren sphere

A raw approximation to estimate the extent of the photoionized gas without computing the radiative transfer explicitly is the concept of the *Strömgren sphere*, where the gas inside the H II regions is considered to be fully ionized and volume of the transition region to the neutral gas outside is negligibly small compared to the ionized volume. Furthermore, a homogeneous density and temperature structure are assumed, which also implies that the recombination rates are the same within the entire ionized volume. In the equilibrium case the volume V can be computed by equating the emission \dot{N}_γ

²¹The modelling of the stellar energy distributions is described in Sect. 3.2.2

²²As described in Sect. 3.3.1.

of ionizing photons with the number of recombination processes during the same time. For a pure hydrogen gas, these assumptions lead to the equation

$$\dot{N}_\gamma = n_e n_{\text{H II}} \alpha_B V = n_{\text{H}}^2 \cdot \frac{4}{3} \pi r_S^3, \quad (1.61)$$

where n_e is the electron number density, $n_{\text{H II}}$ the number density of ionized hydrogen, n_{H} the total hydrogen number density (which under the assumptions above equals both the number density of the hydrogen ions and of the electrons in the ionized volume), α_B the case-B recombination rate and r_S the radius of the ionized region, i.e., the *Strömgen radius*. Eq. 1.61 can be solved for the Strömgen radius:

$$r_S = \sqrt[3]{\frac{3\dot{N}_\gamma}{4\pi\alpha_B n_{\text{H}}^2}}. \quad (1.62)$$

While the assumption of uniform gas properties is – as will be shown in the following chapters – clearly inaccurate, it is still useful for a raw approximation of the ionized volume, which is a prerequisite for setting up the suitable radius or volume grids is used in more accurate simulations.

1.5.3 Bound-bound transitions: Line transport and the two-photon decay of the first excited level of hydrogen

The radiative transition rates between different levels l and u of the same ion can be computed as

$$R_{lu} = B_{lu} \bar{J} \quad (1.63)$$

and

$$R_{ul} = A_{ul} + B_{ul} \bar{J}, \quad (1.64)$$

where A_{ul} , B_{lu} , and B_{ul} are the corresponding Einstein coefficients and \bar{J} is the profile-weighted mean intensity in the line²³. The gas in H II regions is, however, characterized by very low occupation numbers of states other than the ground states (cf. 1.5.2.2). Therefore, it is optically thin for line radiation caused by transitions where the lower energy level is not the ground state as well as for forbidden²⁴ transitions to the ground state. Forbidden transitions to the upper state are extremely unlikely to be triggered by the interaction of an atom or ion with the radiation field and are therefore almost exclusively caused by collisional processes with electrons or other atoms/ions. Concerning the downward transition, the radiative transition rate coefficient is by several orders of magnitude lower than for allowed transitions so that in dense gases, like in stellar photospheres, the radiative de-excitation is negligible compared to the de-excitation by collisional processes. As the collisional de-excitation probability of an excited state is (for otherwise equal conditions) proportional to the electron number density, radiative transitions still play a significant role in the dilute gas of H II regions. For instance, the critical electron density, where collisional de-excitation processes are equally likely as radiative processes, is $n_e = 6.8 \cdot 10^5 \text{ cm}^{-3}$ for the transition of the 1D_2 state of the O III ion into one

²³ \bar{J} is defined as $\bar{J} = \int_0^\infty J_\nu \varphi(\nu) d\nu$, where φ is the line profile function, which is normalized such that $\int_0^\infty \varphi(\nu) d\nu = 1$. The profile function $\varphi(\nu)$ results from the natural line width, the broadening by Doppler shift of the lines by thermal motion of the involved ions and by Doppler shifts due to the macroscopic motion of the gas, for example, due to turbulence or expansion into a less dense environment.

²⁴A forbidden transition is a transition between two quantum states that violates the selection rules for an electronic dipole transition (change of the azimuthal quantum number l by ± 1 , change of the magnetic quantum number by $-1, 0$, or $+1$). Still the transitions may be possible for higher order transitions, like magnetic dipole transitions or electronic quadrupole transitions (Schwabl 2002).

of the 3P levels, which in the radiative case leads to the emission of the “nebulium” lines at λ 4955 Å and λ 5007 Å, but as low as $n_e = 5.1 \cdot 10^2 \text{ cm}^{-2}$ for the transition of the 3P_1 level of the same ion to the “true” ground state 3P_0 , in which an infrared photon with $\lambda = 88.3 \mu\text{m}$ is emitted (data from Osterbrock & Ferland 2006).

By contrast, the optical depth of hydrogen gas for Lyman- α photons emitted by transitions from the first excited state to the ground state of hydrogen exceeds the optical depth for an ionizing photon at the ionization edge of hydrogen by a factor of approximately 10^4 (Osterbrock & Ferland 2006), the corresponding factors for the Lyman- β radiation (transition from the second excited state to the ground state) is $\sim 10^3$, and for the transition from the principal quantum number $n = 19$ to the ground state the factor still is ~ 10 . Most of the photons emitted by Lyman transitions will thus be absorbed by hydrogen atoms in the ground state.

A notable bound-bound transition in ionized gas that leads to the emission of continuum radiation is the two-photon decay of the 2^2S state of neutral hydrogen, which is populated via direct recombination or by transitions from higher energy levels during the recombination cascade. It does not relax into the ground state of hydrogen via the emission of a Lyman- α photon as such a process would be a transition between two states with the same azimuthal quantum number ($\Delta l = 0$), which is not possible for electronic dipole transitions. The Einstein coefficient for the two-photon transition is $A_{2\gamma}(2^2S, 1^2S) = 8.23 \text{ s}^{-1}$, whereas the Einstein-coefficient for the Lyman- α radiation is $A_{\text{Ly}\alpha}(2^2P, 1^2S) \approx 10^8 \text{ s}^{-1}$. Still, the timescale for a two-photon decay process is still short compared to the timescale for the photoionization of a hydrogen atom in the 2^2S state. Additionally, transitions between the 2^2S state to the 2^2P^o states of hydrogen (that then rapidly decays into the ground state) can be caused by collisions with electrons or protons. This process becomes as likely as the two-photon emission for an electron density of $n_e \approx 10^4 \text{ cm}^{-3}$. Therefore it can be assumed that almost each recombination process of a hydrogen atom finally leads to the ground state (Osterbrock & Ferland 2006). The shape of the two-photon emission spectrum has, for example, been discussed by Chluba & Sunyaev (2008). We show this spectrum and a term diagram of the levels involved in the two-photon decay and the Lyman- α emission in Fig. 1.20.

1.5.4 Ion-ion interaction

For a given temperature the mean velocity $\langle v \rangle$ of particles in an ideal, non-relativistic, gas is proportional to the inverse square root of their mass μ :

$$\langle v \rangle = \sqrt{\frac{8k_B T}{\pi\mu}}. \quad (1.65)$$

As the mass of a proton exceeds the mass of an electron by a factor of 1836, the mean speed of the free electrons in a gas of a given temperature T is approximately 42 times higher than the speed of the protons in this gas. For heavier ions the ratio is correspondingly larger. Thus, for a given cross-section collisional processes between electrons and ions occur more often than ion-ion collisions. As a result, most collisional ionization processes and excitation processes are caused by the interaction between ions and free electrons. There are, however, some processes in (partly) ionized gas that are a result of the interaction between several ions, like the mixing of the 2^2S and the 2^2P^o states of hydrogen (see above) and the charge exchange processes²⁵: At the edge of the hydrogen Strömgren sphere where hydrogen is partly ionized, the ionization structure of oxygen is closely linked to that of hydrogen. The reason is that the difference between the ionization energies of neutral hydrogen ($E_{\text{ion}} = 13.598 \text{ eV}$)

²⁵The description of the charge transfer processes follows Osterbrock & Ferland (2006).

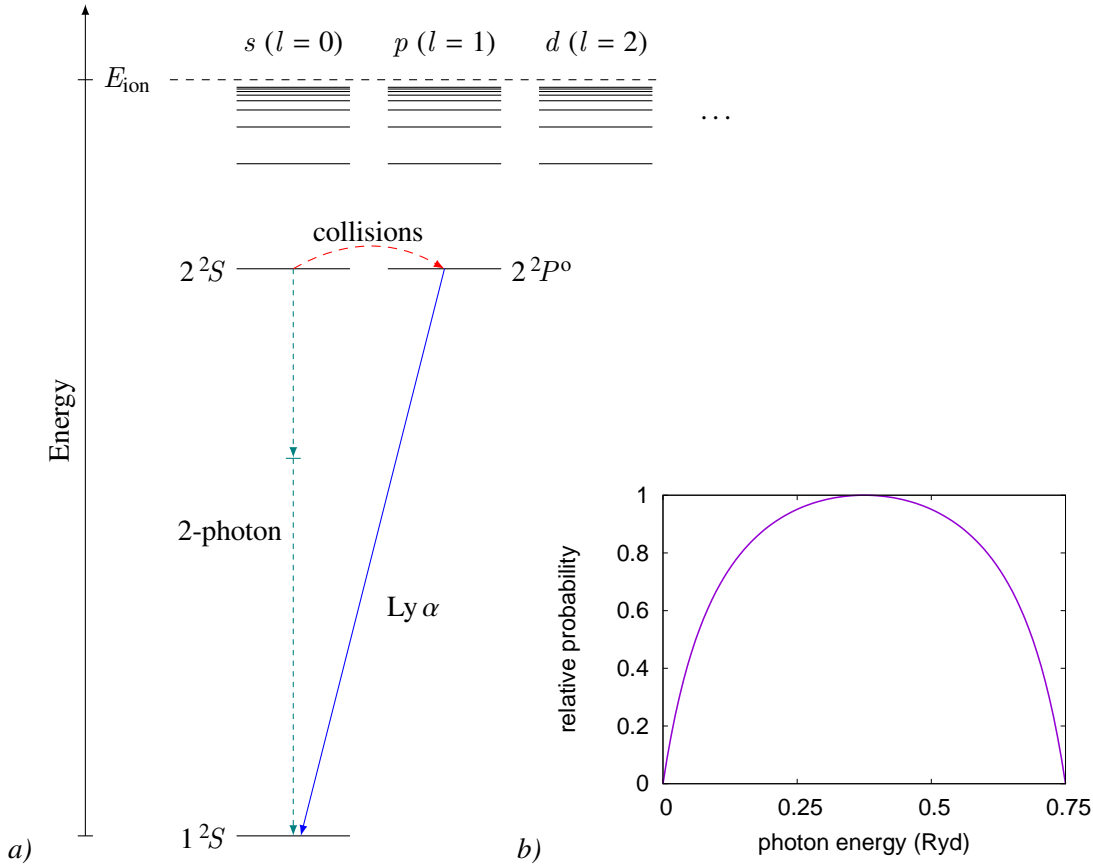


Figure 1.20: *a)* Sketch of the term diagram of hydrogen showing the possible transitions between the states belonging to the principal quantum numbers $n = 1$ and $n = 2$. Only transitions where the orbital angular momentum is changed by $\Delta l = \pm 1$ are allowed, i.e., they can occur as electrical dipole transitions where one photon is emitted (or absorbed). Thus only the 2^2P^o states can decay into the 1^2S ground state via the emission of a Lyman- α photon, which in turn can easily excite another hydrogen atom in the ground state. By contrast, the de-excitation of the 2^2S state either requires a collisional de-excitation process or a decay where two photons are emitted. The sum of the energies of these photons is nearly equal to the energy of a single Lyman- α photon. (The energy difference between the 2^2S state and the 2^2P^o states is only approximately 10^{-5} times the energy difference of these states to the ground state.) Due to their lower energy, the photons emitted in the two-photon process are not able to excite hydrogen atoms in the ground state and can leave the ionized region unabsorbed. The differential likelihood for a given energy of a photon emitted by a two-photon process is shown in image *b)*. As the sum of the energies of the two photons is a constant, the distribution is symmetric. The plot, based on the fit formula provided by Chluba & Sunyaev (2008), is normalized such that the most likely case, the emission of two photons with the same energy, is set to unity.

and neutral oxygen ($E_{\text{ion}} = 13.618 \text{ eV}$) is small compared to the mean kinetic energy of a particle in an H II region ($E_{\text{kin}} = 0.90 \text{ eV}$ for $T = 7500 \text{ K}$). Thus, electrons can be easily exchanged by collisions between the atom-ion pairs of hydrogen and oxygen, establishing the equilibrium



If the charge-transfer reactions establish an equilibrium between neutral hydrogen and singly ionized oxygen on the one side and ionized hydrogen and neutral oxygen on the other side, the number

ratio of neutral to singly ionized oxygen is

$$\frac{n(\text{O I})}{n(\text{O II})} = \left(\frac{g(\text{O I})}{g(\text{O II})} / \frac{g(\text{H I})}{g(\text{H II})} \right) \frac{n(\text{H I})}{n(\text{H II})} \exp(\Delta E_{\text{ion}}/k_B T) = \frac{9}{8} \frac{n(\text{H I})}{n(\text{H II})} \underbrace{\exp(\Delta E_{\text{ion}}/k_B T)}_{\sim 1}, \quad (1.67)$$

where $\Delta E_{\text{ion}} \approx 0.019 \text{ eV}$ is the difference between the ionization energies. As this value is much smaller than the thermal energy in the ionized gas ($kT = 0.83 \text{ eV}$ for $T = 10\,000 \text{ K}$), the exponential term is close to unity. The statistical weights g refer to the ground state of the corresponding ions. The consideration of this equilibrium is particularly important for the computation of the emission of the collisionally excited O I line. The generation of this line requires both neutral oxygen and free electrons, whereby the latter are mainly generated by the ionization of neutral hydrogen. The O II line, in contrast, is mainly generated in regions where the number densities of ionized hydrogen and oxygen exceed the number densities of the neutral atoms of these elements by several orders of magnitude and the main ionization mechanism of both elements is photoionization. The charge-exchange processes therefore do not have a significant effect on the O II emission. In this work we have implemented charge-exchange reactions using data from Kingdon & Ferland (1997). In Fig. 1.21 we show the effect of the charge exchange for the Strömgren spheres of ionized hydrogen and singly ionized oxygen.

1.5.5 Heating and cooling processes and the temperature structure of the gas

The spectral energy distributions of H II regions do not only depend on the abundances of the different ionization stages, but also crucially on the temperature of the gas. The interpretation of observations of H II regions therefore requires an accurate understanding of the heating and cooling processes. In our quantitative description of these processes we will mainly follow Osterbrock & Ferland (2006).

Heating by photoionization. The main heating mechanism for H II regions is heating by photoionization, where the change in the thermal energy of the gas corresponds to the difference between the energy $h\nu$ of the ionizing photon and the threshold energy $h\nu_{lu}$ of the lower ionization stage. The increase of thermal energy per volume unit caused by the photoionization of ions of the state l into ions of the state u thus is

$$\Gamma_{lu}^R = n_l \int_{\nu_{lu}}^{\infty} \frac{4\pi a_{lu}(\nu)}{h\nu} J_\nu h(\nu - \nu_{lu}) d\nu. \quad (1.68)$$

Due to the large abundance of hydrogen and helium, the photoionization heating in H II regions is dominated by the photoionization of these elements.

Cooling by recombination processes. When an electron recombines with an ion, its kinetic and potential energy with respect to the state immediately after the recombination is converted into the energy of a photon emitted in the recombination process. The resulting recombination cooling rate per volume unit is

$$\Lambda_{ul}^R = n_u \left(\frac{n_l}{n_u} \right)^* \int_{\nu_{ik}}^{\infty} \frac{4\pi a_{lu}(\nu)}{h\nu} \left(\frac{2h\nu^3}{c^2} + J_\nu \right) e^{-h\nu/kT} h(\nu - \nu_{lu}) d\nu, \quad (1.69)$$

if the emitted photon is not reabsorbed (Additionally, the potential energy is reduced by $h\nu_{lu}$). As H II regions are optically thin with respect to radiation emitted by transitions where *a*) the lower level is not the ground state (or there is a “forbidden” transition to the ground state) of an ion and *b*) the energy

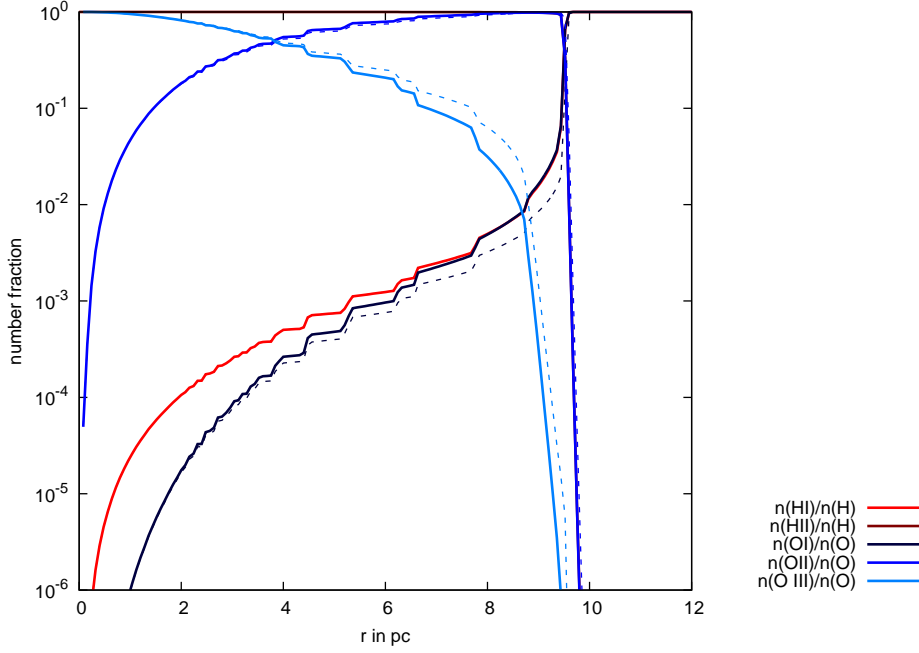


Figure 1.21: Ionization fractions of hydrogen and oxygen (relative to the total number density of all atoms and ions of the corresponding element) as a function of the distance from the source. For the model shown here we have used a main sequence star with an effective temperature of 35 000 K and 11 solar radii which is surrounded by a homogeneous gas with a particle density of $n_{\text{H}} = 10 \text{ cm}^{-3}$. The metallicity of both the star and the surrounding gas was set to the solar value. The solid lines represent the ionization fractions from a simulation that considers charge exchange processes. For comparison, we also show the results for a simulation where no charge exchange processes are considered (dotted lines). The ionization structure of hydrogen is not notably affected (in the plot, the lines for both simulations are indistinguishable), because the abundance of hydrogen is much larger than the abundance of metal ions. For the outer parts of the H II region the ratio of $n(\text{O})/n(\text{O}^+)$ close to the analytic value of $\frac{9}{8}n(\text{H})/n(\text{H}^+)$ (Eq. 1.67) is reached. Additionally, charge transfer processes with neutral hydrogen further reduce the fraction of O III in the outer parts of the ionized volume. In contrast, in the inner parts of the ionized region, O III is the dominant ionization stage of oxygen and the abundance of O II mainly determined by the equilibrium between singly and doubly ionized oxygen. Furthermore, in these regions the number fractions of neutral hydrogen are below 10^{-3} so that charge exchange processes between neutral hydrogen atoms and oxygen ions play a minor role. The steps are an artefact of the spatial discretization used in this simulation.

of the emitted photon lies below the ionization edge of hydrogen, line or continuum radiation that fulfills these conditions is able to escape from the ionized gas (cf. Sect. 1.5.3). The spectral energy distribution (SED) of the continuum radiation created in recombination processes into non-ground level states of hydrogen is shown in Figure 1.22.

Cooling by collisionally excited line radiation. In most H II regions the dominant cooling mechanism is the cooling by line radiation emitted in spontaneous relaxation processes of collisionally excited ions. The collisional excitation rate from a state l into a state u (of the same ion) is

$$C_{lu} = n_e \left(\frac{2\pi}{kT} \right)^{1/2} \frac{h^2}{4\pi^2 m_e^{3/2}} \frac{\Omega_{lu}(T)}{g_l} e^{-h\nu_{lu}/kT} \approx n_e \frac{8.629 \cdot 10^{-6}}{T^{1/2}} \frac{\Omega_{lu}(T)}{g_l} e^{-h\nu_{lu}/kT}, \quad (1.70)$$

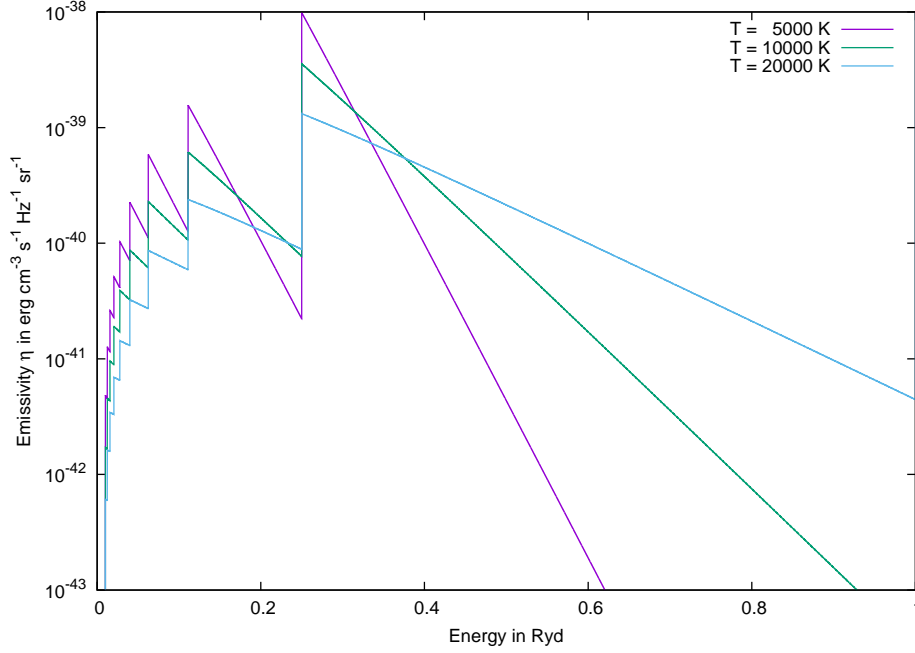


Figure 1.22: Emissivity from recombination into the non-ground state levels of hydrogen for different temperatures as a function of the energy of the emitted photons. The computation has been performed for a pure hydrogen gas with an electron and proton density of 10 cm^{-3} . The emissivity peaks at the ionization-edges of the excited states and decreases exponentially for higher photon energies.

where Ω_{lu} is the collision strength, which has to be computed quantum-mechanically, g_l is the statistical weight of the lower state, m_e is the electron mass and $h\nu_{lu}$ is the energy difference between the states. In the approximative expression on the right-hand side of 1.70 the value of the temperature in Kelvin must be inserted for T . The corresponding collisional de-excitation rate of the state u into the state l , where the energy released by the relaxation of the ion is directly added to the kinetic energy of the colliding electron is

$$C_{ul} = \frac{g_l}{g_u} C_{lu} e^{h\nu_{lu}/kT} = n_e \left(\frac{2\pi}{kT} \right)^{1/2} \frac{h^2}{4\pi^2 m_e^{3/2}} \frac{\Omega_{lu}(T)}{g_u} = n_e \frac{8.629 \cdot 10^{-6}}{T^{1/2}} \frac{\Omega_{lu}(T)}{g_u}, \quad (1.71)$$

where g_u is the statistical weight of the upper state. A collisional excitation process followed by a corresponding collisional de-excitation process does in total not change the thermal energy of the gas. In the low-density gas of H II regions there is, however, a considerable probability of a radiative de-excitation even for forbidden transitions. For the simplified case that only the levels u and l are considered, the probability P_{rad} of a radiative de-excitation process can be computed as

$$P_{\text{rad}} = \frac{A_{ul}}{A_{ul} + C_{ul}}, \quad (1.72)$$

where A_{ul} is the transition probability for the spontaneous (radiative) relaxation of the excited state. With Eq. 1.70 and Eq. 1.72 the cooling by collisionally excited lines can be estimated as

$$\Lambda_{ul}^R \sim n_u h\nu_{lu} C_{lu} P_{\text{rad}} \quad (1.73)$$

if there is only one de-excitation channel or the energies involved in the de-excitation processes are similar (as is the case for the transitions of the 1D state of O III to the 3P states). In the latter case the collisional and radiative transition rates of the transitions to the different sublevels have to be summed up.

In the typical temperature range of the gas in H II regions ($T \sim 10^4$ K) $h\nu > kT$ for transitions in the UV and optical range. As a consequence of the exponential term in Eq. 1.70, the emission of the corresponding lines therefore shows a strong dependence on both the energy difference between the states and the temperature of the gas. For this reason, the collisionally excited line spectrum in H II regions is dominated by metal ions with low-lying excited states, such as N II ($h\nu/kT \sim 2.2$ for $T = 10^4$ K), O II ($h\nu/kT \sim 3.9$), O III ($h\nu/kT \sim 2.8$), S II ($h\nu/kT \sim 2.1$) and S III ($h\nu/kT \sim 1.6$). By contrast, the cooling by collisionally excited line radiation of neutral hydrogen is only important in very metal-poor ($Z \lesssim 0.1 Z_\odot$, see also Section 3.3.1.2) and consequently hot H II regions, because of the high excitation energy of hydrogen atoms (at a temperature of $T = 10^4$ K, $h\nu/kT \approx 11.8$ for the first excited level).

The energy differences between the levels involved in the fine-structure transitions, i.e., transitions between different atomic states characterized by the same principal quantum number, that lead to the emission of mid- to far-IR lines, like the $51.8 \mu\text{m}$ and the $88.4 \mu\text{m}$ lines of O III, are smaller than kT for the entire temperature range found in H II regions. As a result, the exponential term in Eq. 1.70 is close to unity, and does not vary strongly with changes of the temperature. Instead, the $T^{-1/2}$ factor dominates the temperature dependence and the cooling becomes more efficient for lower temperatures. Thus, cooling by IR line emission becomes the dominant cooling process in a metal-rich environment, whereas the emission of optical lines is a non-monotonic function of metallicity: On the one hand, for larger metallicities more ions that can undergo the corresponding transitions are available. On the other hand, the lower temperatures caused by the more effective (IR) cooling lead to a reduced excitation rate. We discuss the temperature-dependence of the line emission in more detail in Section 3.3.1.2. The visible part of the spectrum of an H II region, which is dominated on the one hand by the Balmer recombination lines of hydrogen and on the other hand by forbidden line transitions of collisionally excited metals, is shown in Fig. 1.23.

Cooling by free-free radiation. The free-free emissivity $\eta_{\nu,\text{ff}}$ caused by the interaction between ions of charge of Z and electrons (with charge e and mass m_e) is (in cgs units):

$$\eta_{\nu,\text{ff}} = \frac{1}{4\pi} \frac{32 Z^2 e^4 h}{3 m_e^2 c^3} \left(\frac{\pi h \nu_0}{3kT} \right)^{1/2} n_{\text{ion}} n_e g_{\text{ff}}(\nu, T) e^{-\frac{h\nu}{kT}} \quad (1.74)$$

(e.g., Osterbrock & Ferland 2006). The gaunt factor g_{ff} depends on the frequency ν , the charge of the ion, and the temperature T of the ionized gas: for the temperature range found in H II regions ($T \sim 10^4$ K) the gaunt factor in the optical wavelength range is close to unity, whereas in the radio wavelength range ($\nu \sim 1$ GHz) it can be approximated by

$$g_{\text{ff}}(Z, Z, \nu) \frac{\sqrt{3}}{\pi} \left(\frac{T^{3/2}}{Z\nu} + 17.7 \right) \quad (1.75)$$

(Scheuer 1960), with T in K and ν in Hz.²⁶

²⁶A more detailed, numerical description of the behavior of the gaunt factor as a function of the frequency, the gas temperature and the ion charge has, for example, been provided by Hummer (1988).

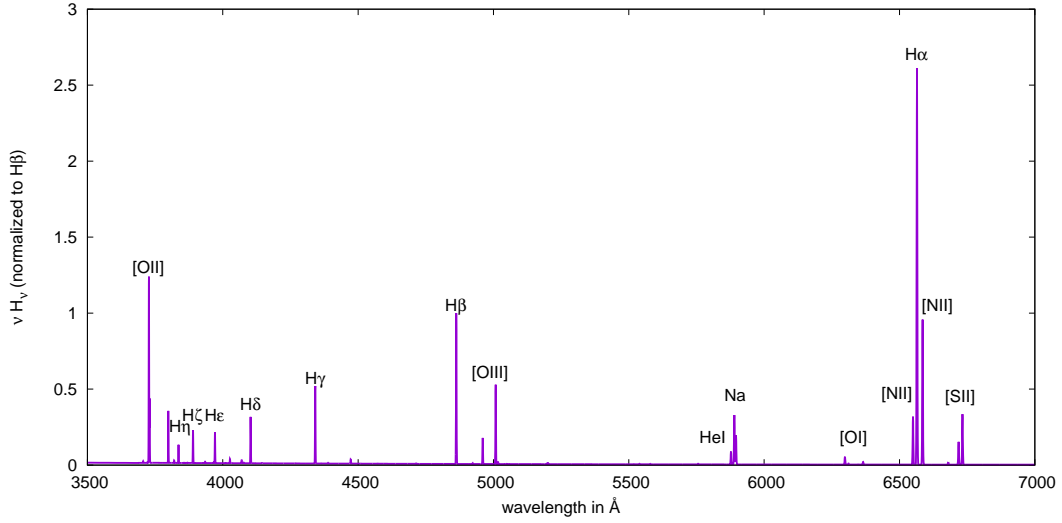


Figure 1.23: Spectral energy distribution of an H II region around a 35 kK model dwarf star from Sect. 3.3.1.2, where the metallicity of both the star and the surrounding ionized gas corresponds to the solar value. In the visible (and near UV) spectral range the radiation emerging from an H II region is dominated by the Balmer series of hydrogen, which is emitted if during the recombination cascade of hydrogen toward its ground state the first excited state (principal quantum number $n = 2$) is populated, and by the radiative decay of collisionally excited states of N II, O II, O III and S II. The square brackets around the ion symbol indicate a forbidden transition, which means that no electronic dipole transitions can occur between the respective upper and lower state. Thus, the excitation can almost exclusively occur via collisions, and even though the radiative transition rate coefficients back into the lower states are by several orders of magnitude lower than allowed transitions, due to the low particle densities in H II regions compared, for example, with stellar atmospheres, there is still a significant probability of a radiative transition into the lower state by higher order transitions (Osterbrock & Ferland 2006).

Integrated over the entire frequency range, the energy loss via free-free emission caused by the interaction of a type of ion with the electrons in the gas is

$$\Lambda_{ff} = \frac{32\pi e^6 Z^2}{3^{3/2} h m_e c^3} \left(\frac{2\pi kT}{m_e} \right)^{1/2} \bar{g}_{ff} n_e n_{\text{ion}}, \quad (1.76)$$

where in the case of H II regions the value for the averaged gaunt factor is $\bar{g}_{ff} \approx 1.3$ (Osterbrock & Ferland 2006).

By applying Kirchhoff's law, the frequency-dependent free-free opacity of ionized gas can be computed as

$$\kappa_{\nu,ff} = n_{\text{ion}} n_e \frac{16\pi^2 Z^2 e^6}{(6\pi m k T)^{3/2} \nu^2 c} g_{ff}. \quad (1.77)$$

As a result, the free-free absorption of H II regions can be neglected in the optical wavelength range, whereas the regions become optically thick for long radio waves. For example, for a spherical H II region with a number density of $n = 20 \text{ cm}^{-3}$ of both electrons and singly ionized ions and a radius of $R = 10 \text{ pc}$ has a maximal optical depth caused by free-free absorption of $\tau_{ff} \approx 10^{-15}$ in the optical frequency range but of $\tau_{ff} \approx 1$ for radio frequencies of 50 MHz.

The thermal equilibrium. Thermal equilibrium is reached if the sum of all heating rates corresponds to the sum of all cooling rates. However, the processes defining these rates can not necessarily be assumed to be time-independent. For example, the properties of the ionizing sources, like the temperature and the luminosity change during the stellar evolution process. We will discuss the “overshooting” of the temperature in gas crossed by an ionization front in Section 3.3.2.2.

1.5.6 The Role of Dust in H II regions

Comparisons of the abundances of different metals in the solar atmosphere and in the gas of H II regions show large differences in the number ratios between these elements. For example, Simpson et al. (1998), Rubin et al. (2007) and Rubin et al. (2008) found an abundance ratio of neon to sulfur that exceeds the ratio found in the solar atmosphere by a factor of more than two both in H II regions within our galaxy and in the galaxies M 83 and M 33. Both neon and sulfur are produced in the α -chain reactions, and thus mostly form in core-collapse supernovae with yields that are almost independent of the initial stellar metallicity (Rubin et al. 2008). The resulting expectation of low variations of the Ne/S ratio with the metallicity of the H II regions are supported by the observations mentioned above. Therefore it is unlikely that the much lower Ne/S ratio in the solar atmosphere is a consequence of differences in the total amount of sulfur in H II regions. Instead, sulfur seems to be depleted from the atomic gas phase into dust (or molecules). By removing metal ions from the gas phase the temperature structure and the line emission is modified. Dust depletion changes the cooling behavior of the gas as it reduces the number of ions that can emit collisionally excited lines and thus remove thermal energy from the H II regions. The depletion and the heating of the gas by emission of photoelectrons from the dust grains may therefore be the explanation for the absence of H II regions that lack collisionally excited and therefore strongly temperature-dependent lines in the optical wavelength range as would be expected in metal-rich, undepleted environments (Shields & Kennicutt 1995). The impact of the dust depletion on the abundances in the atomic gas phase varies from element to element. While, due to their chemical inertness, there is no dust depletion for noble gases, the depletion rates are 0.34 dex for carbon, 0.10 dex for nitrogen and 0.20 dex for oxygen. An overview of the depletion rates has been provided by Shields & Kennicutt (1995), based on data collected by Cowie & Songaila (1986). For silicate-forming elements like silicon and aluminium a depletion by approximately one order of magnitude has been found and the depletion of heavy elements like iron and nickel can reach several orders of magnitude.

1.6 Numerical approaches to solve the equation of radiative transfer in three dimensions

As the previous section has shown, a realistic simulation of photoionized gas has to account for a large number of different processes and a change of one quantity will have a direct or indirect effect on other quantities. The solution of that system of differential and integro-differential equations has to be determined numerically. The radiative transfer and the occupation numbers in H II regions can be evaluated by means of a relatively low (typically in the order of 100) number of sampling points, if the density structure around the radiation source can be considered to be spherically symmetric, so that the radiation field and the occupation numbers have to be computed only once per radius point while they do not depend on the direction with respect to the source. Examples for such a spherically symmetric approach to model H II regions have been described in Ferland et al. (2013) as well as our own group whose modelling code has originally been designed for the computation of synthetic spectra of hot

stars (Pauldrach et al. 2001, 2004, 2012, 2014), but has been adapted to the low particle densities and dilute radiation fields of H II regions as described by Hoffmann et al. (2012) and Weber et al. (2015).

The obvious disadvantage of spherically symmetric models is that they are not able to consider inhomogeneities that do not only depend on the distance from the source, but also on the direction. Furthermore, they can not consistently account for the presence of multiple sources of ionization at different positions in space. Both inhomogeneities and multiple ionizing sources are, however, present in real photoionized regions and are of key importance for large-scale structures like the diffuse ionized gas in galaxies (cf., Sect. 1.3 and Chapter 4).

To provide an accurate numerical description of such situations, the radiative transfer has therefore to be performed in a way that accounts for the three-dimensional structure of the ionized gas and the spatial distribution of the sources.

The main problem that is encountered in simulations of the radiative transfer in 3D is the computational effort. Each element of the simulated system acts both as absorber and emitter of radiation. Thus, without approximations a solution of the radiative transfer completely considering the emission of each of the simulation elements into all directions would require computing the interaction of all volume elements with each other, so that the computational effort would grow with the square of the number of volume elements. For example, a system with 100^3 grid cells or 10^6 particles would require the consideration 10^{12} interactions per frequency point. Below we will describe the advantages and problems of various approaches to reduce the numerical effort needed for the computation or three-dimensional radiative transfer.

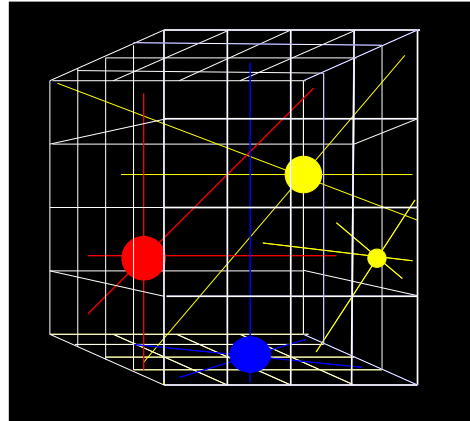
1.6.1 Ray-by-Ray approaches using the “on-the-spot” approximation

The first of these approaches is the ray-tracing method where the radiation field is described by a set of discrete rays emitted from the sources of radiation (cf. Fig. 1.24). Additionally the simulated volume is discretized by a grid- or particle-based approach. The fundamental geometrical task in ray-tracing-based 3-dimensional radiative transfer is to distribute the rays adequately. The central geometrical aspects to meet this task are tracing the segments of each individual ray correctly (cf. Sect. 2.3.1.1) and implementing the isotropic character of the radiation field of every point source by distributing the rays as evenly as possible (e.g., using the tessellation scheme described by Górski et al. 2005). Furthermore, it has to be assured that each volume element is traversed by a sufficient number of rays. The main source of the ionizing diffuse radiation field in H II regions is the recombination of hydrogen and helium ions into the ground state of the corresponding lower ionization stage. The explicit treatment of the diffuse radiation field can therefore be avoided if the *on-the-spot-approximation* is used. In the on-the-spot approximation it is assumed that a photon that is generated by such a recombination process is locally re-absorbed. Numerically this situation can be described by a total recombination rate that is reduced by the rate of recombination processes that directly lead into the ground state of the lower ion (*case-B* recombination rate). As re-emission processes do not have to be computed explicitly it is possible to describe the radiative transfer using a ray-tracing approach along pre-defined lines from source each until the photons leave the simulated volume or the an optical depth is reached, where the ray can be assumed to be completely absorbed. Additionally, a relatively low number of rays is sufficient to avoid “noisy” results²⁷.

However there are two systematic drawbacks of the approach. First, the on-the-spot approximation

²⁷We have found about 10 rays per grid cell to be sufficient to determine the hydrogen Strömgren sphere with an accuracy better than one grid cell for a grid with 100^3 cells where the source of ionization is located at the center of the simulated volume and the Strömgren sphere just fits within the simulated volume. The effects caused by the limited number of rays are also discussed in Sect. 2.5

Figure 1.24: Sketch showing a subset of the rays to be treated in the ray tracing method of radiative transfer. Possible different spectral energy distributions of the sources are indicated by different colors.



assumes a situation where the mean free path of the ionizing photons²⁸ is shorter than the distances along which the properties of the analyzed ionized regions that are relevant for the respective simulation vary significantly. This is the case for the determination of the extent of the ionized region (the “Strömgren volumina”), because the opacity of the gas becomes large near the ionization front. However, in the vicinity of the sources the gas becomes optically thin so that the mean free path may become larger than the distance between the considered volume element and the source (cf. Sect. 1.5.2.4). As a result, the on-the-spot approximation will underestimate the number of unionized particles in the inner part of the ionized volume (as is shown in the plots in Fig. 2.9), which might be relevant, for example, for studies of the Lyman- α forest, where the absorption of the Lyman line radiation crucially depends on the amount of remaining neutral hydrogen along the line of sight²⁹. For single sources of ionization this deviation can be reduced using the *outward-only*³⁰ approximation, where the emission within the gas is explicitly computed and it is assumed that the emitted photons will be transported along the corresponding ray away from the source. Disadvantages of this approach are the additional computational effort and its inability to compute H II regions that are ionized simultaneously by several sources, in which the “outward”-direction is no longer unambiguously defined.

Second, the method is an inaccurate handling of shadowing effects by opaque clumps, as it does not account for the fact that ionizing radiation from the diffuse radiation field can enter the geometrical shadow of the clump with respect to the ionizing source(s) (cf. Fig. 1.25).

The ray-by-ray method has been implemented by Abel et al. (1999), Mellema et al. (2006) and in the method that is described in this work. Details of our implementation can be found in Sect. 2.3.1.

1.6.2 Monte-Carlo Approaches

The basic idea behind Monte-Carlo approaches is to approximate the radiation field by a set of photon packets whose direction is randomly chosen under the constraint that the probability for each direction is equal. These packets can then be absorbed and – possibly after being converted into another energy range – reemitted by the gas until the packages leave the simulation volume. In this way Monte-Carlo

²⁸For a homogeneous gas the mean free path of a photon with the frequency ν can be computed by $\frac{1}{\sum_i \alpha_i(\nu)n_i}$ where the summation in the denominator is carried out over all types of absorbing particles i with a frequency-dependent absorption cross section of $\alpha_i(\nu)$.

²⁹The optical depth of partly ionized gas is larger for Lyman- α line radiation than for radiation of the ionizing continuum (cf. Osterbrock & Ferland 2006)

³⁰The outward-only approximation has been applied in the context of 3D radiative transfer by Morisset et al. (2005) and Morisset (2006).

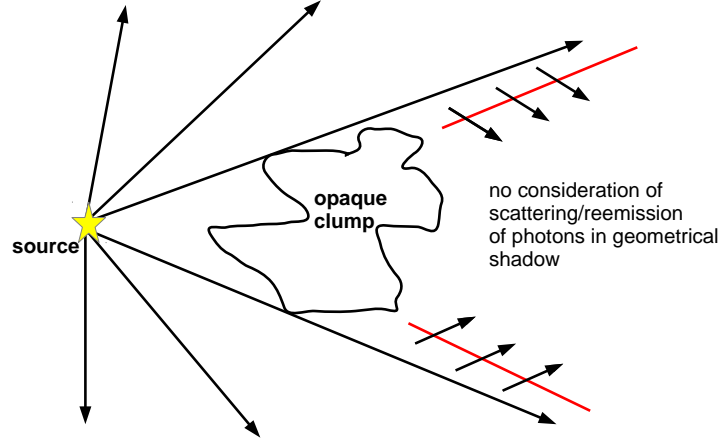


Figure 1.25: The “on-the-spot” approximation of the diffuse radiation field does not consider the ability of emitted or scatted photons from the diffuse radiation field to penetrate into the geometrical shadow of an opaque object.

approaches can explicitly account for the diffuse radiation field.

Implementations of three-dimensional Monte-Carlo radiative transfer are described by Ciardi et al. (2001), Maselli et al. (2003) and Graziani et al. (2013), where the focus is on simulations in the cosmological context, as well as the code described by Ercolano et al. (2003, 2005, 2008), and Hubber et al. (2016), where the method has been applied to galactic H II regions, planetary nebulae and protostellar disks. For a very large number of photon packets, Monte-Carlo approaches are able to describe the properties of the diffuse radiation field accurately and are also able to reproduce shadowing effects correctly. For a low number of photon packets, this method will however suffer from random noise.

1.6.3 Variable Eddington Tensor Formalism

The idea behind the Variable Eddington Tensor approach is to transform the equation of radiative transfer into a form similar to a diffusion equation. Because of this, the radiative transfer is only computed locally, i.e., not every radiation source has to be connected explicitly with each element of the simulated volume. The Variable Eddington tensor method does not compute the change of the intensity I_ν itself, but instead computes the radiative transfer using its moments with regard to the solid angle (cf. Sect. 1.5.1). It has been applied in the context of 3D radiative transfer by Gnedin & Abel (2001), Petkova & Springel (2009) (our description of the variable Eddington tensor is mainly based on that latter work) and Kannan et al. (2018). The relevant moments of the intensity are the mean intensity, the Eddington flux, and the K -Integral.

$$\underbrace{\frac{1}{c} \frac{\partial J_\nu}{\partial t} + \nabla H}_{\frac{1}{4\pi} \int \left(\frac{1}{c} \frac{\partial I_\nu}{\partial t} + n^i \frac{\partial}{\partial x^i} I_\nu \right) d\Omega} = \underbrace{-\kappa_\nu J_\nu + \eta_\nu}_{\frac{1}{4\pi} \int (-\kappa I_\nu + \eta) d\Omega} \quad (1.78)$$

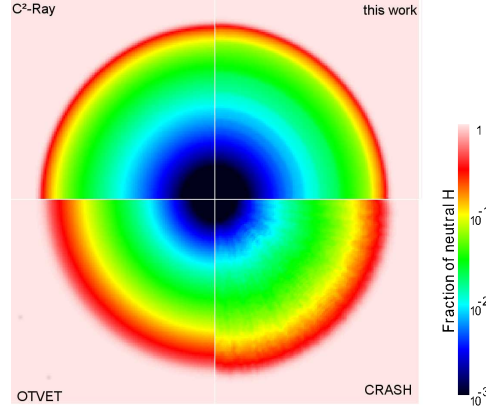


Figure 1.26: Ionization structure in a pure hydrogen gas computed with our method, compared with the results of three methods, where each has a different approach to approximate the radiative transfer: C^2 -Ray (Mellema et al. 2006) and the method described in this work are based on ray-tracing and use the case-B approximation, CRASH (Ciardi et al. 2001) is Monte Carlo approach, and OTVET (Gnedin & Abel 2001) is based on the Variable Eddington Tensor method). The data from the other simulations are taken from Iliev et al. (2006). It can be seen that the methods that use the on-the spot approximation C^2 -Ray and our method give lower abundances of neutral hydrogen in the inner parts of the ionized volume. The small-scale deviations from a purely radius-dependent ionization structure that appear in the output of *CRASH* result from the random distribution of the rays and could be reduced by increasing the number of used photon packets.

and

$$\frac{1}{c} \frac{\partial H_v^j}{\partial t} + \frac{\partial I_v h^{ij}}{\partial x^i} = \underbrace{-\kappa H_v^j}_{\frac{1}{4\pi} \int n^i (-\kappa I_v + \eta) d\Omega}, \quad (1.79)$$

where $h_v^{ij} = K_v^{ij} / J_v$ is called the *Eddington tensor*. In Eq. 1.79, the first moment of the emissivity vanishes if the emission is isotropic.

If the term containing $1/c$ is ignored in Eq. 1.79, the term can be solved for the Eddington flux by

$$H_v^j = \frac{1}{\kappa} \frac{\partial J_v h^{ij}}{\partial x^i}. \quad (1.80)$$

By inserting Eq. 1.80 into Eq. 1.78 the expression

$$\frac{\partial J_v}{\partial t} = c \frac{\partial}{\partial x_j} \left(\frac{1}{\kappa_v} \frac{\partial J_v h^{ij}}{\partial x^i} \right) - c \kappa_v I_v + c \eta_v \quad (1.81)$$

for the temporal change of the mean intensity is obtained. In Eq. 1.79 and Eq. 1.81 the Eddington tensor is not yet defined such that these equations can not be unambiguously solved. As an approximation Gnedin & Abel (2001) and Petkova & Springel (2009) use the optically thin approximation, where it is assumed for the computation of the Eddington tensor that all lines of sight between the sources and the considered volume elements are optically thin. In this case, the K integral can then be computed as

$$K^{ij} \propto \int d^3 x' \rho_\star(\mathbf{x}') \frac{(\mathbf{x} - \mathbf{x}')_i (\mathbf{x} - \mathbf{x}')_j}{(\mathbf{x} - \mathbf{x}')^4}, \quad (1.82)$$

where ρ_\star is the stellar mass density³¹. The computation of Eq. 1.82 can be performed efficiently (with a computational effort of $N \log N$) using the same techniques as used for the computation of the gravitational N -body problem. The assumption of an optically thin medium for the determination of the Eddington Tensor leads to a limited accuracy for the simulation of shadowing effects and the shape of the ionization front if several ionizing sources are present.

Quantitative comparisons between several implementations that are based on different methods can be found in Iliev et al. (2006) and Iliev et al. (2009). Fig. 1.26 shows a comparison of the results for a subset of the implementations of three-dimensional radiative transfer presented in Iliev et al. (2006) for the simulation of isothermal hydrogen gas.

³¹In this approximation it is additionally assumed that the emission per volume unit is proportional to the stellar mass density.

2 Three-Dimensional Modelling of Ionized Gas

I. Did very massive stars of different metallicities drive the second cosmic reionization?¹

The first generation of stars, which formed directly from the primordial gas, is believed to have played a crucial role in the early phase of the epoch of reionization of the universe. Theoretical studies indicate that the initial mass function (IMF) of this first stellar population differs significantly from the present IMF, being top-heavy and thus allowing for the presence of supermassive stars with masses up to several thousand solar masses. The first generation of population III stars was therefore not only very luminous, but due to its lack of metals its emission of UV radiation considerably exceeded that of present stars. Because of the short lifetimes of these stars the metals produced in their cores were quickly returned to the environment, from which early population II stars with a different initial mass function and different spectral energy distributions (SEDs) were formed, already much earlier than the time at which the universe became completely reionized (at a redshift of $z \gtrsim 6$). Using a state-of-the-art model atmosphere code we calculate realistic SEDs of very massive stars (VMSs) of different metallicities to serve as input for the 3-dimensional radiative transfer code we have developed to simulate the temporal evolution of the ionization of the inhomogeneous interstellar and intergalactic medium, using multiple stellar clusters as sources of ionizing radiation. The ultimate objective of these simulations is not only to quantify the processes which are believed to have lead to the reionized state of the universe, but also to determine possible observational diagnostics to constrain the nature of the ionizing sources. The multi-frequency treatment in our combination of 3d radiative transfer – based on ray-tracing – and time-dependent simulation of the ionization structure of hydrogen and helium allows, in principle, to deduce information about the spectral characteristics of the first generations of stars and their interaction with the surrounding gas on various scales. As our tool can handle distributions of numerous radiative sources characterized by high resolution synthetic SEDs, and also yields occupation numbers of the required energy levels of the most important elements which are treated in NLTE and are calculated consistently with the 3 radiative transfer, the ionization state of an inhomogeneous gaseous density structure can be calculated accurately. We further demonstrate that the increasing metallicity of the radiative sources in the transition from population III stars to population II stars has a strong impact on the hardness of the emitted spectrum, and hence on the reionization history of helium. A top-heavy stellar mass distribution characterized by VMSs forming in chemically evolved clusters of high core mass density may not only provide the progenitors of intermediate-mass and supermassive black holes (SMBHs), but also play an important role for the reionization of He II. The number of VMSs required to reionize He II by a redshift of $z \sim 2.5$ is astonishingly close to the number of VMSs required to explain galactic SMBHs if one assumes that

¹The content of this chapter has been published in:

J. A. Weber, A. W. A. Pauldrach, T. L. Hoffmann, and J. S. Knogl
Astronomy & Astrophysics, Volume 555, id.A35, 24 pp.

these have been formed by mergers of smaller black holes.

2.1 Introduction

Electrons and protons combined to form neutral hydrogen when the young universe cooled (at a redshift of $z \approx 1100$), but the continuous absorption troughs blueward of the (redshifted) hydrogen Ly α line, that one would expect to see if the intergalactic medium consisted of neutral (recombined) hydrogen gas, were not found in the spectra of distant objects around $z \approx 2.0$ (Gunn & Peterson 1965). It turns out that one has to look much deeper to find these troughs, and by means of quasar observations, White et al. (2003) and Kashikawa (2007) were able to show that the troughs do exist for objects at a redshift of $z \approx 6.5$, but not for objects at a redshift of $z \approx 5.7$. Obviously, a process has occurred that re-ionized the intergalactic gas in the universe, and this process must have been completed by a redshift of roughly $z \approx 6$.² As a result of this process the number density of neutral hydrogen is now very low in the intergalactic medium (IGM). At which redshifts it was still high is, due to the lack of corresponding observations, more difficult to determine, and one currently has to rely on numerical cosmological simulations to estimate when exactly reionization began. The simulations of Wise & Abel (2007) point for instance to a redshift of roughly $z \approx 30$ as starting point of the reionization process and marking the end of the “cosmic dark ages”³.

Regarding the nature of the sources that have driven reionization we are still left somewhat in the dark. Although it was immediately recognized that quasars, as the brightest single objects in the UV, should have played an important role in this process, a quantitative investigation of the luminosity function of high-redshift quasars showed that their radiation output was not sufficient to reionize the universe (Fan et al. 2006b).⁴ The other likely candidate objects to have significantly driven the reionization process are stars, the first generation of which (so-called population III stars) are assumed to have developed in the dark matter halos that had already formed at those redshifts.

There is reason to believe that due to their primordial composition and the corresponding inefficient cooling of the gas during the star-formation process these population III stars formed on a larger fragmentation scale ($10^2 \dots 10^3 M_{\odot}$) without subfragmenting further (cf. Abel et al. 2000, Bromm et al. 2002), and therefore the IMF of the primordial stars differs significantly from the IMF at present days with a preference to massive stars (Bromm et al. 2002 give masses of $100 \leq M/M_{\odot} \leq 1000$, and temperatures of $T_{\text{eff}} \sim 10^5$ K, which to a large extent turn out to be independent of the stellar masses for these short living ($\tau_{\text{MS}} \sim 2 \cdot 10^6$ yr, cf. Schaerer 2002) objects). Although the exact form of this top-heavy IMF is still under debate⁵, the preference for massive stars leads to huge UV luminosities,

²Fan et al. (2006a) have observed quasars in the redshift range from $5.7 \leq z \leq 6.13$ and have been able to detect deep Gunn-Peterson absorption gaps in Ly α for two quasars ($z = 6.13$ and $z = 6.01$).

³The investigation of the star formation history as a crucial ingredient in reionization modelling requires the consideration of both the large-scale structure formation and the smaller-scale aspects of star formation. At the present stage such considerations are treated with a number of approximations, for example a “threshold density” which describes a certain value of the gas density above which star formation is assumed to occur. We note that a discussion required about the relationship of this threshold value and the onset of star formation can be found in Maio et al. (2009), who concluded that low threshold densities lead to an early onset of star formation ($z \approx 25 \dots 31$), while for larger values the onset of star formation is delayed ($z \approx 12 \dots 16$).

⁴From observations it became evident that, compared to the UV background provided by the stellar content of normal star-forming galaxies, quasars supplied a fraction of less than 30% of the total ionizing radiation required to ionize the IGM (Willott et al. 2005, Mahabal et al. 2005). If the luminosity function of high-redshift quasars turns out to diverge considerably from the one at $z < 3$ (Fan et al. 2001) this estimate will have to be re-examined, but it is considered unlikely because theoretical models indicate that quasars have been a minor contributor to the reionization process even at a redshift of $z \approx 6$ (Volonteri & Gnedin 2009).

⁵In contrast to other studies Clark et al. (2011) found a stronger fragmentation cascade. However, the products at the

and this energy – released at high frequencies – may have been crucial for the evolution of the universe in its early stages.

Thus, the existence and the properties of the first stellar population is closely linked to the reionization history of the universe. But the time period for the appearance of these objects was much shorter than the time required to reionize the IGM, and different stellar populations will have contributed to the reionization at different times. In this context the history of reionization may be divided into three stages. The first one is the “pre-overlap” phase which was characterized by isolated H II regions located in the interstellar medium (ISM) which expanded steadily into the low density IGM. The second one is the “overlap” phase in which the separate H II regions started to merge; this process required a strong rise in the amount of ionizing radiation. The last stage is the “post-overlap” phase, characterized by ionizing the low density IGM on large scales (Gnedin 2000).

A more detailed description of this history has been presented by Cen (2003) whose analysis indicated that the universe was reionized in two steps. The first one occurred up to a redshift of $z \sim 15$ where the ionization was primarily driven by population III stars. As the population III stars returned metals via supernova explosions into their environment, the chemical composition and – as a result – the IMF and SEDs of later populations of stars changed, giving way to metal-enriched population II stars.⁶ This transition from population III to population II stars lead to a decline in the emitted radiation power by a factor of ~ 10 , which in turn lead to a phase, from about $z \approx 13$ to $z \approx 6$, during which hydrogen partly recombined ($n_{\text{H II}}/n_{\text{H}} \geq 0.6$) (Cen 2003). Thus the universe may have come close to a second cosmological recombination at $z \sim 13$. To overcome the threatening re-recombination and to restart the reionization process driven by powerful ionizing sources and maintained by the dilution of the intergalactic gas due to the expansion of the universe, a second step (finishing at $z \sim 6$) was necessary.⁷ But how could the presumably much less massive population II and population I stars fully reionize the hydrogen and helium content of the IGM? Of course, there is strong evidence of an increasing star formation rate (SFR) in this epoch (Lineweaver 2001, Barger et al. 2000), but in particular regarding the reionization of helium not only the *number* of stars is important, but also the characteristics of the SEDs of the stars are much more significant (Wyithe & Loeb 2003). Very massive stars (VMSs) which clearly exceed the assumed upper limit of 100 to 150 M_{\odot} of present-day massive stars have pronounced fluxes in the EUV *at all metallicities* (Pauldrach et al. 2012) and in conjunction with a top-heavy stellar mass distribution may provide such a required SED.

To motivate this idea we note that there are indications of a more top-heavy IMF than the standard one even in present-day galaxies. Harayama et al. (2008) for instance studied the IMF of one of the most massive Galactic star-forming regions – NGC 3603 – to verify whether the IMF really does have an universal shape. What they found does not support this assumption: with $\Gamma = -0.74$ they derived a power-law index for this massive starburst cluster which is considerably less steep than the Salpeter

lower end of the fragmentation cascade should be observed in the local universe, and up to now this has not been the case. We note, however, that Caffau et al. (2012) reported the finding of a $0.8 M_{\odot}$ star with a metallicity of only $Z \approx 5 \cdot 10^{-5} Z_{\odot}$. This means that such a low metallicity may already be sufficient to produce enough fragmentation driven by dust cooling (cf. Klessen et al. 2012 and Schneider et al. 2012) to yield an IMF significantly different from that in the real primordial gas.

⁶Maio et al. (2010) found that the relative population III star formation dropped to $SFR_{\text{popIII}}/SFR_{\text{tot}} \approx 10^{-3}$ at $z \approx 13 \dots 10$. Thus, the transition from population III to population II stars already occurred somewhat earlier than this. We further note that, due to the radiative feedback in the environment of the first stars, the formation of so-called “population III.2” stars occurred even in primordial gas (cf. Norman 2010).

⁷In contrast to the study of Cen (2003), Furlanetto & Loeb (2005) assumed a more continuous transition from population III to population II stars and therefore a more monotonic reionization history. Observations of the 21 cm line of neutral hydrogen with the LOFAR radio interferometer and the Square Kilometer Array (SKA) will allow tracing the expansion of the ionized regions in the redshift range $z = 11.5 \dots 6.5$ (Jelic 2010 and Santos et al. 2011) and help clarify the situation.

IMF ($\Gamma = -1.35$). Their result thus supports the hypothesis that a top-heavy IMF is not unusual for massive star-forming clusters and starburst galaxies even at solar metallicity. They further argued that a common property among starbursts showing such flat IMFs would be the high stellar density in the core of the cluster, and that the variations of the IMF could be linked to the spatial density of the stellar population (according to their results the core mass density of NGC 3603 is at least $6 \cdot 10^4 M_{\odot} \text{pc}^{-3}$).

Moreover, very massive stars are efficient emitters of ionizing photons with approximately 10 times more hydrogen-ionizing photons and 10 000 times more He II-ionizing photons per unit stellar mass than a population with a Salpeter IMF. Pauldrach et al. (2012) discuss a mechanism to form such objects in present-day stellar clusters. They combined consistent models of expanding atmospheres with stellar evolutionary calculations of massive single stars with regard to the evolution of dense stellar clusters, and investigated the conditions necessary to initiate a runaway collision merger which may lead to the formation of a very massive object (up to several $1000 M_{\odot}$) at the center of the cluster, and the possible formation of intermediate-mass black holes (IMBHs).⁸ Interestingly these theoretical models have been observationally supported by two studies which demonstrate the existence of VMSs in the local Universe. The first one was based on HST and VLT spectroscopy from which Crowther et al. (2010) concluded that the dense cluster R136 located in the 30 Doradus region of the Large Magellanic Cloud hosts several stars whose initial masses were up to $\sim 300 M_{\odot}$. The second study concerned the discovery of an optical transient which was classified as a Type Ic supernova (SNF20070406-008). As the observed light curve of this object fits that of a pair-instability supernova with a helium core mass of at least $100 M_{\odot}$, the progenitor of this supernova must have been a VMS (Gal-Yam et al. 2009). Runaway collision mergers clearly exceed the assumed upper limit of $100 \dots 150 M_{\odot}$ for the direct formation of present-day massive stars, and since such mergers can also occur in chemically evolved clusters of high core mass density, they may have played an important role at least in the late stages of the reionization history.

This conclusion is relevant in particular for the reionization of He II to He III, since this process was not yet completed at a redshift of $z \sim 6$. (Spectroscopic observations of He II Lyman α absorption troughs of quasars can be observed even at $z = 2.8$; Reimers et al. 1997, Kriss et al. 2001, and Syphers et al. 2011.) The reionization of He II was therefore considerably delayed compared to the reionization of H I and He I. Whether the appearance of population II and population I VMSs could have been responsible for the reionization of He II has not yet been investigated; it is presently an open point whether these very special stars, or, as assumed by Wyithe & Loeb (2003), Gleser et al. (2005), and McQuinn et al. (2009), quasars, or a mixture of these objects have been responsible for the reionization of He II.

In order to simulate and understand the reionization process different numerical approaches have been developed for a description of the radiative transfer and the evolution of the ionization fronts (e.g., Mellema et al. 2006, Gnedin & Abel 2001, Ciardi et al. 2001, Nakamoto et al. 2001, Razoumov & Cardall 2005, Ritzerveld et al. 2003, Alvarez et al. 2006, Reynolds et al. 2009, Iliev et al. 2009, Trac & Cen 2007, McQuinn et al. 2007, and Wise & Abel 2011). Many of these codes are specialized for a particular task and do not attempt to provide a comprehensive description of the time-dependent ionization structure, including the detailed statistical “equilibrium” of all relevant elements. E.g., for the purpose of simulating the radiative transfer in the early universe it is usually sufficient to just include tabulated ionization and recombination rates for hydrogen and helium, which are modelled as simple two- or three-level systems, to neglect metals, and to assume simplified

⁸Mass segregation as a result of stellar dynamics in a dense young cluster, associated with core collapse and the formation of a runaway stellar collision process, was promoted by Portegies Zwart et al. (2004) to explain ultra-luminous X-ray sources (ULX).

models for the spectral energy distribution of the sources – e.g., black-body radiators or power-law spectra described by a few discrete wavelengths specifying the fluxes in the ranges important for the particular simulations.

Our focus in contrast lies in a sophisticated description of the 3d radiative transfer with respect to high spectral resolution, in order to quantify the evolution of all relevant ionization structures accurately, in particular also with the intent of determining possible observational features, such as line strength ratios from different ions. Metal lines, for instance, could be used to reconstruct the history of metal enrichment and the characteristics of the spectra of the ionizing sources (see, for instance, Graziani et al. 2013) that might be used to discriminate between different scenarios and/or particular aspects of these scenarios. Although only H and He are treated in the present paper, our algorithm in principle allows the implementation of multiple levels for each ionization stage of the metals, and we are currently working on the inclusion of metals as described by Hoffmann et al. (2012). We note in this regard that while metal ions have no direct significance as *absorbers* affecting the radiation field and thus the ionization of hydrogen and helium, metal *cooling* has a significant influence on the temperature structure of the gas and therefore on the temperature-dependent recombination rates of H and He. Thus, the metallicity dependent temperature has an impact on the ionization structure of the most abundant elements (e.g., Osterbrock & Ferland 2006). But this procedure only makes sense if realistic SEDs of the sources driving the reionization of the universe are supplied – from population III to population I stars at various metallicities, temperatures, and masses. To this aim we use a sophisticated model atmosphere code based on a consistent treatment of the expanding atmospheres of massive and very massive stars (cf. Pauldrach et al. 2001 and Pauldrach et al. 2012; note that the winds of hot stars modify the SEDs of the ionizing radiation of the stars dramatically, cf. Pauldrach 1987 and Pauldrach et al. 1994). We are therefore able to calculate the required SEDs to be used as input for the 3d radiative transfer simulating the ionization structure of the ISM and IGM.

In the following we will first introduce the theoretical basis of our simulations covering the concept of 3d radiative transfer and the physical mechanisms which influence the ionization structure of the gas surrounding the sources of ionization. We will further present a numerical method to describe the temporal expansion of the ionization fronts which considers multiple ionization sources (Sect. 2.2). In Sect. 2.3 we discuss important details of our numerical approach and present tests comparing our 3d results with those of analytical solutions, a radially symmetric radiative transfer code, and results from a comparison project initiated by Iliev et al. (2006). In Sect. 2.4 we present first applications of our 3d radiative transfer on showcase simulations of the reionization scenario. Although using simplified initial conditions, we will demonstrate the influence of realistic stellar spectra of massive stars at different metallicities on the ionization structure of the surrounding gas under conditions which correspond to those of the early universe, and we will focus on the different behavior of the expansion of the ionization fronts with respect to a homogeneous gas density and an inhomogeneous cosmological density structure. With regard to the He II reionization problem we further investigate the influence of different input spectra on the ionization structure of He III by performing a series of multi-source simulations. We interpret and summarize our results along with an outlook in Sect. 2.5.

2.2 Three-dimensional radiative transfer as a tool for the description of the epochs of reionization

On larger scales radiation is emitted from point sources and this radiation starts to propagate homogeneously and isotropically in all directions up to a certain distance where material of the environment of the sources is encountered in the form of a density structure, which may also involve inhomogeneities

or fluctuations, and radiative processes start to have a disturbing influence on this well-suited behavior. Moreover, the radiation propagating from the different sources will overlap at specific locations and this produces a time and frequency dependent 3-dimensional pattern of radiation. The evolution of such a radiation field and all its variables – intensity, radiative flux, photon flux – is however well defined and at every point in space characterized by the *equation of radiative transfer*:

$$\left[\frac{1}{c} \frac{\partial}{\partial t} - \frac{H\nu}{c} \frac{\partial}{\partial \nu} + \hat{\mathbf{n}} \cdot \frac{1}{a} \nabla \right] I_\nu(\mathbf{r}, \hat{\mathbf{n}}, t) = \eta_\nu - \chi_\nu I_\nu(\mathbf{r}, \hat{\mathbf{n}}, t) \quad (2.1)$$

This Boltzmann equation (cf. Gnedin & Ostriker 1997) describes the transport of radiative energy via a change of the intensity I_ν , caused by the absorption coefficient $\chi_\nu \equiv \chi_\nu(\mathbf{r}, \hat{\mathbf{n}}, t) = \kappa_\nu(\mathbf{r}, \hat{\mathbf{n}}, t) + \frac{3H}{c}$ and the emissivity $\eta_\nu \equiv \eta_\nu(\mathbf{r}, \hat{\mathbf{n}}, t)$ as a function of position \mathbf{r} (in comoving coordinates), direction $\hat{\mathbf{n}}$, and time t for every frequency ν . In this equation, c is the speed of light, $a \equiv a(t)$ is the cosmological scale factor, $H \equiv H(t) = \dot{a}(t)/a(t)$ is the Hubble expansion rate, and κ_ν is the opacity; as $\kappa_\nu/(3H/c)$ is on the order of $10^4 \dots 10^6$ in the relevant frequency range of a neutral gas with a density equal to the mean density of the universe in the considered redshift range ($0 \leq z \leq 15$), we assume $\chi_\nu = \kappa_\nu$ in the remaining part of this paper.

Neglecting the explicit time derivative term (for a rationale see Sect. 2.2) and the frequency derivative term (justified if the universe does not expand significantly before the corresponding photons are absorbed – cf. Petkova & Springel 2009 and Wise & Abel 2011) in Eq. 2.1, and making use of the identity $\hat{\mathbf{n}} \cdot \frac{1}{a} \nabla = \frac{d}{ds}$, which involves the interpretation of $\hat{\mathbf{n}} \cdot \frac{1}{a} \nabla$ as a directional derivative along a path element s , the equation of radiative transfer becomes for each ray to be considered

$$\frac{dI_\nu(s)}{ds} = \chi_\nu(s)(S_\nu(s) - I_\nu(s)), \quad (2.2)$$

(where, as usual, S_ν represents the source function, defined as the ratio of emissivity to opacity, $S_\nu = \eta_\nu/\chi_\nu$). Equation 2.2 can now be solved formally in an analytical way

$$I_\nu(s) = I_\nu(s_0(n)) e^{\tau_\nu(s_0(n)) - \tau_\nu(s)} + \int_{s_0(n)}^s \eta_\nu(s') e^{\tau_\nu(s') - \tau_\nu(s)} ds'. \quad (2.3)$$

$s_0(n)$ corresponds to the starting point of each ray n , and $\tau_\nu(s) = \int_{s_0(n)}^s \chi_\nu(s') ds'$ is the usual dimensionless optical depth variable quantifying the absorption characteristics of the medium.⁹ Numerically the equation is solved using a suitable discretization scheme dividing the volume into small cells. Since by definition of this discretization scheme the opacity $\chi_\nu(s)$ stays constant along the cell-crossing distance $l_n(m)$ of each specific cell m crossed by the considered ray n , the corresponding optical depth τ can be expressed as

$$\tau_\nu(s_n(m)) = \sum_{m'=m(s_0(n))}^{m(s)} \chi_\nu(m') l_n(m') \quad (2.4)$$

(where $m(s_0(n))$ denotes the cell where the corresponding source of the considered ray n is placed and $m(s)$ denotes the cell which has just been crossed before s is reached) and Eq. 2.3 thus simplifies to

$$I_\nu(s_n(m)) = I_\nu(s_0(n)) e^{-\tau_\nu(s_n(m))}. \quad (2.5)$$

It is now straightforward to calculate from Eq. 2.5 the energy deposited per time in the cells that are

⁹In applications of the IGM the diffuse radiation field (resulting from the emission term in Eq. 2.3) is usually not explicitly treated. We employ the commonly used “on-the-spot approximation” (Zanstra 1931, Baker & Menzel 1938, Spitzer 1998, cf. also Sect. 2.2.2.1) at the present stage, and quantify its influence on the photoionization state in Sect. 2.3.3.3.

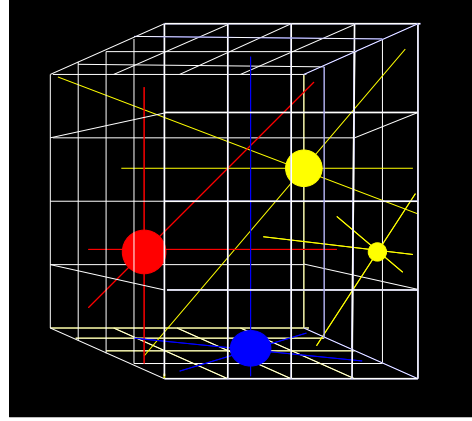


Figure 2.1: Sketch showing a subset of the rays to be treated in the ray tracing method of radiative transfer. All rays start from the sources of radiation (filled dots), but the lifetime of the sources may be much shorter than the ionization time of the volume. Possible different spectral energy distributions of the sources are indicated by different colors.

crossed by a ray n over a distance $s_n(m)$

$$\Delta \dot{E}(s_n(m)) = \int_0^\infty \tilde{L}_\nu(s_0(n)) (1 - e^{-\tau_\nu(s_n(m))}) d\nu. \quad (2.6)$$

Here $\tilde{L}_\nu = L_\nu / N_{\text{rays}}$ is the fraction of the (spectral) luminosity emitted by the source into each of the N_{rays} rays considered per source. (All rays start at sources (cf. Fig. 2.1), which represent single stars or star clusters, each with a specified spectral energy distribution $F_\nu(M_n, Z_n, T_{\text{eff}}(n), R_n)$ and spectral luminosity $L_\nu(s_0(n)) = 4\pi R_n^2 F_\nu(n)$, characterized by the source’s mass M_n , metallicity Z_n , effective temperature $T_{\text{eff}}(n)$, and radius R_n (for single stars, the stellar radius; for clusters, an equivalent radius describing the total radiating surface) – cf. Sect. 2.3.2).

2.2.1 3-dimensional radiative transfer based on ray tracing

Because the equation of radiative transfer has to be solved explicitly for every time step at every point in space, a suitable discretization scheme is required that must be able to deal with possible inhomogeneities in the density distribution of the gas in the considered volume and/or the presence of a variable number of different radiative sources which in general will not possess any kind of symmetry (cf. Figs. 2.1 and 2.2). The natural property of light to propagate along straight lines straightforwardly leads to the concept of a *ray by ray solution* which involves distributing rays isotropically around each source and solving the transfer equation for each of these rays, taking into account the interaction of the gas and the photons along the way.¹⁰

¹⁰Although this ray tracing method appears natural for solving the 3-dimensional radiative transfer, a number of other authors have considered different approaches as well. Monte-Carlo techniques, where the paths of the rays are not computed in advance, but random walks of the photons are assumed instead, are often used (e.g., Ciardi et al. 2001, Ercolano et al. 2003). The primary advantage of this procedure is that it allows scattering and re-emission processes to be included straightforwardly, but its disadvantage is that an extremely large number of photon packets has to be considered to reduce the inherent random noise (cf. Fig. 2.8). A technique that does not involve individual rays is the “moment method” in which the radiative transfer is treated as a diffusion process (e.g., Nakamoto et al. 2001, Petkova & Springel 2009) and which allows

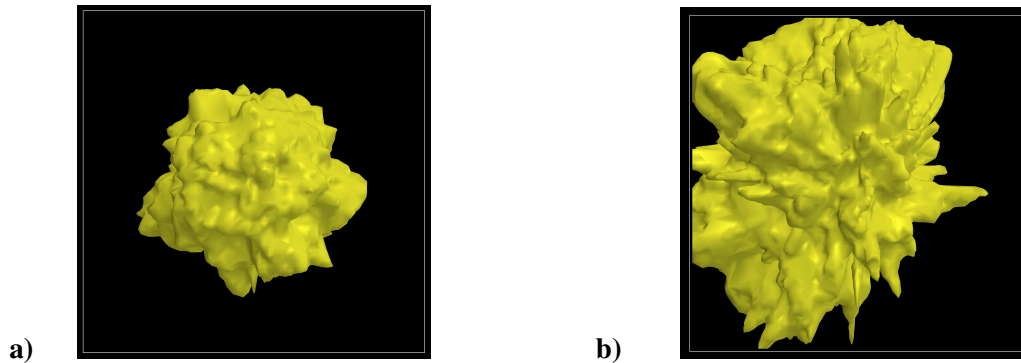


Figure 2.2: Calculated ionization fronts for volumes of gas with inhomogeneous, fractal density structures. As the gas exposed to the ionizing radiation does not exhibit an intrinsic symmetry, a three-dimensional treatment of the radiative transfer is indispensable (for computational details see Sect. 2.3). In image a) the deviations from a homogeneous density distribution are much smaller than in image b), and consequently the shape of the ionized volume is less spherical in b) than in a). (The calculation of the fractal density distributions has been based on the algorithms presented by Elmegreen & Falgarone 1996 and Wood et al. 2005.)

The ray tracing concept along with a spatial discretization scheme described by a Cartesian coordinate system can naturally account for the following three important points:

- a radiation field that is generated by numerous different point sources arbitrarily distributed in space and characterized by individually different spectral energy distributions,
- an inhomogeneous density distribution of the medium,
- the temporal evolution of the radiation field and the propagation of the ionization fronts.

Although in our discretization scheme the physical conditions are treated as being spatially constant within each cell, and we consider (for reasons of efficiency) each of the emitting sources to be located in the center of its respective cell, we can account for arbitrary distributions of the gas and the sources with a resolution limited only by the computational resources. Time-dependencies can in principle be described accurately with a suitably fine resolution in space and time. With regard to the spatial resolution we note that it is also essential that the radiation field of each source is itself discretized with a matching angular resolution so that each cell is crossed by a sufficient number of rays in order to describe the effects of the radiation on the gas correctly (cf. Fig. 2.3 and Sect. 2.3.1).

2.2.2 Physical processes affecting the state of ionization

The basis of any approach in constructing detailed radiative models for the ionization structure of the gas surrounding clusters of sources of ionization is a concept that includes the time-dependent statistical equilibrium for all important ions with detailed atomic physics – described by rate equations –, the energy equation, and the radiative transfer equation at all transition frequencies required. As all of the involved equations have to be solved simultaneously, and as the replication of the required physical

the radiative transfer to be solved very quickly even for a large number of ionizing sources. The drawback of this technique, however, is a low geometric accuracy, in particular with regard to shadowing effects that naturally occur where inhomogeneous density distributions are involved (cf. Fig. 2.2). The basic requirements for an adequate solution of the 3-dimensional radiative transfer therefore lead us and others (Trac & Cen 2007, McQuinn et al. 2007, Wise & Abel 2011) to choose the ray tracing concept for their purposes.

processes, which due to the energy input of the time varying sources continuously modify the physical properties of the surrounding gas, makes the solution of every realistic approach to a formidable problem, the method is not simple at all. We will in the following therefore give a description of the physics to be treated in some detail.

2.2.2.1 The rate equations

As an essential step of the procedure the time-dependent occupation numbers $n \equiv n(\mathbf{r}, t)$ of all ionization stages i, j of the elements considered have to be calculated. The time-dependent statistical equilibrium

$$\frac{d}{dt}n_i = \sum_{i \neq j} \mathcal{P}_{j,i}n_j - \sum_{i \neq j} \mathcal{P}_{i,j}n_i, \quad (2.7)$$

which describes the temporal derivation of the number density of an ionization stage i , and which contains via the rate coefficient $\mathcal{P}_{i,j}$ all important radiative $\mathcal{R}_{i,j}$ and collisional $\mathcal{C}_{i,j}$ transition rates, serves as a basis for this step¹¹. In order to solve these systems of differential equations we define a vector $\hat{\mathbf{n}}$, which contains the number densities of all ionization stages of the considered element, and a tridiagonal matrix \mathbf{G} , which contains in its components $g_{i,j}$ the rate coefficients¹². With these definitions Eq. 2.7 is rewritten as

$$\mathbf{E} \cdot \frac{d}{dt}\hat{\mathbf{n}} + \mathbf{G} \cdot \hat{\mathbf{n}} = \mathbf{0}, \quad (2.8)$$

where for reasons which will become obvious below the unity matrix \mathbf{E} has been applied on the time derivative term on the left hand side of the system of equations. By scaling Eq. 2.8 with the total number density of the element considered, and by replacing the fraction x_k of the ionization stage k by the condition of particle conservation

$$x_k = 1 - \sum_{j, j \neq k}^N x_j, \quad (2.9)$$

where N is the number of ionization stages and \mathbf{x} contains in its components the number densities of the ions relative to the total number density of the element, one gets the final system of inhomogeneous equations

$$\mathbf{E}' \cdot \frac{d}{dt}\mathbf{x} + \mathbf{G}' \cdot \mathbf{x} = \mathbf{b}, \quad (2.10)$$

where the components of \mathbf{G}' are given by $g'_{i,j} = g_{i,j} - g_{i,k}$, and those of \mathbf{b} are $b_i = -g_{i,k}$, and where all coefficients of the redundant k -th row of \mathbf{G}' and \mathbf{b} have been replaced by 1, and those of the k -th column of \mathbf{E} by 0 (with this replacement the unity matrix \mathbf{E} becomes \mathbf{E}') – with these numbers inserted the corresponding components represent in total the condition of particle conservation.

¹¹As just processes which can alter the charge of an ion by ± 1 are considered here, the net change $\frac{d}{dt}n_i$ of the occupation number of an ion i simplifies to

$$\underbrace{n_{i+1}(\mathcal{R}_{i+1,i} + \mathcal{C}_{i+1,i})}_{\mathcal{P}_{i+1,i}n_{i+1}} + \underbrace{n_{i-1}(\mathcal{R}_{i-1,i} + \mathcal{C}_{i-1,i})}_{\mathcal{P}_{i-1,i}n_{i-1}} - \underbrace{n_i(\mathcal{R}_{i,i+1} + \mathcal{C}_{i,i+1} + \mathcal{R}_{i,i-1} + \mathcal{C}_{i,i-1})}_{\mathcal{P}_{i,i+1}n_i + \mathcal{P}_{i,i-1}n_i}$$

Note that the number densities $n_{i,u}$ of specific atomic levels l, u of the ionization stages are not explicitly required at this stage – cf. Sect. 2.2.2.2 – and that the advection term has been neglected.

¹² $g_{i,i-1} = -\mathcal{P}_{i-1,i}$; $g_{i,i} = \mathcal{P}_{i,i-1} + \mathcal{P}_{i,i+1}$; $g_{i,i+1} = -\mathcal{P}_{i+1,i}$.

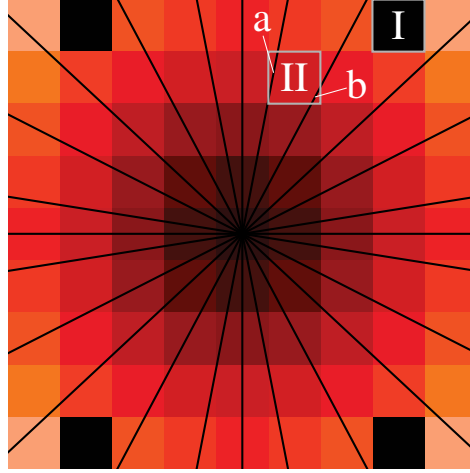


Figure 2.3: Illustration of the spatial discretization scheme by example of a 2D layer containing 9×9 cells. The different physical conditions in each cell are represented by the different cell colors, and the black lines indicate the rays used in the radiative transfer. Insufficient ray densities where some cells are not crossed by any ray (e.g., cell I) must be avoided as this will lead to spurious results since the corresponding cells will not feel the effects of the radiation field.

Modelling the temporal evolution of the ionization structure. The solution of the time-dependent rate equations (Eq. 2.10) required for modelling the temporal evolution of the ionization structures is not straightforward, because this system forms a set of stiff differential equations, and this means that the occupation numbers can change by several orders of magnitude for a gradual increase of the timescale¹³. On the other hand, for constant coefficients $\mathcal{P}_{i,j}$ ¹⁴ the rate equations form a set of linear differential equations, and such a system can in principle be solved by an eigenvalue approach. With respect to this approach the general solution for the differential equations is based on the time independent “equilibrium” solution \mathbf{x}^∞ of the inhomogeneous system

$$\mathbf{G}' \cdot \mathbf{x}^\infty = \mathbf{b}, \quad (2.11)$$

and the solution of the homogeneous system

$$\mathbf{E}' \cdot \frac{d}{dt} \mathbf{x}_{\text{hom}}(t) + \mathbf{G}' \mathbf{x}_{\text{hom}}(t) = \mathbf{0}, \quad (2.12)$$

which result in the composed solution

$$\mathbf{x}(t) = \mathbf{x}_{\text{hom}}(t) + \mathbf{x}^\infty \quad (2.13)$$

¹³This is of course not the case for those parts of the medium, which are still recombined or are already completely ionized – these parts are close to their respective statistical equilibria \mathbf{x}^∞ –; it is however obvious that time dependent drastic changes of the ionization fractions occur, if the ionization fronts reach the material, and since the ionization fronts of different ions are furthermore located at different spatial positions for every time step (cf. Sect. 2.2.1 and Sect. 2.3.1.3), the application of standard approaches – like the methods by Euler and Runge-Kutta which represent explicit methods, or the method by Rosenbrock (cf. Press et al. 1992) which represents an implicit method – is extremely problematic in order to find an accurate solution for the differential equations.

¹⁴We note that the rate coefficients actually depend on the radiation field and the electron density of each cell, which in turn are functions of the simulated ionization structure. To assume that the rate coefficients can be kept constant over a time step is nevertheless a reasonable approximation, since this assumption is consistent with the description of the physical state of the cells, given that the same assumption has been applied for the spatial discretization scheme.

of Eq. 2.10.

While the last component \mathbf{x}^∞ of the composed vector is obtained by a direct solution of Eq. 2.11, the more interesting homogeneous component $\mathbf{x}_{\text{hom}}(t)$, which contains in its coefficients just difference values, can not always be determined straightly; its physical behavior however results directly from the structure of Eq. 2.12

$$\mathbf{x}_{\text{hom}}(t) = (\mathbf{x}(t_k) - \mathbf{x}^\infty) \cdot e^{-\delta(t-t_k)}, \quad (2.14)$$

where t_k marks the begin of the considered time step, and δ is the eigenvalue of the system¹⁵.

The numerical solution of the time-dependent behavior of the ionization structures is on basis of the eigenvalue approach stable, even for large time steps (cf. Sect. 2.3.3). Nevertheless is an appropriate choice of the time step sizes extremely important, since the evolution of the ionization structures has to be traced with a sufficient temporal accuracy. In the frame of our approach it turned out that the time step-size can be controlled quite well by the following extrapolation method, which limits the maximal relative change of the ionization state within one time step,

$$\Delta t_k = \Delta t_{k-1} \min_{\text{all cells } m} \left(f \cdot \left| \frac{n_{\text{HI}}(m, t_{k-1})}{n_{\text{HI}}(m, t_{k-1}) - n_{\text{HI}}(m, t_{k-2})} \right| \right), \quad (2.15)$$

where Δt_{k-1} is the duration of the previous time step, and $n_{\text{HI}}(m, t_{k-2})$ and $n_{\text{HI}}(m, t_{k-1})$ are the number densities of neutral hydrogen at the beginning of the previous and the current time steps, respectively¹⁶.

An adequate description of the evolution of the ionization structures furthermore requires the consideration of the cosmological expansion for every time step via a scaling of the path elements $\Delta s_n(m, t)$ described by $\hat{\mathbf{n}} \cdot \frac{1}{a(t)} \nabla = \frac{d}{ds(t)}$ (cf. Eq. 2.1), i.e., the correct cosmological scale factor $a(t)$ has to be known for every time step of the simulation. For the redshift range of our simulations the scale factor can be approximated quite well by the formula

$$a(t) = \left(\frac{\Omega_{m,0}}{\Omega_{\Lambda,0}} \right)^{1/3} \sinh^{2/3} \left(\frac{3}{2} H_0 t \sqrt{\Omega_{\Lambda,0}} \right), \quad (2.16)$$

where H_0 is the Hubble constant at $z = 0$, and $\Omega_{m,0}$ and $\Omega_{\Lambda,0}$ are the usual relative contributions of matter and dark energy to the total energy of the present universe (cf. Carroll & Ostlie 2006). This is used to recompute all path elements $\Delta s_n(m, t)$ for each time step t_k according to

$$\Delta s_n(m, t_k) = \Delta s_n(m, t_{k-1}) \cdot \frac{a(t_k)}{a(t_{k-1})} \quad \forall n \forall m. \quad (2.17)$$

The particle densities $n(m, t_k)$ giving rise to the emission and absorption coefficients in the radiative transfer equation are expressed in units of the volumes $\Delta V(m, t_k)$ of the grid cells, which scale with the cube of the same factor $a(t_k)/a(t_{k-1})$, have to be rescaled analogously via

$$n(m, t_k) = n(m, t_{k-1}) \cdot \frac{\Delta V(m, t_{k-1})}{\Delta V(m, t_k)} = n(m, t_{k-1}) \cdot \left(\frac{a(t_{k-1})}{a(t_k)} \right)^3 \quad \forall m. \quad (2.18)$$

¹⁵For elements which have only two or three ionization stages an analytical solution for the eigenvalue δ has been found, and for the case of a two state system this eigenvalue is simply described by $\delta = \mathcal{P}_{1,2} + \mathcal{P}_{2,1}$ (cf. Schmidt-Voigt & Koeppen 1987).

¹⁶The interval of the new time step is determined on basis of the biggest change of the fraction of neutral hydrogen during the previous time step and the parameter f is used to adjust this value. Small values of f obviously lead to shorter time steps, and these are required for a correct description of the temporal evolution of the ionization structure, whereas large values reduce the number of necessary iterations in cases where just a stationary solution is of interest (the values chosen for f range from 0.1 to 1.0; in Sect. 2.3.3 it is shown how f affects the accuracy of the simulations).

2.2.2.2 The rate coefficients

In the following paragraphs we describe briefly the ionization and recombination rates we used as coefficients for the rate matrix \mathbf{G} . Under nebular conditions, only ionization from the ground state will be important, whereas recombination may occur also to excited levels.¹⁷ Therefore the total rates between two ionization stages are given by the sums of the rate coefficients of the specific atomic energy levels l – ground state or excited level of the lower ionization stage i – and u – ground state or excited level of the upper ionization stage $i + 1$

$$n_i \mathcal{P}_{i,j} = \sum_{\substack{l \in i \\ u \in i+1}} n_l P_{lu}, \quad n_j \mathcal{P}_{j,i} = \sum_{\substack{u \in i+1 \\ l \in i}} n_u P_{ul}, \quad (2.19)$$

where P_{lu} and P_{ul} are the rate coefficients connecting these levels, and which contain all important radiative (R_{ul} , R_{lu}) and collisional (C_{ul} , C_{lu}) transition rates.

Photoionization and computation of the mean intensity. The photoionization rates are obtained by performing the frequency integral over the mean intensity J_ν weighted by the frequency-dependent ionization cross-section $\alpha_{lu}(\nu)$

$$R_{lu} = \int_{\nu_{lu}}^{\infty} \frac{4\pi\alpha_{lu}(\nu)}{h\nu} J_\nu d\nu, \quad (2.20)$$

where ν_{lu} denotes the threshold frequency for the corresponding ionization edge. The computation of the ionization structures thus requires the calculation of the mean intensities J_ν for every grid cell. As these physical quantities cannot simply be calculated as numerical integrals of the radiative intensities over the entire sphere – $4\pi J_\nu = \oint I_\nu d\omega$, here $d\omega$ represents the solid angle –, as is the case for radiative transfer models which are based on plane-parallel or spherically symmetric geometries, a recipe for the evaluation of the J_ν values, which takes into account the discrete nature of the rays, must be provided. This recipe requires on the one hand knowledge of the function value \dot{N}_ν , which describes the number of photons transported per time and frequency by a ray n to the edge of a considered cell m positioned at a distance $s_n(m)$ from the starting point of the ray (cf. Sect. 2.2)

$$\dot{N}_\nu(s_n(m)) = \frac{\tilde{L}_\nu(s_0(n)) e^{-\tau_\nu(s_n(m))}}{h\nu} \quad (2.21)$$

(note that this equation results directly from the considerations of Eq. 2.4 and Eq. 2.6), and the function value $\Delta \dot{N}_\nu(m, n)$ of the number of photons absorbed in the considered cell from ray n via the ray segment $l_n(m)$ is analogously given by

$$\Delta \dot{N}_\nu(m, n) = \dot{N}_\nu(s_n(m)) \left(1 - e^{-\chi_\nu(m) l_n(m)}\right). \quad (2.22)$$

Summing over all rays crossing the considered cell by ray segments finally gives the function value $\Delta \dot{N}_\nu(m)$ of the total number of photons absorbed in the cell

$$\Delta \dot{N}_\nu(m) = \sum_{\substack{\text{ray} \\ \text{segments } n(m)}} \dot{N}_\nu(s_n(m)) \left(1 - e^{-\chi_\nu(m) l_n(m)}\right). \quad (2.23)$$

The recipe requires on the other hand also knowledge about the total number of radiative processes occurring per time and frequency unit in a cell. This number, the number of the sum of absorbing

¹⁷Thus, transitions between the levels must also be considered, to allow cascading to the ground level. The rate coefficients for these line transitions from level l to level l' are given by $R_{ll'} = A_{ll'}$ where $A_{ll'}$ are the Einstein coefficients of the transitions.

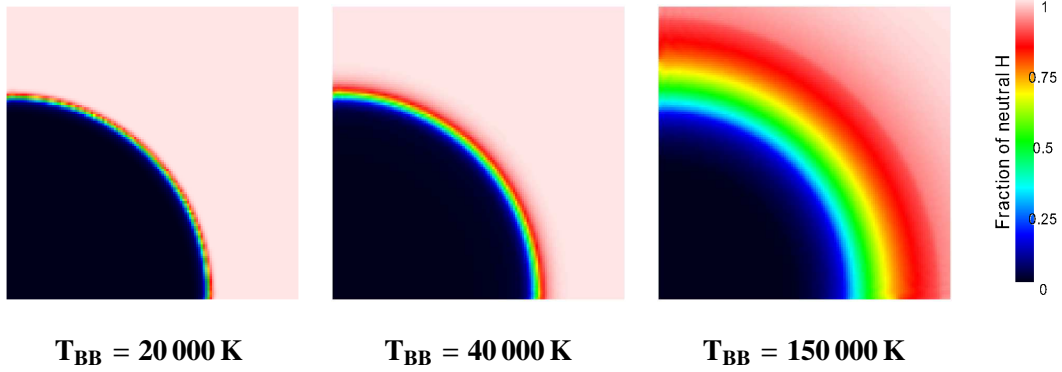


Figure 2.4: Calculated hydrogen equilibrium ionization structure as a function of the spectral energy distribution of the ionizing source, exemplified by black bodies with different temperatures but the same number of ionizing photons. Due to smaller values of the absorption cross section for photons with higher energies the shell of the “ionization front” becomes thicker for harder ionization spectra. This well-known effect can be reproduced only by models with a sufficient number of frequency points in the ionization continuum. The first panel corresponds to the result one usually obtains if the gas is illuminated by a monochromatic source.

particles in a cell – given by the product of the number densities of potential absorbers and their cross-sections, which defines as a sum the opacity $\chi_\nu(m)$, times the volume V of the cell times the number of available photons per time and frequency unit in the cell –, is represented by the function value¹⁸

$$\Delta \dot{R}_\nu(m) = \chi_\nu(m) \cdot V \cdot \frac{4\pi J_\nu(m)}{h\nu}. \quad (2.24)$$

The recipe is thus based on the fact that the number of radiative processes consuming photons in a cell has to be equal to the number of photons absorbed along the ray segments in that cell. That is, $\Delta \dot{R}_\nu(m) = \Delta \dot{N}_\nu(m)$ and the consistent value of the mean intensity J_ν is obtained from Eq. 2.23 and Eq. 2.24

$$J_\nu(m) = \sum_{\substack{\text{ray} \\ \text{segments } n(m)}} \frac{\tilde{L}_\nu(s_0(n)) e^{-\tau_\nu(s_n(m))} [1 - e^{-\chi_\nu(m)l_n(m)}]}{4\pi \chi_\nu(m) V}. \quad (2.25)$$

Radiative recombination. The radiative recombination rate coefficients are computed analogously to the photoionization rates

$$R_{ul} = \left(\frac{n_l}{n_u}\right)^* \int_{\nu_{lu}}^{\infty} \frac{4\pi \alpha_{lu}(\nu)}{h\nu} \left(\frac{2h\nu^3}{c^2} + J_\nu\right) e^{-h\nu/kT(m)} d\nu, \quad (2.26)$$

where k is the Boltzmann constant, $T(m)$ is the local value of the temperature stratification of the gas, and $\left(\frac{n_l}{n_u}\right)^*$ is the Saha-Boltzmann factor – the ratio of the occupation numbers that would be reached in the case of thermodynamic equilibrium.¹⁹

¹⁸For example, if only photoionization by one type of particle is considered as opacity source, then $\chi_\nu(m) = n_i(m)\alpha_{lu}(\nu)$, and $\Delta \dot{R}_\nu(m)$ is given by $\Delta \dot{R}_\nu(m) = V \cdot n_i(m) \cdot \frac{4\pi \alpha_{lu}(\nu)}{h\nu} J_\nu(m)$, as it must be to be consistent with Eqs. 2.19, 2.20, and 2.24.

¹⁹As we apply the so called “on-the-spot approximation” in the present stage, the total radiative recombination rate $\mathcal{R}_{j,i}$ has to be reduced by the process of direct recombination to the ground state of the lower ionization stage (in the frame of this approximation it is assumed that photons which are emitted by recombinations to the ground state are locally re-absorbed – case-B approximation). For large gas temperatures ($T > 10\,000$ K) collisions between atoms/ions and electrons are also important processes, we thus use for the collisional ionization rates an approximative formula – cf. (Mihalas, 1978, p. 134) – and the collisional recombination rates are computed by multiplying these ionization rates with the Saha-Boltzmann factor.

2.2.2.3 The temperature structure

As the recombination rates (but also emission line intensities and other diagnostic observables) depend directly on the temperature (cf. Eq. 2.26), accurate ionization structure modelling requires simultaneously determining the local temperature at every point in the gas. The physical basis for this is the microscopic energy equation which, in principle, states that the energy going into and coming out of the material must be conserved. The standard method for determining the temperature is balancing the energy gains and losses to the electron gas, including all processes that affect the electron temperature: bound-free transitions (ionization and recombination), free-free transitions, and inelastic collisions with ions. Pauldrach et al. (2001) and Hoffmann et al. (2012) give an overview of how the considered heating and cooling rates are computed in our simulations. In contrast to the method described there, however, here we do not restrict our computations to the stationary case, but instead account for temporal changes of the energy content in a grid cell with a time-dependent approach²⁰ in parallel with the time-dependent computation of the ionization structure (cf. Sect. 2.2.2.1). At the present stage we consider the ionization of only hydrogen and helium and therefore neglect cooling processes by metals (e.g., collisional cooling by the O III ion) which are dominant for metallicities characteristic of population II and population I stars. In models which simulate an already partly metal-enriched universe we therefore approximate the temperature from case to case with plausible values.

2.2.2.4 The spectral energy distribution of the radiation field

The simulation of the evolution of the ionization structures – obtained via an iteration of the radiative transfer and the rate equations – requires a representative set of frequency points at which the radiative transfer equation has to be solved. The total number of frequency points which has to be considered in this regard depends on the atomic physics which determines the distribution of the frequency points over the relevant spectral range²¹. As only hydrogen and helium have been treated as elements for the simulations presented in this paper, just hundred frequency points had yet to be considered. Table 2.1 shows the distribution of the required points over the relevant spectral range, and Fig. 2.4 demonstrates the effect of the wavelength-dependent absorption cross-section on the transition of neutral to ionized hydrogen. The images in the figure show the ionization structure obtained for blackbody sources of different temperatures, but the same number of hydrogen-ionizing photons per second (10^{49}).²² For a soft ionizing spectrum (e.g. $T_{\text{eff}} = 20\,000\text{ K}$) most of the ionizing photons have energies slightly above the Lyman-edge, and because of the large value of the ionization cross section at this frequency, the ionization front is displayed by a thin shell (this is the result one usually obtains if the gas is illuminated by a monochromatic source). In contrast, a hard ionizing spectrum (e.g. $T_{\text{eff}} = 150\,000\text{ K}$) produces a mean energy of the photons which is considerably above the Lyman-edge, and since the ionization cross section has smaller values at such frequencies, the photons penetrate deeper into the gas – because of their larger mean free paths

$$\lambda_{\nu} = \frac{1}{\sum_i \chi_i(\nu)}, \quad (2.27)$$

²⁰For the required iterative procedure we use a linearized “Euler-method” to extrapolate a temperature that balances the heating and cooling rates along with the temporal changes.

²¹We note that the structure of the photoionization cross-sections demands the photoionization integrals (Eq. 2.20) to be evaluated on a logarithmic wavelength scale.

²²The simulated volume, which is filled with hydrogen with a number density of 1 cm^{-3} and a gas temperature of $10\,000\text{ K}$, has an edge length of 101 pc .

Table 2.1: The 100 frequency points presently treated in our 3d radiative transfer calculations have been distributed over the important energy intervals as follows:

Energy Interval	No. of frequency points
$h\nu < E_{\text{ion,H I}}$	32
$E_{\text{ion,H I}} \leq h\nu < E_{\text{ion,He I}}$	20
$E_{\text{ion,He I}} \leq h\nu < E_{\text{ion,He II}}$	26
$E_{\text{ion,He II}} \leq h\nu$	22

(where the total opacity χ_ν has contributions $\chi_i(\nu)$ from each type of absorbing atom/ion i) – and the “ionization front” is therefore displayed by a thick shell. *This well-known effect can be reproduced only by models with a sufficient number of frequency points in the ionization continuum.*

2.3 Implementation and optimization details of the algorithm

The physical equations described in Sect. 2.2 are the guiding principles for the algorithm used to calculate the radiative transfer in a homogeneous or inhomogeneous gaseous medium. The numerical procedures which realize this algorithm are based on an iterative solution of the time-dependent radiative transfer (cf. Sect. 2.3.2) and the time dependent statistical description of the microphysical state of the gas, which together characterize the ionization structures in the medium surrounding the clusters of ionizing radiation sources with their characteristic properties and spatial distribution. The numerical procedures in turn are based on discretization schemes, the requisite accuracy of which determine the required lengths of the time steps, the extent of the cubic cells, the number and orientation of the rays, and the number and distribution of the frequency points. Using these iteration and discretization schemes the mean intensities are calculated per frequency interval for every cell by tracing all rays in sequential order, and from these intensities the occupation numbers are determined via a solution of the rate equations for each cell and time step. Thus, the implementation of the iteration cycle is governed by the geometrical aspects of the ray by ray solution and the time-dependencies of the equation schemes. To specify these items we will in the following section describe how the geometrical structure in our simulations is established in detail. In this regard special emphasis will be given to the ray distribution used for the radiative sources, and to the tedious calculation of the lengths of the ray segments within the cells (Sect. 2.3.1). The accuracy of our method will finally be tested in this section by some benchmark tests (cf. Sect. 2.3.3).

2.3.1 Ray tracing in a Cartesian grid

The fundamental geometrical task in grid- and ray-tracing-based 3-dimensional radiative transfer is to distribute the rays correctly. The two main geometrical aspects to meet this task are (a) tracing the segments of each individual ray correctly (cf. Sect. 2.3.1.1) and (b) implementing the isotropic character of the radiation field of every point source by distributing the rays as evenly as possible (cf. Sect. 2.3.1.2), furthermore assuring that each cell is traversed by a sufficient number of rays²³ (cf. Sect. 2.3.1.3). With respect to the second concern we have applied and tested two different approaches: a conventional latitude/longitude method where the directional vectors are equally-spaced in polar angle, and for each polar angle equally-spaced in azimuth (cf. Abel et al. 1999), and a method based on dividing the surface of a sphere into elements of equal area (Górski et al. 2005) and using the

²³Otherwise, a cell might not notice the presence of the radiation field (cf. Fig. 2.3).

directions of the centers of these areas as directional vectors for the rays. As these tests have shown that the latter method distributes the rays more evenly and thus leads to less discretization artifacts, we have decided to use this one.

2.3.1.1 Tracing the segments of a single ray

A source at coordinates (x_S, y_S, z_S) embedded in a Cartesian grid of cubic cells of identical size emits rays whose directions are defined by ϑ , the angle between the directional vector and the “north pole” (positive z axis), and the azimuthal angle φ (measured from the x axis). To compute the radiative transfer along the rays we have to know which cells are passed by which rays and how long is the segment of a ray that crosses a cell. To obtain this information we follow each ray from its source to the edge of the simulation volume and determine in sequence which border between grid cells will be crossed next by the ray. This is done via a calculation of the distances r_{yz}, r_{xz}, r_{xy} to the next yz -, xz -, xy -plane crossings in the direction of the ray. (For this purpose it is convenient to choose a coordinate system where the unit is equal to the length of a cube; in the simulation the actual physical length of a grid cell is then given by a simple scaling law.) The values r_{yz}, r_{xz}, r_{xy} thus indicate the distances from the origin of the source to the next point where a grid cell is crossed and the shortest of these distances is the one which defines the ray segment $l(m)$ (cf. Eq. 2.4 and Eq. 2.25).²⁴

2.3.1.2 Distribution of the rays

As the radiation field of an ideal point source is isotropic, any discretization of the radiation field should approximate this as close as possible and distribute the rays as uniformly as possible. Furthermore, as the luminosity of the source has to be divided among all rays, it would be highly advantageous if all rays were to correspond to approximately the same solid angle as seen from the source. Thus we have selected a method where the surface of a sphere around the radiation source is split into almost uniformly distributed segments of equal area, so that the directional vectors to the segment centers correspond to equal solid angles and are almost isotropically distributed (“hierarchical equal-area iso-latitude pixelization” method, HEALPix; Górski et al. 2005). These vectors are then used as

²⁴With the projections of the unit vector in the direction of the ray on the axes $e_x = \cos \varphi \sin \vartheta$, $e_y = \sin \varphi \sin \vartheta$, $e_z = \cos \vartheta$, and $\sigma_x = \text{sign}(e_x)$, $\sigma_y = \text{sign}(e_y)$, $\sigma_z = \text{sign}(e_z)$, one gets for the distances r to the next plane crossings (with $r_{yz|xz}$ both, r_{yz} and r_{xz} are identified)

$$r_{yz|xz}(m+1) = \frac{\left| (p_{x|y}(m) + (\sigma_{x|y} + 1)/2) - x_S | y_S \right|}{\max(\varepsilon, |\cos \varphi \sin \vartheta|)},$$

$$r_{xy}(m+1) = \frac{\left| (p_z(m) + (\sigma_z + 1)/2) - z_S \right|}{\max(\varepsilon, |\cos \vartheta|)},$$

where m is a counter variable for the cells that have been crossed by the ray, and the ε -terms are introduced to prevent a division by zero (cf. Abel et al. 1999; ε is chosen to be a small positive number), and the position indices of the crossed cells relative to the cell of the source are indicated by the components p_x, p_y, p_z . Along with $s(m+1)$, the length of the ray at the end of the current cell (cf. Eq. 2.4 and Eq. 2.6), the new position indices p_x, p_y, p_z (of the exit point of the ray $\hat{=}$ entrance point to the next cell) are obtained from:

- if $r_{yz|xz|xy}(m+1) \leq \min(r_{xz|yz|yz}(m+1), r_{xy|xy|xz}(m+1))$, then

$$s(m+1) = r_{yz|xz|xy}(m+1) \qquad p_{y|x|x}(m+1) = p_{y|x|x}(m)$$

$$p_{x|y|z}(m+1) = p_{x|y|z}(m) + \sigma_{x|y|z} \qquad p_{z|z|y}(m+1) = p_{z|z|y}(m);$$

and one gets for the ray segments used in Eq. 2.22 $l(m) = s(m+1) - s(m)$.

This procedure is repeated for each ray n . Finally, all ray segments are scaled by the corresponding physical size of the unit cell.

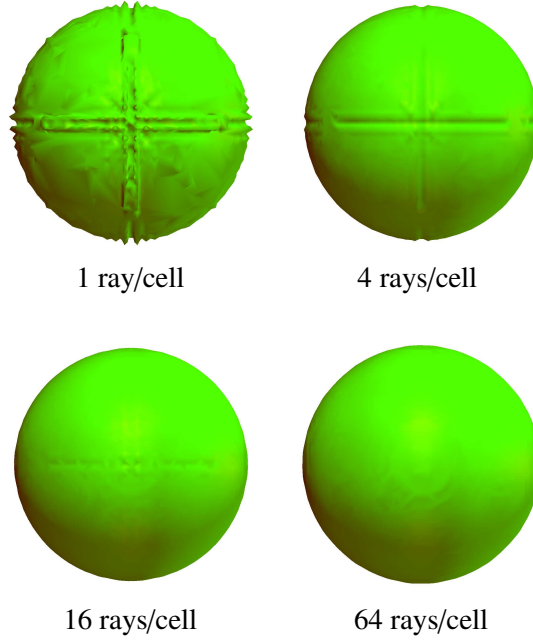


Figure 2.5: Computed ionization front around a single source in a homogeneous medium as a function of increasingly fine discretization in angles. The volume consists of 61^3 grid cells and is seen pole-on (i.e., from along the z axis). Deviations from the ideal spherical shape are particularly obvious close to the planes defined by the coordinate axes in the models with a low number of rays (top row). Only with a sufficient number of rays can the models reproduce the physically expected spherical shape (bottom row).

the directions of the rays.²⁵

2.3.1.3 Exploitation of symmetries

One of our modifications of the algorithm outlined above for computing the geometry of the rays regards the symmetry of the ray distribution of the individual sources. Because of this symmetry it is sufficient to compute the directional vectors just in one octant and to mirror the calculated geometrical

²⁵By dividing the sphere into two polar caps and an equatorial region the rays lie here on $4N_R - 1$ iso-latitude rings, and each of the $2N_R + 1$ rings in the equatorial zone contains a constant $4N_R$ rays, whereas the number of rays per latitude in the polar regions increases with increasing distance from the pole by 4 per ring (controlled by a resolution parameter $N_R = 1, 2, 4, 8, \dots$ the total number of rays therefore is $N = 12N_R^2$). The directions of the rays, ϑ measured from the north pole (positive z axis) and φ measured from the x axis, are then given by

$$\cos \vartheta = 1 - \frac{1}{3} \left(\frac{i}{N_R} \right)^2 \quad [i = 1, \dots, N_R - 1], \quad \varphi = 2\pi \frac{j - \frac{1}{2}}{4i} \quad [j = 1, \dots, 4i],$$

in the north polar cap ($2/3 < \cos \vartheta \leq 1$), and with $\xi(i) = ((i - N_R + 1) \bmod 2)$ by

$$\cos \vartheta = \frac{2}{3} \left(2 - \frac{i}{N_R} \right) \quad [i = N_R, \dots, 2N_R], \quad \varphi = 2\pi \frac{j - \frac{\xi(i)}{2}}{4N_R} \quad [j = 1, \dots, 4N_R].$$

in the northern equatorial region ($0 \leq \cos \vartheta \leq 2/3$) including the equator. These are mirrored in z for the rays in the southern hemisphere.

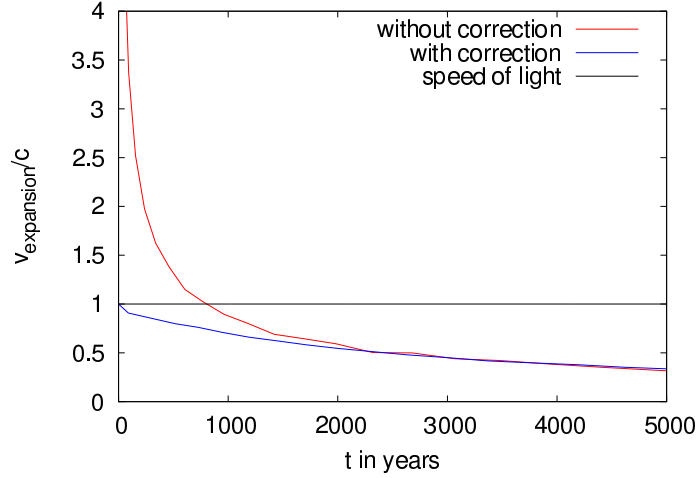


Figure 2.6: Comparison of the corrected expansion velocity of the ionization fronts (blue line) with the uncorrected one (red line) in units of the speed of light. The correction is necessary, because the explicitly time dependent term appearing in the equation of radiative transfer is not considered in our simulations. As a consequence the ionization fronts can in an artificial way propagate faster than the speed of light (cf. Sect. 2.3.2). These quasi-super-luminous expansions of the ionization fronts are avoided by delaying to the correct time step the computation of the radiative transfer for cells that can not in physical reality be reached by light emitted by the source since its appearance. For the setup of the simulation a black-body radiator with an effective temperature of 95 000 K and a radius of 9 solar radii embedded in a pure hydrogen gas with a particle density of $n = 10^{-4} \text{cm}^{-3}$ and a temperature of 10 000 K has been assumed.

factors at the planes defined by the coordinate axes.²⁶ By choosing the size of the octant as large as the entire simulated volume, the same geometrical information can be used for all sources assumed within the volume.

Besides the distribution of the rays the actual number of rays used is essential for the quality of the radiative transfer, because higher ray densities lead to a better representation of isotropy with less discretization artifacts, and in the (theoretical) limit of an infinite number of rays, the radiation field defined by the rays correctly describes the true (continuous) radiation field. Contrariwise, isotropy can be badly violated by using an insufficient number of rays, even if a good distribution algorithm is chosen. The dependence of the accuracy of the radiative transfer on the number of rays is demonstrated in Fig. 2.5.

For this test case we have chosen a single ionizing source embedded in a homogeneous isothermal gas. Because of symmetry we know that the resulting ionized volume in the gas must be spherical. (As the used geometry is independent of the density structure of the gas, the results regarding the minimum ray density necessary for an accurate description are of course also applicable for non-symmetric problems as well.) We have found that the deviations from the ideal sphere are maximal along the planes defined by coordinate axes. This is the case for both the HEALPix method as well as the equal polar angle intervals method. For an accurate representation (within the limits of the Cartesian cell grid) of the true shape of the ionized volume we need at least 10 rays per cell even in the corners of the simulation volume farthest removed from the source.

²⁶We have also tested a method in which segments of multiple rays are merged near the source to reduce the amount of ray segments that need to be processed (hierarchically ordered splitting procedure as described by Abel & Wandelt 2002). However, we found this description for the radiation field less accurate than the one without ray splitting/merging, and the additional administrative overhead not worth the small reduction in computing time achieved.

2.3.2 Accounting for the finite speed of light

Although the geometrical properties of the rays are essential for a correct description of the radiative transfer, the evolution of the ionization structures are primarily determined by the ionizing luminosities of the sources; and this means that for conditions where the ratio of photon emission rate to the gas density is very high the radius of the physical ionization front can propagate even at velocities which are close to the speed of light c . For cases where recombinations are extremely rare (e.g., at low gas densities) this behavior can even analytically be described: As essentially every emitted photon ionizes one hydrogen atom, which under these idealized conditions then remains permanently ionized, the volume of the ionized region, $V = (4\pi/3)r^3(t)$ as a function of time, multiplied by the particle number density, n , will be equal to the total number of emitted photons, $\dot{N} \cdot t$. Thus, assuming spherical symmetry

$$\dot{N} \cdot t = V \cdot n = \frac{4\pi}{3} r^3(t) \cdot n. \quad (2.28)$$

The time-dependent radius of the ionization front and its temporal derivative therefore are

$$r(t) = \sqrt[3]{\frac{3\dot{N}t}{4\pi n}}, \quad \frac{dr}{dt} = \sqrt[3]{\frac{3\dot{N}}{4\pi n}} \frac{d}{dt} t^{1/3} = \frac{1}{3} \sqrt[3]{\frac{3\dot{N}}{4\pi n}} t^{-2/3}. \quad (2.29)$$

But, at the beginning of the irradiation this simple model predicts an expansion rate of the ionization front which is faster than the speed of light:

$$\frac{dr}{dt} > c \text{ for } t < \frac{1}{3} \sqrt[3]{\frac{\dot{N}}{4\pi n c^3}}. \quad (2.30)$$

Since physical ionization fronts can not really propagate faster than the speed of light, we avoid such quasi-super-luminous expansions of the ionization fronts by delaying to the correct time step the computation of the radiative transfer for cells that can not in physical reality be reached by light emitted by the source since its appearance. This method is reasonable if, after being turned on, the luminosities of the sources do not vary considerably during the light travel time through the ionized volume. Figure 2.6 shows the speed of the ionization front as a function of its radius computed using our method, taking into account both recombination as well as the above described correction procedure.

2.3.3 Benchmark Tests

To test the accuracy of our method we have performed a series of calculations which we compare in this section to an analytical approximation, results from other 3-dimensional radiative transfer codes published in the literature (Iliev et al. 2006), and a detailed spherically symmetric model.

2.3.3.1 Temporal expansion of a Strömgren sphere in a homogeneous hydrogen gas

A very simple test case is offered by the expansion of a Strömgren sphere in a homogeneous isothermal medium consisting of pure hydrogen, since under these approximations the temporal behavior of the sphere can be described analytically

$$r(t) = \sqrt[3]{\frac{3\dot{N}(1 - e^{-n\alpha_B t})}{4\pi n_H^2 \alpha_B}}, \quad (2.31)$$

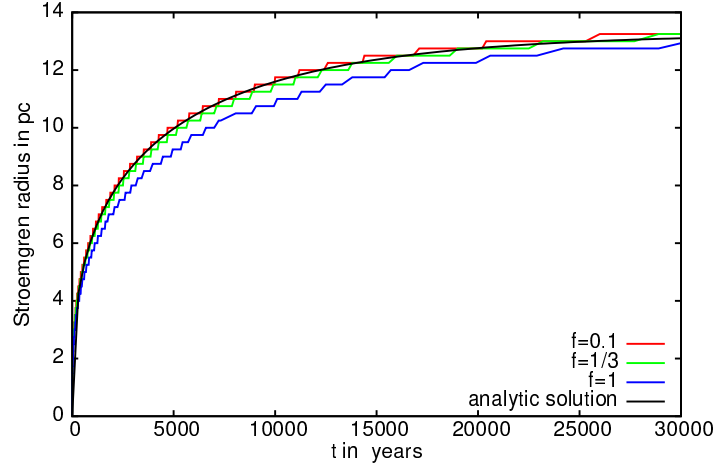


Figure 2.7: Time-dependent evolution of a Strömgen sphere in a hydrogen gas ($n = 10 \text{ cm}^{-3}$, $T = 7500 \text{ K}$) surrounding a hot star described by a blackbody radiator with an effective temperature of 40000 K and a radius of 9 solar radii for different values of the parameter f which controls the time step size (cf. Eq. 2.15). As is shown, the simulated expansion of the ionization front becomes slower for increasing time steps, and the analytic solution for the expansion of the ionization front described by Eq. 2.31 (black line) is for a value of $f = 0.1$ quite well represented by our simulation (red curve).

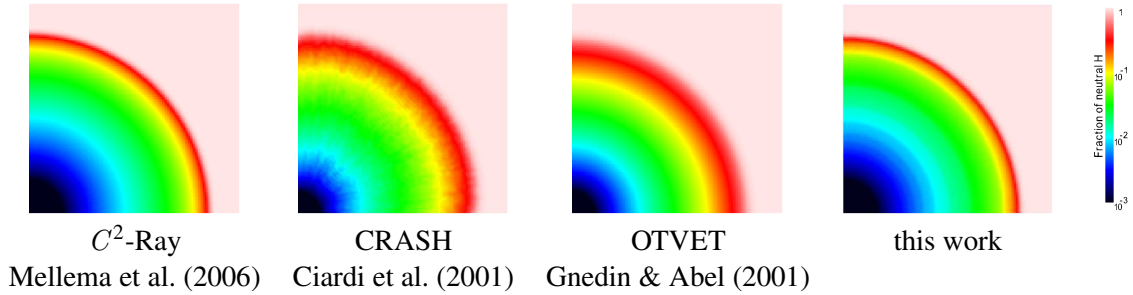


Figure 2.8: Ionization structure in a pure hydrogen gas from four model codes using different approaches for computing the radiative transfer: C^2 -Ray and our method (ray-tracing), CRASH (Monte Carlo), and OTVET (variable Eddington tensor method). The model parameters are as specified by Iliev et al. (2006): particle density 10^{-3} cm^{-3} ; illumination by a monochromatic source emitting $5 \cdot 10^{48}$ hydrogen-ionizing photons/s; box size 6.6 kpc .

where \dot{N} is the number of emitted ionizing photons per time unit, a_B is the case-B recombination coefficient and n_H is the number density of hydrogen (Iliev et al. 2006). In Fig. 2.7 we compare this analytical solution with the result of a series of our simulations produced by a variation of the parameter f which controls the time step size (cf. Eq. 2.15). The comparison shows on the one hand that for $t \rightarrow \infty$ the asymptotic value $r(t)$ is almost identical with the analytic solution, on the other hand it is also shown that the usage of larger time steps leads to slower expansions of the simulated Strömgen spheres. The explanation of this behavior is based on the fact that while the ionization fractions are updated during a time step the radiative transfer is not, and reflects the (higher) opacities at the beginning of the time step. Therefore, the number of photons reaching the cells just behind the ionization front is underestimated for long time steps. (Still, very large time steps can be used if the aim of the simulation is to compute the equilibrium state of the irradiated gas instead of an accurate description of the temporal evolution of the ionization structure.)

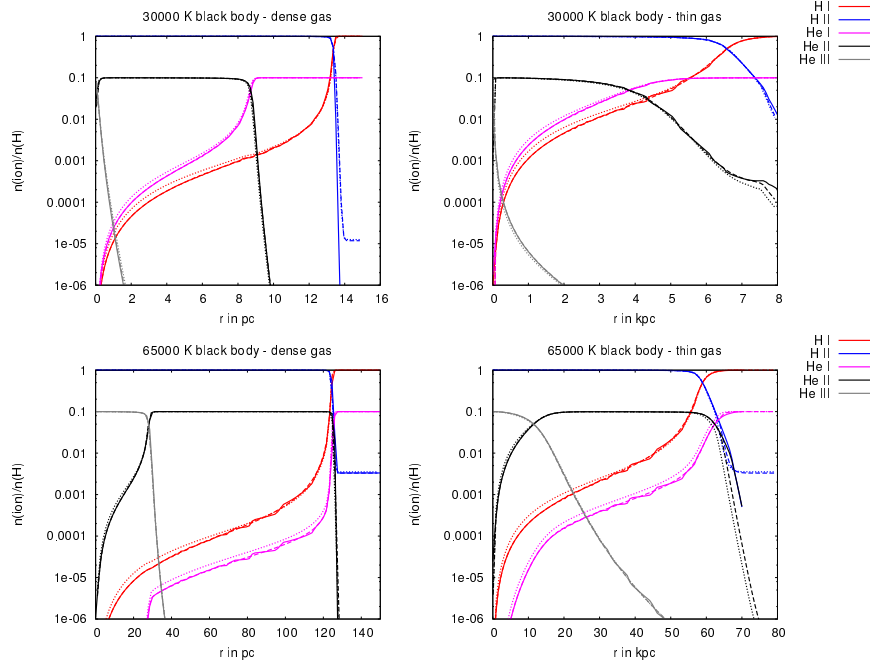


Figure 2.9: Strömgren radii and the radius-dependent H and He ionization fractions calculated with our 3d radiative transfer method (solid lines) compared to those from our spherically symmetric method. For the latter we use either the on-the-spot approximation (dashed lines) or a correct description of the diffuse radiation field (dotted lines). In the upper panels the ionizing source is a $T = 30\,000$ K blackbody emitting 10^{49} hydrogen-ionizing photons per second, representing a late O-type star (the temperature of the gas has been fixed to $7\,500$ K), and in the lower panels a $65\,000$ K blackbody emitting $8 \cdot 10^{51}$ hydrogen-ionizing photons per second, representing a VMS in the lower panel (the temperature of the gas has been fixed to a value of $10\,000$ K). The gas densities are $n_{\text{H}} = 10\text{ cm}^{-3}$ for the plots on the left and $n_{\text{H}} = 10^{-3}\text{ cm}^{-3}$ for those on the right.

2.3.3.2 Comparison with other 3-dimensional radiative transfer methods

To compare the ionization structure from our code with that from other 3d radiative transfer codes we have computed models using the parameters specified in the cosmological radiative transfer comparison project (Iliev et al. 2006). Fig. 2.8 shows our result for the ionization state of a pure hydrogen gas enclosed in a box of the size of 6.6 kpc and illuminated by a monochromatic ionizing source in comparison with other simulations, namely the C^2 -Ray simulation, which also uses the ray-tracing method, the CRASH simulation, which utilizes a Monte Carlo technique, and the OTVET simulation, which uses the variable Eddington tensor method. Although the results of the various methods do not reveal identical shapes, the fact that the structures of the C^2 -Ray simulation on the left hand side of the figure and ours on the right hand side of the figure are almost indistinguishable is a mutually satisfactory result, since both procedures are based on the same technique. (Other codes based on ray tracing give similar results to these two.)

2.3.3.3 Comparison of Cartesian and spherically symmetric models

For a test which also includes helium as a gas component in our 3d radiative transfer model we used a spherical symmetric equilibrium model (cf. Hoffmann et al. 2012) as reference. We present two sets of models, one using a hydrogen number density of 10 cm^{-3} (a typical value for H II regions) and one using a hydrogen number density of 10^{-3} cm^{-3} (a typical value for a cosmological density field at

early epochs). (As usual we set the He number fraction to $n_{\text{He}}/n_{\text{H}} = 0.1$.) For both gas densities we show in Fig. 2.9 resulting ionization structures in the gas: in the upper panels for a $T = 30\,000$ K blackbody emitting 10^{49} hydrogen-ionizing photons per second, representing a late O-type star, and in the lower panels for a $65\,000$ K blackbody emitting $8 \cdot 10^{51}$ hydrogen-ionizing photons per second, representing a very massive star (cf. Sect. 2.4.1).

In those models where we make use of the on-the-spot approximation in the spherically symmetric models, we get exactly the same results – within the resolution of the grid – as for our 3d calculations: not only are the Strömgren radii the same, but also the radius-dependent ionization fractions of H and He are almost identical for both the soft and the hard spectrum source. If we don't apply the on-the-spot approximation and instead treat the diffuse radiation field correctly in the spherically symmetric models, we find deviations on the order of 20% for the occupation numbers of the neutral stages of hydrogen and helium in the inner regions. The reason for this is that part of the reemitted photons is not reabsorbed locally, as suggested by the on-the-spot approximation, but, due to the low number of available absorbers, at larger distances. However, these small deviations are irrelevant with regard to the positions of the ionization fronts and thus the sizes of the Strömgren spheres.

2.4 Photoionization models for H II regions around luminous stars in the early universe

With this new method in hand we will present in the following first exemplary simulations of our 3d radiative transfer applied to the reionization scenario. As different characteristics of the spectral energy distributions of the sources of ionization in general have a considerable impact on the power of ionization, the application of oversimplified spectra in radiative transfer codes – e.g., black-body radiators which are based on just a few discrete wavelengths – can lead to incorrect or deceptive results. In order to quantify such possible systematic errors in the context of hot massive stars we first will perform a comparison of blackbody and realistic spectral energy distributions at different metallicities stressing for the ionizing spectra of the relevant stellar populations used as ionizing sources the importance of metal enrichment. As our focus lies on a high spectral resolution of the 3d radiative transfer describing the evolution of the most important ionization structures of the IGM in certain epochs, we will in this concern not just concentrate on a massive star representing the top of a Salpeter IMF, but also on a very massive star (VMS) resulting from a cluster-collapse as a runaway collision merger (cf. Pauldrach et al. 2012 and references therein).

In the introduction we discussed that the reionization process may have occurred in two distinct steps (Cen 2003), where the first one was primarily driven by population III stars and was concluded at a redshift of $z \sim 15$, whereas the second one, which completed the reionization with radiation from population II/I stars, finished at a redshift of $z \sim 6$. With respect to time-dependent simulations of the reionization scenario we will therefore perform in a first step multi-source simulations for population III stars in homogeneous and inhomogeneous cosmological gas distributions representing the first stage of the reionization process in order to investigate on the one hand the evolution of the ionization fronts into the IGM and on the other hand the fraction of photons which can escape from the ISM surrounding the ionizing sources and thus build up the ionization fronts in the IGM. In an advanced step we further will combine our predicted SEDs of massive and very massive stars with time-dependent 3d radiative transfer simulations of the IGM in order to describe the second stage of reionization. Although our models are still based on simplified initial conditions, the general requirements that might have allowed the much less massive population II and population I stars to fully reionize the IGM – this approach is basically motivated by the increasing star formation rate

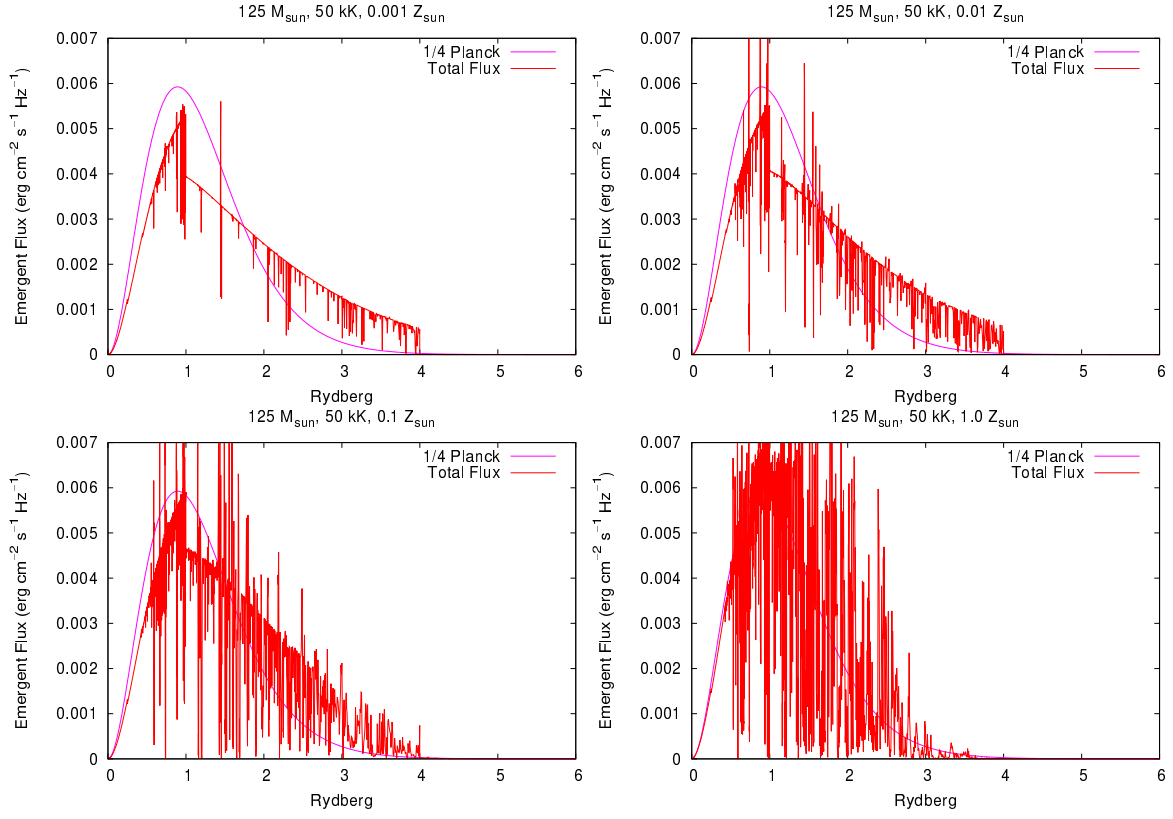


Figure 2.10: Emergent Eddington flux H_ν versus wavelength calculated for $125 M_{\odot}$ stars with effective temperature 50 000 K and different metallicities – 0.001, 0.01, 0.1 and $1.0 Z_{\odot}$ (from upper left to lower right) – compared to an equivalent blackbody.

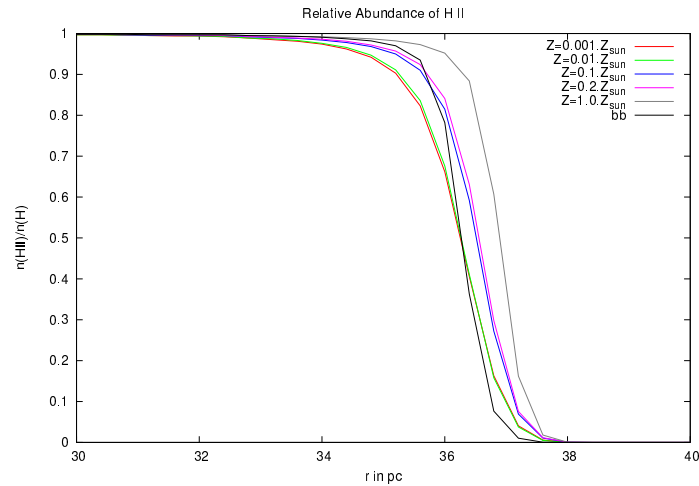


Figure 2.11: Ionized hydrogen fraction in a H/He gas ($n_{\text{H}} = 10 \text{ cm}^{-3}$, $n_{\text{He}}/n_{\text{H}} = 0.1$, and $T_{\text{gas}} = 10\,000 \text{ K}$) surrounding the above $125 M_{\odot}$ stars, again in comparison to that of an equivalent blackbody. The variation of the stellar metallicity only has a small influence on the Strömgen radii.

Table 2.2: Logarithm of the number Q of H-, He I-, and He II-ionizing photons emitted per second by a massive star ($M = 125 M_{\odot}$, $R = 21.7 R_{\odot}$, and $T_{\text{eff}} = 50\,000$ K) as a function of metallicity Z , compared to those of an equivalent black body. The third column lists the consistently calculated mass-loss rates \dot{M} of the stellar models.

Z/Z_{\odot}	\dot{M} ($10^{-6} M_{\odot}/\text{yr}$)	$\log Q_{\text{H}}$	$\log Q_{\text{He I}}$	$\log Q_{\text{He II}}$
1.0	29.0	50.28	49.66	42.84
0.2	13.3	50.26	49.77	46.90
0.1	9.2	50.26	49.78	46.89
0.01	2.0	50.25	49.81	46.56
0.001	0.1	50.25	49.82	45.91
black body		50.25	49.54	47.14

in this epoch (Lineweaver 2001) – can already be investigated even at this stage. Regarding the reionization of He II to He III in particular, we investigate further the influence and relevance of a top-heavy-IMF connected to very massive stars. Whether the appearance of population II and population I VMSs could have been responsible for the reionization of He II will therefore be examined as a crucial point.

2.4.1 Comparison of blackbody and realistic spectral energy distributions at different metallicities as ionizing sources

Motivated by the fact that metallicities which are different from zero can have a strong influence on the spectral energy distributions (SED) of massive stars and that the ionizing fluxes can at certain frequencies ranges therefore depart decisively from those of blackbody radiators we computed comparison models using synthetic SEDs from atmospheric models instead of blackbodies as ionizing sources. To limit the scope of this challenge we do not attempt to trace the metallicity dependent characteristics of the spectral energy distributions of a complete set of stellar populations we rather want to demonstrate the effects of metallicity on the spectra and furthermore the ionized structures by means of a series of striking objects.

A massive star representing the top of a Salpeter IMF. As striking stellar objects are primarily characterized by their mass, we have chosen a $125 M_{\odot}$ star with an effective temperature of $T_{\text{eff}} = 50\,000$ K and a radius of $R = 21.7 R_{\odot}$ as a first example. Figure 2.10 shows spectral energy distributions computed for this object assuming different metallicity values (ranging from 0.001 to 1.0 Z_{\odot} – the spectra have been calculated on basis of the method described by Pauldrach et al. 2001, 2012). With respect to the mass each of these models represents obviously a star which can be regarded to mark the top of a metallicity dependent Salpeter IMF. As suspected, Fig. 2.10 shows clearly that an enhancement of metallicity has a drastic influence on the SEDs. While the hydrogen-ionizing flux ($\lambda < 911 \text{ \AA}$) is primarily influenced by P-Cygni spectral lines, shorter wavelengths, as the He II ionization edge at $\sim 228 \text{ \AA}$, are also influenced by NLTE-effects affecting the bound-free thresholds of certain ionization stages (cf. Pauldrach et al. 2012) and producing in comparison with blackbody radiators considerable differences.

The results of our 3d radiative transfer calculations for the radial density distribution of ionized hydrogen surrounding the $125 M_{\odot}$ stars with different metallicities are shown in Fig. 2.11. (The parameters of the model correspond to a typical H II region: $n_{\text{H}} = 10 \text{ cm}^{-3}$, $n_{\text{He}}/n_{\text{H}} = 0.1$, and $T_{\text{gas}} = 10\,000$

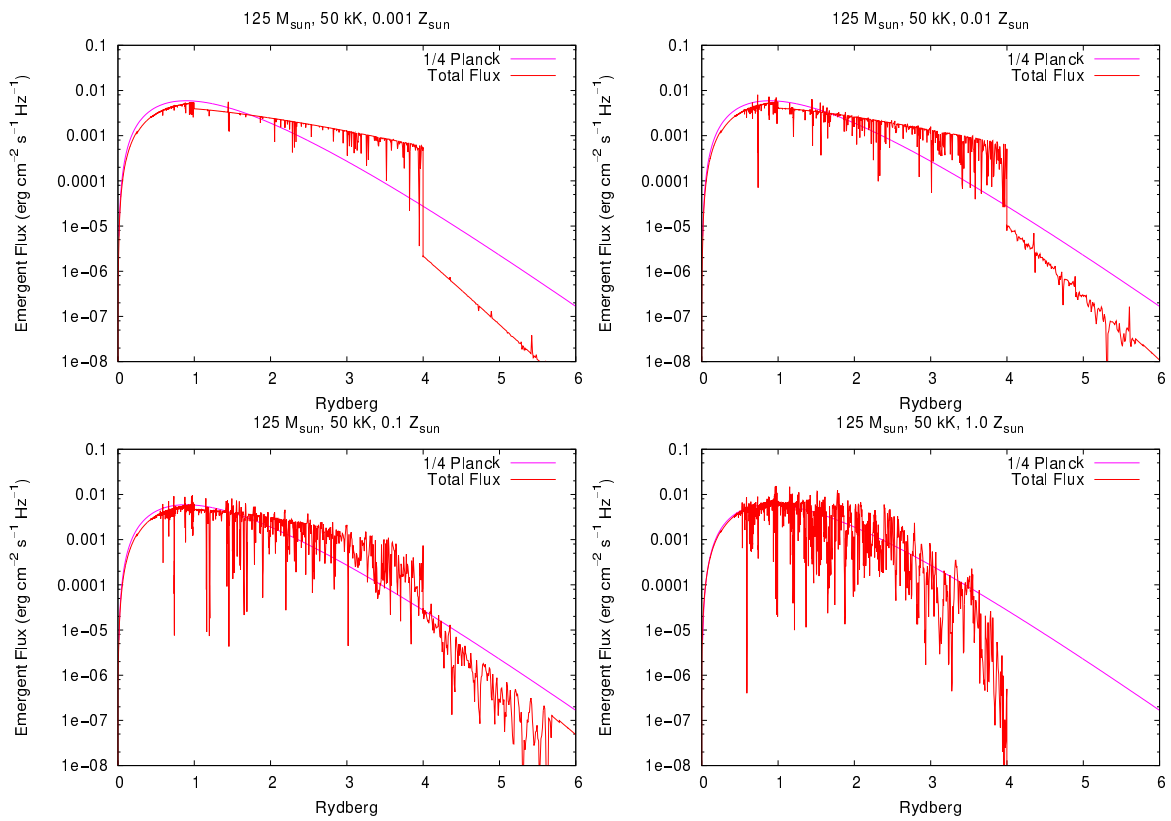


Figure 2.12: As Fig. 2.10, but the flux is now shown on a logarithmic scale. On this scale it is verified that the ionizing fluxes shortward of the He II ionization edge (4 Rydberg) vary considerably along with a change of the metallicity (cf. Table 2.2).

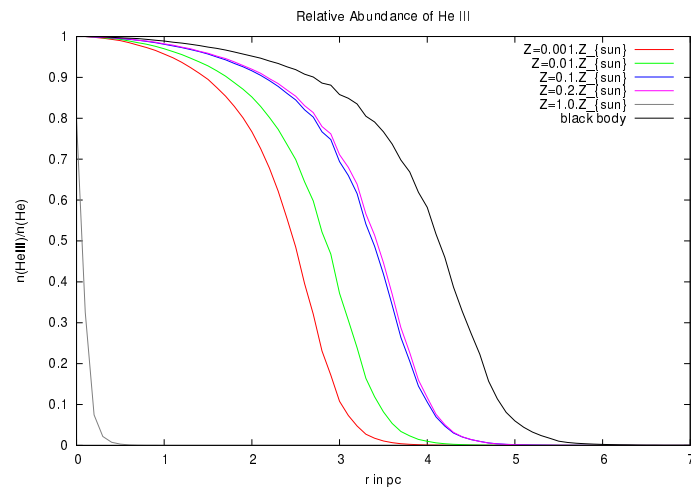


Figure 2.13: As Fig. 2.11, but the ionization fraction of He III is now shown (cf. Table 2.2). In contrast to hydrogen the efficiency to ionize He II depends in this stellar parameter range crucially on the metallicity of the stars, leading to a strong influence on the Strömgen radii.

K.) Although at the effective temperature of 50 000 K of the ionizing source the difference of the solar metallicity spectrum to the blackbody spectrum leads to a considerable difference of $\sim 4\%$ for the hydrogen Strömngren radius – corresponding to a difference of $\sim 12\%$ in the ionized volume –, the variation of the metallicity of the stars does not have a huge influence on the number of hydrogen-ionizing photons, and therefore a replacement of especially the lowest metallicity spectrum ($0.001 Z_{\odot}$) by a blackbody spectrum, which leads to a radial error of $\sim 3\%$ which corresponds to a maximal error of $\sim 9\%$ in the ionized volume, may appear to be legitimate.

However, the similarity of the hydrogen Strömngren spheres presented here results primarily from the fact that the influence of the metals in the gas and therefore the corresponding cooling and heating processes have been neglected. A consistent computation including metals would actually lead to smaller temperatures for larger metallicities and thus result in smaller Strömngren spheres (Osterbrock & Ferland 2006). An even larger influence on the ionization structure of the metals in the gas and thus on the gas temperatures and Strömngren spheres will be caused by the non-LTE line blocking and blanketing²⁷ in the expanding atmospheres of the massive stars which ultimately Pauldrach et al. 2001 – a superficial impression of this behavior can also be obtained by a thorough inspection of Fig. 2.10). From these arguments it is quite obvious that our Fig. 2.11 does not yet represent an ultimate result!

Regarding the radial density distribution of He III differences of the Strömngren radii which originate from different metallicities of the ionizing sources are considerably more pronounced (cf. Fig. 2.13) – as an example, the difference of the blackbody to the spectrum calculated with solar metallicity leads to a difference in the He III Strömngren radius by a factor of 30. But these differences are not necessarily a monotonic function of increasing metallicity of the ionizing sources. With respect to our calculations the number of emitted He II-ionizing photons increases from the model with $Z = 10^{-3} Z_{\odot}$ to the model with $Z = 0.2 Z_{\odot}$, whereas it decreases drastically – by 4 orders of magnitude – for the model with solar metallicity (cf. Figure 2.12 and Table 2.2, which show that there is no strict relationship between the metallicity and the emission of He II-ionizing photons). These results show clearly that the number of He II-ionizing photons is not just strongly influenced by the effective temperature and hence the mass of the relevant objects, but also by the evolution of the metallicity. Employing blackbody spectra in general therefore leads for the cases of helium and metals whose ionization energies exceed those of H I and He I to inaccurate ionization structures. As exactly the elements which are affected by this approximation are producing the characteristic and in principle observable emission lines, such a weak-point in the computation of the ionization structures would make as a consequence a comparison to observations extremely disputable (cf. Rubin et al. 1991a, Sellmaier et al. 1996, and Rubin et al. 2007).

A very massive star as a runaway collision merger from a cluster-core collapse. As a second example of our investigation of the influence of realistic spectral energy distributions of massive stars on the ionization structures of the surrounding gas we have chosen an even more impressive stellar object: a $3000 M_{\odot}$ star. Such stars are expected to form as runaway collision mergers in cluster-

²⁷Non-LTE refers to detailed modelling of the statistical equilibrium of the occupation numbers of the atomic levels, obtained from actually solving the system of rate equations, without assuming the approximation of local thermodynamic equilibrium (LTE). The effect of line blocking refers to an attenuation of the radiative flux in the EUV and UV spectral ranges due to the combined opacity of a huge number of Doppler-shifted metal lines present in massive stars in these frequency ranges. It significantly influences the ionization and excitation and the momentum transfer of the radiation field through radiative absorption and scattering processes. As a consequence of line blocking, only a small fraction of the radiation is re-emitted and scattered in the outward direction, whereas most of the energy is radiated back to the surface of the star, leading there to an increase of the temperature (“backwarming”). Due to this increase of the temperature, more radiation is emitted at lower energies, an effect known as line blanketing.

Table 2.3: As Table 2.2, but for a very massive star ($M = 3000 M_{\odot}$, $R = 79 R_{\odot}$, and $T_{\text{eff}} = 65\,000\text{ K}$) as a function of hydrogen mass fraction X and metallicity Z .

X	Z/Z_{\odot}	\dot{M} ($10^{-6}M_{\odot}/\text{yr}$)	$\log Q_{\text{H}}$	$\log Q_{\text{He I}}$	$\log Q_{\text{He II}}$
0.70	0.05	132.	51.89	51.55	49.77
0.70	1.0	385.	51.92	51.50	49.60
0.40	1.0	260.	51.88	51.53	49.33
black body			51.89	51.39	49.66

core collapses, and via feedback effects due to their enormous radiation and strong stellar winds they naturally have a considerable impact on their environment and the local star formation (cf. Sect. 2.1).

Figs. 2.14 and 2.16 show the SEDs of three model atmospheres of such a star ($L = 10^8 L_{\odot}$, $T_{\text{eff}} = 65\,000\text{ K}$; cf. Pauldrach et al. 2012) computed for different metallicities ($Z = 0.05 Z_{\odot}$ and $Z = 1.0 Z_{\odot}$) and different hydrogen mass fractions X (70 % and 40 %). Together with the consistently calculated mass loss rates the ionizing fluxes of the model stars are listed in Table 2.3. The luminosities of these VMSs exceed those of massive O stars at the top of a Salpeter or Kroupa-IMF by one to two orders of magnitude.

Although the hydrogen-ionizing fluxes of these models are close to those of a corresponding blackbody (Fig. 2.14 and Table 2.3), increasing metallicity and/or increasing helium mass fraction leads to a clear decrease of the He II-ionizing fluxes: while the metal-poor star with a normal helium content has a He II-ionizing flux 29 % larger than that of a corresponding blackbody, for the helium-enriched star with solar metallicity it is 53 % *smaller* (Fig. 2.16 and Table 2.3). As a consequence of this behavior the hydrogen Strömgren radii differ from the blackbody Strömgren radius by only 3 % (Fig. 2.15), but the He III Strömgren radii show differences to the corresponding blackbody value of up to 25 % (Fig. 2.17).

The differences between our very massive stars and a black body are small, however, when compared to the differences between our very massive stars and our normal $125 M_{\odot}$ massive stars. The hydrogen-ionizing fluxes of the $3000 M_{\odot}$ stars are a factor of 40 larger than those of the $125 M_{\odot}$ stars, while the He II-ionizing fluxes of the $3000 M_{\odot}$ stars exceed those of the $125 M_{\odot}$ stars by a factor of 800 to several 10^6 , depending on the metallicity (Table 2.2 and Table 2.3). Due to the large luminosities and effective temperatures of the very massive stars the radii of the hydrogen Strömgren spheres thus differ by a factor of 3.5 and those of the He III Strömgren spheres by a factor of up to 100 (Fig. 2.15 and Fig. 2.17).

We conclude from this that the transition from normal massive stars to very massive stars could strongly influence the relative volumes of He III to H II. This assessment does not change if the fluxes are normalized to the same hydrogen-ionizing photon rate: in this case the He II-ionizing fluxes of the VMSs are still at least a factor of 20 larger. As this finding may be of importance for a possible scenario of the cosmic He II-reionization, we will return to this point in Sect. 2.4.2.2.

2.4.2 Time-dependent simulations for different characteristics of the reionization scenario

In order to better understand the reionization process of the universe, the evolution of the ionization fronts expanding in the IGM has to be examined in some detail using a numerical treatment of the radiative transfer and the microphysics of ionization and recombination. For this purpose we present

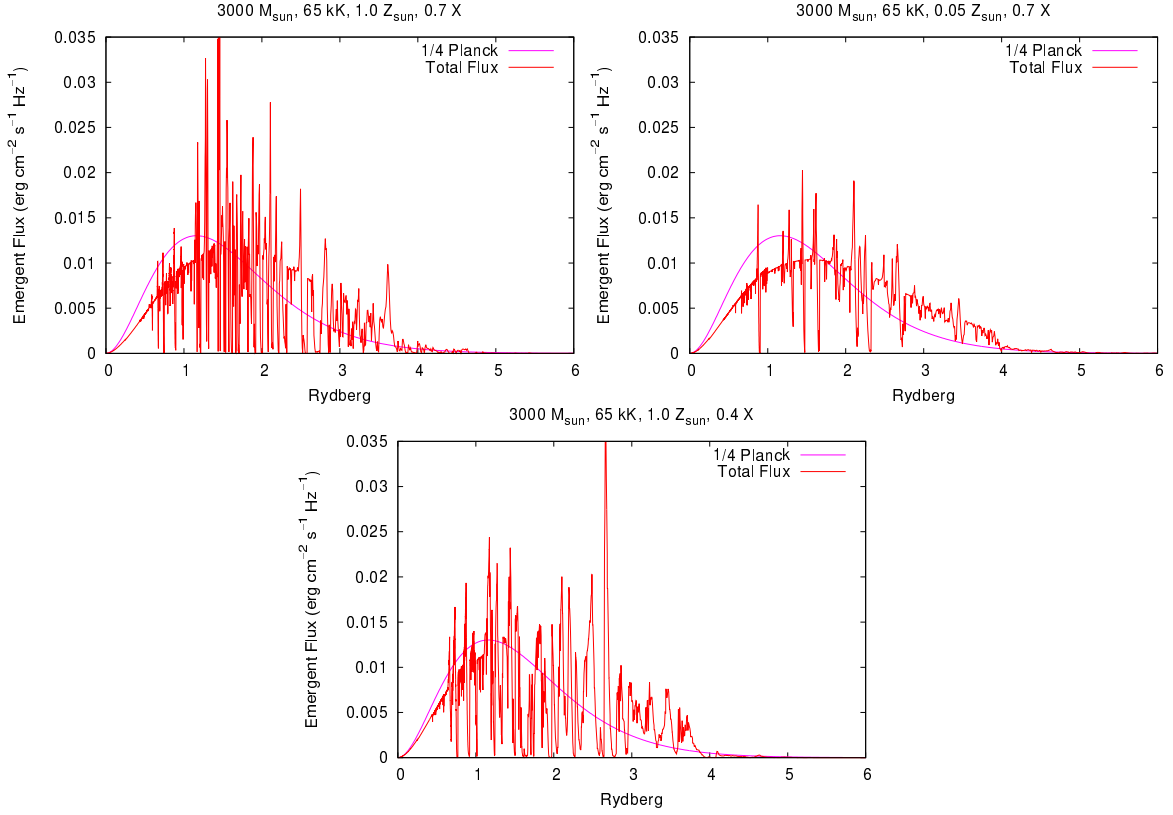


Figure 2.14: Emergent Eddington flux H_ν versus wavelength calculated for very massive $3000 M_\odot$ stars with effective temperature 65 000 K and radius $79 R_\odot$, for different compositions (a metallicity of 1.0 and 0.05 Z_\odot and a hydrogen mass fraction of 0.7 (first row), and a metallicity of 1.0 Z_\odot and a hydrogen mass fraction of 0.4 (second row)), compared to an equivalent blackbody.

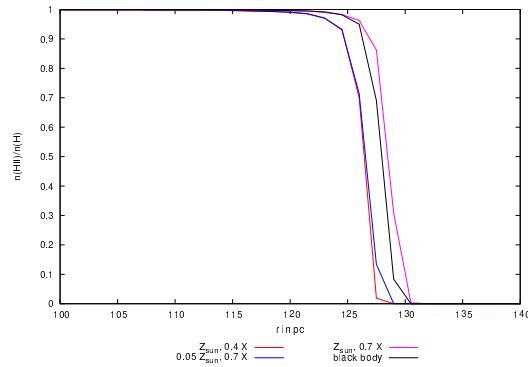


Figure 2.15: Ionized hydrogen fraction in a H/He gas ($n_{\text{H}} = 10 \text{ cm}^{-3}$, $n_{\text{He}}/n_{\text{H}} = 0.1$, and $T_{\text{gas}} = 10\,000 \text{ K}$) surrounding the above very massive stars, again in comparison to that of an equivalent blackbody. Here also, the variation of the stellar metallicity only has a small influence on the Strömgren radii.

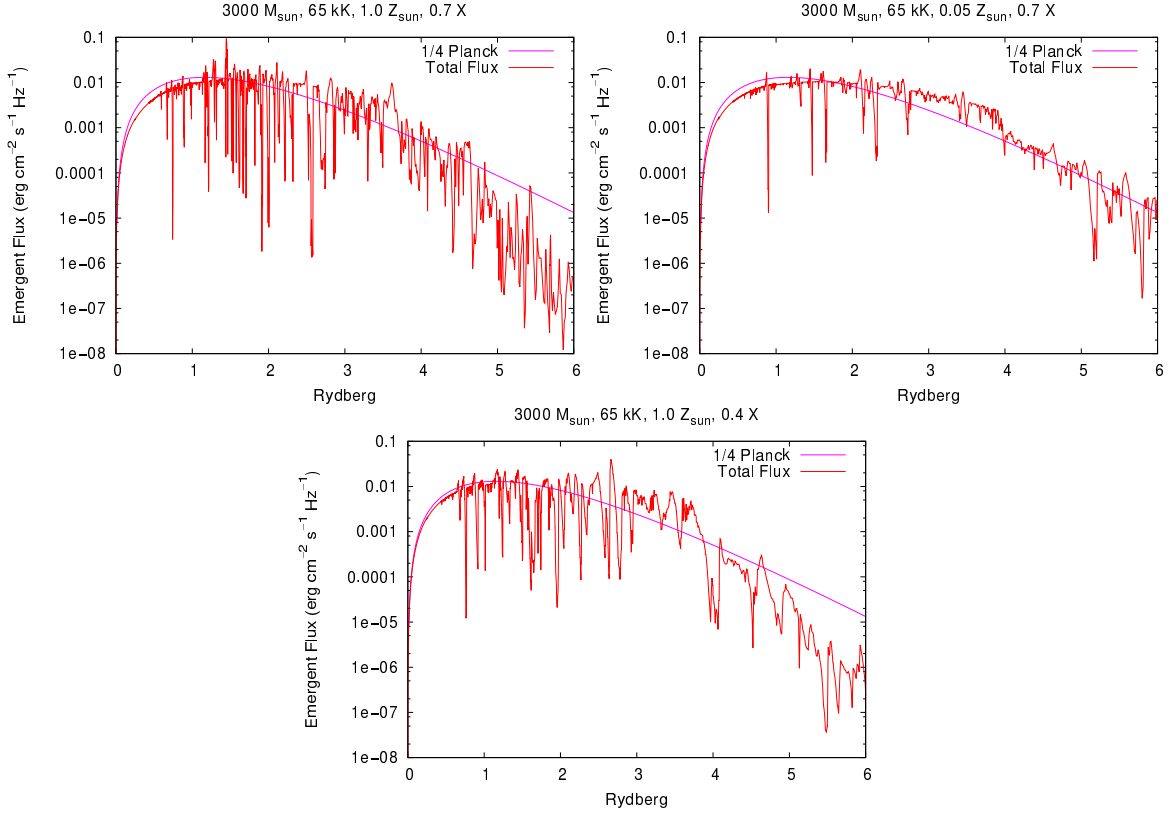


Figure 2.16: As Figure 2.14, but the flux is now shown on a logarithmic scale. On this scale the variation of the fluxes in the range above the He II ionization edge with metallicity is verified. For a metallicity of $0.05 Z_{\odot}$, there is a considerably stronger flux of these photons than for the models with Z_{\odot} . Because of the larger He abundance, the model at the bottom shows less emission in the He II-ionizing part of the spectrum.

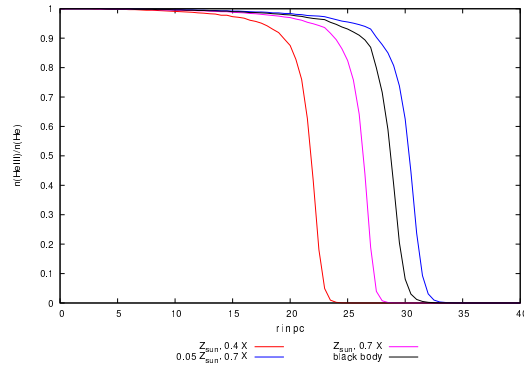


Figure 2.17: As Fig. 2.15, but the ionization fraction of He III is now shown (cf. Table 2.3). The efficiency to ionize He II rises for higher fractions of hydrogen and lower metallicities in the stars. This leads to Strömgren radii around VMSs which are a factor of up to 100 larger than those around “normal” $125 M_{\odot}$ stars (cf. Fig. 2.13).

in this section typical results of our 3d radiative transfer simulations for representative values of the densities and star formation rates. In these simulations we use clusters of massive population III stars (for the simulations representing the first stage of reionization) and population II/I stars (for the second

stage of reionization) as ionization sources, surrounded by an environment reflecting the intergalactic cosmological gas.

2.4.2.1 Multi-source simulations for population III stars in homogeneous and inhomogeneous gas distributions

As already mentioned in the introduction, the time around $z \sim 13.5$ marks the transition from population III to population II/I stars and leads to a decline in the emitted radiative power. On the other hand, the star formation rate of population III stars was highest around $z \sim 15$, shortly before this stellar generation died out. For the first part of the reionization process that was driven by population III stars we have therefore selected this redshift for our calculations.

First stage of the reionization scenario in a homogeneous gas distribution. Representing the first stage of the reionization history we have calculated models which simulate a volume of $(330 \text{ kpc})^3$ in proper coordinates at $z = 15$ (which is a volume of $(5.3 \text{ Mpc})^3$ in comoving coordinates at $z = 0$) resolved into 101^3 grid cells. The temperature of the gas has been kept constant ($T = 10\,000 \text{ K}$, cf. Cen (2003)), and the simulations use randomly distributed clusters of massive population III stars surrounded by a primordial environment characterized – as a rough approximation of the real situation – by a homogeneous intergalactic cosmological gas with a hydrogen number density of $8 \cdot 10^{-4} \text{ cm}^{-3}$ (reflecting the mean baryonic density of the universe at the given redshift, cf. Yoshida et al. 2004). The spectra of the multiple ionizing sources with a representative temperature of $95\,000 \text{ K}$ have been approximated by blackbodies (at such a high temperature and a negligible metallicity the number of hydrogen-ionizing photons is almost perfectly described by blackbody emitters, cf. Sect. 2.4.1). Although we have not accounted for structures on smaller scales in this simulation, we have compared the assumed distances of our clusters with the distances between the largest clusters investigated by Gnedin & Bertschinger (1996) and found reasonable agreement. Each of our ten clusters emits $4 \cdot 10^{53}$ hydrogen-ionizing photons per second, which corresponds to a star formation rate of $9.5 \cdot 10^{-3} M_{\odot} \text{ yr}^{-1}$ per comoving Mpc^3 (matching the rate deduced from Cen 2003, and Hernquist & Springel 2003 at a redshift of $z = 15$) and represents the emission of 4 000 population III stars with a mass of $100 M_{\odot}$ and a lifetime of 3 Myr (El Eid et al. 1983, Schaerer 2002).²⁸

The evolution of the ionization fronts expanding into the IGM in our simulation is shown in Fig. 2.18. This simulation predicts that the clusters of population III stars as predicted by the theoretical star formation rate can ionize the intergalactic hydrogen on a timescale of just $t \sim 50 \text{ Myr}$ (corresponding to $\Delta z \sim 1.5$ at $z = 15$). Although cosmic variance could modify the reionization timescales when going to larger box sizes, this result is nevertheless significant, since our chosen volume with regard to the assumed and the observed mean distances of the cluster structures in this epoch is representative for the first stage of the reionization history of the universe. The time around $z \sim 15$ is the “optimum” period for this reionization phase since in this epoch the star formation rate of population III stars (Cen 2003), and thus the photon emission rate, rises rapidly, just before the changeover to population II stars significantly cuts down on the emission rate of ionizing photons. Thus, our results indicate that the small contributions to the reionization before $z \sim 15$ are mostly insignificant for ionizing the universe completely, and the exact time of the beginning of the process is not essential.

²⁸We note that our simulations are based on the assumption that the stellar population appears instantaneously and does not fade away. We further assume that there is an enhanced absorption of ionizing photons with respect to denser gas inside the clusters (from an investigation of smaller-scale structures surrounding the sources of ionization (cf. Fig. 2.22) we inferred that half of the ionizing photons should be absorbed within the denser gas inside the clusters for such an environment); thus, we assume that the escape fraction of the photons is 50 % ($f_{\text{esc}} = 0.5$).

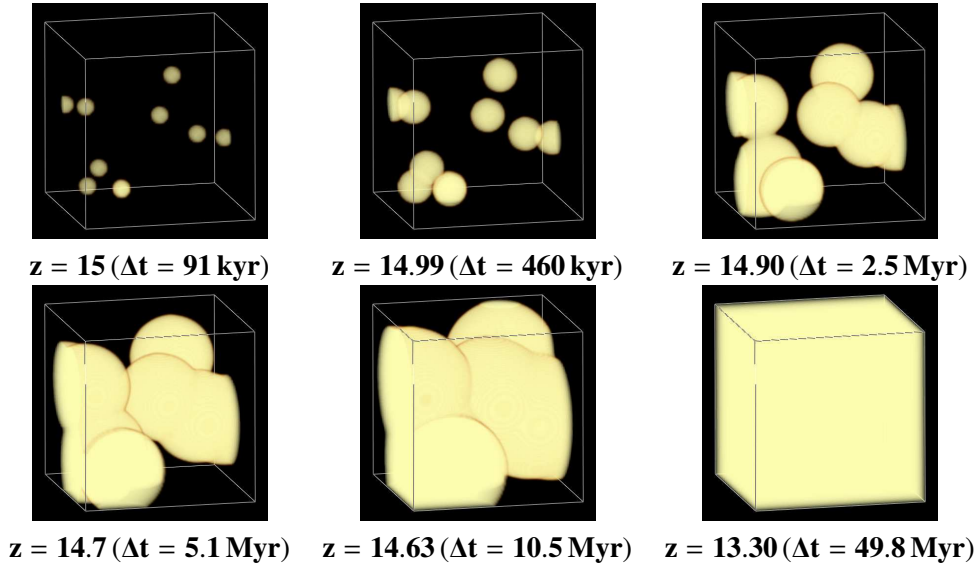


Figure 2.18: The evolution of hydrogen ionization fronts expanding into the IGM in a simulation representing the first stage of the reionization history around $z = 15$. The volume is $(5.3 \text{ Mpc})^3$ in comoving coordinates, resolved in 101^3 grid cells containing ten randomly distributed clusters of massive population III stars. Each cluster emits $4 \cdot 10^{53}$ hydrogen-ionizing photons per second, corresponding to a star formation rate of $9.5 \cdot 10^{-3} M_{\odot} \text{ yr}^{-1}$ per comoving Mpc^3 . The evolution of the ionization fronts starts with a set of discrete H II regions which begin to overlap after approximately 1 Myr. Hydrogen is completely ionized after 50 Myr (corresponding to $\Delta z \sim 1.5$ at $z = 15$).

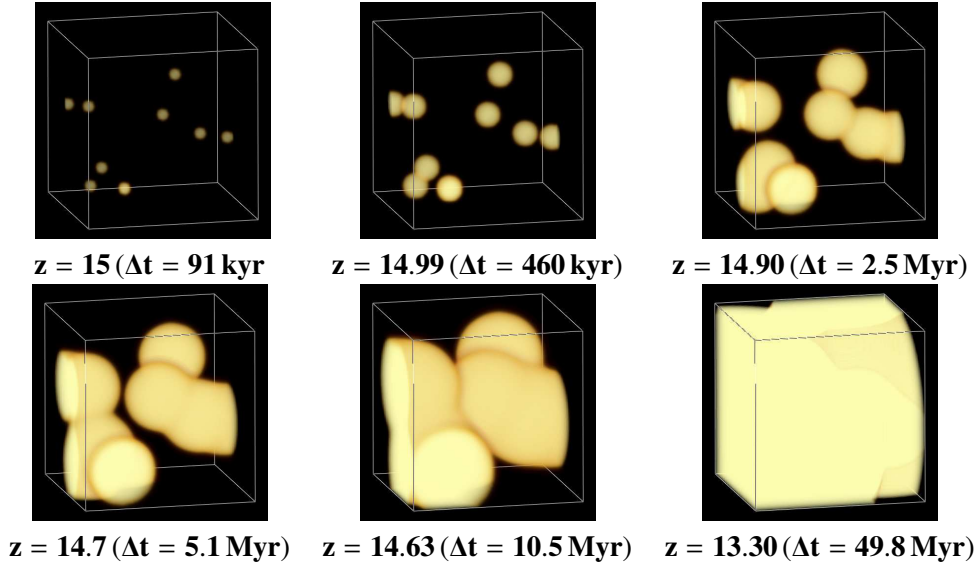


Figure 2.19: As Fig. 2.18, but showing He III. Due to the high effective temperatures (95 000 K) of population III stars and the correspondingly high emission rate of He II-ionizing photons the reionization of He II occurs on a timescale comparable to that of the reionization of hydrogen.

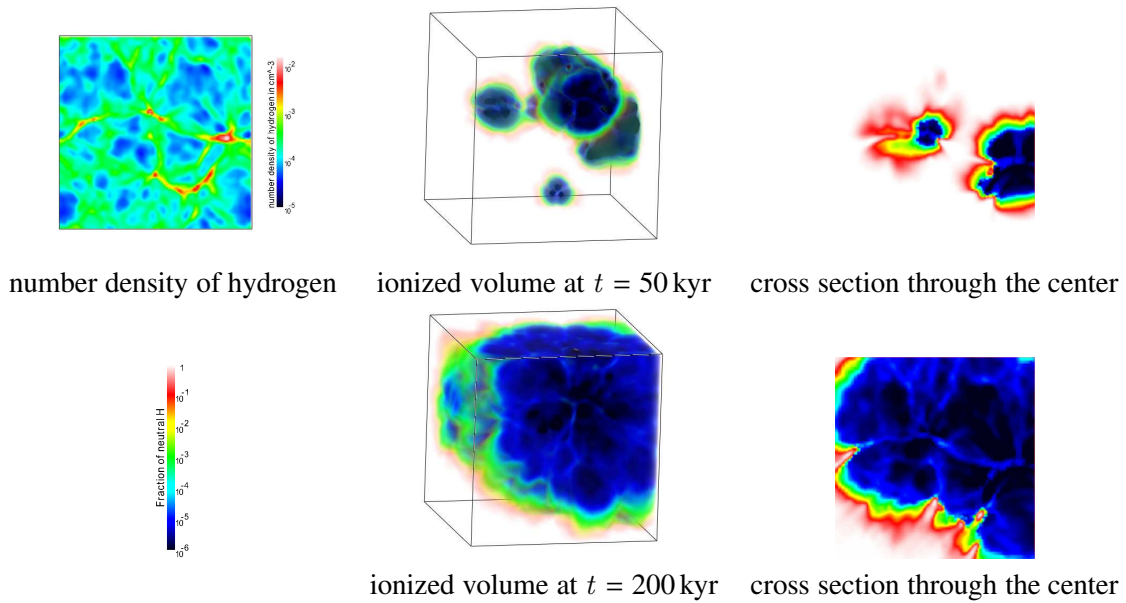


Figure 2.20: Simulation of the ionization of hydrogen in a volume of $(50 \text{ kpc})^3$ (proper units) containing an inhomogeneous cosmological density field – the structure of the gas density has been obtained from simulations by Ryu et al. (1993). The image on the upper left hand side shows the number density of hydrogen along a plane through the center of the volume. The gas is illuminated by 16 clusters involving sources with an effective temperature of 95 000 K and emitting a total of $\dot{N} = 4 \cdot 10^{53}$ hydrogen-ionizing photons per second. The ionization fraction of hydrogen is shown as 3d views of the ionized volume and as cuts along a plane through the center of the volume after 50 kyr and 200 kyr.

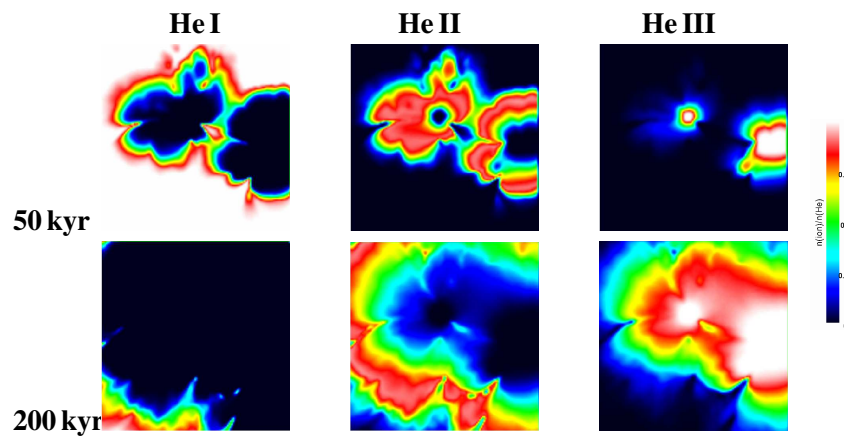


Figure 2.21: For the same simulation as in Fig. 2.20 cross-sections through the center, which display the relative abundances of the ionization stages of helium, are shown after 50 kyr and 200 kyr.

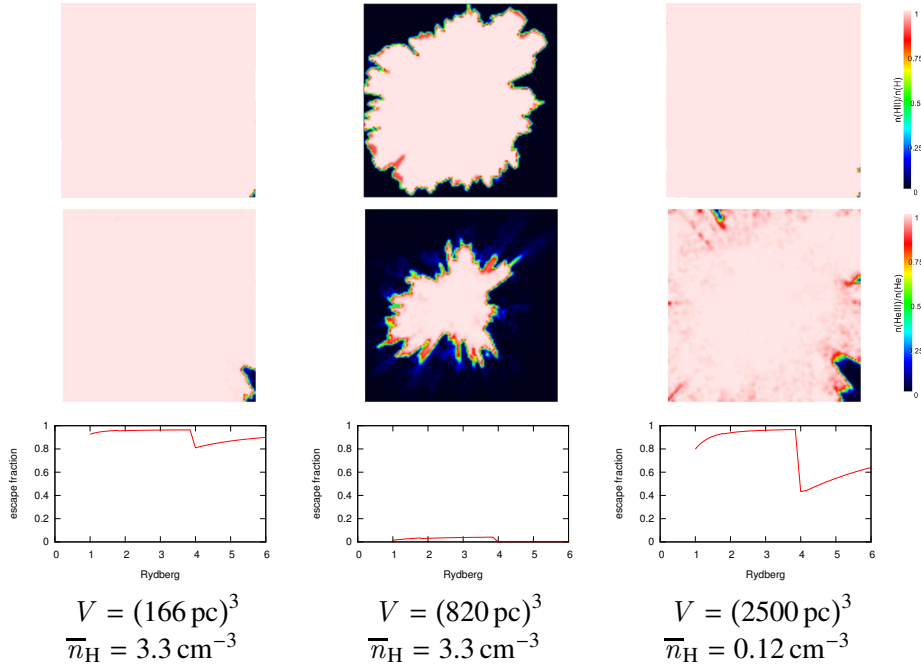


Figure 2.22: Relative abundances of H II (top row) and He III (second row) for fractal density structures with the specified mean hydrogen number densities \bar{n}_H and volumes V . The third row shows the calculated escape fractions as a function of photon energy for each of the simulations. While the escape fraction represents the “matter bounded” case in the left hand side model ($f_{\text{esc}} = 1$), the center model represents the “radiation bounded” case ($f_{\text{esc}} = 0$). In all cases the escape fraction for He II-ionizing photons is smaller than the escape fraction for H I-ionizing photons.

As the large temperatures of massive population III stars result in considerably hard spectra, it is not surprising that the timescale of the reionization of He II into He III is not much different from the timescale of the reionization of hydrogen (each of our ten clusters emits $2 \cdot 10^{52}$ He II-ionizing photons per second, which is 1/20 of the amount of hydrogen-ionizing photons per second). Thus, if the first stage of reionization had really been driven, as currently suspected, by a stellar population dominated by massive hot primordial stars, helium would also have been reionized to a large extent into He III at a redshift of $z \sim 13$ (cf. Fig. 2.19). This would not have been the case, however, if the population III stars had a much softer spectrum (cf. Sect. 2.4.2.2) – as is indicated by some simulations which show a stronger fragmentation even for primordial gas (Clark et al. 2011). Whether helium had also been reionized into He III during the first stage – by a redshift of $z \sim 13$ – therefore depends crucially on the emergence of massive population III stars in sufficient numbers. Whether these objects had been the dominant species of the stellar population that illuminated the very early universe can only be discovered by observations. In this regard the James Webb Space telescope as well as the European Extremely Large Telescope (E-ELT), the Giant Magellan Telescope (GMT) and the Thirty Meter Telescope (TMT) are expected to be able to observe clusters of bright population III stars at redshifts of $z \approx 13 \dots 15$, and thus will help to improve our present knowledge of the stellar content governing the first stage of reionization.

Details of the reionization process in an inhomogeneous cosmological density field. It is obvious that the assumption of a homogeneous universe as applied to our models above is just a rough approximation of the real situation. As a consequence of this approximation effects which depend

on small-scale inhomogeneities of the density structure of the gas and which in turn may considerably affect the reionization process can not be taken into account. Examples of such effects are the interrelation of the density structure and the local star formation rate – mutual back-reactions of the processes involved give rise to the inhomogeneous behavior of the ISM and are responsible for the presence of H II regions –, and the “porosity” of the medium which determines the escape fraction of ionizing photons that can exit their local environment and reach the intergalactic regions.

In order to study in particular the latter point, and thus the influence of multiple sources on their environment consisting of an inhomogeneous density structure on smaller scales, we have calculated a model which simulates in proper coordinates a volume of $(50 \text{ kpc})^3$ resolved into 128^3 grid cells. The density structure used for this simulation is based on results of hydrodynamical simulations from an N -body gas dynamics code (cf. Ryu et al. 1993 and Iliev et al. 2006). As this density profile had been calculated for cosmological conditions which are consistent with a redshift of $z = 9$ only, we rescaled it to conditions corresponding to a redshift of $z = 15$. The sources, which are located at the peaks of the structured density profile (pink dots in the upper left image of Fig. 2.20), cover 16 smaller clusters with a total emission rate of $\sim 4 \cdot 10^{53}$ hydrogen-ionizing photons per second (thus, all of the clusters in this simulation collectively represent one of the clusters in the homogeneous case (cf. Fig. 2.18)). As before, they are treated as blackbody radiators representing stars with an effective temperature of 95 000 K.

The results of this simulation, for which the gas temperature has again been held fixed at a value of 10 000 K, are presented in Fig. 2.20 for hydrogen and Fig. 2.21 for helium. The overall impression of the images reflects the behavior of considerably more complex ionization structures for the inhomogeneous density structure compared to those of the homogeneous models. This impression is certainly true and the irregular form of the ionization fronts and the larger fraction of neutral hydrogen in the higher-density filaments is evident. The simulations also show that the ionization stages He II and He III coexist over a considerable part of the volume (cf. Fig. 2.21).

The most important aspect of the inhomogeneous structure of the ISM is its “porosity”, and the characteristic parameter relevant for cosmic reionization simulations is the fraction of emitted ionizing photons that can escape the local environment and reach the intercluster medium and thus affect the reionization process. This so-called escape fraction is defined as the ratio of the number of photons not absorbed in a specified local reference volume to the total number of emitted photons. In order to calculate escape fractions for realistic scenarios of density distributions surrounding ionizing sources we have constructed a number of fractal density structures as proposed by Wood et al. (2005) (see also Elmegreen & Falgarone 1996). These structures are meant to represent the even smaller scales of star formation regions and evolved starburst clusters, as, for example, NGC 3603 and its surrounding thin ionized gas.

Fig. 2.22 shows the H II and He III ionization structures and the escape fractions as functions of the photon energy for three different representative models. In each case the central radiation source emits $8.5 \cdot 10^{52}$ H I-ionizing and $4.0 \cdot 10^{51}$ He II-ionizing photons per second (corresponding to a blackbody with a temperature of 95 000K). With a mean hydrogen number density of 3.3 cm^{-3} the first model corresponds to an H II region associated with star-formation clouds in the local universe (a volume of $(166 \text{ pc})^3$, somewhat larger than the extension of the Carina nebula with a diameter of approximately 100 pc, cf. Smith et al. (2000), but smaller than NGC 604, cf. Melnick 1980). In this simulation, both hydrogen and helium are almost completely ionized and the majority of both H I-ionizing and He II-ionizing photons are able to escape from the simulated volume. In the next simulation the mean gas density has been retained, but the volume has been extended to $(820 \text{ pc})^3$, which is approximately twice the size of NGC 604. In this case, less than 5 % of the H I-ionizing and almost none of the He II-ionizing photons are able to escape the volume. The last model has a mean

hydrogen number density of 0.12 cm^{-3} and a volume of (2.5 kpc). This model approximates a typical spiral arm surrounded by the thin diffuse ionized gas (DIG) that in present-day disk galaxies contains a large fraction of the interstellar ionized gas (cf. Greenawalt et al. 1998, Hoffmann et al. 2012 and references therein). In this simulation the gas is almost transparent for soft H I-ionizing radiation, but it absorbs approximately 50 % of the He II-ionizing radiation (the escape fraction depends on the photon energy and reaches its minimum for photons whose energy is just above the ionization edge of He II). Within the energy intervals defined by the ionization edges, the frequency-dependent ionization cross section (cf. Sect. 2.2.2.2) leads to a radiation hardening, i.e. the escape fraction rises with larger photon energies. We note that the numerical values of the escape fractions can vary strongly even for small changes of the density structure and the properties of the ionizing sources, such that our results are just estimates for the escape fractions.

2.4.2.2 Simulations for the second stage of reionization using SEDs of massive and very massive stars

In this section we will focus on a high spectral resolution description of the 3d radiative transfer applied to the evolution of the ionization structures in the second stage of the reionization process, which was completed for hydrogen by a redshift of $z \sim 6$ and for helium by a redshift of $z \approx 3$ (cf. Sect. 2.1). As sources of ionization we consider metal-enriched population II stars, which had already come into being during this epoch. Although these objects are in general significantly cooler and less massive than the population III stars, they are numerous and powerful due to the strongly increased star formation rate during this epoch (Lineweaver 2001, Barger et al. 2000). Furthermore, there are indications that these stellar populations may have had top-heavy-IMFs which additionally generated VMSs (cf. Sect. 2.1).

With regard to reionization we simulate a volume of $(5.3 \text{ Mpc})^3$ in comoving units and assume (as in our simulations for the first stage of reionization) a homogeneous gas density corresponding to the mean baryonic density of the universe at this epoch. Although these approximations are quite restrictive (cf. Sect 2.4.2.1) we are convinced that the principal circumstances that would allow the much less massive population II and population I stars to fully reionize at least the hydrogen content of the IGM can be investigated in their essence with this approach.

Scenario based on stars representing the top of a Salpeter IMF. In this first step we combine the calculated SEDs of massive stars (cf. Fig. 2.10) with our time-dependent 3d radiative transfer simulations. The ionizing sources in these simulations represent clusters of stars, and their total hydrogen-ionizing photon emission rates are modelled on basis of a cluster with a Salpeter IMF. We have, however, approximated the spectral energy distribution of the cluster by the SEDs of its most luminous constituents, which we take to be $125 M_{\odot}$ stars.

Depending on their evolution, galaxies and even different star forming regions within a single galaxy may have significantly different metallicities of their gas and, as a consequence, also of their young stellar populations²⁹. We have therefore not used the same SED for all sources but instead use that of a $125 M_{\odot}$ star with a metallicity of $Z = 0.1 Z_{\odot}$ for 5 of the 10 clusters, and that of a $Z = 1.0 Z_{\odot}$ model for the others. Based on our simulations in Sect. 2.4.2.1 we have chosen an escape fraction of $f_{\text{esc}} = 0.1$ as a plausible value for stars embedded in H II regions.

To model the luminosity of the clusters, we have used the population synthesis code Starburst99 (Leitherer et al. 1999, Leitherer et al. 2010) in continuous star formation mode on the basis of the

²⁹E.g., the Small Magellanic Cloud has a metallicity of 1/6 solar (Dufour 1984), while the metallicity of M 83 is at least twice solar (Dufour et al. 1980, Rubin et al. 2007).

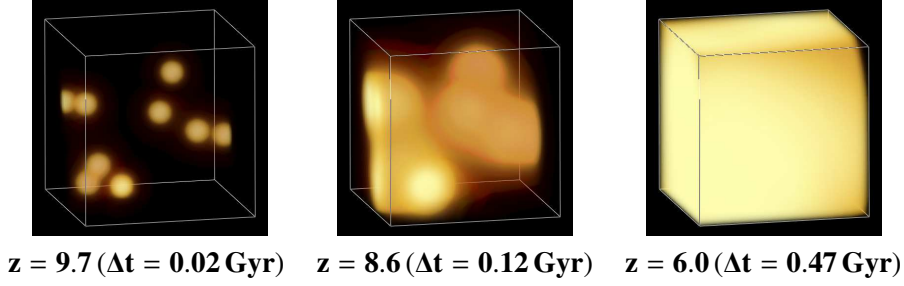


Figure 2.23: Simulation representing the second stage of the cosmic reionization, showing the evolution of the hydrogen ionization fronts in the IGM. The volume is $(5.3 \text{ Mpc})^3$ in comoving units and contains ten randomly distributed clusters of massive population II/I stars following a Kroupa IMF. The radiation of the clusters is able to reionize the hydrogen content of the simulation volume within the redshift interval from $z \sim 10$ to $z \sim 5.8$. (Δt is the time interval since the beginning of the simulation at $z = 10$.)

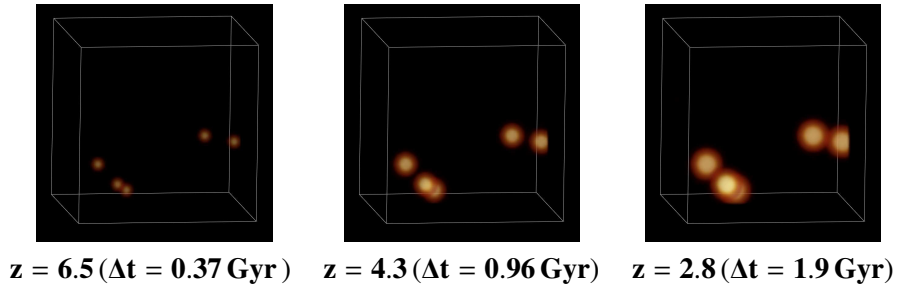


Figure 2.24: As Fig. 2.23, but showing He III. At a redshift of $z \sim 2.8$ (for which observations indicate that the reionization of He was completed) only 1.4% of helium is ionized to He III in this simulation. Thus, due to their low emission rates of He II-ionizing photons, stellar populations with Salpeter-like IMFs obviously cannot contribute significantly to the cosmic reionization of helium.

mean cosmological star formation rate at the respective redshift (cf. Lineweaver 2001, Barger et al. 2000). The total luminosity of our sources (measured by their hydrogen-ionizing photon emission rates) was chosen to match the emission rates predicted by the Starburst99 model³⁰ for the corresponding volume. In the redshift range $10 > z > 6$ we assume a star formation rate of $0.02 M_{\odot} \text{ Mpc}^{-3} \text{ yr}^{-1}$, in agreement with the mean value given for that interval by Lineweaver (2001), resulting in an emission rate of $4.7 \cdot 10^{53}$ H-ionizing and $1.0 \cdot 10^{50}$ He II-ionizing photons per second. For $6 > z > 3$ we increased the star formation rate to $0.05 M_{\odot} \text{ Mpc}^{-3} \text{ yr}^{-1}$, leading to an enhanced emission of ionizing photons (H-ionizing flux of $1.2 \cdot 10^{54}$ photons per second and He II-ionizing flux of $2.5 \cdot 10^{50}$ photons per second). As shown in Fig. 2.23 the radiation of these cluster populations is able to reionize the hydrogen content of the simulation volume within the redshift interval from $z \sim 10$ to $z \sim 5.8$.

For stars with solar metallicity the He II-ionizing flux is reduced by more than four decades compared to stars with 0.1 solar metallicity (cf. Sect. 2.4.1) while there is no large variation of the H-

³⁰The Starburst99 model uses a modified Salpeter IMF (“Kroupa IMF”, Kroupa 2001) with an upper limit of $125 M_{\odot}$ and a lower limit of $0.1 M_{\odot}$ and two different slopes: $\Gamma = -0.3$ for $0.1 M_{\odot} \leq M < 0.5 M_{\odot}$ and $\Gamma = -1.3$ for $0.5 \leq M \leq 125$. The emergent fluxes refer to a model for a population with solar metallicity.

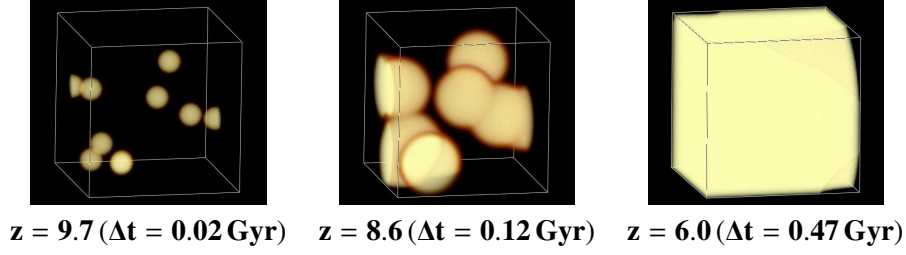


Figure 2.25: As Fig. 2.23, but with clusters dominated by very massive stars ($3000 M_{\odot}$). These clusters are also able to reionize the hydrogen content of the simulation volume within the redshift interval from $z \sim 10$ to $z \sim 5.7$.

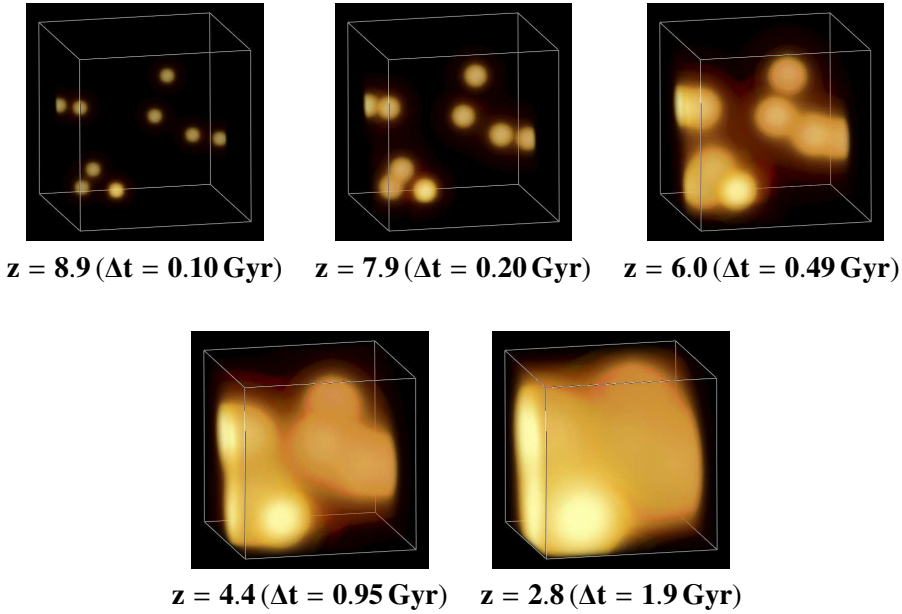


Figure 2.26: As Fig. 2.25, but showing He III. In contrast to our simulation using normal stellar populations (Fig. 2.24) the clusters dominated by very massive stars can ionize the helium content of the simulation volume within approximately 2 Gyr, completing the reionization at a redshift of about $z \sim 2.5$. Thus, this scenario based on VMSs as the possible progenitors of IMBHs and SMBHs offers an alternative picture for the as yet unexplained cosmic reionization of helium. In these simulations recombination is not entirely negligible, in particular for helium, where the calculations including recombination yield a number of ionized particles about a factor of two smaller than it would yield for a calculation without recombination.

ionizing flux. Only 1.4% of the He II atoms are ionized by the stellar populations in this simulation up to the redshift of $z \sim 2.8$ (Fig. 2.24) for which observations indicate that the reionization of He was completed (Reimers et al. 1997) – we note that replacing the spectra of the $Z = Z_{\odot}$ clusters by SEDs of low-metallicity (e.g., $Z = 0.1 Z_{\odot}$) stars would not help much, since this would increase the fraction of He III only by a factor of less than 2, when compared to the “mixed” population presented in this section. Thus, it appears plausible that stellar populations with Salpeter-like IMFs are the main con-

tributors to the reionization process of hydrogen, but due to the low emission rates of He II-ionizing photons they cannot contribute significantly to the ionization of He II.

Scenario based on stars representing runaway collision mergers. As the reionization of He II is considerably delayed compared to the reionization of H I, it appears likely that the sources of ionization responsible for the reionization of He II are different from those which caused the reionization of H and neutral He (cf. Sect. 2.1). Runaway collision mergers clearly exceed the assumed upper limit of the mass of present-day massive stars, but they are 1 to 2 orders of magnitude more efficient in producing He III-ionizing photons than normal hot stars based on a standard IMF, and since these stars can appear especially in chemically evolved clusters of high core mass density, thus at the temporal beginning of the star bursts, they may play an important role in these late stages of the reionization history.

To compare the efficacy of collisional mergers to that of “normal” stars with regard to the reionization of He, our second simulation uses the same star formation rate as before ($0.02 M_{\odot} \text{Mpc}^{-3} \text{yr}^{-1}$ for $10 > z > 6$ and $0.05 M_{\odot} \text{Mpc}^{-3} \text{yr}^{-1}$ for $z < 6$), but instead of a Salpeter IMF we assume that a fraction of 1% of the newly formed stellar mass is involved in mergers to become very massive stars³¹. (This assumption is based on the observationally determined ratio between the central black hole mass and the stellar mass in galaxies with active galactic nuclei at redshifts of $z \sim 4$ (Targett et al. 2012) as well as for the redshift range $1 < z < 2$ (Bennert et al. 2011) which is in the order of 1 %.³²) For this simulation we approximate the cluster SED by that of a $3000 M_{\odot}$ star with a metallicity of $Z = 0.05 Z_{\odot}$ and, given that these objects are not created directly from gas clouds, but are the product of merging processes of already-formed stars, we assume an escape fraction of $f_{\text{esc}} = 0.5$ on the basis that these objects are able to remove the gas from their environment more quickly than ordinary massive stars due to their extremely strong winds (Pauldrach et al. 2012). The lifetime of such a very massive star is $2 \cdot 10^6$ yr (Pauldrach et al. 2012), resulting in a mean number of 20 VMSs within the simulated volume at any given time for the redshift range $10 > z > 6$ (with a total emission of $1.5 \cdot 10^{53}$ H-ionizing photons per second and $1.2 \cdot 10^{51}$ He II-ionizing per second) and 50 VMSs for the redshift range $6 > z > 2.5$ (with a total emission of $3.8 \cdot 10^{53}$ H-ionizing and $2.9 \cdot 10^{51}$ He II-ionizing photons per second).

With regard to hydrogen this scenario is similar to the one using the Salpeter IMF, resulting in a reionization completed at a redshift of $z \sim 5.7$ (cf. Fig. 2.25). For helium however, the VMSs are much more successful, producing 60 % of the photons required to fully ionize He II up to a redshift of $z \sim 2.8$ (Fig. 2.26). As the figure clearly shows, this scenario based on the possible progenitors of IMBHs and SMBHs offers an alternative or at least complementary picture for the pending explanation of the reionization of He.

³¹Collisional mergers in dense starforming regions have been simulated on basis of N -body simulations by Portegies Zwart et al. (1999), Portegies Zwart & McMillan (2002), Gürkan et al. (2004), and Freitag et al. (2006). The properties of merger products have further been investigated by Suzuki et al. (2007) who find that neither the mass loss by the merging process nor the stellar winds are sufficient to inhibit the growth process of the runaway merger products in dense clusters. Very massive stars are therefore possible progenitors of the IMBHs (cf. Belkus et al. 2007, Pauldrach et al. 2012) that in turn might form the SMBHs found in the centers of galaxies (Ebisuzaki et al. 2001).

³²For the present-day universe Magorrian et al. (1998) found, analyzing a sample of 32 nearby galaxies, that the mass of dark massive objects in the centers of galaxies (which are likely to be black holes) is approximately 0.6 % of the stellar mass within the galactic bulges in the corresponding host galaxies. Also, a similar mass ratio (2 %) between a central black hole and the stellar content has been found for the globular cluster ω Centauri (Noyola et al. 2010).

2.5 Summary, conclusions, and outlook

The impact of massive stars on their environment is of major importance not only for the evolution of most galaxies but also for the ionization balance of the IGM. Although rare by number, massive stars dominate the life cycle of gas and dust in star forming regions and are responsible for the chemical enrichment of the ISM and IGM. This is mainly due to the short lifetimes of massive stars, which favors the recycling of heavy elements on short timescales. Furthermore, since massive stars mostly group in young clusters, the combined amount of momentum and energy released by these clusters into the ISM controls the dynamical evolution of the gas, leading to the formation of superbubbles and triggered continuous star formation. The evolutionary behavior of these starbursts is obviously controlled by the metallicity, as is the steepness of the IMF, which can be more top-heavy than previously thought even in present-day galaxies. A common property among starbursts showing such flat IMFs is a high stellar density in the core of the clusters, and very recently strong evidence has been found that in these cases nature favors the formation of massive stars with masses $> 100 M_{\odot}$ (Harayama et al. 2008, Crowther et al. 2010). Moreover, during the evolution of dense stellar clusters runaway collision mergers can occur, leading to the formation of VMSs (objects of several $1000 M_{\odot}$) *even in chemically evolved clusters* (cf. Belkus et al. 2007, Pauldrach et al. 2012), and therefore runaway collision mergers can play an important role in the late stages of the reionization history of the universe, whose detailed description is still one of the key unknowns in present cosmological research.

It is known meanwhile that the first generations of stars have not been the most important contributors to this process, since there is evidence that the universe was reionized in two steps (Cen 2003). The first one occurred – primarily driven by population III stars – up to a redshift of $z \sim 15$, and after a second cosmological almost-recombination phase (around $\Delta z \sim 5$, see Cen 2003) the reionization was driven by other powerful ionizing sources and completed at $z \sim 6$. Along with an increasing metallicity and star formation rate in this epoch (Lineweaver 2001, Barger et al. 2000), a top-heavy-IMF and VMSs – which are efficient emitters of ionizing photons with approximately 10 times more hydrogen-ionizing photons and 10 000 times more He II-ionizing photons per unit stellar mass than stars with a Salpeter IMF (cf. Pauldrach et al. 2012) – are determining factors for this process.

In this paper we have investigated whether such an extended view of the evolution of the universe from its dark ages to its final reionized state leads to a better understanding of the reionization process. For this purpose we have developed a 3-dimensional radiative transfer code (based on a ray-tracing method) in order to describe the evolution of the ionization fronts at different length scales. The main focus of this code is a comprehensive description of the time-dependent ionization structure with regard to a high spectral resolution of the ionizing spectra in order to accurately quantify the evolution of the ionization structures of different elements. Although only H and He are treated in the present paper, our algorithm allows the implementation of multiple levels for each ionization stage of the metals, and we are currently working on the inclusion of all important elements as described by Hoffmann et al. (2012). (As metal cooling has a significant influence on the temperature structure of the gas and therefore on the temperature dependent recombination rates and thus on the ionization structure of the most abundant elements, the temperature structure has to be treated consistently.) The geometrical aspects and the evolution of the ionization fronts have been extensively tested by comparisons to analytical models, the results of radially symmetric calculations, and tests presented by the “Cosmological Radiative Transfer Comparison Project” (Iliev et al. 2006). We found good agreement in all of these cases, showing that the important physical mechanisms which control the temporal expansions of the ionization fronts in homogeneous and inhomogeneous gas structures surrounding numerous sources of ionization have been implemented accurately.

For a realistic modelling of ionization fronts not only the structure of the ISM and IGM has to be

correctly considered, but also the spectral energy distributions (SEDs) of the ionizing sources used as input for the radiative transfer. Thus, based on a sophisticated model atmosphere code which treats the physics of expanding stellar atmospheres consistently, an accurate simulation of realistic SEDs from population III to population I stars at various metallicities, temperatures, and masses has been an important aspect of our work. As different characteristics of the SEDs of the sources generally have a strong impact on the power of ionization, the usual application of oversimplified spectra (such as blackbodies) can lead to incorrect or misleading results with respect to the thickness and the extent of the ionization fronts in radiative transfer codes. We have *quantified* such possible systematic errors in the context of hot massive stars via a comparison of blackbody and realistic SEDs we have calculated at different metallicities. The results we present for the radial ionization structure of hydrogen and helium surrounding a $125 M_{\odot}$ star with different metallicities show that the variation of the metallicity of the star does not have a huge influence on the number of *hydrogen*-photons. However, this result does not reflect the influence of the metals in the gas which have been neglected up to now. A consistent computation including metals will actually lead to smaller temperatures for larger metallicities and thus result in smaller Strömgren spheres; then, an even larger influence on the ionization structure of the metals in the gas and thus on the gas temperatures and Strömgren spheres will be caused by non-LTE effects acting in the expanding atmospheres of the stars and determining the shapes of the SEDs, since in this case not only the number of ionizing photons is decisive but also their spectral distribution. Regarding the radial density structure of He III, the differences of the Strömgren radii which result from different metallicities of the ionizing sources are already considerably more pronounced due to this reason. This result clearly shows that the number of He II-ionizing photons is not just strongly influenced by the effective temperature and hence the mass of the objects, but also by the evolution of the metallicity. Employing blackbody spectra in general therefore leads to – at least in the case of helium and metals whose ionization energies exceed those of H – oversimplified ionization structures which do not represent the real structures. As exactly those elements which are affected by this approximation produce the observable emission lines, such a weakness in the simulation of the ionization structures would make a comparison to forthcoming observations questionable.

As a central application of our models with high spectral resolution we considered a number of different physical scenarios leading to ionizing sources with corresponding characteristics of the SEDs, which we compared to analogous calculations carried out with blackbodies. In particular we considered massive stars with 125 solar masses, representing the top of a Salpeter IMF, and very massive stars with 3 000 solar masses which are expected to form as runaway collision mergers in cluster-core collapses. Due to the large luminosities and effective temperatures of the latter objects the emitted number of H I-ionizing photons is, compared to stars at the top of a Salpeter IMF, larger by a factor of 40. This leads to hydrogen Strömgren radii around VMSs which are a factor of 3.5 larger than those around normal massive stars at the top of a Salpeter IMF. The effect is even more pronounced for He III where the VMS-Strömgren radii exceed those of the $125 M_{\odot}$ stars by a factor of up to 100. The reason for this behavior is of course the ratio of the ionizing fluxes blueward of the He II-threshold, which favors very massive stars by several orders of magnitude. VMS can thus have a distinct influence on the ionization structure of helium in their environment.

In the context of the first stage of the reionization history we have shown results of representative 3d radiative transfer simulations which are based on clusters of massive population III stars with effective temperatures of $T_{\text{eff}} \sim 10^5$ K surrounded by homogeneous gas with primordial composition, whose density corresponds to the mean density of the universe at a redshift of $z \sim 15$. The calculations showed that our population III stars were able to reionize H as well as He on a timescale of just $t \sim 50$ Myr (corresponding to $\Delta z \sim 1.5$ at $z = 15$) within our chosen volume of $(5.3 \text{ Mpc})^3$. As the assumption of a homogeneous universe is just a rough approximation of the real situation, we have fur-

ther calculated models based on inhomogeneous density structures, simulating volumes that comprise multiple ionizing sources on smaller scales. The “clumpiness” of the gas (including the star-forming density peaks of the ISM) results in considerably more complex ionization structures than those of models with homogeneous gas distributions, and as a consequence the fraction of ionizing photons which can escape their local environment and reach the intercluster medium can differ significantly. To estimate these escape fractions we have modelled inhomogeneous environments with fractal density structures of different sizes and mean densities ranging from the density of star-forming H II regions to the one of the diluted interstellar gas. In the simulations the escape fractions for the ionizing photons, and thus their ability to leak into the IGM and contribute to the ionization process of the universe, depend crucially on the size of the density peaks the ionizing sources are embedded in, ranging from less than 5 % for a very large and therefore radiation-bounded H II region, to almost 100 % for a smaller, matter-bounded H II region where the hydrogen content is almost completely ionized and the gas is therefore transparent to radiation. We note that even small variations in the number of absorbers can lead to strong changes of the escape fractions; thus, a precise determination of this value would require knowledge of the statistics of the density distribution in the small-scale environment of the sources (i.e., on the order of parsecs to a few kiloparsecs). Furthermore, for a given density distribution the escape-fractions are a function of the photon energy, and reach their minimum just blueward of the ionization edge of He II. The spectral energy distribution of the ionizing radiation escaping into the IGM may thus be different from the intrinsic SEDs of the stellar sources.

Although the initial conditions with respect to the structure and the content of the clusters are not yet precisely known, the result that population III stars have been able to reionize H and He within the generally accepted time frame is not spectacular, since it just reflects the current state of knowledge. The more interesting question regards the second stage of reionization – which completed at a redshift of $z \sim 6$ (for H) resp. at a redshift of $z \sim 2.8$ (for He) –, since it is by no means clear whether the metal-enriched and thus significantly cooler and less massive population II and population I stars, given a reasonable cluster structure and composition, have been able to fully reionize the hydrogen and helium content of the IGM. To investigate this scenario we have combined our predicted SEDs of massive and very massive stars with our time-dependent 3d radiative transfer simulations of the IGM. (Note that while the assumption of blackbody sources is not too bad an approximation for stars of primordial composition, it is not an adequate description of the real SEDs of later stellar populations. For the study of the second stage of reionization the results of realistic model atmospheres – as presented here – must therefore serve as input spectra.)

Based on plausible numbers for a standard population we have approximated in a first step the SED of a cluster with a Salpeter IMF by the SED of its most luminous members, namely $125 M_{\odot}$ stars. Our calculations show that these objects have certainly been able to reionize H again (for our chosen volume the process required a time scale of $\Delta t \sim 500$ Myr, corresponding to the redshift interval between $z \sim 10$ and $z \sim 6$), but not He II (not even up to a redshift of $z \sim 2$ – note that the observations show that the reionization of He II was considerably delayed compared to the reionization of H). This latter finding is not unexpected, given that other investigations (Wyithe & Loeb 2003, Glezer et al. 2005, and McQuinn et al. 2009) had concluded from similar considerations that the sources of ionization responsible for the reionization of He II are different from those which caused the reionization of H.

To investigate whether the appearance of very massive, already metal-enriched population II and population I stars could have been responsible for the reionization of He II we replaced the $125 M_{\odot}$ stars by runaway collision mergers of $M = 3\,000 M_{\odot}$ with an effective temperature of 65 000 K, which clearly exceed the assumed upper mass limit of present-day massive stars and which are up to 2 orders of magnitude more efficient in producing ionizing photons than a normal stellar population is. The result is striking: In contrast to the case where the stellar populations follow a Salpeter or Kroupa IMF

our simulations now show that the universe could have been reionized within approximately 2 Gyr (corresponding to a redshift of $z \sim 2.5$) in an environment where a fraction of 1 % of the mass formed into stars consists of mergers resulting in very massive stars. We note that this percentage is consistent with the mass ratio obtained for IMBHs and SMBHs relative to the stellar mass found in active galaxies and globular clusters like ω Centauri, and that such VMSs might be progenitors of IMBHs and SMBHs. This result therefore offers an alternative or complementary scenario for the explanation of the reionization of He II to He III, and implies that a more realistic simulation of the entire reionization process of the universe must take into account the complete set of stellar populations and not just the primordial generation of stars.

It will therefore be necessary to understand the chemical evolution and the structure formation at the corresponding epochs more precisely and to establish comprehensive grids of realistic SEDs representing the time dependent content of the clusters and the cluster structures. Our future work will further focus on a more sophisticated description of the 3d radiative transfer with respect to high spectral resolution in order to quantify the evolution of all relevant ionization structures accurately. On basis of synthetic emission spectra calculated for the 3d structure of the ionized gas we will try to determine possible observational features (such as line strength ratios from different ions) that may be used to discriminate between the details of different reionization scenarios. Knowledge of such features will be important for comparisons with more detailed observations at high redshifts, which are expected to become available during the next years.

Acknowledgments We thank an anonymous referee for helpful comments which improved the paper and we further wish to thank I. Iliev for granting us access to the data of the *Cosmological Radiative Transfer Codes Comparison* and N. Gnedin for providing us with the IFRIT program used for some visualizations of our results. The calculations were performed on high-performance computing facilities at the LRZ (Leibniz Rechenzentrum) and the University of Munich which is to be acknowledged. This work was supported by the *Deutsche Forschungsgemeinschaft (DFG)* under grant PA 477/9-1 and PA 477/18-1.

3 Three-dimensional modeling of ionized gas.

II. Spectral energy distributions of massive and very massive stars in stationary and time-dependent modelling of the ionization of metals in H II regions¹

H II regions play a crucial role in the measurement of the chemical composition of the interstellar medium and provide fundamental data about element abundances that constrain models of galactic chemical evolution. Discrepancies that still exist between observed emission line strengths and those predicted by nebular models can be partly attributed to the spectral energy distributions (SEDs) of the sources of ionizing radiation used in the models as well as to simplifying assumptions made in nebular modeling. One of the main influences on the nebular spectra is the metallicity, both nebular and stellar, which shows large variations even among nearby galaxies. Although nebular modeling often involves testing of different nebular metallicities against their influence on the predicted spectra, adequate grids of stellar atmospheres and realistic SEDs for different metallicities are still lacking. This is unfortunate because the influence of stellar metallicity on nebular line strength ratios, via its effect on the SEDs, is of similar importance as variations in the nebular metallicity. To overcome this deficiency we have computed a grid of model atmosphere SEDs for massive and very massive O-type stars covering a range of metallicities from significantly subsolar ($0.1 Z_{\odot}$) to supersolar ($2 Z_{\odot}$). The SEDs have been computed using a state-of-the-art model atmosphere code that takes into account the attenuation of the ionizing flux by the spectral lines of all important elements and the hydrodynamics of the radiatively driven winds and their influence on the SEDs. For the assessment of the SEDs in nebular simulations we have developed a (heretofore not available) 3D radiative transfer code that includes a time-dependent treatment of the metal ionization. Using the SEDs in both 1D and 3D nebular models we explore the relative influence of stellar metallicity, gas metallicity, and inhomogeneity of the gas on the nebular ionization structure and emission line strengths. We find that stellar and gas metallicity are of similar importance for establishing the line strength ratios commonly used in nebular diagnostics, whereas inhomogeneity of the gas has only a subordinate influence on the global line emission. Nebular diagnostics as a quantitative tool for measuring the abundances in the interstellar gas can be used to its full potential only when the influence of SEDs, metallicity, and geometric structure of the nebula are taken into account. For these purposes, detailed stellar SEDs like those of our grid are an essential ingredient for the photoionization models used to predict nebular emission line spectra.

¹The content of this chapter has been published in:
J. A. Weber, A. W. A. Pauldrach, and T. L. Hoffmann
Astronomy & Astrophysics, Volume 583, id.A63

3.1 Introduction

In the present phase of the universe the number and mass fraction of hot massive stars is small compared to the total stellar population; however, the impact of these objects on their environment is decisive for the evolution of the host galaxies. For instance, metals are produced in the cores of massive stars, and in the later evolutionary stages of these objects these metals are distributed via stellar winds in the late phases and supernova explosions into the surrounding interstellar gas. This mechanism also influences the subsequent star formation in these environments (cf. Woosley & Weaver 1995, François et al. 2004, Maio et al. 2010, Hirschmann et al. 2013, Sandford et al. 1982, Oey & Massey 1995, and Bisbas et al. 2011). As massive stars have short lifetimes of only a few million years, their locations and their chemical compositions are still closely correlated with the environment where they formed. They can thus be used as tracers for the chemical states and metallicity gradients of galaxies. Furthermore, in disk galaxies hot massive stars are the most important emitters of ionizing radiation. They act as the primary energy supply sources for H II regions and they are involved in the process of energy maintenance required for the dilute, but extended, diffuse ionized gas (cf. Haffner et al. 1999, Rossa & Dettmar 2000 and Hoffmann et al. 2012). Thus, not least with respect to their luminosities of up to $L \sim 10^8 L_{\odot}$ (Pauldrach et al. 2012), hot massive stars are important players in the evolution of massive star clusters, especially in starburst clusters and galaxies. The significance of these starbursts is not only that they heat the intergalactic medium and enrich it with metals, but that massive stars themselves are also useful diagnostic tools. Stellar wind lines can presently be identified in the spectra of individual O-supergiants up to distances of 20 Mpc. Because of their high star formation rates and the resulting large number of young stars, starburst galaxies show the distinctive spectral signatures of hot massive stars in the integrated spectra of starburst galaxies even at redshifts up to $z \sim 4$ (Steidel et al. 1996, Jones et al. 2013). These spectral features can provide important information about the chemical composition, the stellar populations, and thus the galactic evolution even at extragalactic distances. That this is feasible has already been demonstrated by Pettini et al. (2000), who showed that the O-star wind line features can indeed be used to constrain star formation processes and the metallicity. By comparing theoretical population synthesis models with observational results, it is possible to reconstruct the physical properties and the recent evolution of these objects (Leitherer & Heckman 1995, Leitherer et al. 1999, Leitherer et al. 2010).

We are thus close to the point of making use of complete and completely independent quantitative spectroscopic studies of the most luminous stellar objects. To realize this objective a diagnostic tool for determining the physical properties of hot stars via quantitative UV spectroscopy is required. The status of the ongoing work to construct such an advanced diagnostic tool that includes an assessment of the accuracy of the determination of the parameters involved has recently been described by Pauldrach et al. (2012). They have shown that the atmospheric models developed for massive stars are already realistic with regard to quantitative spectral UV analysis calculated along with consistent dynamics, which allows the stellar parameters to be determined by comparing an observed UV spectrum to a set of suitable synthetic spectra. The astronomical perspectives are enormous, not only for applications of the diagnostic techniques to massive O-type stars, but also extended to the role of massive stars as tracers of the chemical composition and the population of starbursting galaxies at high redshift. In all of these applications a close connection between observations and accurate theoretical modeling of the stellar spectra is required, and this is also the case for the physical properties and observational features of H II regions, which are closely connected with the spectra and luminosities of their ionizing sources: hot massive stars (cf. Rubin et al. 1991b, Sellmaier et al. 1996, Giveon et al. 2002, Pauldrach 2003, Sternberg et al. 2003).

The analysis of H II regions, which is primarily based on emission line diagnostics, is a power-

ful method with which to gain information about the chemical properties and evolution of galaxies. Because the strength of the emission lines depends on the properties of the gas (density, chemical composition) and the properties of the sources of ionization (luminosity, spectral energy distribution), quantitative analyses of these lines are used to determine abundances in H II regions in galaxies of different metallicities and to draw conclusions about the spectral energy distributions of the irradiating stellar fluxes and thus about the upper mass range of the stellar content of the clusters. High-quality far-infrared spectra of extragalactic H II regions taken with the Spitzer Space Telescope are discussed and interpreted, for example, by Rubin et al. 2007, Rubin et al. 2008; work is also in progress to determine abundance gradients within single galaxies, e.g., by Márquez et al. 2002, Stanghellini et al. 2010.

One of the most important ingredients of galaxies, clusters, and structures to be considered and to be determined in this context is obviously the metallicity. Not only are the properties of stars and nebulae influenced to a large extent by the metal abundances, but the metals are in turn also provided locally and their distribution is modified by the physical behavior of the stellar content. Thus, it is not surprising that the metallicities found in the interstellar medium differ considerably even within groups of galaxies. The metallicity found in the Large Magellanic Cloud, for example, has a value of $Z_{\text{LMC}} \approx 0.4 Z_{\odot}$, whereas the metallicity in the Small Magellanic Cloud has been determined to $Z_{\text{SMC}} \approx 0.15 Z_{\odot}$ (Dufour 1984). Both values are significantly smaller than the metallicity in the Milky Way which seems to correspond roughly to the solar value. However, the term “solar abundance” itself is somewhat vague, since studies in the past decade have surprisingly yielded significantly lower number fractions of the most abundant metals such as C, N, O, and Ne (Asplund et al. 2009) than the previously determined values (e.g., Grevesse & Sauval 1998). Other examples of large differences to the galactic metallicity in the local universe are M 83 ($Z \approx 2 Z_{\odot}$, Bresolin & Kennicutt 2002) and blue low surface-brightness galaxies ($Z \approx 0.1 Z_{\odot}$, Roenback & Bergvall 1995). Beyond that, metallicities vary not only from galaxy to galaxy, they also vary within the disks of certain galaxies. Based on observations of H II regions at increasing distances from the center of our Galaxy, Rudolph et al. (2006) have found a decline of the oxygen abundance, for instance.

In order to make further progress in the diagnostics of the emission line spectra of H II regions one obviously has to account for the metallicity-dependence of the calculated spectral energy distributions (SEDs) of massive stars. One of the most important obstacles in this regard is the fact that massive stars show direct spectroscopic evidence of winds throughout their lifetime, and these winds modify the ionizing radiation of the stars considerably (cf. Pauldrach 1987) and contribute significantly to the state and energetics of the atmospheric structures in a metallicity-dependent way. Modeling hot star atmospheres is complicated by the fact that the outflow dominates the physics of the atmospheres, in particular regarding the density stratification and the radiative transfer, which are substantially modified through the presence of the macroscopic velocity field. In the frame of a consistent treatment of the hydrodynamics, the hydrodynamics influence the non-LTE model², and are in turn controlled by the line force determined by the occupation numbers and the radiative transfer of the non-LTE model (cf. Pauldrach 1987, Pauldrach et al. 1990, Pauldrach et al. 1994, Pauldrach et al. 2001, and Pauldrach et al. 2012).

One of the objectives of this paper is to present a grid of advanced stellar wind spectra for O-type dwarfs and supergiants at different metallicities (Sect. 3.2) computed using hydrodynamic atmo-

²We use term non-LTE to refer to the detailed modeling of the statistical equilibrium of the occupation numbers of the atomic levels, obtained from actually solving the system of rate equations, without assuming the approximation of local thermodynamic equilibrium (LTE, where the level populations would follow a Saha-Boltzmann distribution at the local temperature and density).

spheric models that include a full treatment of non-LTE line blocking and blanketing³ and the radiative force. In the second part of this paper the influence of the computed SEDs on the properties of the irradiated interstellar gas is differentially investigated. In Sect. 3.3 we apply our computed SEDs to a series of simulations of sample H II regions in order to investigate the dependence of the temperature and ionization structures on the ionizing spectra and the metallicity of the gas. At first we restrict the simulations to H II regions which are illuminated by a single star and which consist of 1D (i.e., spherically symmetric) homogeneous density structures. These restrictions are dropped in the second part of this section, where the effects of multiple radiative sources and inhomogeneous density structures on H II regions are investigated and discussed using our recently developed 3D radiative transfer models. In Sect. 3.4 we will summarize our results along with our conclusions.

3.2 Stellar wind models for O-type dwarfs and supergiants at different metallicities

In this section we apply our method for modeling the expanding atmospheres of hot stars to a basic grid of massive O-stars. The objective of these calculations is to present ionizing fluxes and SEDs for massive dwarfs and supergiants at different metallicities that can be used for the quantitative analysis of emission line spectra of H II regions.

3.2.1 The general concept for calculating synthetic spectra and SEDs of massive stars

Our approach to modeling the expanding atmospheres of hot, massive stars has been described in detail in a series of previous papers (Pauldrach 1987, Pauldrach et al. 1990, 1993; Pauldrach et al. 1994, Taresch et al. 1997, Haser et al. 1998, Pauldrach et al. 1998, 2001, 2004, 2012), and we summarize the salient points here. Our method is based on the concept of homogeneous, stationary, and spherically symmetric radiation-driven atmospheres. Although this is an approximation to some extent, it is sufficient to reproduce all important characteristics of the expanding atmospheres in some detail.

A complete model atmosphere calculation consists of (a) a solution of the hydrodynamics describing velocity and density of the outflow, based on radiative acceleration by Thomson, continuum, and line absorption and scattering (an essential aspect of the model, because the expansion of the atmosphere alters the emergent flux considerably compared to a hydrostatic atmosphere); (b) determination of the occupation numbers from a solution of the rate equations containing all important radiative and collisional processes, using sophisticated model atoms and corresponding line lists⁴; (c) calculation of the radiation field from a detailed radiative transfer solution taking into account not only continuum, but also Doppler-shifted line opacities and emissivities⁵; and (d) computation of the temperature

³The effect of line blocking refers to an attenuation of the radiative flux in the EUV and UV spectral ranges due to the combined opacity of a huge number of metal lines present in hot stars in these frequency ranges. It drastically influences the ionization and excitation and the momentum transfer of the radiation field through radiative absorption and scattering processes. As a consequence of line blocking, only a small fraction of the radiation is reemitted and scattered in the outward direction, whereas most of the energy is radiated back to the surface of the star, leading there to an increase of the temperature (called backwarming). Because of this increase in temperature, more radiation is emitted at lower energies, an effect known as line blanketing.

⁴In total 149 ionization stages of the 26 most abundant elements (H to Zn, apart from Li, Be, B, and Sc) are considered; a detailed description of the atomic models used is given in Sect. 3 and Table 1 of Pauldrach et al. 2001, and in Sect. 2 of Pauldrach et al. 1994 where several tables and figures that explain the overall procedure are shown. Low-temperature dielectronic recombination is included.

⁵If different spectral lines get shifted across the same observer's frame frequency by the velocity field in the envelope,

from the requirement of radiative (absorption/emission) and thermal (heating/cooling) balance. An accelerated Lambda iteration (ALI) procedure⁶ is used to achieve consistency of occupation numbers, radiative transfer, and temperature. If required, an updated radiative acceleration can be computed from the converged model, and the process repeated.

In addition, secondary effects such as the production of EUV and X-ray radiation in the cooling zones of shocks embedded in the wind and arising from the nonstationary, unstable behavior of radiation-driven winds can, together with K-shell absorption, be optionally considered (based on a parametrization of the shock jump velocity; cf. Pauldrach et al. 1994, 2001). However, they have not been included in the models presented here, since they affect only high ionization stages like O vi which are not relevant for the analysis of emission line spectra of H II regions.

Of course, it needs to be clarified whether the spectral energy distributions calculated by our method are realistic enough to be used in diagnostic modeling of H II regions. Although the radiation in the ionizing spectral range cannot be directly observed, the predicted SEDs can be verified indirectly by a comparison of observed emission line strengths and those calculated by nebular models (cf. Giveon et al. 2002; Rubin et al. 2007, 2008; Sellmaier et al. 1996). A more stringent test can be provided by a comparison of the synthetic and observed UV spectra of individual massive stars, which involves hundreds of spectral signatures of various ionization stages with different ionization thresholds, and covering a large frequency range: because almost all of the ionization thresholds lie in the spectral range shortward of the hydrogen Lyman edge (cf. Pauldrach et al. 2012), and the ionization balances of all elements depend sensitively on the ionizing radiation throughout the entire wind, the ionization balance can be traced reliably through the strength and structure of the wind lines formed throughout the atmosphere. In this way a successful comparison of observed and synthetic UV spectra (Pauldrach et al. 1994, 2001, 2004, 2012) ascertains the quality of the ionization balance and thus of the SEDs.

line overlap, which is responsible for multiple-scattering events, takes place. The method used to solve this problem is an integral formulation of the transfer equation using an adaptive stepping technique on every ray (in p, z geometry) in which the radiation transfer in each micro-interval is treated as a weighted sum on the microgrid,

$$I(\tau_0(p, z)) = I(\tau_n)e^{-(\tau_n-\tau_0)} + \sum_{i=0}^{n-1} \left(e^{-(\tau_i-\tau_0)} \int_{\tau_i}^{\tau_{i+1}} S(\tau) e^{-(\tau-\tau_i)} d\tau(p, z) \right),$$

where I is the specific intensity, S is the source function and τ is the optical depth. To accurately account for the variation of the line opacities and emissivities due to the Doppler shift, all line profile functions are evaluated correctly for the current microgrid-coordinates on the ray, thus effectively resolving individual line profiles (cf. Pauldrach et al. 2001); thus, the effects of line overlap and multiple scattering are naturally included. On the basis of this procedure the application of the Sobolev technique gives for the radiative line acceleration

$$g_{\text{lines}}(r) = \frac{2\pi}{c} \frac{1}{\rho(r)} \sum_{\text{lines}} \chi_{\text{line}}(r) \int_{-1}^{+1} I_{\nu_0}(r, \mu) \frac{1 - e^{-\tau_s(r, \mu)}}{\tau_s(r, \mu)} \mu d\mu,$$

where

$$\tau_s(r, \mu) = \chi_{\text{line}}(r) \frac{c}{\nu_0} \left[(1 - \mu^2) \frac{v(r)}{r} + \mu^2 \frac{dv(r)}{dr} \right]^{-1}$$

is the Sobolev optical depth and ν_0 is the frequency at the center of each line ($\chi_{\text{line}}(r)$ is the local line absorption coefficient, μ is the cosine of the angle between the ray direction and the outward normal on the spherical surface element, $v(r)$ is the local velocity, and c is the speed of light). A comparison of the line acceleration of strong and weak lines evaluated with the comoving-frame method and the Sobolev technique disregarding continuum interaction is presented in Fig. 5 of Pauldrach et al. (1986), and a comparison of the comoving-frame method and the Sobolev-with-continuum technique is shown in Fig. 3 of Puls & Hummer (1988), demonstrating the excellent agreement of the two methods.

⁶For the latest update of the general method see Pauldrach et al. (2014).

3.2.2 Synthetic spectra and SEDs from a model grid of massive stars

Our model grid comprises massive stars with effective temperatures ranging from 30 000 to 55 000 K and luminosities from $10^5 L_{\odot}$ to $2.2 \cdot 10^6 L_{\odot}$ (Table 3.1). The model parameters correspond to those used by Pauldrach et al. (2001) and were chosen in accordance with the range of values deduced from observations.

We compute stellar models for metallicities of 0.1, 0.4, 1.0, and $2.0 Z_{\odot}$ and compare the results for two different data sets for the solar metallicities, the abundances given by Grevesse & Sauval (1998) that had been used by Pauldrach et al. (2001) and the updated values published by Asplund et al. (2009). The latter values were determined using the comparison of the solar spectrum with 3D radiative transfer simulations of the solar photosphere and differ from the former determinations by up to 38% percent for the most abundant metals (see Table 3.2).

The influence of the metallicity on the winds of hot stars. As the winds of hot stars are primarily driven by metal lines, the chemical composition of the stellar atmosphere is a decisive factor controlling the strength of the winds. Although larger metallicities lead in general to stronger winds (Kudritzki et al. 1987, Pauldrach 1987, and Pauldrach et al. 2012), not all elements act on the winds in the same way because of their different line strength distributions (cf. Pauldrach 1987). For example, an increase in the abundances of the iron group elements (Fe, Ni) will increase the mass-loss rate and correspondingly decrease the terminal velocity, whereas an increase in the abundances of some lighter elements (C, N, O, S, Ne, Ar) will increase the terminal velocity and correspondingly decrease the mass-loss rate. Thus, different wind parameters may be obtained if the abundance ratios are changed, even if the total metallicity is kept constant.⁷

We will, however, not consider such second-order effects in the present work. Instead, our computed mass-loss rates shown in Table 3.1 are based on the values of the mass-loss rates presented by Pauldrach et al. (2001), scaled by the corresponding factors derived from the metallicity dependence of the wind strengths exhibited by self-consistent hydrodynamical radiation-driven wind calculations (details of this procedure are described by Pauldrach et al. 2012). We have also applied our hydrodynamical radiation-driven wind calculations to a grid of very massive stars (VMS) with initial masses between $150 M_{\odot}$ and $3000 M_{\odot}$, effective temperatures T_{eff} between 40000 K and 65000 K, and metallicities Z of $0.05 Z_{\odot}$ and $1 Z_{\odot}$ (Table 3.3; the stellar parameters are based on theoretical evolutionary models as described by Belkus et al. 2007; see also Pauldrach et al. 2012).

Synthetic spectra and SEDs obtained from the O-star grid. As a primary result of our computations, Figs. 3.10–3.13 show the emergent ionizing fluxes together with the corresponding shapes of the continuum for the models of our grid. As can be verified from these figures the influence of the line opacities, i.e., the difference between the hypothetical continuum and the real emergent flux, increases from objects with cooler effective temperatures to those with hotter effective temperatures and from dwarfs to supergiants. This result is not surprising since it is a consequence of the behavior of the most important dynamical parameter, the mass-loss rate \dot{M} , which is directly coupled to the stellar luminosity. Thus, the mass-loss rate increases with the effective temperature and the luminosity class (Table 3.1), and the optical depths of the spectral lines, which increase accordingly, produce, along with the increasing mass-loss rate, a more pronounced line blocking effect in the wind part of the atmosphere. As can be seen from Figs. 3.10–3.13, this behavior saturates for objects with effective

⁷A discussion of the dependence of the mass-loss rate and the corresponding consistently calculated terminal velocity on metallicity has been presented by Kudritzki et al. (1987).

Table 3.1: Mass-loss rates for different metallicities derived for our grid of model stars, based on the solar abundances determined by Asplund et al. (2009).

Model	Z/Z_{\odot}	R/R_{\odot}	$\log g$ (cgs)	$\log(L/L_{\odot})$	\dot{M} ($10^{-6} M_{\odot}/\text{yr}$)
Dwarfs					
D-30	0.1	12	3.85	5.02	0.0019
	0.4				0.0039
	1.0				0.0061
	2.0				0.0086
D-35	0.1	11	3.80	5.21	0.014
	0.4				0.026
	1.0				0.042
	2.0				0.059
D-40	0.1	10	3.75	5.36	0.079
	0.4				0.16
	1.0				0.24
	2.0				0.33
D-45	0.1	12	3.90	5.72	0.41
	0.4				0.83
	1.0				1.32
	2.0				1.9
D-50	0.1	12	4.00	5.91	1.7
	0.4				3.5
	1.0				5.4
	2.0				7.9
D-55	0.1	15	4.10	6.27	5.2
	0.4				12.1
	1.0				21
	2.0				32
Supergiants					
S-30	0.1	27	3.00	5.72	2.3
	0.4				3.8
	1.0				5.2
	2.0				6.4
S-35	0.1	21	3.30	5.77	3.3
	0.4				5.7
	1.0				8.2
	2.0				10.6
S-40	0.1	19	3.60	5.92	2.9
	0.4				6.4
	1.0				10.8
	2.0				16
S-45	0.1	20	3.80	6.17	3.0
	0.4				7.7
	1.0				15
	2.0				24
S-50	0.1	20	3.90	6.35	6.0
	0.4				13.1
	1.0				21
	2.0				38

Table 3.2: Comparison of the values of the solar abundances determined by Asplund et al. (2009) (AGS) and Grevesse & Sauval (1998) (GS) for the most abundant metals. The corrections obtained by AGS are based on a realistic 3D model of the solar atmosphere (Asplund 2005) and give values which are roughly 20% to 30% lower than the previous values obtained by GS for the most abundant elements C, N, O, and Ne.

Element	AGS $12 + \log\left(\frac{n}{n_{\text{H}}}\right)$	GS $12 + \log\left(\frac{n}{n_{\text{H}}}\right)$	correction (%)
C	8.43 ± 0.05	8.52 ± 0.06	-19
N	7.83 ± 0.05	7.92 ± 0.06	-19
O	8.69 ± 0.05	8.83 ± 0.06	-28
Ne	7.93 ± 0.10	8.08 ± 0.06	-29
Mg	7.60 ± 0.04	7.58 ± 0.05	+5
Si	7.51 ± 0.03	7.55 ± 0.05	-9
S	7.12 ± 0.03	7.33 ± 0.11	-38
Ca	6.34 ± 0.04	6.36 ± 0.02	-5
Fe	7.50 ± 0.04	7.50 ± 0.05	0
total metallicity	9.02	9.13	-22

temperatures larger than $T_{\text{eff}} = 45\,000\text{ K}$, since in these cases higher main ionization stages are encountered (e.g., Fe v and Fe vi which have a smaller number of bound-bound transitions (cf. Pauldrach 1987)). The effect of line blocking is thus strongest for supergiants of intermediate T_{eff} .

The figures show that the SEDs depend sensitively on the stellar parameters (especially the effective temperature), and also on the metallicity.⁸ This influence on the spectra is not only due to the direct line-blocking effect caused by the metals, but also indirectly due to changes in the hydrodynamic structure that occur as a consequence of the influence of the metallicity on the radiative line acceleration.

In Table 3.4 we list for each model the number of photons emitted per second capable of ionizing H, He, He⁺, O⁺, Ne⁺, and S⁺. The hydrogen ionizing flux determines (along with the density structure and temperature of the gas) the extent of the ionized volume while helium is an important absorber for the hard ionizing radiation. The ionization products of considered ionization stages of metals are effective line radiation emitters in gaseous nebulae and therefore play an important role in the corresponding line diagnostics. Their line emission also significantly contributes the energy balance of the ionized gas. The corresponding ionizing fluxes of stellar sources are therefore decisive for the properties of the gas in their environment.

Although the number of hydrogen-ionizing photons depends only weakly on metallicity in the stellar temperature range of our grid, significant differences of up to several orders of magnitude are found for the ionization stages of He⁺ and Ne⁺. These pronounced anti-correlations between the ionizing fluxes and the stellar metallicity indicate strongly that the influence of stellar metallicity on nebular line strength ratios is of similar importance to that of variations in the nebular metallicity.⁹ However, we also note that the relative influence of the stellar metallicity on the number of emitted ionizing photons decreases for larger effective temperatures and hence harder ionizing spectra.

⁸The synthetic stellar wind spectra and SEDs for our grid of massive stars can be copied from [... model data].

⁹Although larger metallicities in general lead to a lower emission rate of photons in the energy range above the ionization edge of He I, we notice exceptions to this anti-correlated behavior, such as the O II and Ne II ionizing fluxes of the 30 000 K dwarf models. However, these fluxes are 2 to 4 decades smaller than those of the 35 000 K models, and this means that even a small variation in the effective temperature in this temperature range will have a similar effect on the ionizing fluxes as a variation of the metallicity.

Table 3.3: Stellar parameters and mass-loss rates at different metallicities for the computed models of very massive stars (cf. Pauldrach et al. 2012).

T_{eff} (K)	Z/Z_{\odot}	R/R_{\odot}	$\log g$ (cgs)	$\log(L/L_{\odot})$	\dot{M} ($10^{-6} M_{\odot}/\text{yr}$)
$M_* = 150 M_{\odot}$					
40 000	0.05	40	3.40	6.57	4.7
	1.00				26
50 000	0.05	25.8	3.79		5.0
	1.00				23
$M_* = 300 M_{\odot}$					
40 000	0.05	68	3.24	7.03	59
	1.00				220
$M_* = 600 M_{\odot}$					
50 000	0.05	43.5	3.94	7.03	6.0
	1.00				34
$M_* = 1000 M_{\odot}$					
45 000	0.05	92	3.51	7.50	53
	1.00				190
65 000	0.05	44.5	4.14	7.50	35
	1.00				98
$M_* = 3000 M_{\odot}$					
45 000	0.05	164	3.49	8.00	285
	1.00				923
65 000	0.05	79	4.12	8.00	132
	1.00				385

Very massive stars. As a first indication to what extent very massive stars can be identified by their ionizing influence on the environment, we list in Table 3.5 the photon emission rates of our very massive star models in the different ionization continua. The SEDs of the hottest of these stars with an effective temperature of 65 000 K and masses of $1000 M_{\odot}$ and $3000 M_{\odot}$ are characterized by ratios of He II-ionizing to H-ionizing fluxes that exceed those of even the hottest “normal” O-type model stars (the 55 000 K dwarfs) by a factor of 5 to 10, while for the cooler very massive star models the ratios are similar to those of the normal O-star models.¹⁰ We will simulate the effects of the very massive star model SEDs on their surrounding H II regions in Sect. 3.3.2.2. Plots of the SEDs of the VMS are shown in Figs. 3.14 and 3.15. The corresponding data sets can be copied from the links provided there.

¹⁰The ratio is lower for the 45 000 K model star with $3000 M_{\odot}$ at solar metallicity due to the very high mass-loss rate of this model, which causes the He-ionizing photons to be absorbed partly in the wind. The mass-loss rate of the 45 000 K model is higher than that of the 65 000 K model with the same luminosity because the higher surface gravity of the hotter star leads to a higher wind velocity but a lower mass-loss rate.

Table 3.4: Numerical values of the integrals of ionizing photons emitted per second for the ionization stages of H, He, He⁺, O⁺, Ne⁺, and S⁺, as well as the luminosity at the reference wavelength $\lambda = 5480 \text{ \AA}$. With respect to their ionization energies these ions are important in the context of emission line diagnostics. The integrals are defined as $Q_X = \int_{\nu_X}^{\infty} (L_\nu/h\nu) d\nu$, where $h\nu_X$ is the ionization energy of ion X . (The ionization energy is 1.72 Ryd for S II, 1.81 Ryd for He I, 2.77 Ryd for O II, and 3.01 Ryd for Ne II.)

Model	Z/Z_\odot	$\log Q_{\text{H}}$	$\log Q_{\text{He}}$	$\log Q_{\text{He}^+}$	$\log Q_{\text{O}^+}$	$\log Q_{\text{Ne}^+}$	$\log Q_{\text{S}^+}$	$L_\nu(5480 \text{ \AA})$ (10^{22} erg/s/Hz)
Dwarfs								
D-30	0.1	47.60	45.02	38.97	42.92	41.10	45.95	3.85
	0.4	47.58	45.03	36.49	42.89	41.12	45.82	4.09
	1.0	47.56	45.09	35.23	42.96	41.31	45.76	4.17
	2.0	47.71	45.34	35.62	43.26	41.62	45.86	4.06
D-35	0.1	48.67	47.58	42.15	46.55	45.50	47.74	4.22
	0.4	48.66	47.56	41.51	46.29	44.53	47.71	4.21
	1.0	48.68	47.58	37.41	46.17	44.22	47.70	4.36
	2.0	48.68	47.49	37.61	45.83	44.00	47.63	4.45
D-40	0.1	49.09	48.43	43.95	47.76	46.97	48.51	4.19
	0.4	49.08	48.35	43.67	47.47	46.41	48.44	4.30
	1.0	49.08	48.31	43.78	47.30	46.17	48.41	4.38
	2.0	49.06	48.25	43.87	47.07	45.98	48.36	4.53
D-45	0.1	49.53	48.96	45.22	48.37	47.70	49.02	6.60
	0.4	49.52	48.89	45.24	48.19	47.43	48.97	7.27
	1.0	49.50	48.83	45.12	47.97	47.12	48.92	7.43
	2.0	49.50	48.78	45.00	47.77	46.84	48.88	7.75
D-50	0.1	49.76	49.26	46.07	48.72	48.11	49.32	7.69
	0.4	49.75	49.22	46.17	48.60	47.91	49.29	8.44
	1.0	49.74	49.19	46.04	48.42	47.64	49.26	8.79
	2.0	49.74	49.16	45.77	48.28	47.41	49.23	9.50
D-55	0.1	50.14	49.71	46.88	49.23	48.70	49.76	12.93
	0.4	50.14	49.72	47.18	49.19	48.54	49.77	13.62
	1.0	50.14	49.72	47.11	49.11	48.36	49.77	14.07
	2.0	50.14	49.69	46.76	48.90	48.11	49.74	16.04
Supergiants								
S-30	0.1	49.27	48.00	37.72	46.55	44.90	48.16	22.22
	0.4	49.25	47.88	36.04	46.26	44.06	48.04	22.97
	1.0	49.25	47.85	35.32	45.54	43.35	48.01	22.98
	2.0	49.22	47.78	35.29	45.18	41.85	47.94	23.90
S-35	0.1	49.48	48.63	37.34	47.73	46.82	48.73	15.54
	0.4	49.47	48.55	37.45	47.25	46.18	48.66	16.27
	1.0	49.47	48.47	37.50	46.83	45.92	48.59	16.28
	2.0	49.47	48.36	36.56	46.21	45.55	48.49	16.98
S-40	0.1	49.67	49.01	45.06	48.32	47.51	49.10	15.01
	0.4	49.67	48.93	38.94	48.03	47.11	49.03	15.70
	1.0	49.66	48.81	38.54	47.57	46.70	48.95	16.68
	2.0	49.66	48.70	38.06	47.07	46.27	48.86	18.15
S-45	0.1	49.98	49.41	45.97	48.81	48.12	49.47	19.12
	0.4	49.97	49.35	45.79	48.67	47.78	49.43	19.62
	1.0	49.97	49.28	39.23	48.30	47.37	49.36	22.52
	2.0	49.98	49.19	38.85	47.92	46.97	49.29	23.92
S-50	0.1	50.21	49.73	46.76	49.21	48.59	49.78	20.66
	0.4	50.20	49.70	46.79	49.08	48.34	49.76	21.97
	1.0	50.20	49.69	46.41	48.88	48.06	49.75	23.66
	2.0	50.21	49.69	46.23	48.84	47.81	49.75	24.80

Table 3.5: Numerical values of the integrals of ionizing photons emitted per second by very massive stars. The structure of the table corresponds to Table 3.4.

T_{eff}	Z/Z_{\odot}	$\log Q_{\text{H}}$	$\log Q_{\text{He}}$	$\log Q_{\text{He}^+}$	$\log Q_{\text{O}^+}$	$\log Q_{\text{Ne}^+}$	$\log Q_{\text{S}^+}$	$L_{\nu}(5480 \text{ \AA})$ (10^{22} erg/s/Hz)
$M_* = 150 M_{\odot}$								
40 000	0.05	50.32	49.68	45.87	49.06	48.29	49.76	64
	1	50.31	49.54	39.10	48.34	47.42	49.67	69
50 000	0.05	50.42	49.95	46.83	49.46	48.90	50.00	33
	1	50.42	49.91	46.85	49.20	48.33	49.98	38
$M_* = 300 M_{\odot}$								
40 000	0.05	50.91	50.36	44.21	49.73	49.08	50.42	160
	1	50.97	50.24	39.25	48.83	47.62	50.36	205
$M_* = 600 M_{\odot}$								
50 000	0.05	50.85	50.39	47.04	49.91	49.38	50.44	93
	1	50.85	50.25	47.36	49.68	48.99	50.34	107
$M_* = 1000 M_{\odot}$								
45 000	0.05	51.32	50.60	46.96	49.76	48.86	50.69	398
	1	51.30	50.70	47.06	49.79	48.75	50.80	427
65 000	0.05	51.39	51.01	49.06	50.55	50.06	51.08	144
	1	51.38	51.03	49.19	50.64	50.20	51.08	153
$M_* = 3000 M_{\odot}$								
45 000	0.05	51.84	51.25	47.99	50.53	49.74	51.32	1092
	1	51.83	50.91	40.68	49.34	48.44	51.08	1249
65 000	0.05	51.88	51.55	49.77	51.15	50.68	51.59	403
	1	51.92	51.50	49.49	51.04	50.56	51.55	378

3.3 Application of the calculated SEDs to one- and three-dimensional simulations of H II regions: influence on the emission line intensities

The ionized gas of H II regions reemits most of the extreme ultraviolet (EUV) energy output of the star in a limited number of lines in the UV, the optical, and the IR. The comparatively high intensities in these lines allows observing the ionized gas even if the central source is visually much fainter, making it possible to determine the temperatures and metallicities of the ionized gas even of extragalactic star-forming regions (cf. Zaritsky et al. 1994, Moy et al. 2001, Rubin et al. 2008, Rubin et al. 2010, Rubin et al. 2012, Pilyugin et al. 2013). Additionally, the emission lines of H II regions can be measured using narrow-band filters allowing for observations which simultaneously provide information about the emission spectrum and the spatial structure of an object. This method has been applied to examine the metallicities of H II regions as a function of the position within their host galaxies (cf. Cedrés et al. 2012) or to analyze the substructure of the gas in a single H II region (cf. Heydari-Malayeri et al. 2001).

In this section we investigate the influence of the computed stellar SEDs on the properties of H II regions with homogeneous and with inhomogeneous density structures. Via simulated sample H II

regions we examine how the temperature and ionization structures in the gas depend on the ionizing spectra and the stellar and nebular metallicity. The question remains, however, to what extent these models may represent real-world H II regions. The metallicity, the complex geometric structures of H II regions, and the clumpiness of the medium are usually quantitatively unknown, but may affect the analysis. If discrepancies are encountered, it is often difficult to decide which of the assumptions is responsible for the disagreement found. The computed stellar SEDs themselves can be tested, if the atmospheric models are sufficiently consistent, by their own predicted UV spectra, since the spectral lines and the corresponding ionization fractions in the stellar winds are influenced by the EUV radiation field via the same atomic processes (though at different temperatures and densities) as those that shape the nebular spectra under influence of the emergent stellar flux. In a series of papers we have shown that our consistently calculated synthetic spectra are in sufficiently good agreement with the observed UV spectra of O stars (cf. Pauldrach et al. 1994, Pauldrach et al. 2001, Pauldrach et al. 2004, Pauldrach et al. 2012).

In this work we will therefore study the influence of these effects separately. We begin in Sect. 3.3.1 with simple homogeneous models with spherical geometry to explore the influence of the stellar SEDs, covering the range of effective temperatures and metallicities given by the grid of stellar models presented in Sect. 3.2.2.

Next, we will analyze how the assumption of “perfect” spherically symmetric nebulae influences the emission line diagnostics by comparing the results from homogeneous, spherical models to those from 3D models using a fractally inhomogeneous density structure (such as described by Elmegreen & Falgarone 1996 and Wood et al. 2005). The simulations of these structures will be performed using the 3D radiative transfer code described by Weber et al. (2013). This code has been extended for the present paper such that it can account for the ionization structure and the line emission of the most abundant metal ions and the resulting influence of these ions on the energy balance of the H II regions – for the first time with full time-dependence (see Sect. 3.3.2.1).

Third, we will compare the gas temperatures and the related line emission of evolving H II regions with the respective values of steady-state regions. The motivation is that the description of H II regions as steady-state systems is an approximation which neglects the evolution of star-forming regions (cf. Preibisch & Zinnecker 2007 and Murray 2011) and the short lifetimes of the massive stars (cf. Langer et al. 1994) that act as sources of ionization.

Real-world star-forming regions such as the Orion nebula (cf. Muench et al. 2008) and the η Carinae region (cf. Smith 2006) contain not just a single hot star as ionizing source, but several. In the last step of this work we will therefore replace the single-star ionizing sources in the models by clusters of stars. We compute the ionization structure and total emergent fluxes of a single H II region illuminated by a dense cluster and compare the results with those from a simulation where larger distances between the ionizing sources lead to the formation of partly separate H II regions. Additionally we will investigate the possibility of finding very massive stars (VMS) in star-forming regions by means of the line emission from the gas ionized by the associations.

As an essential ingredient in the simulations we focus here on the accurate description of the time-dependent ionization structure of the metals. Schmidt-Voigt & Koeppen (1987) had presented a computationally efficient approach where the ionization structure of a given element is determined by interpolating between the initial conditions and the stationary case using a single eigenvalue of the system of rate equations (see below), but this approach is not accurate if more than two consecutive ionization stages of an element have to be considered, because the interpolation does not account for the fact that the transition between two noncontiguous ionization stages requires the creation of ions of the intermediate stages. In the method by Graziani et al. (2013) the radiative transfer and the computation of the occupation numbers are performed consistently for hydrogen and helium. For the

occupation numbers of the metal ions and the temperature of the gas pre-computed results from the Cloudy code (Ferland et al. 2013), which describes the stationary states of H II regions using spherical symmetry, are used. These results are selected from a database such that they match the 3D results for the occupation numbers of H and He ions, and the radiation field.

Our approach on the other hand is to apply a numerical method which treats the ionization stages of all the metals we account for in the same consistent way as hydrogen and helium. The occupation numbers $n \equiv n(\mathbf{r}, t)$ of all ionization stages i, j of the elements considered are calculated using the equation of the time-dependent statistical “equilibrium” (Pauli Master Equation, Pauli 1928)

$$\frac{d}{dt}n_i(t) = \sum_{i \neq j} \mathcal{P}_{j,i}n_j(t) - \sum_{i \neq j} \mathcal{P}_{i,j}n_i(t), \quad (3.1)$$

which describes the temporal change of the number density of all ionization stages i , and contains in the rate coefficients $\mathcal{P}_{i,j}$ all important radiative ($\mathcal{R}_{i,j}$) and collisional ($\mathcal{C}_{i,j}$) transition rates.

For the solution of these systems of differential equations we chose an approach that combines integrating the condition of particle conservation within the rate matrices (as described by Mihalas 1978) with providing a robust solution for temporal evolution of the system. To realize this aim we define, following the notation by Marten (1993), a vector \mathbf{x} , which contains in its components the number fractions of all considered N ionization stages relative to the total number density of the element and a matrix \mathbf{G}' , where the components are defined as $g'_{i,i} = (\sum_{j=1, j \neq i}^N \mathcal{P}_{i,j}) + \mathcal{P}_{i,k}$ and $g'_{i,j} = -\mathcal{P}_{j,i} + \mathcal{P}_{k,i}$. The fraction $x_k(t)$ of the ionization stage k is replaced by the condition of particle conservation:

$$x_k(t) = 1 - \sum_{j=1, j \neq k}^N x_j(t). \quad (3.2)$$

The resulting inhomogeneous system of differential equations is

$$\mathbf{E}' \cdot \frac{d}{dt} \mathbf{x}(t) + \mathbf{G}' \cdot \mathbf{x}(t) = \mathbf{b}, \quad (3.3)$$

where the components of \mathbf{b} are $b_i = \mathcal{P}_{k,i}$ and where all coefficients of the redundant k -th row of \mathbf{G}' and \mathbf{b} have been replaced by 1, and those of the k -th column of \mathbf{E} by 0 (with this replacement the unity matrix \mathbf{E} becomes \mathbf{E}') – with these numbers inserted the corresponding components represent in total the condition of particle conservation.

For the spherically symmetric models of Sect. 3.3.1 we focus on the stationary case (where the time-derivative in Eq. 3.3 disappears) in order to make the results for the H II regions models using our new stellar SEDs as ionizing sources comparable to the results of other simulations. In Sect. 3.3.2 we present our results for the time-dependent ionization structure of metals in H II regions in the context of the description of our 3D radiative transfer code.

3.3.1 Spherically symmetric models of H II regions

The standard procedure for simulations of emission line spectra of H II regions is still mostly founded on spherically symmetric models (cf. Stasińska & Leitherer 1996, Hoffmann et al. 2012, and Ferland et al. 2013). They remain useful as a comparative tool because the wavelength region of the ionizing sources blueward of the Lyman edge cannot be observed directly, but the spectral energy distribution of the ionizing flux can nevertheless be studied with such models by means of their influence

on the emission line spectra of gaseous nebulae. Such tests are, however, not altogether without uncertainties owing to the additional dependence of the emission line strengths on the chemical composition of the gas in the H II regions.

Below we outline our numerical approach to investigating these dependencies quantitatively for spherically symmetric model H II regions. The results obtained with this method are then discussed for a grid of models with different metallicities, using stellar SEDs computed for different temperatures and metal abundances (Sect. 3.2.2).

3.3.1.1 The numerical approach applied for the computation of the spherical H II region models

The basic equations describing the temperature and ionization structure of H II regions are similar to those used to describe non-LTE stellar atmospheres in statistical equilibrium. For the computation of the spherically symmetric models of gaseous nebulae we therefore use a modified version of the WM-basic stellar atmosphere code (Sect. 3.2.1), which has been adapted to the dilute radiation fields and low gas densities of H II regions (cf. Hoffmann et al. 2012). This approach yields descriptions of steady-state H II regions, in which ionization and recombination, as well as heating and cooling, are in equilibrium at every radius point. In such a stationary state Eq. 3.3 simplifies to

$$\mathbf{G}' \cdot \mathbf{x}^\infty = \mathbf{b}. \quad (3.4)$$

This equation must be solved iteratively until it converges to the final value for the stationary state \mathbf{x}^∞ , because the rate coefficients that define the entries of \mathbf{G}' themselves depend on the occupation numbers \mathbf{x} : on the one hand, the recombination and collisional ionization rate coefficients in a gas are proportional to the electron density, which in turn mainly depends on the ionization structure of the most abundant elements hydrogen and helium; on the other hand, the radiative ionization rates are determined by the mean intensity J_ν , which is influenced by the ionization-dependent opacity of the matter between the radiation sources and the considered point in the simulation volume, and by the emissivity of the surrounding gas.

In our approach J_ν is computed using a radiative transfer procedure that is performed along a number of parallel rays intersecting radius shells around the source at different angles, describing the radius- and direction-dependent intensities I_ν . The mean intensity at a given radius is computed by evaluating the integral $J_\nu = \frac{1}{2} \int_{-1}^1 I_\nu d\mu$, where μ is the cosine of the angle between a ray and the outward normal at a given radius. The diffuse radiation field created by recombination processes and electron-scattering is treated correctly, avoiding approximations regarding the propagation of photons such as “case B” or “outward-only”.

Apart from the ionization structure, the emission spectrum of an H II region primarily depends on the temperature of the gas because the recombination and collisional excitation rates are functions of the temperature. The interpretation of observations of H II regions thus requires an accurate understanding of the microphysical processes that lead to gains and losses of the thermal energy of the gas, which in turn determines the temperature structure. The processes regarded for the computation of the energy balance in H II regions are heating by photoionization and cooling by radiative recombination, as well as free-free and collisional bound-bound processes.

The low density of the interstellar gas (compared to the gas in stellar atmospheres) leads to small collisional de-excitation rates. Thus radiative transitions of collisionally excited lines are important or even the dominant cooling processes in H II regions.¹¹ We extend the modeling described by

¹¹A collisional excitation process that is followed by the corresponding collisional de-excitation process in total does

Hoffmann et al. (2012) to include the cooling rates connected to the forbidden radiative de-excitation processes of collisionally excited substates of the ground levels of C II, N II, N III, O III, O IV, Ne III, S III, and S IV. The cooling by fine-structure transitions is computed by multiplying the collisional transition rates into the excited states with the probability of the corresponding radiative de-excitation processes and the energy of the photons emitted during the relaxation back into the ground state.¹²

3.3.1.2 Dependence of the properties of H II regions on the ionizing sources

In our systematic series of simulations we examine the ionization and temperature structures and the resulting emission spectra of the gas in homogeneous H II regions irradiated by single stars. In this series we consider the temperature range of O stars (30 000 K to 55 000 K) and we use the same composition for both nebular and stellar matter¹³, covering the metallicity range of star-forming regions in the present-day universe. In a second series, we keep the gas at solar metallicity in order to analyze the influence of the metallicity-dependent stellar SEDs (using our 40 000 K dwarf stars) on the temperature and ionization structure of the H II regions independently from the effects of the metallicity of the gas of the H II regions.

The dependence of the ionization structure of H II regions on the metallicity and the stellar SEDs. In a steady-state H II region, the number of recombinations in the ionized volume (the Strömgen sphere) must equal the stellar emission rate of ionizing photons. Thus, the sizes of the Strömgen spheres depend on the SEDs of the ionizing stars and on the recombination rates of the ions in the H II regions.

In the presented grid the radii $r_{\text{H II}}$ of the hydrogen Strömgen spheres grow significantly for lower metallicities, but otherwise equal stellar parameters R , $\log(g)$, and T_{eff} (see Figs. 3.16 and 3.17). For instance, the hydrogen Strömgen radius for a metallicity of $0.1 Z_{\odot}$ is approximately 50% larger than the Strömgen radius for $2.0 Z_{\odot}$ in the case of the 40 000 K dwarf stars. As shown in Table 3.4 the hydrogen-ionizing fluxes of O stars are – for otherwise equal stellar parameters – almost independent of metallicity. The different Strömgen radii are therefore primarily a consequence of the different recombination rates, which increase for lower temperatures of the ionized gas as they occur for higher metallicities. This relation results because radiative decays of collisionally excited states of metal

not modify the thermal energy content of the gas. The probability of a radiative de-excitation is computed as $p_{\text{rad}} = n_{\text{crit}}/(n_e + n_{\text{crit}})$, where n_e is the electron density and n_{crit} is the critical density, defined as the electron density for which the collisional de-excitation rate is equal to the radiative de-excitation rate. For instance, the critical density of the 3P_1 state of O III, which can be de-excited by the emission of a far-infrared photon with $\lambda = 88 \mu\text{m}$, is $5.1 \cdot 10^2 \text{ cm}^{-3}$. This value is considerably lower than the critical density of $6.8 \cdot 10^5 \text{ cm}^{-3}$ for the 1D_2 state of the O III ion, which is de-excited by the emission of the O III 5007 Å + 4959 Å lines. We use the values from Osterbrock & Ferland 2006.

¹²The collision strengths used for the computation of the collisional excitation rates are taken from Blum & Pradhan (1992), Butler & Zeppen (1994), Lennon & Burke (1994), and Tayal & Gupta (1999) (as collected in Osterbrock & Ferland 2006). The nebular approximation is applied for the computation of transition rates into collisionally excited fine-structure levels, i.e., the computation of the fine-structure transitions is based on the assumption that almost all ions are in their ground state and excitations from non-ground levels do not have to be considered.

¹³The assumption that the chemical composition of H II regions is equal to the composition of the embedded stars is not necessarily realistic because the formation of dust can lead to a depletion of metals from the gas phase. Shields & Kennicutt (1995) find, for instance, a depletion of $\approx 50\%$ for carbon, $\approx 40\%$ for oxygen, and $\approx 20\%$ for nitrogen for solar metallicity, while according to their results sulfur remains almost undepleted. In contrast, a significant depletion of sulfur is found by Rubin et al. (2007, 2008). There are variations in the metal depletion rates among different H II regions because the formation and destruction of dust depends on the chemical composition and temperature of the gas, and on the radiation field.

ions are the dominant cooling processes in the ionized gas.¹⁴ Cooler temperatures in turn increase the recombination coefficients of H II and other ions (cf. Osterbrock & Ferland 2006) and hence reduce the ionized volumes.

The size of the He II Strömgren sphere is of particular importance because it marks the boundary where all photons with energies above the He I ionization threshold have been used up, and consequently no significant amounts of metal ions requiring ionization energies above that of He I will be found. Among these ions are N III, O III, Ne III, and S IV. The volumes where helium is ionized are considerably smaller than the hydrogen Strömgren spheres for stellar effective temperatures of $T_{\text{eff}} = 30\,000$ K. The radii of the hydrogen Strömgren spheres exceed the radii of the helium Strömgren spheres by a factor of approximately 3 in the case of the dwarf stars. In contrast, for the supergiants the corresponding factor is approximately 1.5. This results from a lower ratio of He-ionizing to H-ionizing photons for the dwarf models compared to the supergiant models (Table 3.4). Helium is singly ionized up to the Strömgren radius of hydrogen in H II regions where the effective temperature of the stellar sources is $\geq 40\,000$ K.

The radius range in which helium is fully ionized, i.e., where He III is the most abundant ionization stage of helium, is small in comparison to the hydrogen Strömgren sphere for dwarf and supergiant O stars. These He III regions are too small to be resolved in those of our simulations in which the ionizing source is one of the 30 000 K or 40 000 K model stars (with the exception of the supergiant model with $0.1 Z_{\odot}$ where He III is the most abundant ionization stage for $\approx 0.05 r_{\text{H II}}$). Only the dwarf and supergiant stars with effective temperatures of 50 000 K have appreciable He III Strömgren spheres that reach $\approx 0.05 r_{\text{H II}}$ (for $2.0 Z_{\odot}$) to $\approx 0.10 r_{\text{H II}}$ (for $0.1 Z_{\odot}$).

Although the number densities of metal ions are much smaller than the number densities of hydrogen and helium ions, metals have a large impact on the energy balance of the ionized gas, and interpretation of metal line ratios as markers for the galactic evolution (cf. Balser et al. 2011 and the references therein) requires knowledge of the relation between the ionization fractions of metals and the SEDs of the ionizing sources. For example, the O III/O II ratio results from the O II ionizing flux, which in turn depends not only on the effective temperature of the ionizing sources, but also on their metallicity and their atmospheric density stratification. In the H II regions around the 30 000 K dwarf stars, O III is the most abundant ionization stage of oxygen just within less than the innermost $\approx 0.05 r_{\text{H II}}$ for all metallicities. The O II-ionizing fluxes of the supergiants at 30 000 K exceed the fluxes of the dwarf stars of the same effective temperature by approximately 3 dex, which results in a more extended volume in which O III is the dominant ionization stage of oxygen. The extension of this volume strongly depends on metallicity. Its radius $r_{\text{O III}}$ is $\approx 0.4 r_{\text{H II}}$ for $0.1 Z_{\odot}$, but drops to $\approx 0.1 r_{\text{H II}}$ for a metallicity of $2.0 Z_{\odot}$.

The O II-ionizing fluxes of 40 000 K supergiants, which differ by ≈ 1.3 dex between the model with $0.1 Z_{\odot}$ and $2.0 Z_{\odot}$, show a stronger metallicity dependence than the O II-ionizing fluxes of the dwarf stars with the same effective temperature, which differ by ≈ 0.6 dex. Consequently, the radii of the O III dominated parts of the H II regions around the supergiants vary more ($r_{\text{O III}} \approx 0.98 r_{\text{H II}}$ for $0.1 Z_{\odot}$, $r_{\text{O III}} \approx 0.55 r_{\text{H II}}$ for $2.0 Z_{\odot}$) than the radii around the dwarf stars ($r_{\text{O III}} \approx 0.97 r_{\text{H II}}$ for $0.1 Z_{\odot}$, $r_{\text{O III}} \approx 0.87 r_{\text{H II}}$ for $2.0 Z_{\odot}$). The ion O III is the most abundant ionization stage within the entire Strömgren spheres for dwarf and supergiant stars of all metallicities for an effective temperature of 50 000 K.

Like the O III fraction relative to the total amount of oxygen, the fraction of S IV decreases for higher

¹⁴In the outer parts of the H II regions with $0.1 Z_{\odot}$, the collisional excitation of neutral hydrogen atoms becomes the most important cooling process. The collisional cooling by hydrogen increases near the Strömgren radius owing to the larger abundances of neutral hydrogen. The result is that there is no increase in the temperatures in the outer parts of the ionized regions, unlike for the higher metallicities, where such maxima are caused by radiation hardening.

metallicities as can be expected in view of the almost identical ionization energies of S III (2.56 Ryd) and O II (2.58 Ryd). Still, the relative fraction of S IV is considerably smaller than the relative fraction of O III within the same H II region. The reason is the smaller ionization cross section from the ground-state of S III ($0.36 \cdot 10^{-18} \text{ cm}^2$ at the ionization edge) compared to that of O II ($10.4 \cdot 10^{-18} \text{ cm}^2$ at the ionization edge).

The above result that low stellar metallicities lead to harder ionizing spectra and thus to a larger fraction of high ionization stages is in agreement with spectroscopic observations. For example, Rubin et al. (2007, 2008) found rising $\langle \text{Ne}^{2+} \rangle / \langle \text{Ne}^+ \rangle$ and $\langle \text{S}^{3+} \rangle / \langle \text{S}^{2+} \rangle$ ratios for increasing distance from the galactic centers of M 83 and in M 33, based on mid-IR observations with the Spitzer Space telescope. This relation is likely to be connected with the lower metallicities in the outer parts of the galaxies (cf. Rubin et al. 2007). Further observations of the metal-poor galaxy NGC 6822 (Rubin et al. 2012) have found larger fractions of the higher ionization stages than in M 83 (supersolar metallicity) or in M 33 (roughly solar metallicity). These results might, however, additionally be influenced by other factors, such as different stellar mass functions or different effective temperatures of the ionizing stars as a function of the chemical composition of the star-forming gas.

In Figure 3.1 we compare the simulated $\langle \text{Ne}^{2+} \rangle / \langle \text{Ne}^+ \rangle$ and $\langle \text{S}^{3+} \rangle / \langle \text{S}^{2+} \rangle$ ratios of our model H II regions with the corresponding ion ratios determined from the observations described by Rubin et al. (2007, 2008).¹⁵ The figure also shows that the metallicity-dependence of the ionization structure decreases for larger effective temperatures of the ionizing stars as can be expected from the ionizing fluxes shown in Table 3.4.

Emission line spectra of H II regions at different metallicity. Comparing observed emission line spectra to synthetic nebular models is the most important approach for obtaining information about the temperature, the density, and the ionization structure of H II regions. To investigate the variations in the emission line ratios, we have computed the fluxes of the collisionally excited optical lines [N II] 6584 Å + 6548 Å, [O II] 3726 Å + 3729 Å, [O III] 5007 Å + 4959 Å, and [S II] 6716 Å + 6731 Å for each of our H II region models. In Table 3.6 the results are shown relative to the corresponding H β emission.

In most cases the strongest line emission in the optical range is reached for a metallicity of $0.4 Z_{\odot}$. This non-monotonic behavior is the result of two opposing metallicity-dependent effects. On the one hand, a higher metallicity increases the number density of ions that are potential line emitters. On the other hand, the lower temperature of the gas decreases the probability of a collisional excitation process, which finally leads to the emission of optical line radiation. The effect of the lower temperatures dominates for $2.0 Z_{\odot}$ where in most cases the fluxes for this metallicity are the weakest among the considered metallicities.¹⁶ This is explained by the equation for the rate coefficients for the collisional

¹⁵For this comparison we scaled the ionizing fluxes to 10^{49} hydrogen-ionizing photons per second and used a hydrogen number density in the gas of 1000 cm^{-3} to match the assumptions in Rubin et al. (2008).

¹⁶The cooling by the infrared transitions between the fine-structure levels partly leads to simulated temperatures of the gas, which are below 3000 K for a metallicity of $2.0 Z_{\odot}$. This result is also obtained with other nebular model codes, e.g., Cloudy (Ferland et al. 2013). Such low temperatures, however, have not been observed in H II regions. The reason for this discrepancy is not entirely clear. Shields & Kennicutt (1995) have analyzed the impact of dust within high-metallicity H II regions and attribute the lack of H II regions with very low temperatures to the depletion of metals from the gas phase by the formation of dust and the heating by the emission of electrons from the UV-irradiated dust grains. The spectral properties of H II regions in the metal-rich ($Z \approx 2 Z_{\odot}$) star-forming galaxy M 83 with relatively weak collisionally excited emission features have been described in detail by Bresolin & Kennicutt (2002), who stress that for these conditions a determination of the electron temperature by means of emission line analysis could not be carried out accurately.

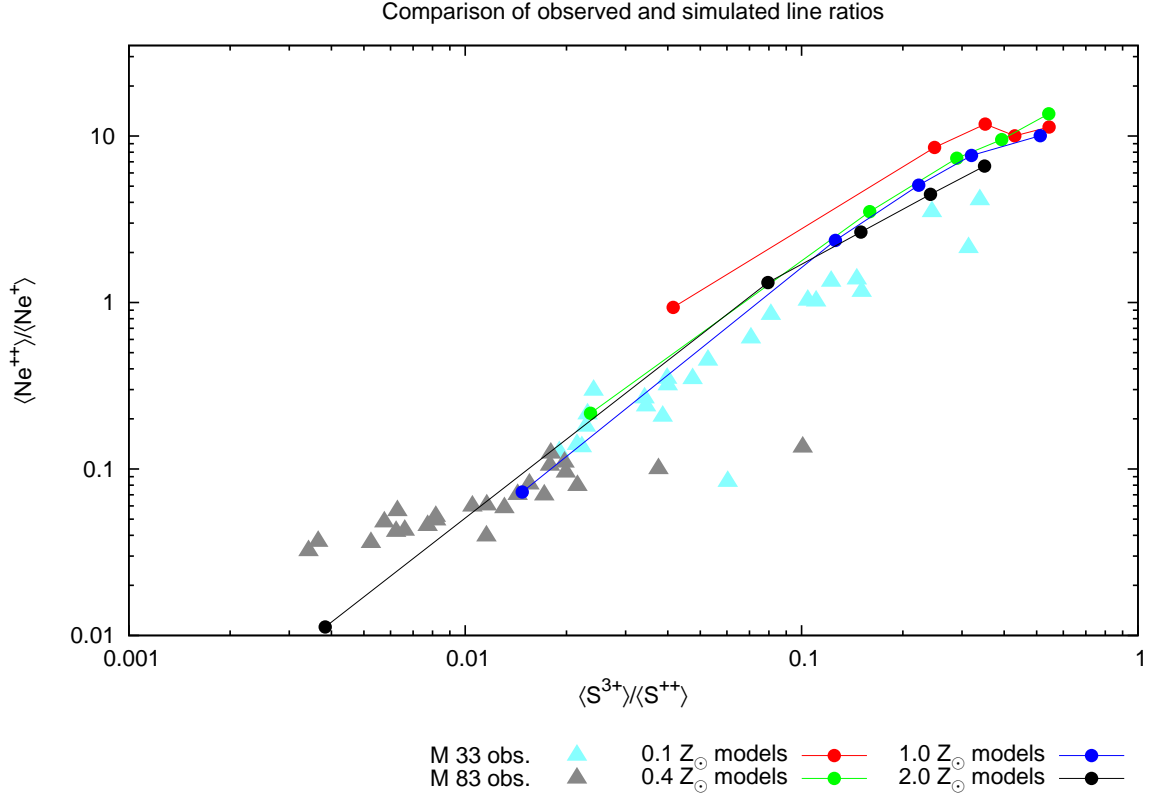


Figure 3.1: Comparison of observed ionic number ratios $\langle S^{3+} \rangle / \langle S^{2+} \rangle$ and $\langle Ne^{2+} \rangle / \langle Ne^+ \rangle$ to the corresponding results from our model H II regions. The triangles represent H II regions in the metal rich galaxy M 83 (gray, values from Rubin et al. 2007) and M 33 (cyan triangles, values from Rubin et al. 2008); the circles represent model H II regions using as ionizing sources dwarf stars with temperatures from 35 000 K to 55 000 K and metallicities of 0.1 Z_{\odot} to 2.0 Z_{\odot} . The lower metallicities are correlated with a larger fraction of the higher ionization stages both in the observations and the synthetic H II region models.

excitation,

$$C_{lu} = n_e \left(\frac{2\pi}{kT} \right)^{1/2} \frac{\hbar^2}{m_e^{3/2}} \frac{\Omega_{lu}(T)}{g_l} e^{-h\nu_{lu}/kT} \quad (3.5)$$

(Mihalas 1978; n_e is the number density of electrons, m_e the electron mass, $\Omega_{lu}(T)$ the velocity-averaged collision strength, a slowly varying function of temperature, $h\nu_{lu}$ the transition energy, and g_l the statistical weight of the lower level), which leads to qualitatively different temperature dependences for collisionally excited lines in different wavelength ranges. The exponential term in Eq. 3.5 rises strongly with increasing temperature if the energy difference between the levels is large compared to kT , as is the case for lines in the visible and ultraviolet range. For the lines in the mid-infrared to far-infrared range, the energy difference between the upper and the lower level is significantly smaller than kT . Thus, the exponential term is close to unity in the entire temperature range found in H II regions and the rate coefficients are roughly proportional to the inverse square root of the temperature. This implies that the cooling by infrared lines becomes more effective for decreasing temperatures,

i.e., there is a positive feedback between the lower temperatures and the infrared line cooling. As a result, a small increase in the metallicity has a strong influence on the temperature structure if it causes the infrared transitions mentioned above to become the dominant cooling processes.

The influence of metallicity-dependent SEDs on the temperature and ionization structure of gas with fixed metallicity. In addition to the models where stellar and gas metallicity are equal, we have computed models where the metallicity of the gas is fixed at $1.0 Z_{\odot}$, but the metallicity of the stellar sources is varied in order to analyze the effects of stellar SEDs independently of the effects of the chemical composition of the gas. The simulations have been performed using the four different 40 000 K dwarf star models.

The sizes of the hydrogen Strömgren spheres show variations of approximately 5%, which are mainly caused by lower recombination rates in the gas around the lower-metallicity stars where the temperatures are higher than in the gas surrounding the model stars with higher metallicities.¹⁷ The differences are more pronounced for the ionization structure of oxygen and sulfur, especially for the ratios O II/O III and S III/S IV. For the model with a metallicity of $2.0 Z_{\odot}$, O III is the most abundant ion of oxygen within the inner $\approx 0.85 r_{\text{H II}}$, while this is the case for $\approx 0.97 r_{\text{H II}}$ at a metallicity of $0.1 Z_{\odot}$. For S IV the corresponding values are $0.28 r_{\text{H II}}$ and $0.59 r_{\text{H II}}$, respectively.

The emission of the [O III] 5007 Å + 4959 Å lines increases with decreasing stellar metallicities as a result of the higher temperatures and the larger fraction of O III ions. At a metallicity of $0.1 Z_{\odot}$ the emission of these lines is twice as strong as at $2.0 Z_{\odot}$ (last part of Table 3.6). In contrast, the emission of lines associated with singly ionized atoms, like [N II] 6584 Å + 6548 Å and [O II] 3726 Å + 3729 Å, decreases for lower stellar metallicities because the number of singly ionized ions of these elements is reduced as the shells in which they are the dominant ionization stage become thinner.

3.3.2 Three-dimensional, time-dependent simulations of the ionization structures of the metals in H II regions

We will now abandon the assumption of a homogeneous gas and a spherically symmetric ionized bubble and discuss the effects of inhomogeneities of the gas density. This is motivated by the fact that H II regions are obviously not homogeneous spheres, but are characterized by a more complex structure. The inhomogeneous density structure of H II regions has been treated, for example, by Wood & Mathis (2004); Wood et al. (2005), who focused on the ability of photons to escape from a “porous” H II region into the diffuse component of the ionized gas in a galaxy; Wood et al. (2013), who studied the consequences of inhomogeneous density structures for the determination of metallicities in H II nebulae; and by Dale & Bonnell (2011), Walch et al. (2012), and Dale et al. (2013), who studied the interaction between stellar radiation fields and the density structure of ionized gas. Apart from the metallicity it is therefore the complex geometric structure and the embedded clumps that are of importance for the nebular models and a corresponding comparison of the calculated emission line strengths with the observed spectral features.

To include such effects in our computations we have developed a 3D radiative transfer code based on the approach by Weber et al. (2013), but considerably extended to account for the time-dependent ionization structure of the metals within the gas. In the description of our method we will first introduce our ray-tracing approach to 3D radiative transfer. Subsequently, we will present a solution of the time-dependent rate equations and treat the influence of the metal ions on the evolution of the

¹⁷The emission of photons whose energies considerably exceed the Lyman-Edge is higher for lower metallicities. Consequently, the mean gain of thermal energy per ionization process is larger.

Table 3.6: Comparison of the nebular emission line ratios for a grid of H II regions where the ionizing source is in each case one of the model stars. We show the ratio of some important nebular line strengths obtained from spherically symmetric nebular models with varying metallicity to the H β emission in these model H II regions.

Model	Z/Z_{\odot}	[N II] 6584 + 6548 Å	[O II] 3726 + 3729 Å	[O III] 5007 + 4959 Å	[S II] 6716 + 6731 Å
Same metallicity for H II region and star (dwarfs)					
D-30	0.1	0.77	1.51	0.00	0.33
	0.4	1.43	1.63	0.00	0.73
	1.0	1.48	0.94	0.00	0.85
	2.0	0.86	0.29	0.00	0.56
D-35	0.1	0.44	1.59	1.66	0.15
	0.4	1.06	2.45	1.63	0.38
	1.0	1.29	1.70	0.68	0.49
	2.0	1.06	0.56	0.05	0.38
D-40	0.1	0.09	0.45	4.62	0.09
	0.4	0.29	0.99	5.88	0.21
	1.0	0.35	0.73	2.99	0.24
	2.0	0.23	0.28	0.58	0.16
D-45	0.1	0.06	0.28	5.47	0.07
	0.4	0.16	0.58	8.34	0.18
	1.0	0.20	0.48	4.52	0.21
	2.0	0.12	0.20	1.00	0.13
D-50	0.1	0.04	0.21	5.98	0.07
	0.4	0.12	0.43	10.07	0.18
	1.0	0.15	0.41	6.57	0.21
	2.0	0.09	0.22	1.88	0.13
D-55	0.1	0.03	0.14	6.60	0.06
	0.4	0.08	0.31	12.40	0.17
	1.0	0.11	0.34	10.56	0.22
	2.0	0.08	0.24	3.79	0.16
Same metallicity for H II region and star (supergiants)					
S-30	0.1	0.60	1.95	0.69	0.14
	0.4	1.33	2.33	0.46	0.37
	1.0	1.30	1.25	0.09	0.41
	2.0	0.64	0.25	0.01	0.25
S-35	0.1	0.15	0.78	3.62	0.07
	0.4	0.56	1.92	3.18	0.19
	1.0	1.15	1.91	0.84	0.28
	2.0	1.17	0.74	0.04	0.26
S-40	0.1	0.07	0.35	4.99	0.06
	0.4	0.20	0.79	6.25	0.14
	1.0	0.48	1.16	2.13	0.18
	2.0	0.97	0.87	0.15	0.21
S-45	0.1	0.04	0.23	5.77	0.05
	0.4	0.12	0.49	8.41	0.13
	1.0	0.17	0.46	3.91	0.15
	2.0	0.27	0.24	0.66	0.09
S-50	0.1	0.03	0.16	6.34	0.05
	0.4	0.08	0.33	10.84	0.14
	1.0	0.10	0.38	7.35	0.17
	2.0	0.07	0.19	2.40	0.13
Different metallicity for H II region ($Z = Z_{\odot}$) and star					
D-40	0.1	0.24	0.49	5.11	0.30
	0.4	0.29	0.57	3.42	0.25
	1.0	0.35	0.73	2.99	0.24
	2.0	0.43	0.93	2.42	0.25

temperature structure. Finally, we will describe the generation of synthetic narrowband images, which can link the theoretical models with observations.

This numerical approach will be applied to inhomogeneous, fractally structured gas with various metallicities and sources of ionization. The results of these computations results will be compared with the results obtained for a homogeneous gas distribution. In addition, we will account for the temporal evolution of H II regions and study the effects of the distribution of the sources within clusters of hot stars on the emergent emission line flux of the surrounding ionized gas.

3.3.2.1 Three-dimensional radiative transfer based on ray tracing

The propagation of light along straight lines leads directly to the concept of a ray-by-ray solution, where the luminosity of each source is distributed among a set of rays originating from the source. The main aspects of the ray-by-ray solution are the isotropic distribution of rays around each source and the solution of the radiative transfer equation along each of these rays.

The sources are characterized by a specified spectral energy distribution F_ν and luminosity $L_\nu(l) = 4\pi R_l^2 F_\nu(l)$, where R_l is the radius of the l -th source. The frequency-dependent luminosity L_ν of each source is distributed evenly¹⁸ among N_{rays} rays, such that each ray is associated with a luminosity of $\tilde{L}_\nu = L_\nu/N_{\text{rays}}$. The rays are then traced from the source(s) until the border of the simulated volume is reached.

The integrated form of the radiative transfer equation along a ray is

$$I_\nu(s) = I_\nu(s_0(n)) e^{-\tau_\nu(s_0(n)) - \tau_\nu(s)} + \int_{s_0(n)}^s \eta_\nu(s') e^{-\tau_\nu(s') - \tau_\nu(s)} ds', \quad (3.6)$$

where $I_\nu(s)$ is the intensity at the position s , $s_0(n)$ corresponds to the starting point of each ray n , $\eta_\nu(s')$ is the emissivity of the gas¹⁹ at the position s' , and $\tau_\nu(s) = \int_{s_0(n)}^s \chi_\nu(s') ds'$ is the optical depth with respect to the source.

The simulated volume is discretized into a Cartesian grid of cells and each of the sources is located in the center of one of these cells. The energy deposited per time in the cells crossed by a ray n along the distance $s_n(m)$ between the source and the entry point into a cell m is then calculated as

$$\Delta \dot{E}(s_n(m)) = \int_0^\infty \tilde{L}_\nu(s_0(n)) (1 - e^{-\tau_\nu(s_n(m))}) d\nu \quad (3.7)$$

(for details see Weber et al. 2013).

Temporal evolution of the ionization structure of metals. Modeling the evolution of the ionization structures is not straightforward. The rate equations form a stiff set of differential equations as the timescales for the various ionization and recombination processes in the cell may differ by several orders of magnitude. Furthermore, the timescales differ between various cells depending on whether they are passed by an ionization front and how distant they are from the sources of ionization. However, the eigenvalue approach presented here provides a novel method of solving the rate equations in a stable and efficient way.

¹⁸To ensure that each of the rays represents a solid angle of the same size we use the HEALPix method described by Górski et al. (2005) for the distribution of the rays.

¹⁹In the 3D simulations we apply the on-the-spot approximation (Zanstra 1931, Baker & Menzel 1938, Spitzer 1998) for hydrogen and helium to account for the diffuse radiation field. This approximation assumes that photons generated by a recombination process which directly leads into the ground state of the recombined particle are locally reabsorbed. Thus, the diffuse ionization field is not considered explicitly; instead, the rates for recombination processes that directly lead into the ground state are subtracted from the total recombination rates.

The solution

$$\mathbf{x}(t) = \mathbf{x}^\infty + \mathbf{x}_{\text{hom}}(t) \quad (3.8)$$

of the inhomogeneous system of differential equations defined by Eq. 3.3 is composed of the equilibrium solution \mathbf{x}^∞ of Eq. 3.4 and the solution of the corresponding homogeneous system

$$\mathbf{E}' \cdot \frac{d}{dt} \mathbf{x}_{\text{hom}}(t) + \mathbf{G}' \cdot \mathbf{x}_{\text{hom}}(t) = \mathbf{0}, \quad (3.9)$$

which is written in components as

$$\begin{pmatrix} \frac{dx_{\text{hom},1}}{dt} \\ \vdots \\ \frac{dx_{\text{hom},N-1}}{dt} \\ 0 \end{pmatrix} + \begin{pmatrix} g'_{1,1} & \cdots & g'_{1,N-1} & 0 \\ \vdots & \ddots & \ddots & \vdots \\ g'_{N-1,1} & \cdots & g'_{N-1,N-1} & 0 \\ 1 & \cdots & 1 & 1 \end{pmatrix} \cdot \begin{pmatrix} x_{\text{hom},1} \\ \vdots \\ x_{\text{hom},N-1} \\ x_{\text{hom},N} \end{pmatrix} (t) = \begin{pmatrix} 0 \\ 0 \\ \vdots \\ 0 \end{pmatrix}. \quad (3.10)$$

In Eq. 3.10 the condition of particle conservation is as an example inserted for $k = N$. The particle conservation implies that the sum of all components of a solution of the homogeneous system of differential equations is 0. For the solution $\mathbf{x}_{\text{hom}}(t)$ of Eq. 3.10, the k -th component is thus computed as

$$x_{\text{hom},k}(t) = - \sum_{i=1, i \neq k}^N x_{\text{hom},i}(t). \quad (3.11)$$

The general structure of the solution for the components of the homogeneous equation different from k is

$$x_{\text{hom},i}(t) = \sum_{j=1}^{N-1} v_{i,j} e^{-\delta_j(t-t_0)} \gamma_j, \quad (3.12)$$

where $v_{i,j}$ is the i -th component of the j -th eigenvector of the system of differential equations obtained from Eq. 3.10 by removing the k -th line of \mathbf{x} and the k -th line and k -th column of \mathbf{G}' ; δ_j are the corresponding eigenvalues. The values of γ_j are defined by the occupation numbers at t_0 , the beginning of the respective time step.

Equations 3.11 and 3.12 are combined in matrix-vector notation using a matrix \mathbf{V} composed of the eigenvectors \mathbf{v}_j , but additionally contains in its k -th row and j -th column the negative of the scalar product $\mathbf{1} \cdot \mathbf{v}_j$ (where the vector $\mathbf{1}$ contains the entry 1 in each of its components):

$$\mathbf{x}_{\text{hom}}(t) = \mathbf{V} \cdot \boldsymbol{\delta}(t) \cdot \boldsymbol{\gamma} = \begin{pmatrix} \mathbf{v}_1 & \mathbf{v}_2 & \cdots & \mathbf{v}_{N-1} \\ -\mathbf{1} \cdot \mathbf{v}_1 & -\mathbf{1} \cdot \mathbf{v}_2 & \cdots & -\mathbf{1} \cdot \mathbf{v}_{N-1} \end{pmatrix} \cdot \boldsymbol{\delta}(t) \cdot \boldsymbol{\gamma} \quad (3.13)$$

The diagonal matrix $\boldsymbol{\delta}(t)$ has entries $\delta_{j,j} = e^{-\delta_j(t-t_0)}$, and $\boldsymbol{\gamma}$ is a vector that contains in its j -th row the coefficient γ_j (in Eq. 3.13 we set $k = N$ again).

The vector $\boldsymbol{\gamma}$ is determined by inserting the occupation numbers for $t = t_0$ which are known from the previous time step. In this case $\boldsymbol{\delta}$ becomes the identity matrix and from Eq. 3.12 follows

$$\tilde{\mathbf{V}} \cdot \boldsymbol{\gamma} = \tilde{\mathbf{x}}_{\text{hom}}(t_0) = \tilde{\mathbf{x}}(t_0) - \tilde{\mathbf{x}}^\infty, \quad (3.14)$$

where $\tilde{\mathbf{V}}$ corresponds to the matrix \mathbf{V} without the k -th row (the k -th row is also removed for $\tilde{\mathbf{x}}_{\text{hom}}$ and $\tilde{\mathbf{x}}^\infty$). Equation 3.14 is solved for $\boldsymbol{\gamma}$ by

$$\boldsymbol{\gamma} = \tilde{\mathbf{V}}^{-1} (\tilde{\mathbf{x}}_{\text{hom}}(t_0) - \tilde{\mathbf{x}}^\infty). \quad (3.15)$$

With Eqs. 3.15 and 3.13, the values for $\mathbf{x}_{\text{hom}}(t)$

$$\mathbf{x}_{\text{hom}}(t) = \mathbf{V} \cdot \boldsymbol{\delta}(t) \cdot \tilde{\mathbf{V}}^{-1} (\tilde{\mathbf{x}}(t_0) - \tilde{\mathbf{x}}^{\infty}) \quad (3.16)$$

are obtained. The result for $\mathbf{x}(t)$ is the initial value for the next time step and after the recomputation of the rate coefficients the matrix \mathbf{G}' is updated. We currently consider the ionization stages I and II of hydrogen; I to III of helium; and I to IV of carbon, nitrogen, oxygen, neon, and sulfur, but in principle the method can be extended to any number of ionization stages and any set of elements required to describe the respective problem. The presented method has proven to be numerically very stable. Particle conservation is preserved for each element with a relative deviation of less than 10^{-8} .

In the next paragraphs we describe the computation of the rate coefficients for the recombination and ionization processes which via the rate matrix \mathbf{G}' determine the temporal evolution of the ionization fractions in $\mathbf{x}(t)$.

Recombination Rates. The relevant recombination processes in the interstellar gas are radiative and dielectronic recombination. In radiative recombination processes a free electron is captured by an ion and its kinetic and potential energy (relative to the bound state immediately after the recombination) is converted into the energy of the emitted photon. In dielectronic processes the energy of the captured electrons excites another electron of the ion, resulting in a doubly excited intermediate state. Dielectronic recombinations can only occur for discrete electron energies because of the additional bound-bound process. The recombination rate coefficient of an ion j in a grid cell m filled with gas at a temperature of $T(m)$ is given by $\mathcal{R}_{j,j-1}(m) = \alpha_j(T(m)) \cdot n_e(m)$, where $n_e(m)$ is the number density of electrons and $\alpha_j(T(m))$ is the total recombination coefficient, composed of a radiative contribution $\alpha_{r,j}(T(m))$ and a dielectronic contribution $\alpha_{d,j}(T(m))$:

$$\alpha_j(T(m)) = \alpha_{r,j}(T(m)) + \alpha_{d,j}(T(m)). \quad (3.17)$$

For the temperature-dependent radiative recombination coefficients of metal ions of type j in cell m , we use the approximate formula

$$\alpha_{r,j}(T(m)) = A_j T'^{-X_j}(m), \quad (3.18)$$

where $T'(m) = T(m)/10\,000$ K is the temperature of the gas in units of 10 000 K. The fit parameters A_j and X_j are taken from Aldrovandi & Pequignot (1973), Aldrovandi & Pequignot (1976), Shull & van Steenberg (1982), and Arnaud & Rothenflug (1985).

The dielectronic recombination rates for low temperatures, where kT is smaller than the energy needed to create the excited intermediate states, as is typically the case in H II regions, are described by the fit formula (Nussbaumer & Storey 1983)²⁰

$$\alpha_{d,j}(T(m)) = 10^{-12} \cdot \left(\frac{a_j}{T'(m)} + b_j + c_j T'(m) + d_j T'^2(m) \right) \cdot T'^{-3/2}(m) e^{-f_j/T'(m)} \text{cm}^3 \text{s}^{-1}. \quad (3.19)$$

Here a_j , b_j , c_j , d_j , and f_j are fit parameters which depend on the type of the ion.

²⁰An online collection of the radiative and dielectronic recombination data of metal ions that contains the values used in this work is provided by D. A. Verner, <http://www.pa.uky.edu/~verner/rec.html>.

An additional contribution to the dielectronic recombination rate that becomes relevant for higher temperatures where kT is in the order of the excitation energy has been described by (Burgess 1964) and is approximated by

$$\alpha_{dh,j}(T(m)) = B_j \left(\frac{T}{\text{K}} \right)^{-3/2} (m) e^{-T_{0,j}/T(m)} \left(1 + C_j e^{-T_{1,j}/T(m)} \right). \quad (3.20)$$

The values for the fit parameters B_j , C_j , $T_{0,j}$, and $T_{1,j}$ were obtained from the same sources as the radiative recombination coefficients. The total dielectronic recombination rate $\alpha_{d,j}$ is obtained by adding up the low-temperature and the high-temperature contributions (Storey 1983). The fit functions for the recombination rates already consider recombination to all levels. The recombination rates for hydrogen and helium are computed by interpolating the tables provided by Hummer (1994) and Hummer & Storey (1998).

Photoionization rates and computation of the mean intensity. The photoionization rates $R_{lu}(m)$ from a level l in one ionization stage to a level u in the next ionization stage are calculated as

$$R_{lu}(m) = \int_{\nu_{lu}}^{\infty} \frac{4\pi a_{lu}(\nu)}{h\nu} J_\nu(m) d\nu, \quad (3.21)$$

where $J_\nu(m)$ is the mean intensity, ν_{lu} the threshold frequency for the considered ionization process, and $a_{lu}(\nu)$ the frequency-dependent ionization cross section.²¹

To determine the average intensity J_ν needed to compute the radiative rates, we proceed as follows. From our discussion of the radiative transfer we already know the total energy absorbed (per unit time) by a cell, namely that given by Eq. 3.7. The number of photons absorbed per unit time in the cell in a particular transition is given by the same integral, with the integrand divided by the energy $h\nu$ of a photon and weighted by the relative contribution of that transition to the total opacity,

$$\begin{aligned} \sum_{\text{ray segments}} \int \frac{\tilde{L}_\nu^{(\text{inc.})} (1 - e^{-\tau_\nu}) \chi_{lu}(\nu)}{h\nu \chi_\nu^{\text{tot}}} d\nu &= \\ &= V n_l R_{lu} = V n_l \int \frac{4\pi a_{lu}(\nu)}{h\nu} J_\nu d\nu, \end{aligned} \quad (3.24)$$

²¹For the computation of the frequency-dependent ionization cross section, we use the Seaton approximation (Seaton 1958)

$$a_{lu}(\nu) = a_{0,lu} \left(\beta_{lu} \left(\frac{\nu}{\nu_{lu}} \right)^{-s_{lu}} + (1 - \beta_{lu}) \left(\frac{\nu}{\nu_{lu}} \right)^{-s_{lu}-1} \right), \quad (3.22)$$

where $a_{0,lu}$, β_{lu} , and s_{lu} are fit parameters for the numerical results of the quantum-mechanical calculations of the cross sections as a function of photon energy. The nebular approximation is applied and only ionization processes from atoms in the ground state are considered, but there may be several ionization channels with different electronic states of the ionization product. The total ionization rate in this case is $\mathcal{R}_{i,j} \approx \sum_{u=u_0}^{u_{\text{max}}} R_{l_0,u}$, where l_0 is the ground-level of ion i and the summation is carried out over the considered upper levels.

In addition to the radiative ionization rates we also compute the collisional ionization rate coefficients by applying an approximation from Seaton as given by Mihalas (1978),

$$C_{lu} = n_e \frac{1.55 \cdot 10^{13}}{(T/\text{K})^{1/2}} \bar{g} \frac{e^{-h\nu_{lu}/kT}}{h\nu_{lu}/kT}, \quad (3.23)$$

where \bar{g} takes the value 0.1, 0.2, or 0.3 for an initial ionic charge of 0, 1, or ≥ 2 , respectively.

where $\tilde{L}_\nu^{(\text{inc.})}$ is again (for every ray passing through that cell) the luminosity of the ray incident on the cell, τ_ν is the total optical depth of the cell along that ray, and V is the volume of the cell. Since $\chi_{lu}(\nu)$ is simply $n_l a_{lu}(\nu)$, we see that the expression for J_ν that ensures consistency between radiative transfer and rate equations is

$$J_\nu = \frac{1}{4\pi V} \sum_{\substack{\text{ray} \\ \text{segments}}} \frac{\tilde{L}_\nu^{(\text{inc.})} (1 - e^{-\tau_\nu})}{\chi_\nu^{\text{tot}}}, \quad (3.25)$$

which is (as it must be) independent of the actual transition considered in the discussion above, and can be used to compute the photoionization rates of all elements and ionization stages (for more details see Weber et al. 2013).

The temperature structure of evolving H II regions. The assumption that in an H II region the heating and the cooling rates are in balance (as in the time-independent spherically symmetric approach presented in Sect. 3.3.1) and the temperature of the gas consequently remains constant is only valid for a steady-state H II region. However, in evolving H II regions the heating and cooling rates are in general not equal and the variation of the thermal energy content within the considered volume elements of the simulated gas has to be taken into account explicitly. Our simulations account for the photoionization of hydrogen and helium as heating processes. The photoionization heating rate (per volume) from a state l into the state u is

$$\Gamma_{lu}(m) = n_l \int_{\nu_{lu}}^{\infty} \frac{4\pi a_{lu}(\nu) h(\nu - \nu_{lu})}{h\nu} J_\nu(m) d\nu, \quad (3.26)$$

where n_l is the occupation number of the lower state l and $h\nu_0$ the ionization energy. Again we assume the nebular approximation that all ionization processes take place from the ground state of an ion.

The considered cooling processes are the radiative recombination of hydrogen (Hummer 1994) and helium (Hummer 1994, Hummer & Storey 1998), as well as the radiative decay of collisionally excited ions.²² Furthermore, the simulations account for the cooling by free-free radiation (Osterbrock & Ferland 2006).

The heating and cooling rates are used to compute the change of the thermal energy content of the gas within a grid cell m . The temperature $T(m)$ of the gas in a cell m is computed from the total content of thermal energy $E_{\text{therm}}(m)$ in that cell by

$$\begin{aligned} \frac{3}{2} N_{\text{part}}(m) k T(m) &= \frac{3}{2} V n_{\text{part}}(m) k T(m) = E_{\text{therm}}(m), \\ T(m) &= \frac{2 E_{\text{therm}}(m)}{3 V n_{\text{part}}(m) k}. \end{aligned} \quad (3.27)$$

Here $N_{\text{part}}(m)$ is the number of gas particles (electrons, atoms, and ions) within a grid cell, $n_{\text{part}}(m)$ the number density of the particles, and $V(m)$ the volume of the grid cell. After each time step Δt , the thermal energy $E_{\text{therm}}^{\text{new}}(m)$ is recomputed as

$$E_{\text{therm}}^{\text{new}}(m) = E_{\text{therm}}^{\text{old}}(m) + (\Gamma(J_\nu(m)) - \Lambda(n_e(m), T(m))) \cdot V \cdot \Delta t, \quad (3.28)$$

²²For references concerning the collisional processes in the relevant ions, see Sect. 3.3.1.1. The values for neutral hydrogen were obtained from Anderson et al. 2000.

where

$$\Gamma(J_\nu(m)) = \sum_i n_i \Gamma_i(J_\nu(m))$$

and

$$\Lambda(n_e(m), T(m)) = \Lambda_{\text{ff}}(n_e(m), T(m)) + \sum_i n_i \Lambda_i(n_e(m), T(m))$$

are the total heating and cooling rates per volume unit. The summations are carried out over all ionization stages i , where n_i are the number densities of the ions. The heating and cooling rate coefficients, $\Gamma_i(J_\nu(m))$ and $\Lambda_i(n_e(m), T(m))$, depend in turn on the radiation field described by the mean intensity J_ν , on the electron density n_e , and the temperature T within a given grid cell. The free-free cooling rate is denoted by Λ_{ff} , Δt is the length of a time step, and $E_{\text{therm}}^{\text{old}}(m)$ is the thermal energy content of the cell m before the time step. The rates Γ_i and Λ_i already include the contributions of the different heating and cooling processes connected to an ionization stage i .

Computing synthetic images. Images of gaseous nebulae show 2D projections of the 3D emission pattern of these objects. To link the results of our simulations with possible observations we create synthetic images that can be compared with narrow-band images taken in the wavelength range around diagnostically important emission lines.

The dilute gas found in H II regions is almost transparent for the radiation of lines in the visible or infrared part of the spectrum if they are either emitted during the transition to a non-ground-level state (e.g., the lines of the Balmer series of hydrogen) or by a forbidden transition into a ground-level state (e.g., the forbidden line of O II at 3729 Å). If the absorption and scattering terms are negligible, the intensity of the radiation at a given wavelength is given by

$$I_\nu = \int_{s_c}^{s_d} \eta_\nu(s) ds. \quad (3.29)$$

Here η_ν is the emissivity of the medium and the integration over s along the line of sight is carried out between the point closest to the observer, s_c , and the point most distant from the observer, s_d . We consider the frequency-integrated intensities \bar{I} and emissivities²³ $\bar{\eta}$ of the examined emission lines because the wavelength resolution in the 3D radiative transfer is not sufficient to resolve the line profiles. The number of emitted photons dN per solid angle $d\Omega$, detector surface dA , and time dt therefore is

$$\frac{d^3 N}{d\Omega dA dt} \approx \frac{\bar{I}}{h\nu_0} = \int_{s_c}^{s_d} \frac{\bar{\eta}(s)}{h\nu_0} ds \quad (3.30)$$

for each of the considered lines, where ν_0 is the frequency of the center of the line. In our discretization scheme the integration along the line of sight is replaced by a summation of the emissivities multiplied by the lengths $\Delta s(m)$ of the ray segments through the cells.

The small-angle approximation that the rays connecting the observer and all parts of the emitting regions are parallel can be used if the emission regions are small compared to their distance from the observer (as we assume in our simulations). In our case the summation is carried out along one of the coordinate axes (Fig. 3.2).

²³The frequency-integrated emissivity of a line within a cell is computed as $\bar{\eta}(m) = \frac{1}{4\pi} \frac{dE(m)}{dt dV}$. Here $dE(m)$ is the energy of the line emission in the time interval dt per volume dV . The numerical values for the emission of the recombination lines of hydrogen and helium are based on data given in Osterbrock & Ferland (2006), while the computation of the emission of collisionally excited lines corresponds to the computation of the cooling by these lines as described in Sect. 3.3.1.1.

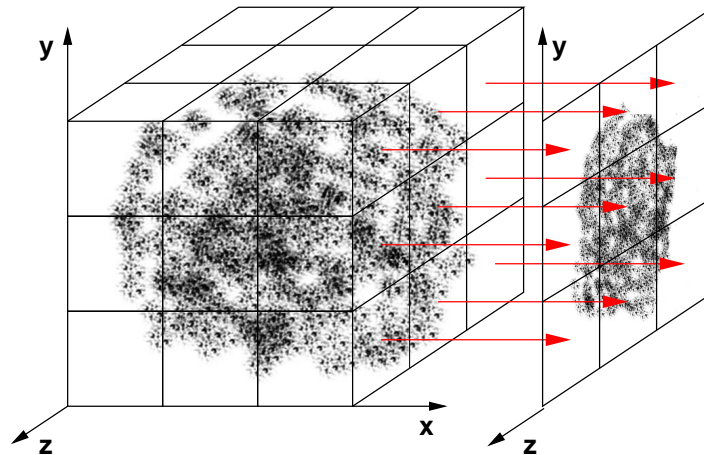


Figure 3.2: 2D projections of the calculated 3D structures represent synthetic images. The synthetic images of the strengths of emission lines are generated by integrating the emissivities along one of the coordinate axes (in the picture shown along the x -axis).

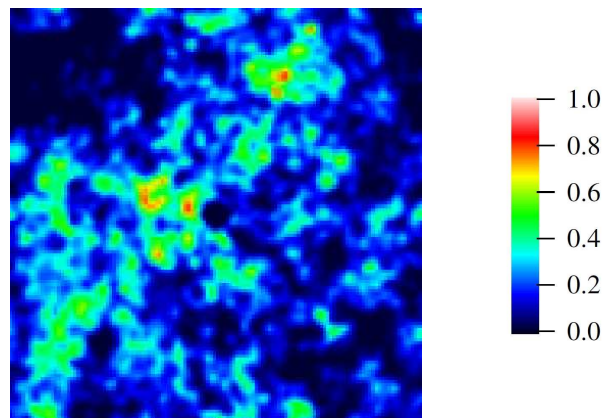


Figure 3.3: Cross section through a region of inhomogeneously distributed gas with a fractal density distribution (scaled to 50 hydrogen atoms per cm^{-3}) which is used for the 3D simulations shown in Figs. 3.4 to 3.9. The volume has a size of $(40 \text{ pc})^3$ and is resolved into 101^3 grid cells.

3.3.2.2 Applications of the three-dimensional approach for the simulation of H II regions around hot stars

The presented 3D approach is now applied to examine various aspects of the interaction between hot stars and inhomogeneous H II regions which have been outlined in the introduction of Sect. 3.3.

Comparison between homogeneous and inhomogeneous H II regions. First we use our procedure to simulate the interaction of the radiation field of hot stars and the inhomogeneous H II regions surrounding these stars. The inhomogeneous H II models are based on a fractal density distribution similar to the distributions that have been used to describe the interstellar gas by Elmegreen & Falgarone (1996) and by Wood et al. (2005). The results are then compared with the ionization structures and emission properties of homogeneous H II regions with the same mean densities, metallicities, and sources of ionization.

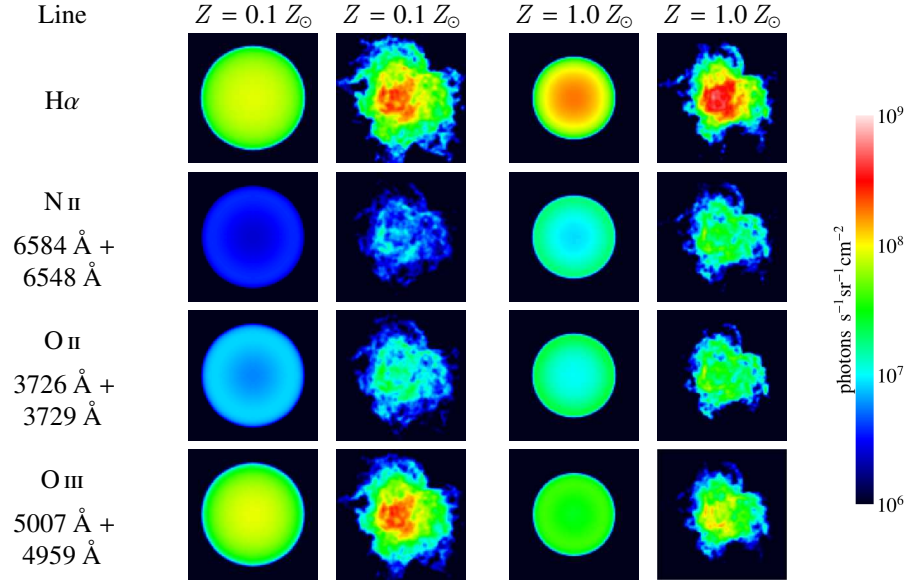


Figure 3.4: Synthetic images indicating the distribution of the emission line strengths of H α , [N II] 6584 Å + 6548 Å, [O II] 3726 Å + 3729 Å, and [O III] 5007 Å + 4959 Å for two different values of the metallicity ($0.1 Z_{\odot}$ and $1.0 Z_{\odot}$). Compared are cases where the gas is spherically symmetric with a homogeneous density structure ($n_{\text{H}} = 10 \text{ cm}^{-3}$) and cases where the gas is fractally structured with an inhomogeneous density structure of the same mean density. The source of ionization is located in the center of the simulated volume ($[40 \text{ pc}]^3$) and is represented by the respective 40 000 K dwarf star (D-40) at the same metallicity as the gas (Sect. 3.2.2).

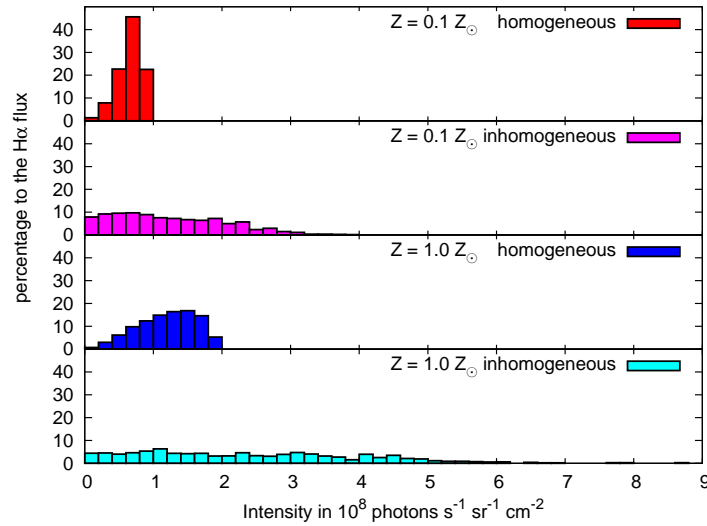


Figure 3.5: The synthetic images based on the fractally structured H II regions shown in Fig. 3.4 reveal not only considerably different distributions of the emission line strengths, but also of the intensity patterns compared to those of the corresponding homogeneously structured H II regions. The histograms illustrate this behavior for the H α line by showing the contribution to the total H α flux of all (projected) cells in a given intensity bin. While for the homogeneous gas (red/blue) the photon distribution is characterized by a pronounced peak near its maximum value, reached for the line of sight through the center of the H II region, a broader distribution is obtained for the inhomogeneous models (magenta/cyan), where the maximum values are approximately a factor of 4 larger, resulting from lines of sight through dense clumps. The histograms also reveal that the highest photon-numbers of the $0.1 Z_{\odot}$ models are lower than those of the corresponding $1.0 Z_{\odot}$ models. This behavior is due to the lower temperature levels that are obtained for gases of higher metallicities and which result in higher recombination rates and thus in smaller ionized volumes (Sect. 3.3.1.2).

In the inhomogeneous models, the mean number density of hydrogen is set to 9 cm^{-3} for the fractal structures in the simulations. Additionally, the simulated gases contains a homogeneous fraction of 1 cm^{-3} . The total number densities n_{H} of hydrogen atoms vary between 1 cm^{-3} (where the contribution of the fractal density field is zero) and 93 cm^{-3} . The density distribution of the gas is also characterized by the clumping factor $f_{\text{cl}} = \langle n_{\text{H}}^2 \rangle / \langle n_{\text{H}} \rangle^2$ of ≈ 1.75 and the standard deviation of the hydrogen number density $(\langle n_{\text{H}}^2 \rangle - \langle n_{\text{H}} \rangle^2)^{1/2} = 8.7 \text{ cm}^{-3}$. In Fig. 3.3 we show the number density of hydrogen for the mid-plane of the simulated volume, which in the presented simulations contains the source or sources of ionization. As the recombination and collisional excitation rates are proportional to the product of the number densities of the corresponding ions and the number density of electrons, they are approximately proportional to the square of the hydrogen number density in the ionized volumes. In the simulated inhomogeneous volume of gas the line emission per volume unit of the gas thus differs by more than 3 dex for a given temperature and number ratio of the ions. For this density structure we perform simulations of H II regions around 40 000 K dwarf stars with metallicities of $0.1 Z_{\odot}$ and $1.0 Z_{\odot}$, where the relative metallicity in the gas of the H II regions is the same as in the stellar atmospheres and the metallicity is assumed to be constant within the simulated volume.

The ionization fractions within the simulated volume, the total emission of some diagnostically important optical lines, and the maximum intensities for these lines in the synthetic images of the simulated H II regions are compared in Table 3.7. We find that the ratio between the number fractions of ionized hydrogen in the homogeneous and in the inhomogeneous models is approximately 1.6, which roughly agrees with the clumping factor. This behavior is a result of the proportionality of the recombination rates and the square of the gas density. By definition the mean square of the hydrogen density in the inhomogeneous case exceeds the mean square of the hydrogen density in the homogeneous case by the clumping factor. Consequently, a smaller number fraction of ionized hydrogen results for identical sources of ionization. Likewise, the clumping increases the neutral fraction for the other considered elements.

Figure 3.4 shows the projected images of the resulting photon emission rates $\bar{I}/h\nu_0$ of the H α line and of the collisionally excited lines of [N II] 6584 Å + 6548 Å, [O II] 3726 Å + 3729 Å, and [O III] 5007 Å + 4959 Å. In the homogeneous case the density of the electrons and hydrogen ions varies only marginally over most of the ionized volume. The emission of the H α line, which in the temperature range found in typical H II regions is primarily a recombination line, consequently shows little structure apart from a decrease from the center to the border of the Strömgren sphere, which is a geometrical effect – the length of a path through a sphere decreases for larger impact parameters with respect to the source. In contrast, N II and O II primarily exist within the outer regions of the hydrogen Strömgren sphere. In the projected image of the line emission, this leads to a ring-like distribution of the projected emission line strengths. Figure 3.4 shows that for the inhomogeneous density structures the emission is more peaked around those lines of sight that intersect the density maxima (“clumps”).

How regions with different intensities in Fig. 3.4 contribute to the total flux is shown in the histograms in Fig. 3.5, using the H α line emission as an example. The histogram covers the range for the values of $\bar{I}/h\nu_0$ which appear in our synthetic images with 50 equidistant bins from 0 to $9 \cdot 10^8 \text{ photons s}^{-1} \text{ sr}^{-1} \text{ cm}^{-2}$. For each bin we add up the contribution to the total flux of all pixels whose intensities lie within the corresponding intensity intervals. In the homogeneous models the highest H α intensities are reached for the lines of sight around the center of the ionized volume, while for the inhomogeneous models there is a broader distribution of the intensities. The histogram shows that for the inhomogeneous models the largest intensities exceed the largest intensities for the homogeneous case by a factor of about 4 to 5. Table 7 shows that similar factors also occur for the maximum intensities of the considered collisionally excited lines. Moreover, the contribution of high intensities for $1.0 Z_{\odot}$ is larger than for $0.1 Z_{\odot}$ in the homogeneous and in the inhomogeneous case. The rea-

Table 3.7: Comparison of ionization structures and emission properties of the homogeneous and inhomogeneous H II regions shown in Fig. 3.4. In addition to the integrated ionization fractions of important elements we present the total luminosities of several observationally important lines and give for each of these lines the maximum intensity reached along the lines of sight.

	0.1 Z_{\odot}				1.0 Z_{\odot}			
	homogeneous		fractal		homogeneous		fractal	
integrated ionization fractions in %								
	I	II	III	IV	I	II	III	IV
H	73.6	26.4			83.4	16.6		
He	72.1	27.9	0.0		82.1	17.9	0.0	
C	0.0	80.9	18.7	0.3	0.0	88.6	11.1	0.3
N	71.7	7.1	20.9	0.3	81.5	5.9	12.4	0.2
O	71.3	7.0	21.8	0.0	81.1	5.9	13.0	0.0
Ne	71.1	9.0	19.9	0.0	80.9	7.2	11.9	0.0
S	0.0	75.2	16.9	7.9	0.0	85.1	9.8	5.1
total line emission in units of 10^{37} erg s $^{-1}$								
H α		1.71			1.71			
[N II] 6584 Å + 6548 Å		0.10			0.11			
[O II] 3726 Å + 3729 Å		0.37			0.40			
[O III] 5007 Å + 4959 Å		1.98			1.84			
maximum line strength in units of 10^8 photons s $^{-1}$ sr $^{-1}$ cm $^{-2}$								
H α		0.88			3.95			
[N II] 6584 Å + 6548 Å		0.04			0.26			
[O II] 3726 Å + 3729 Å		0.09			0.55			
[O III] 5007 Å + 4959 Å		0.91			4.07			

son is that the recombination coefficient is larger and the ionized volume smaller owing to the lower temperatures for the larger metallicity (Sect. 3.3.1.2), which leads to a reduced ionized volume. The total H α emission is, however, nearly proportional to the number of ionization processes of hydrogen, which are almost the same in both models. As the same emission occurs in a smaller volume, larger intensities result. (The small differences between the hydrogen ionizing fluxes of the D-40 models at 0.1 Z_{\odot} and 1.0 Z_{\odot} are of minor importance.)

Temporal behavior of the ionization and temperature structure in model H II regions We next investigate the time-dependence of the ionization and the temperature structure of the gas during the expansion of H II regions into previously neutral interstellar gas with a fractal density structure. These simulations were performed for the 40 000 K dwarf stars with metallicities of 0.1 Z_{\odot} and 1.0 Z_{\odot} (the metallicities within the gas of the H II regions match the metallicities in the stellar atmospheres). In these simulations the total mass density of the gas in each cell is assumed to remain constant.²⁴

²⁴In our simulations we do not consider the advection of matter, i.e., we neglect velocity fields in the H II regions. Furthermore, we assume that the sources are created instantaneously, i.e., we do not account for stellar evolution. While stellar evolution processes are obviously not negligible for actual H II regions, the simulations using this approximation neverthe-

The results are presented in Figs. 3.6 and 3.7. In both cases the temperature increases quickly during the ionization process of previously neutral gas crossed by the ionization front. The heating rate is proportional to the number of ionization processes for a given ionizing spectrum. Therefore, the heating rate is increased until the gas is ionized to a large extent, such that it becomes optically thin for the ionizing radiation. Unlike the heating rates, the relevant cooling rates are approximately proportional to the square of the electron density, i.e., they continuously increase during the ionization process. Consequently, the cooling rates reach their maximum later than the heating rates and the rise in the temperature of the gas during the ionization process is followed by a decrease until the equilibrium temperature is reached. In the inner parts of the ionized region where the ionization timescale and consequently the heating timescale are considerably shorter than the recombination and cooling timescale, the temperature maximum reached depends on the ionizing SED rather than on the metallicity-dependent efficiency of the cooling within the gas. This overshooting effect of the temperature is more pronounced for the simulation of the H II region with solar abundance presented in Fig. 3.7 than for the metal-poor region in Fig. 3.6 because of the lower equilibrium temperature for the larger metallicity. When the ionized volume is close to its equilibrium value and the outer parts of the equilibrium Strömgren volume are ionized, the ionization process is slower than for the inner regions of the H II region because of the more dilute radiation field and the timescale for the heating process becomes comparable to the cooling timescale. As a result, the value of the temperature peak relative to the equilibrium value is lower than in the inner regions of the H II region.

The overshooting of the temperatures affects the emission spectrum of the expanding nebula such that the intensities of collisionally excited lines like the optical [O II] and [O III] lines decrease when the gas cools down. The effect is more pronounced for the gas with $1.0 Z_{\odot}$ (Fig. 3.7) than for the gas with $0.1 Z_{\odot}$ (Fig. 3.6).

A comparison of the temperature and the density of the ionized gas in the first two rows of Fig. 3.7 shows that the cooling process is faster for denser gas. For given temperature and ionization fractions, the thermal energy content increases linearly with the density of the gas. On the contrary, the cooling rates are approximately proportional to the square of the density and the cooling timescale is therefore roughly proportional to the inverse of the gas density.

Simulations of interstellar gas irradiated by clusters of hot stars. Finally, we want to see how these results change if we replace the single star in the previous models by a small cluster of stars and study the effects of a different spatial distribution of the stellar sources. The aim of this comparison is to get a rough idea of how the spatial distribution influences the total nebular emission, and we therefore simply use single stars as ionizing sources, and do not attempt to model a cluster SED via population synthesis.

We first assume that these stars are in close proximity to each other (which we realize by placing them in the same grid cell) and are formed instantaneously at the same time. For the composition of the cluster we assume three 30 000 K stars and two 35 000 K stars (models D-30 and D-35), which together have approximately the same quantity (89%) of the hydrogen-ionizing photon flux as our 40 000 K model dwarf star at solar metallicity, although the total luminosity of the cluster exceeds that of the 40 000 K model star by a factor of 2.8. We assume solar metallicity for both stars and gas.

The softer SED of the ionizing radiation of the cluster results in a considerably smaller fraction of N III, O III, Ne III, and S IV as a comparison of Tables 3.7 and 3.8 shows, although the similar hydrogen-ionizing fluxes (and the identical metallicity which results in comparable temperatures and consequently recombination rates) lead to almost identical hydrogen Strömgren volumina. In the temporal

less show the general behavior of gas crossed by an ionization front.

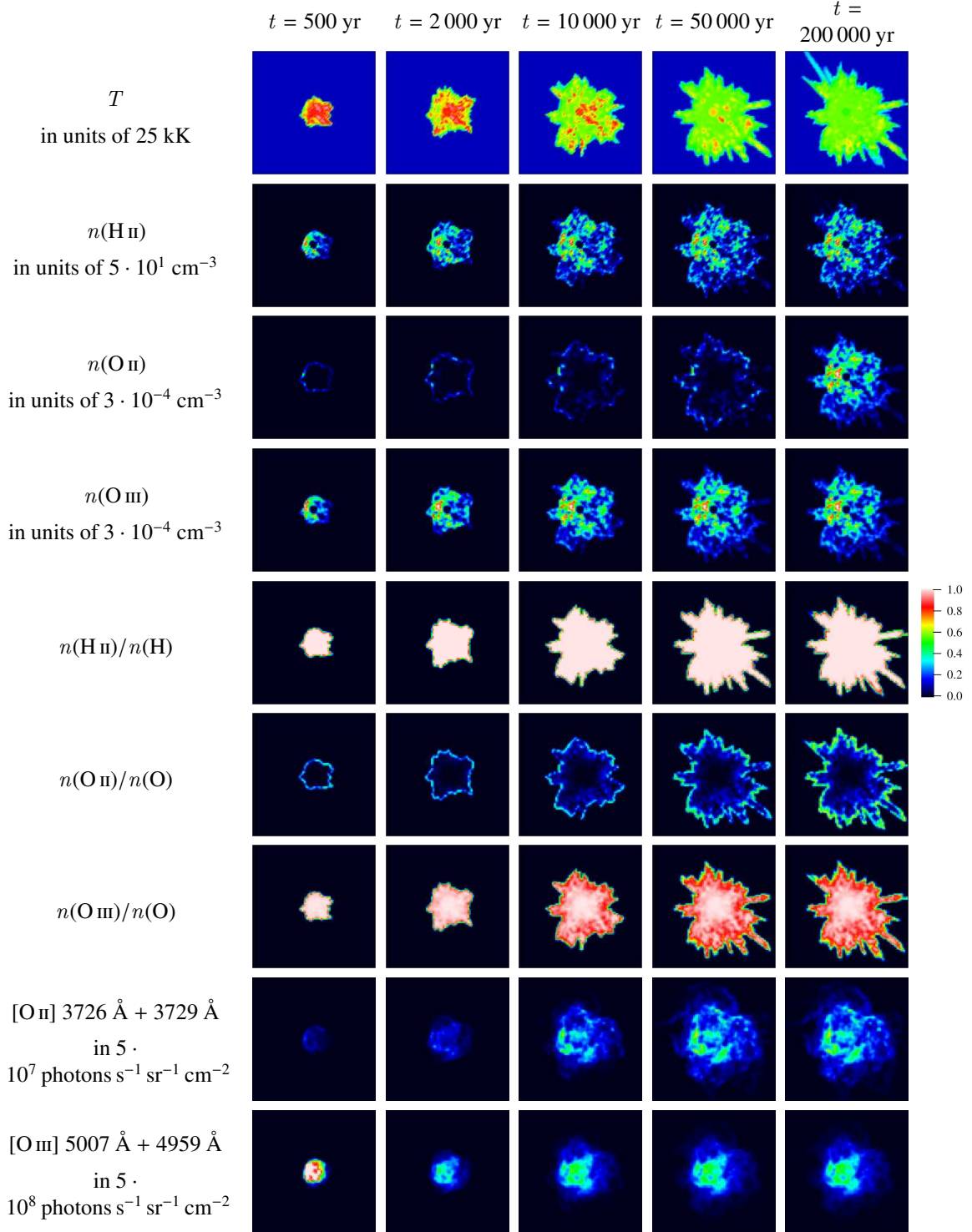


Figure 3.6: Temporal evolution of a H II region expanding in a volume of $(40 \text{ pc})^3$ filled with inhomogeneously distributed (initially neutral) gas. The top seven rows show cross sections through the center of the volume and show the temperature and the absolute as well as relative number densities of the ions H II, O II, and O III. The lower two rows show synthetic images of the line intensities of [O II] 3726 Å + 3729 Å and [O III] 5007 Å + 4959 Å. In these models, both the central ionizing star (a 40 000 K dwarf) and the gas have a metallicity of $0.1 Z_{\odot}$.

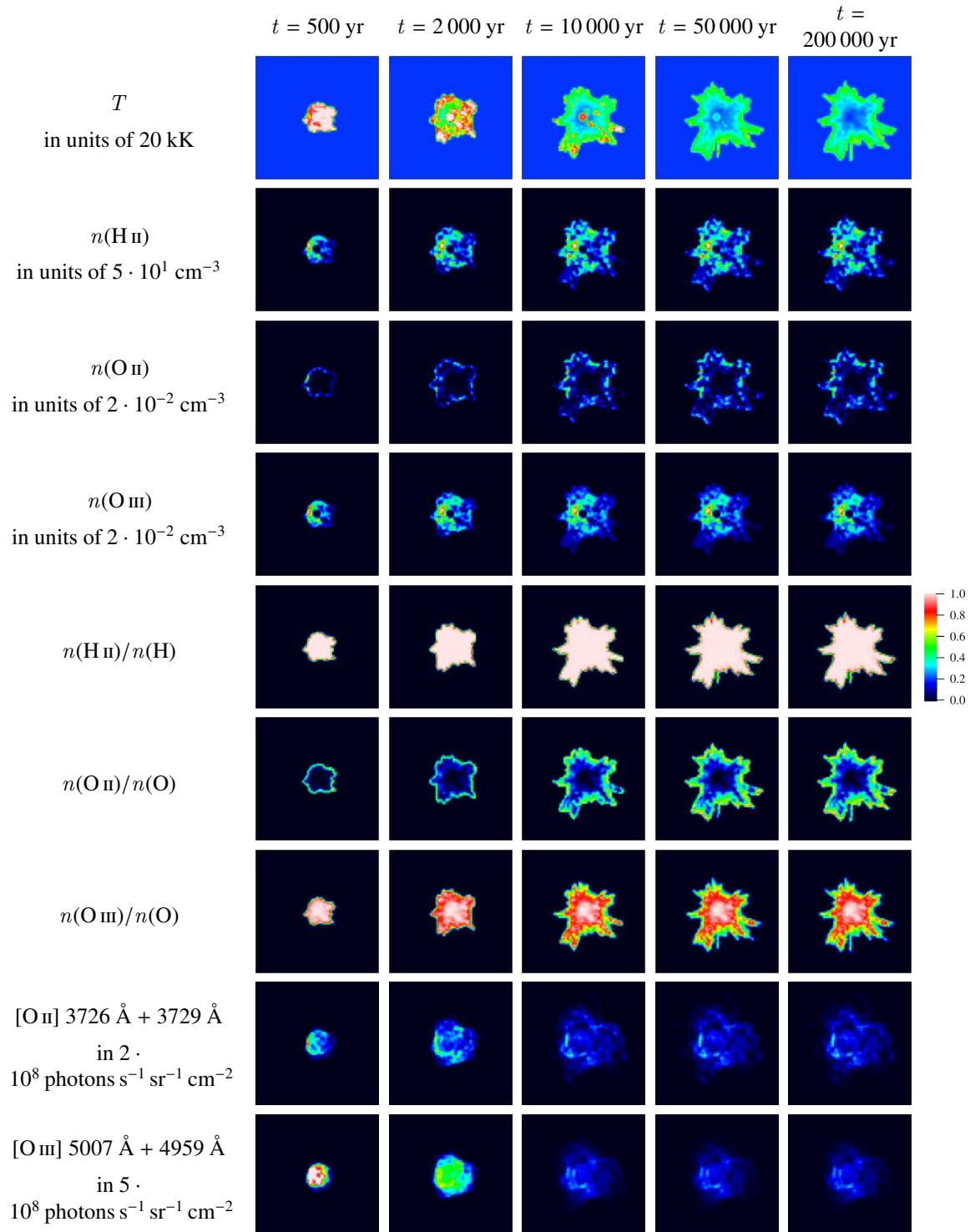


Figure 3.7: As Fig. 3.6, but a solar metallicity is assumed for both the gas of the H II region and the ionizing source.

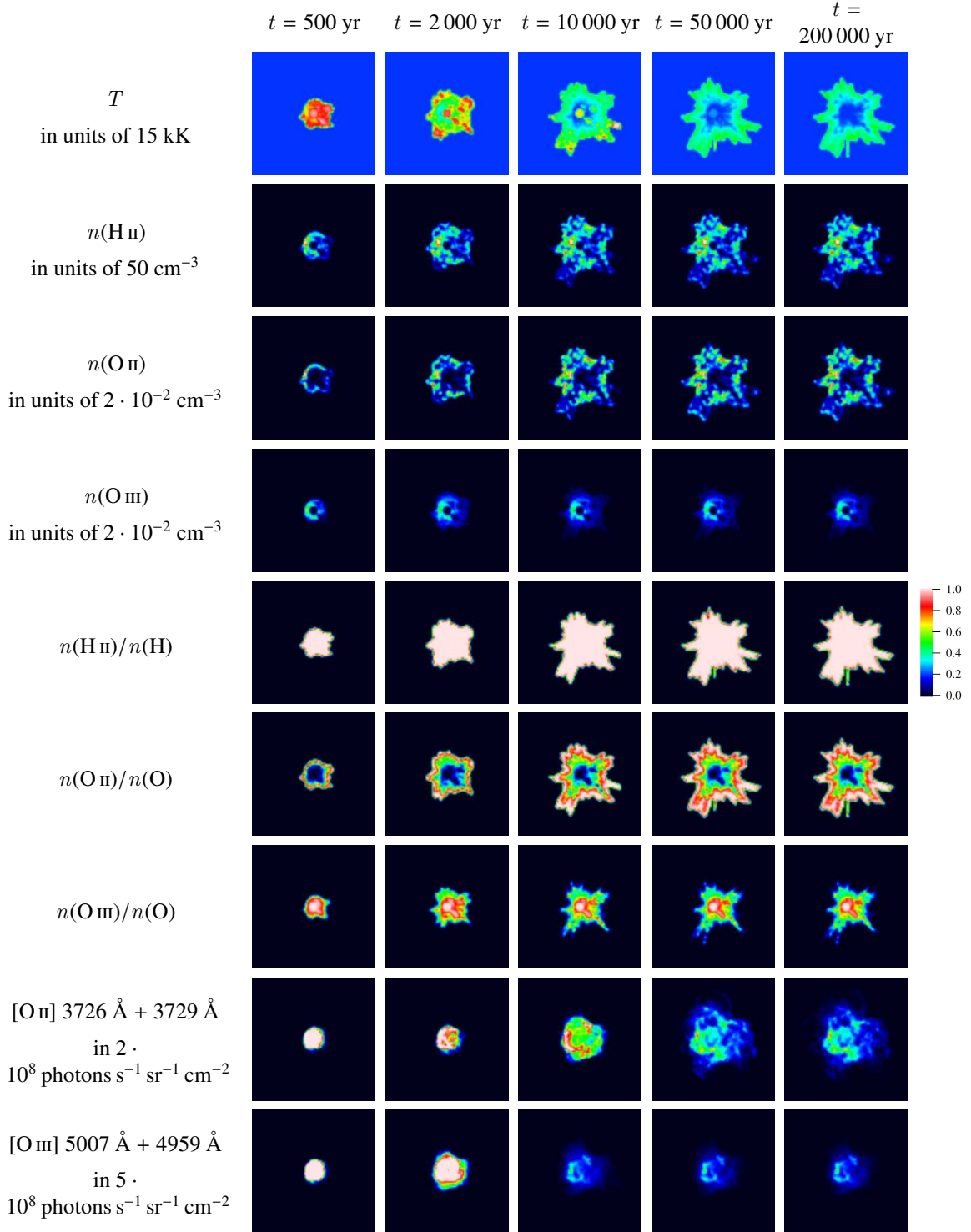


Figure 3.8: As Fig. 3.7, but instead of a single 40 000 K dwarf star, two 35 000 K dwarf model stars and three 30 000 K dwarf model stars ($1.0 Z_{\odot}$) are located in the center of the simulated volume. The total H-ionizing flux is 89% of the flux of the 40 000 K star with solar metallicity, resulting in a similar ionized volume, but because of the softer ionizing spectrum the fraction of singly ionized oxygen is larger than in the simulation with the 40 000 K star.

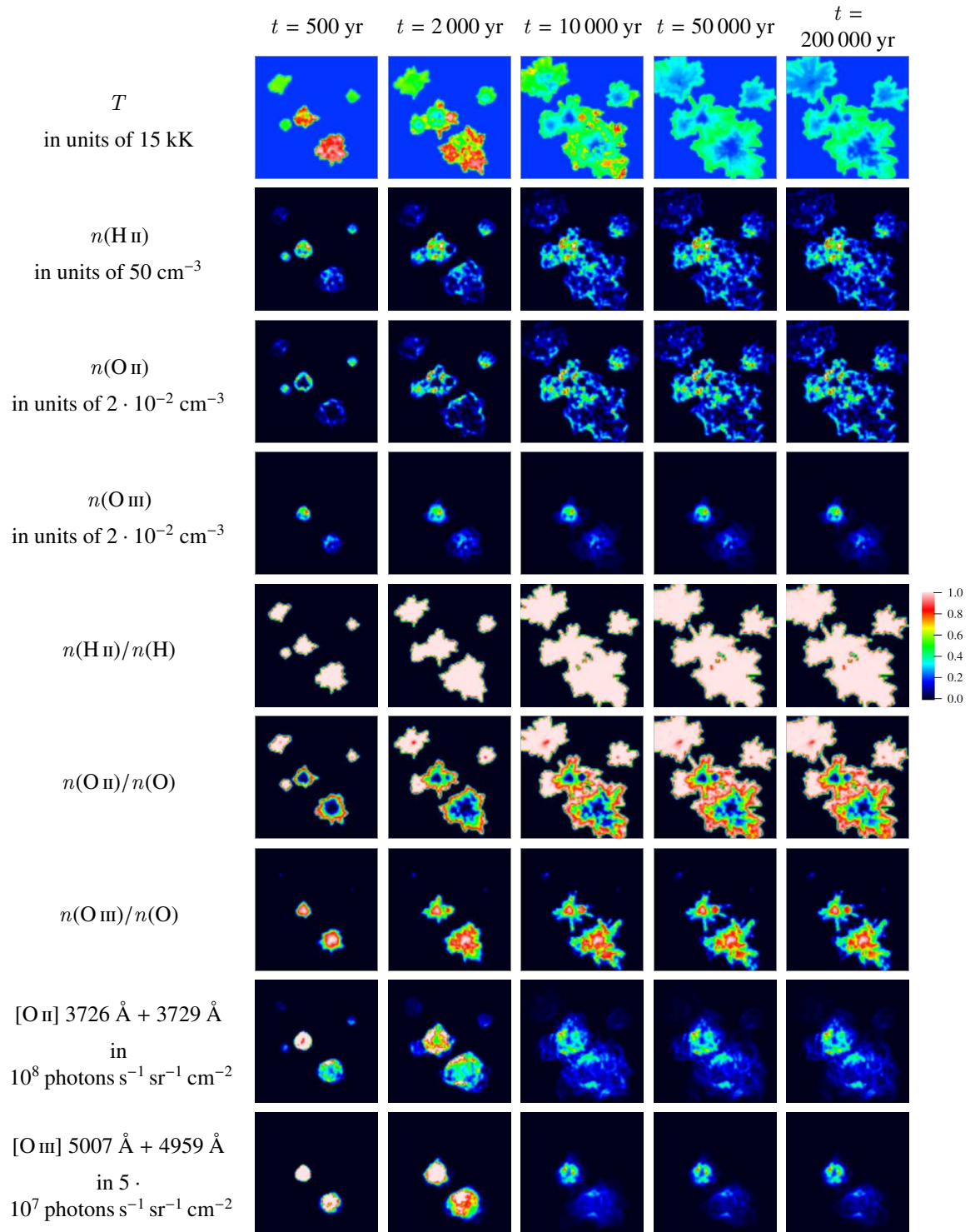


Figure 3.9: As Fig. 3.8, but here the distances between the ionizing stars are similar to the extent of the H II regions. The images show the expansion and the partial merging of the ionized volumes around these stars. The hotter (35 000 K) stars are recognized by the high temperature regions of the gas and those regions where O III is the dominant ionization stage of oxygen.

Table 3.8: Comparison of H II regions ionized by clusters with the same stellar content (two 35 000 K and three 30 000 K stars with solar metallicity), but different spatial distributions of the stars. In the first case, the distances between the stars are small when compared to the size of the Strömgren sphere. In the second case, the distances between the sources are similar to the diameters of the ionized volumes.

	dense cluster				sparse cluster			
integrated ionization fractions in %								
	I	II	III	IV	I	II	III	IV
H	91.5	8.5			90.0	10.0		
He	95.9	4.1	0.0		95.1	4.9	0.0	
C	0.0	97.9	2.1	0.0	0.0	97.9	2.3	0.0
N	90.9	7.0	2.1	0.0	89.1	8.6	2.3	0.0
O	90.9	8.1	1.0	0.0	89.2	9.7	1.1	0.0
Ne	91.4	8.4	0.1	0.0	90.2	9.7	0.1	0.0
S	0.0	93.7	6.2	0.1	0.0	93.4	6.4	0.1
total line emission in 10^{37} erg s ⁻¹								
H α		1.80				1.80		
[N II]		0.42				0.44		
[O II]		0.52				0.54		
[O III]		0.06				0.07		
max. line strength in 10^8 photons s ⁻¹ sr ⁻¹ cm ⁻²								
H α		8.49				7.92		
[N II]		1.66				1.30		
[O II]		1.19				1.00		
[O III]		0.43				0.49		

evolution there is an overshooting of the temperature of the gas passed by the ionization fronts like in our simulations containing single stars. The evolution of the ionized gas around this cluster is shown in Fig. 3.8.

The results for the ionization fractions and the line emission do not change significantly (i.e., by less than 15%) if the distances between the stars are increased even up to the typical sizes of the Strömgren spheres, such that no single H II region is formed, but the ionized volumes around the stars merge only partially (see Fig. 3.9).

As is expected from the different SEDs, the ionization structure of oxygen around the different types of stellar sources varies significantly among the single H II regions. In the regions around the 35 000 K stars O II is the most abundant ionization stage of oxygen up to approximately half the distance between the sources and the border of the hydrogen Strömgren volume. Around the 30 000 K stars, the volumes in which O III is more abundant than O II are too small to be spatially resolved within our simulation. This is in agreement with the ionizing fluxes presented in Table 3.4 and the results of the spherically symmetric H II region models in Sect. 3.3.1.2.

Spectroscopic signature of H II regions around very massive stars. The direct detection of very massive stars (Sect. 3.2.2) is a problematic procedure for two reasons. First, they are rare objects such

that even the closest of these objects are likely to exist only on extragalactic distance scales. Second, their occurrence is correlated with massive stellar clusters where they might form by stellar mergers (cf. Pauldrach et al. 2012), such that observations of distant objects are likely to suffer from crowding effects. In this section we therefore examine the possibility of identifying VMS by means of the emission spectrum of the surrounding H II regions. We simulate H II regions around the 45 000 K and 65 000 K stars with $M_* = 3000 M_\odot$, which represent the stars with the highest masses in our VMS grid, and the 40 000 K and 50 000 K stars with $M_* = 150 M_\odot$, which are close to the currently known upper mass limit of O stars. The luminosity has been chosen to correspond to a stellar content of $3000 M_\odot$, i.e., we simulate single $3000 M_\odot$ stars and clusters of twenty $150 M_\odot$ stars. The size of the simulation volume is $(400 \text{ pc})^3$. In the simulations all stars are located in the center of this volume. In Fig. 3.20 we show the emission line intensities for [O II] 3726 Å + 3729 Å, [O III] 5007 Å + 4959 Å, [O III] 88.3 μm, and [O IV] 25.9 μm.

The volume containing singly ionized helium is considerably smaller than the hydrogen Strömgen volume around the $3000 M_\odot$ model star with $T_{\text{eff}} = 45\,000 \text{ K}$ and solar metallicity because of the strong absorption within the stellar wind of this object (see Sect. 3.2.2). Outside the He I/He II Strömgen sphere no ionization stage of oxygen above O II is reached. Consequently, the [O II] 3726 Å + 3729 Å line emission exceeds the emission of the [O III] 5007 Å + 4959 Å lines, which is not the case for the other dwarf or supergiant models with $T \geq 40\,000 \text{ K}$. Both O II and O III exist in the part of the ionized volume where the predominant ionization stage of helium is He II, but the fraction of O III increases for higher effective temperatures of the ionizing stars. The O IV emission line at $25.9 \mu\text{m}$ and the He II recombination line at $\lambda = 4696 \text{ Å}$ are emitted by regions where helium is ionized to He III, i.e., around objects with large effective temperatures such as the 65 000 K model VMS. The latter lines have been detected in starburst galaxies (Lutz et al. 1998). Here hot ($T > 50\,000 \text{ K}$) very massive stars created by mergers in dense clusters may provide a complementary explanation to shocks (Lutz et al. 1998) or the photoionization by Wolf-Rayet stars (Schaerer & Stasińska 1999). The O IV line is, however, strongly metallicity-dependent as for lower metallicity there is a smaller number of potential emitters and the collisional excitation rate coefficient is reduced for larger temperatures of the metal-poor gas (Sect. 3.3.1.2). Therefore, the emission of the [O IV] by gas around very hot and very massive stars is more likely to be observed in an already chemically enriched environment.

3.4 Summary and conclusions

In this work we have presented state-of-the-art spectral energy distributions of hot, massive stars as a contribution to the study of the line emission from the ionized gas around stars and stellar clusters. Such H II regions are essential tracers for the state and evolution of galaxies because they are closely connected to star formation processes and their emission line spectra provide information about the chemical composition, the structure, and the dynamics of the interstellar gas in galaxies, but their spectra depend to a large extent on the SEDs of the ionizing stellar sources.

Our stellar model grid comprises O-type dwarf and supergiant stars with temperatures from 30 000 K to 55 000 K and metallicities between $0.1 Z_\odot$ and $2.0 Z_\odot$, representing the metallicity range of star-forming regions in the present-day universe. A comparison of the ionizing fluxes for different metallicities shows that even for the same effective temperature there are considerable differences (up to several orders of magnitude) in the emission rates of photons in the energy ranges required to produce key ionic species (such as O III or Ne III, which have important diagnostic lines). In most cases the fluxes in these energy ranges decrease with increasing stellar metallicities because of the enhanced line blocking in the atmospheres of the stars.

Additionally, we have computed the ionizing fluxes of very massive stars that possibly form through collisional mergers in dense massive clusters and may considerably exceed the mass limit of O-type stars forming directly from molecular gas clouds. For these objects we have considered masses from $150 M_{\odot}$ to $3000 M_{\odot}$ and temperatures from 40 000 K to 65 000 K.

We have used the SEDs in spherically symmetric photoionization models to gauge the effect of stellar and gas metallicity on the ionization structure of the H II regions. As expected from a direct assessment of the SEDs, for a given stellar effective temperature the integrated number fractions of the different ionization stages of the metals in the gas strongly depend on the metallicity-dependent SEDs for those species whose ionization energies lie above the ionization edge of He I. Even at the same metallicity and temperature, the results differ significantly between dwarfs and supergiants owing to the influence of the much stronger stellar winds of supergiants on the SEDs.

To judge the effects of an inhomogeneous distribution of the gas on the nebular line emission we have used our 3D radiative transfer code, augmented to account for the metals C, N, O, Ne, and S, to compute integrated line-of-sight intensities and synthetic narrowband images. Although an inhomogeneous density structure leads to higher peaks in the distribution of the observable line intensities for a given mean density of the gas, we find no relative changes above 20% in the total emission per line.

With regard to the temporal evolution of the ionization and temperature structure of the H II regions we find an overshooting of the gas temperatures significantly above the equilibrium value during the transition of the gas from initially neutral to ionized. However, because of the short timescales, and because in reality the ionizing sources themselves evolve, this is unlikely to be of practical significance for the analysis of H II regions with current models.

Finally, we have studied the effects of clustering of stars in two limiting cases, a dense cluster where the distances between the stars become irrelevant compared to the extent of the combined H II region, and a loose association where the distances between the stars are of the same order as the Strömgren radii, so that the individual H II regions only partly overlap. We find that the differences between the two models in the number fractions of the ionization stages and the total emission rates per line remain moderate – the total emitted fluxes of the considered emission lines differ by less than 10%.

Although spherically symmetric modeling of H II regions is still an important tool for determining the global properties of the ionized gas and for performing systematic examination of large sets of different input parameters, 3D radiative transfer models accounting for inhomogeneous density structures, several sources of ionization, and a time-dependent evolution of the ionized medium are able to provide additional information for studying H II regions in more detail. A comparison of the results from these models with narrow-band or spectrally resolved observations allows detailed information to be obtained about the internal structure of H II regions and about its relation to the ionizing stars.

3.5 Figures and model data

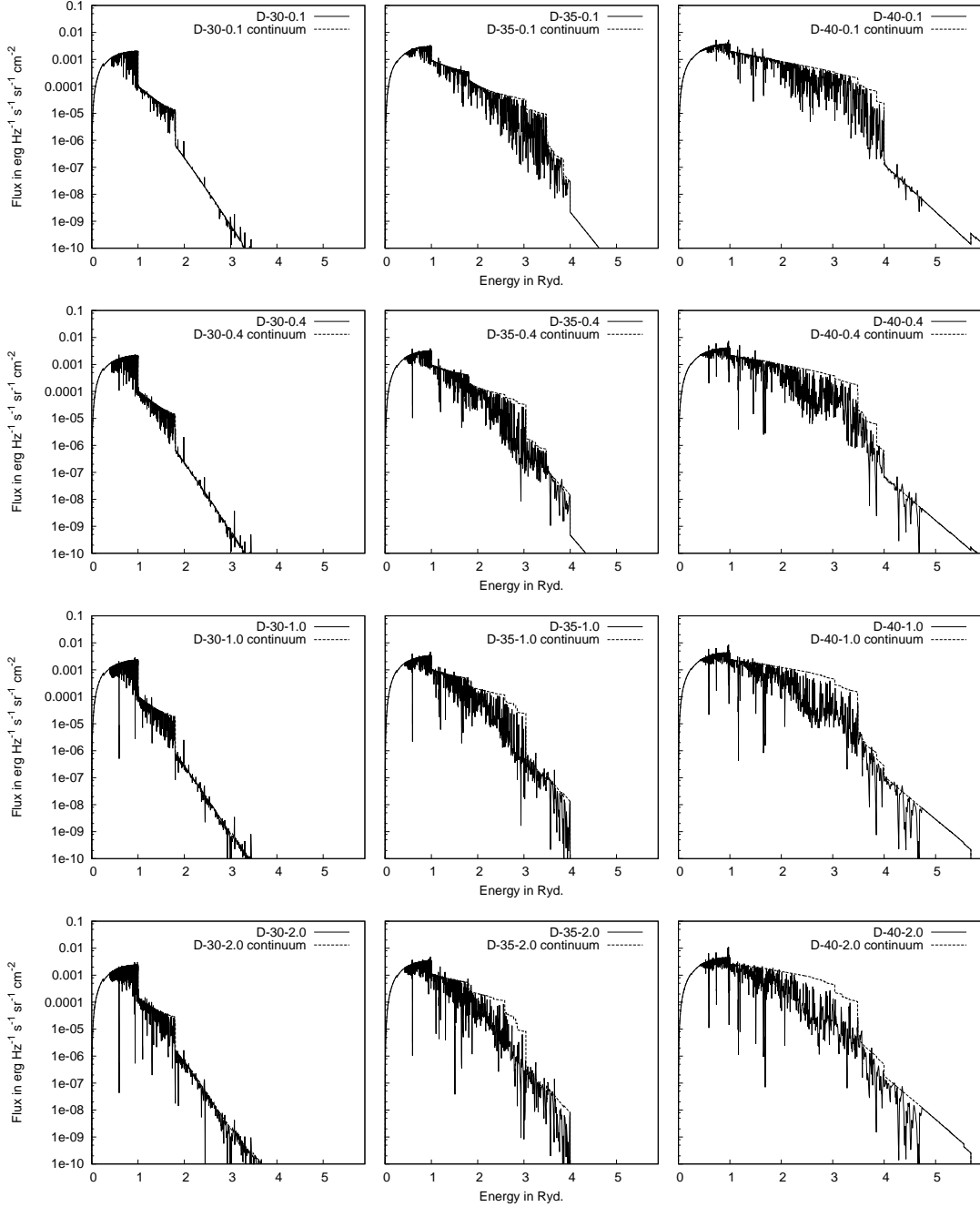


Figure 3.10: Computed spectra and corresponding continua (Eddington flux H_ν , in $\text{erg}/\text{cm}^2/\text{s}/\text{Hz}$ versus the photon energy in Rydberg) for the dwarf models at $T_{\text{eff}} = 30\,000\text{ K}$ (left column), $T_{\text{eff}} = 35\,000\text{ K}$ (middle column), and $T_{\text{eff}} = 40\,000\text{ K}$ (right column) and different metallicities (0.1, 0.4, 1.0, and 2.0 times the solar metallicity from top to bottom). The data can be copied from [D30-D40 model data]²⁵.

²⁵The four columns in the data file contain (from left to right) the wavelength in Angstroms (\AA), the Eddington flux H_ν , in $\text{erg}/\text{cm}^2/\text{s}/\text{Hz}$, the continuum flux in the same units, and the normalized spectrum that is obtained by dividing the second

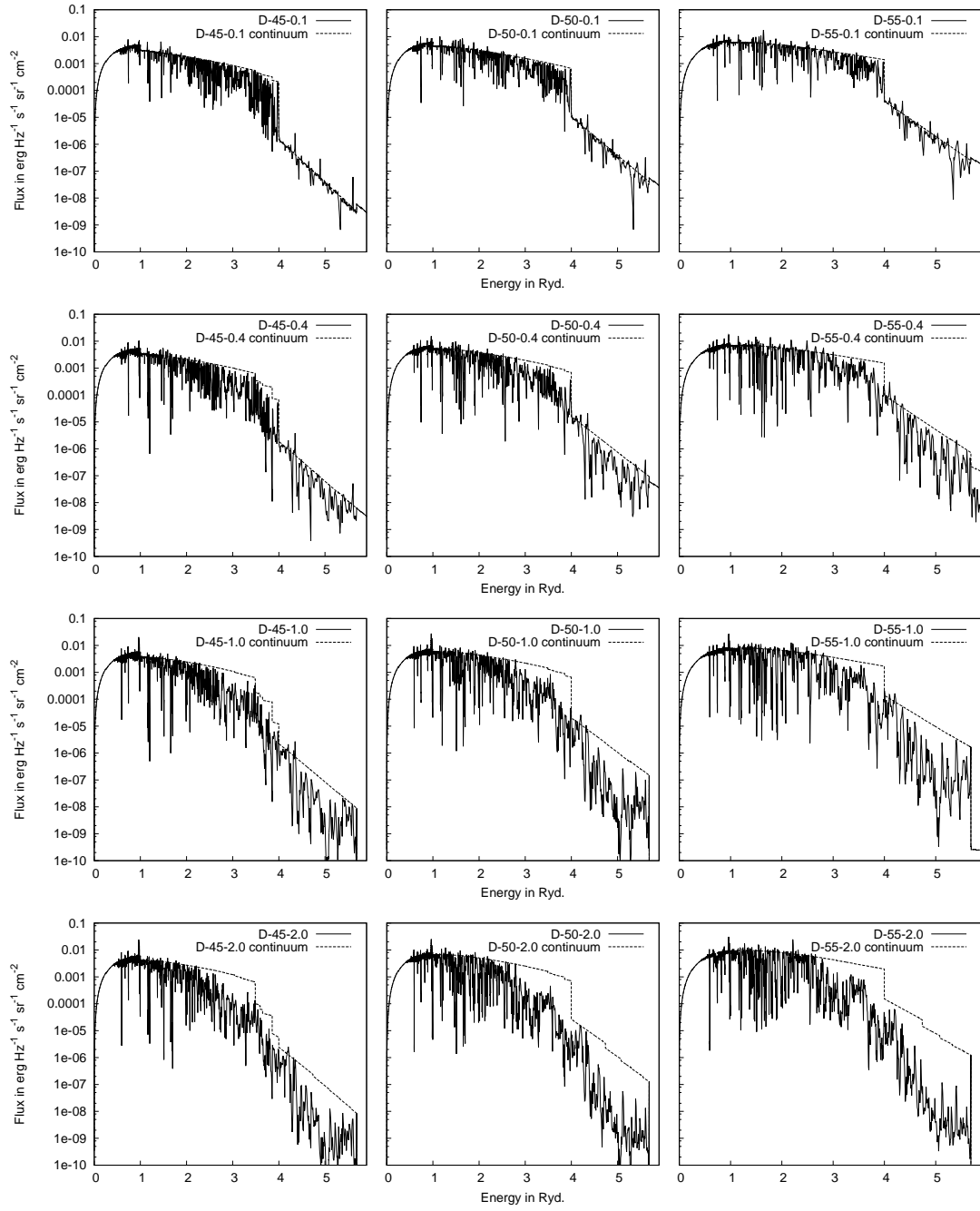


Figure 3.11: Same as Fig. 3.10 but for $T_{\text{eff}} = 45\,000\text{ K}$, $T_{\text{eff}} = 50\,000\text{ K}$, and $T_{\text{eff}} = 55\,000\text{ K}$. The data can be copied from [D45-D55 model data].

column by third column. The flux has been normalized to correspond to the effective temperature at the photospheric radius.

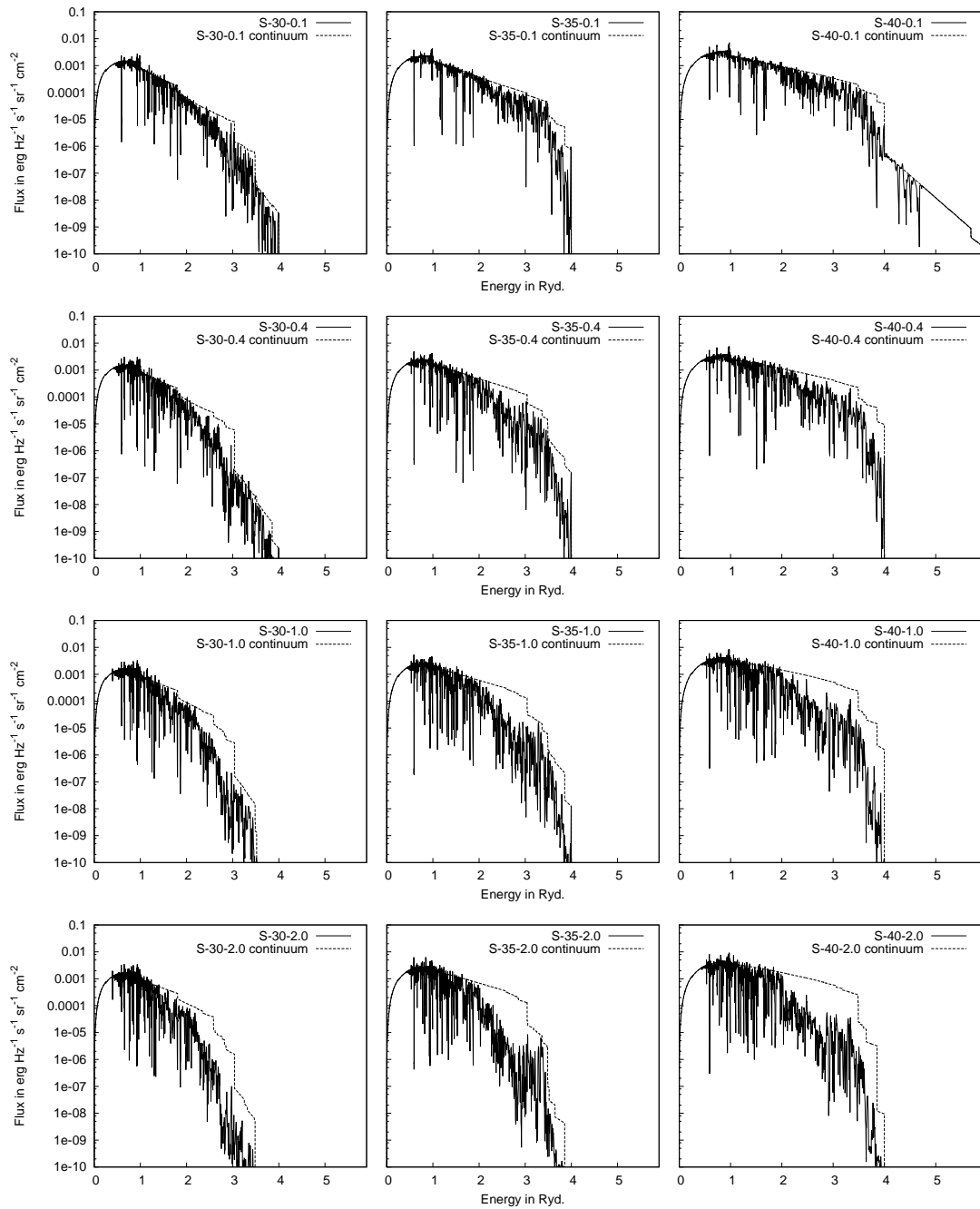


Figure 3.12: Same as Fig. 3.10 but for supergiant models with $T_{\text{eff}} = 30\,000$ K, $T_{\text{eff}} = 35\,000$ K, and $T_{\text{eff}} = 40\,000$ K. The data can be copied from [S30-S40 model data].

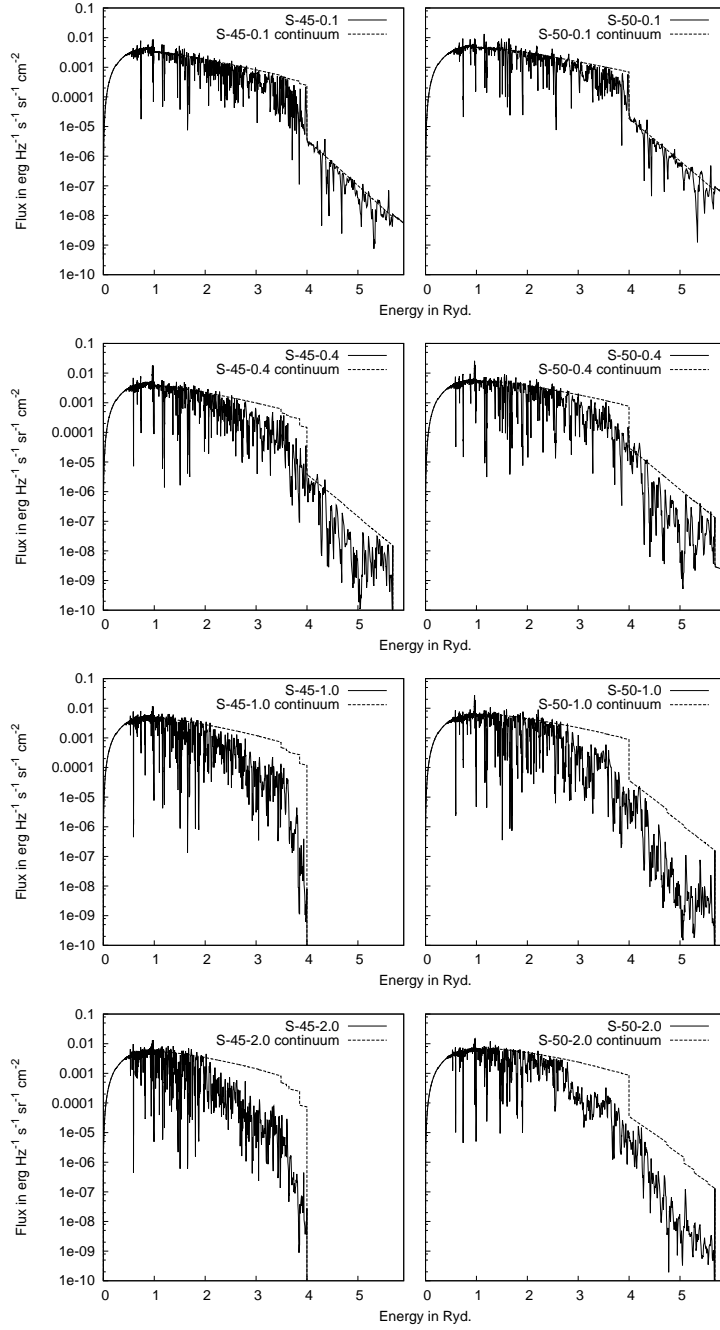


Figure 3.13: Same as Fig. 3.10 but for supergiant models with $T_{\text{eff}} = 45\,000\text{ K}$ and $T_{\text{eff}} = 50\,000\text{ K}$. The data can be copied from [S45-S50 model data].

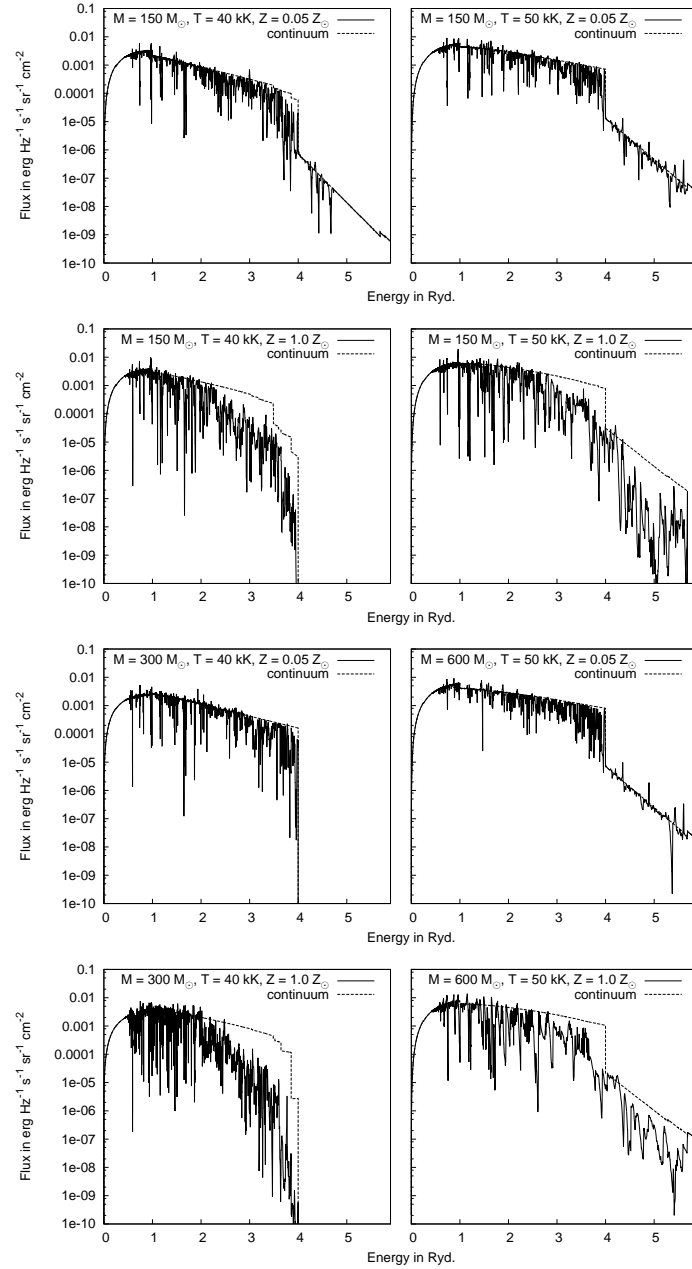


Figure 3.14: Same as Fig. 3.10 but for VMS models in the mass range between $150 M_{\odot}$ and $600 M_{\odot}$. The data can be copied from [M150-M600 model data].

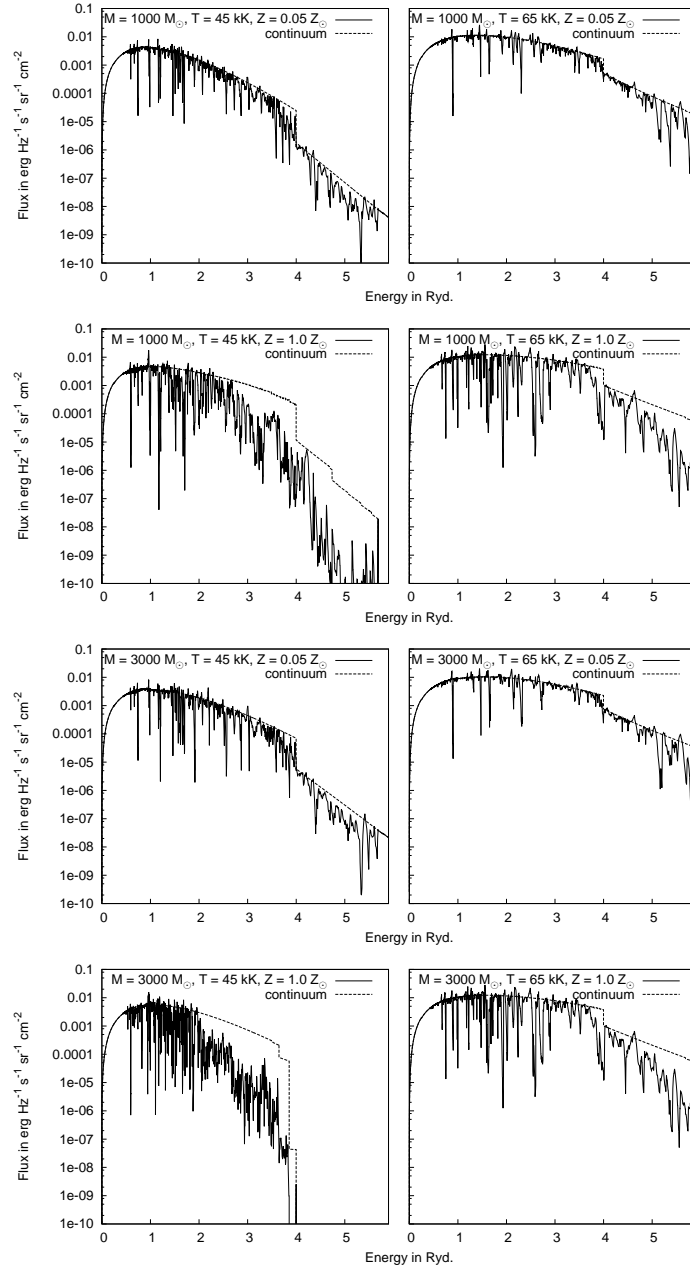


Figure 3.15: Same as Fig. 3.10 but for VMS models in the mass range between $1000 M_{\odot}$ and $3000 M_{\odot}$. The data can be copied from [M1000-M3000 model data].

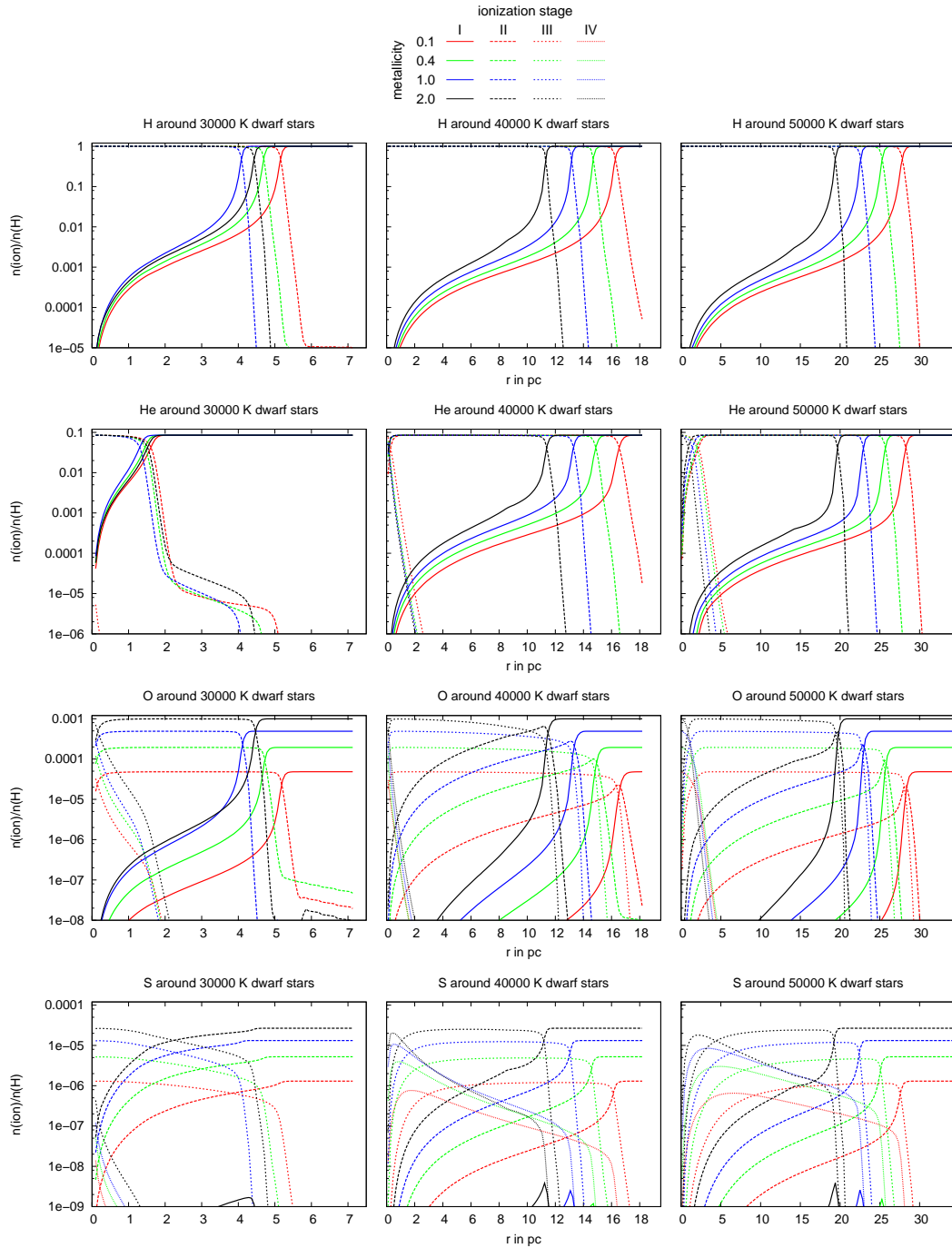


Figure 3.16: Ionization structures of hydrogen, helium, oxygen, and sulfur of H II regions around dwarf stars of effective temperatures of 30 000 K, 40 000 K, and 50 000 K at different metallicities (a homogeneous gas with a hydrogen particle density of 10 cm^{-3} and the same chemical composition as the central star is assumed). Because the number of hydrogen-ionizing photons varies only slightly for stars with the same effective temperature and luminosity class (Table 3.4), the larger hydrogen Strömberg radii obtained for lower metallicities are primarily caused by the larger temperatures of the gas, which in turn are caused mainly by the direct influence of the lower metallicities of the gas (see Fig. 3.18).

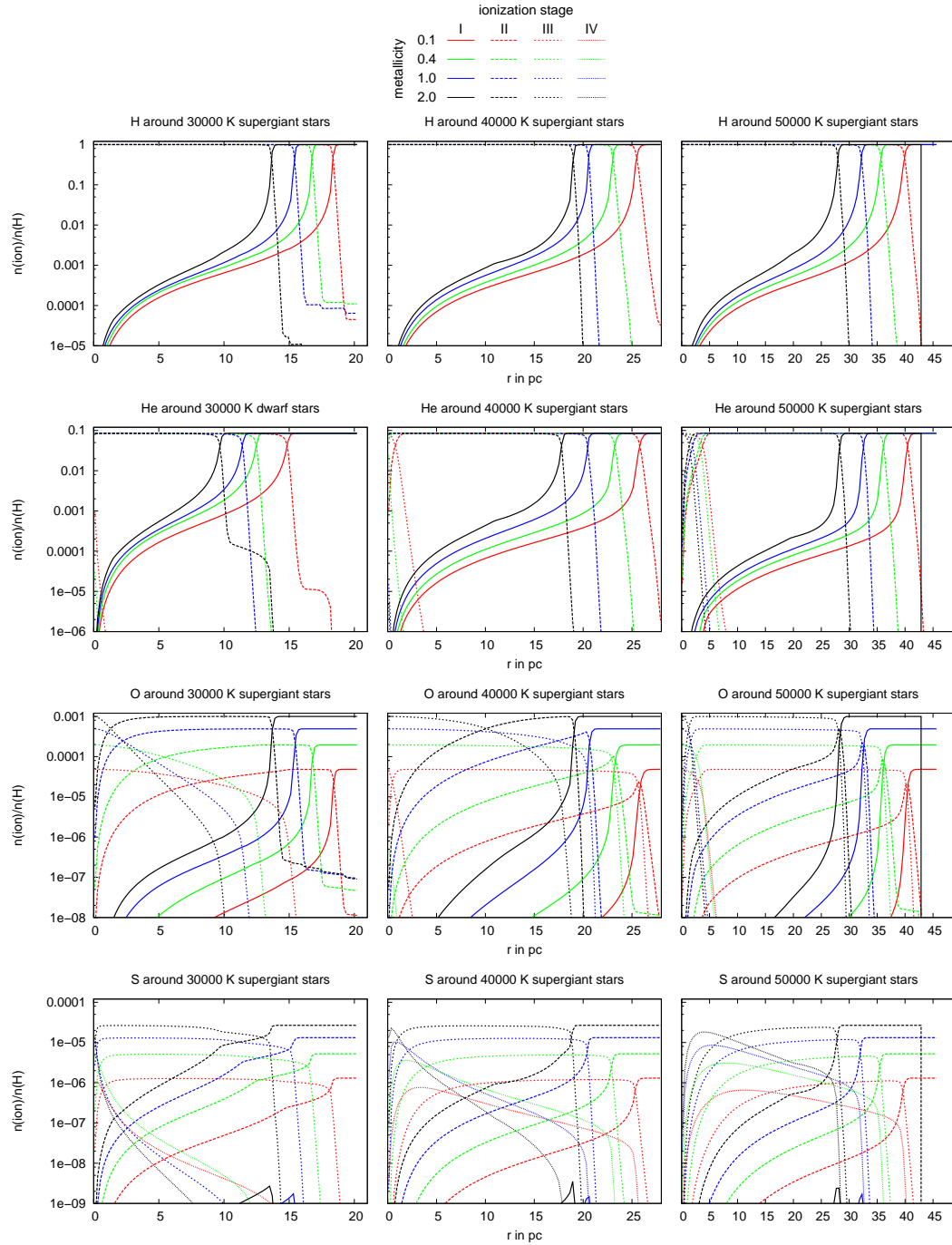


Figure 3.17: Same as Fig. 3.16, but using supergiants as ionizing sources.

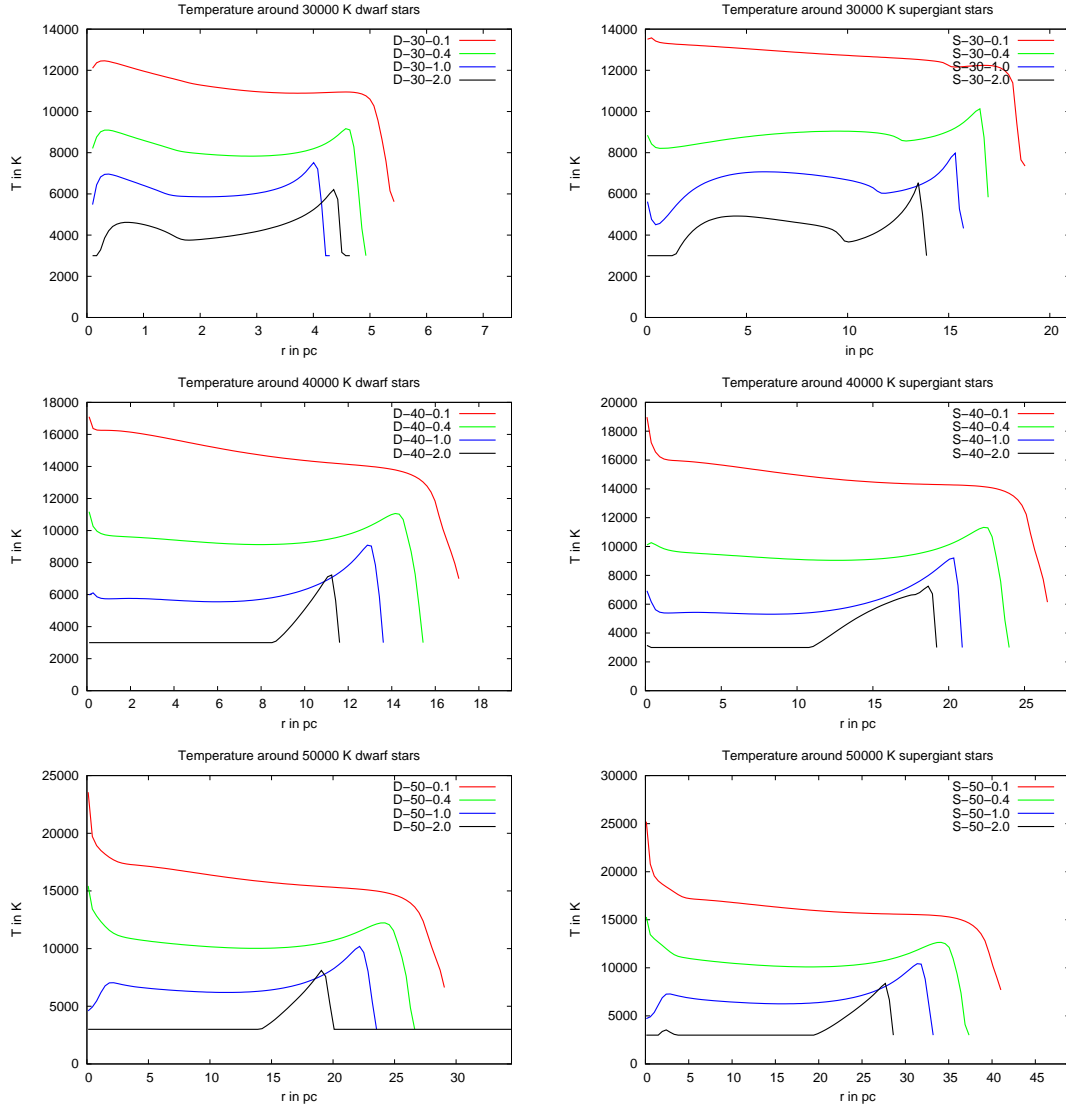


Figure 3.18: Temperature structures of H II regions around dwarf stars and supergiants of effective temperatures of 30 000 K, 40 000 K, and 50 000 K at different metallicities (using the same physical conditions for the gas as in Fig. 3.16). The influence of the metallicity on the temperature of the gas is primarily a result of the reduced number of metal particles that contribute to the cooling of the gas (metal-poorer H II regions are thus characterized by considerably higher temperatures than H II regions with larger metal abundances), but it is also a result of the harder ionization spectra obtained for metal-poorer stars (see Figs. 3.10–3.13), which results in a larger energy input by photoionization heating; the temperature of the gas therefore rises with decreasing metallicity of the irradiating stars (see also Fig. 3.19).

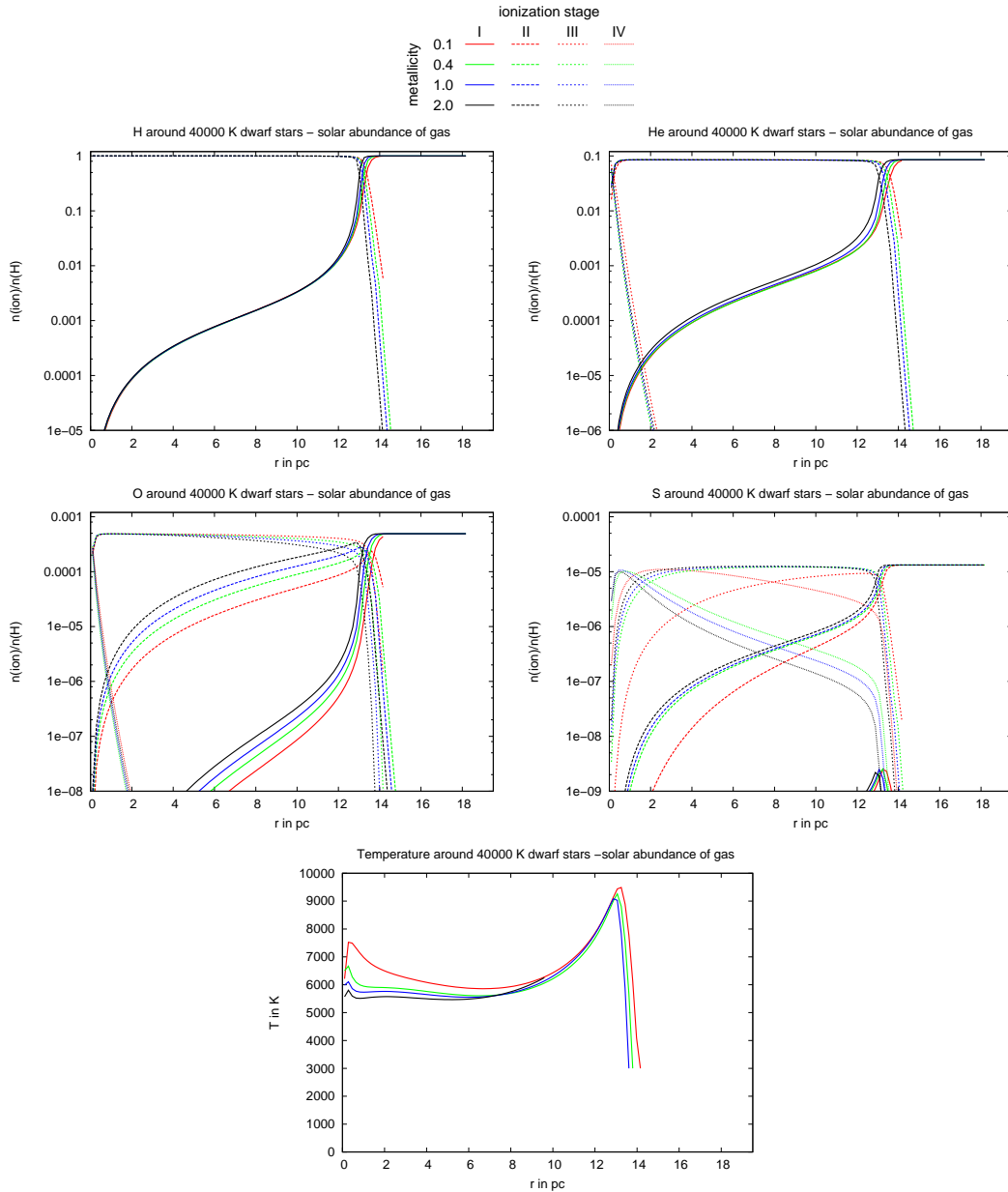


Figure 3.19: Comparison of the ionization structures of H, He, O, and S, and the temperature structure of H II regions for cases where the chemical composition of the gas is not the same as that of the irradiating star (for the gas a hydrogen particle density of 10 cm^{-3} and solar metallicity is assumed, whereas for the stars a 40000 K dwarf model with metallicity from $0.1 Z_{\odot}$ to $2.0 Z_{\odot}$ is used). In this way the influence of the metallicity-dependent ionizing spectra on the physical behavior of the gas can be investigated independently of the influence of the metallicity of the gas. As the stellar spectra differ for different metallicities especially in the energy range above the ionization edge of He I, the differences obtained for the ionization structures of O and S are more pronounced than those of H and He. These differences lead to enhanced ionization fractions of O II and S III for the spectra of low-metallicity stars, because the spectra of these stars are “harder” than those of high-metallicity stars of the same effective temperature (see Figs. 3.10–3.13). As a consequence of this behavior the temperature of the gas also increases, but this effect is smaller than in the case where the metallicity of the gas is the same as that of the star (Fig. 3.18).

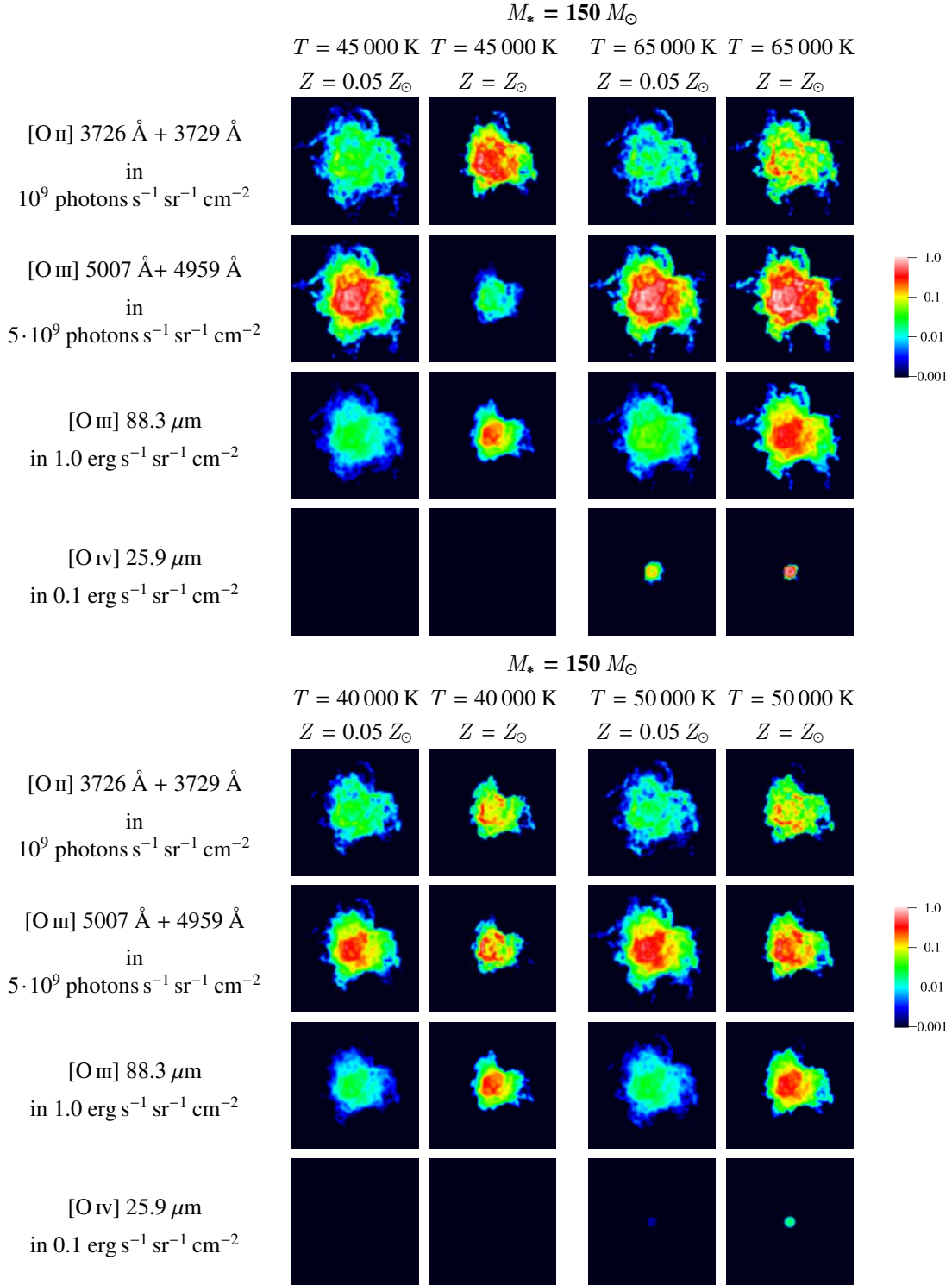


Figure 3.20: Synthetic images showing the intensities of important emission lines from various ionization stages of oxygen around very massive stars with metallicities of $0.05 Z_\odot$ and $1.0 Z_\odot$. Lower metallicity means lower densities of the metal ions in the gas, but the corresponding reduction of the optical emission lines is partly compensated by the higher temperatures and the resulting higher rate coefficients for collisional excitation. The values are shown using a logarithmic color scale because the emission line strengths vary strongly between the different models.

4 Numerical Models for the Diffuse Ionized Gas in Galaxies

II. Three-dimensional radiative transfer in inhomogeneous interstellar structures as a tool for analyzing the diffuse ionized gas¹

The diffuse ionized gas (DIG) constitutes the largest fraction of the total ionized interstellar matter in star-forming galaxies, but it is still unclear whether the ionization is driven predominantly by the ionizing radiation of hot massive stars, as in H II regions, or whether additional sources of ionization have to be considered. Key to understanding the ionization mechanisms in the DIG is the line emission by the ionized gas.

We systematically explore a plausible subset of the parameter space involving effective temperatures and metallicities of the ionizing sources, the effects of the hardening of their radiation by surrounding “leaky” H II regions with different escape fractions, as well as different scenarios for the clumpiness of the DIG, and compute the resulting line ratios for a number of diagnostic optical emission lines.

For the ionizing fluxes we compute a grid of stellar spectral energy distributions (SEDs) from detailed, fully non-LTE model atmospheres that include the effects of stellar winds as well as line blocking and blanketing. To calculate the ionization and temperature structure in the interstellar gas we use spherically symmetric photoionization models as well as state-of-the-art three-dimensional (3D) non-LTE radiative transfer simulations, considering hydrogen, helium, and the most abundant metals. We first apply these methods to classical H II regions around hot stars, using the model SEDs at different metallicities and effective temperatures as ionizing sources, and compute the spectral energy distributions of the escaping radiation for different escape fractions of hydrogen-ionizing photons. In a second step, we study the effects of the escaping radiation on the more dilute and extended DIG.

At one-tenth solar metallicity, radiation hardening by the H II regions surrounding the stars is mostly due to hydrogen and helium, whereas at solar metallicity absorption by metals plays a significant role. The effects of hardening are seen primarily in the increase (relative to H β) of the emission in the most important cooling lines of the gas, singly ionized nitrogen and oxygen at lower effective temperatures of the ionizing stars, and doubly ionized oxygen at higher effective temperatures. Particularly important in this regard is that for low effective temperatures nearly the entire He I-ionizing radiation is absorbed in the H II regions, thereby preventing the formation of high ionization stages like O III in the DIG. The ionization structure of the DIG depends strongly on both the clumping factor $f_{\text{cl}} = \langle n_{\text{H}}^2 \rangle / \langle n_{\text{H}} \rangle^2$ and the large-scale distribution of the gas. In our simulations about 10% of the ionizing radiation produced by hot massive stars is sufficient to ionize the DIG up to a height of

¹The content of this chapter has been submitted by **J. A. Weber**, A. W. A. Pauldrach, and T. L. Hoffmann to *Astronomy & Astrophysics*,

approximately 1 kpc above the galactic plane for a clumping factor close to the observed value of $f_{\text{cl}} \sim 5$. Even small changes in simulation parameters like the clumping factor can lead to considerable variation in the ionized volume. Both for a more homogeneous gas and a very inhomogeneous gas containing both dense clumps and channels with low gas density, the ionized region in the dilute gas above the galactic plane can cease to be radiation-bounded, allowing the ionizing radiation to leak into the intergalactic medium.

4.1 Introduction

Besides cool molecular or atomic clouds with temperatures of approximately ten to a few hundred K, the warm neutral gas, and the very hot and thin fraction of the interstellar gas with temperatures on the order of one million K, which is heated, for instance, by supernova shocks, the interstellar medium contains a component of ionized material with an intermediate temperature of $T \approx 10\,000$ K. One part of this component are H II regions around hot stars (dwarf or supergiant stars of the spectral classes O/B or central stars of planetary nebulae), but a significant amount of the mass and the line emission by intermediate-temperature gas is additionally contributed by dilute gas with a density of ~ 0.1 hydrogen ions per cubic centimeter, called *warm ionized medium* (WIM, often used when referring to gas in the Milky Way) or *diffuse ionized gas* (DIG, usually referring to the diffuse gas in other galaxies), which can be found – in contrast to H II regions immediately connected to star formation – at heights of up to a few kpc above the galactic plane.²

The nature of the energy sources that keep the DIG ionized is still not well understood. Photoionization by the radiation of the embedded sources is the dominant type of energy input for classical H II regions around hot stars; observations suggest that it also plays an important role for the ionization of the DIG.

For instance, Haffner et al. (1999) and Zurita et al. (2002) found a correlation between spiral arms and the presence of diffuse ionized gas. The ratio of the hydrogen recombination radiation photons originating from H II regions and the DIG has been determined observationally by Zurita et al. (2000), who found, based on an analysis of the observed emission measures in six nearby galaxies³, that the total emission from the DIG is in the range of approximately 30% to 70% of the emission originating from the denser H II regions. Assuming ionization of the DIG predominantly by photons leaking from H II regions, this would require about half of the ionizing photons to escape from these H II regions.

Some of the spectral features found in the DIG are, however, considerably different from the features of dense H II regions ionized by embedded hot stars. Observations of the warm ionized medium in our galaxy by Reynolds (1985) showed that the $[\text{O III}]/\text{H}\alpha$ line ratio is considerably smaller in the Galactic WIM than in typical H II regions. Reynolds & Tufté (1995) found only weak emission from the helium recombination line at 5876 \AA , which indicates that the helium within the WIM of the Milky Way is mostly neutral. Measurements of the temperature of the gas, like the comparison of the nebular and auroral lines of N II performed by Reynolds et al. (2001), show temperatures clearly above the value characteristic for the gas in H II regions, which also leads to enhanced emission in the collisionally excited optical lines of singly ionized nitrogen and sulfur. An extensive study of the

²We will hereafter use the general term “DIG” to refer to the diffuse gas, and the expression “H II region” to describe the relatively dense ionized gas in the direct environment of hot massive stars. We note, however, that there is no well-defined distinction between those phases.

³The emission measure is defined as the integral of the square of the electron density along the line of sight, as most processes that determine the emissivity of the gas (recombination, collisional excitation, and thermal free-free emission) scale, for otherwise identical conditions, with the square of the gas density.

properties of the WIM in the solar environment of the Milky Way, based of observations using the Wisconsin $H\alpha$ Mapper spectrograph, has been presented by Madsen et al. (2006).

Observations by Greenawalt et al. (1997) find indications of a softer ionizing spectrum than in typical $H\text{ II}$ regions also for the DIG of M 31, although the difference appears to be less pronounced than in the Milky Way, as the spectra show $[\text{O III}]$ emission as well as the presence of the helium recombination line at 5876 \AA , which indicates an appreciable fraction of ionized helium. The dominance of only singly ionized metals in the DIG of the solar environment in the Milky Way cannot, however, be considered a general property of the entire DIG in spiral galaxies. Observations of edge-on galaxies (Otte et al. 2001, Collins & Rand 2001a) show that in a part of these objects the $[\text{O III}]/H\alpha$ ratio rises at large heights above the galactic planes, while large $[\text{N II}]/H\alpha$ and $[\text{S II}]/H\alpha$ ratios are also observed. Evidence for a hardening of the ionizing spectra at high galactic altitudes has also been provided by Spitzer Space Telescope observations of three edge-on galaxies in the mid infrared by Rand et al. (2011), where a rising $\text{Ne III}/\text{Ne II}$ ratio for larger distances from the galactic disks was found. The differences between the observations indicate that the energy sources, the temperature structure, and the ionization structure of the DIG may differ considerably from galaxy to galaxy or among different parts of the same galaxy.

Two main explanations for the differences between the spectra of classical $H\text{ II}$ regions and the DIG have been put forward, which are likely to be complementary: filtering effects modifying the spectral energy distribution of the ionizing radiation, and the presence of additional sources of ionization and heating. Filtering effects have been studied, for example, by Hoopes & Walterbos (2003) and Wood & Mathis (2004) and are partly able to explain the larger temperatures of the DIG (compared to $H\text{ II}$ regions) due to the radiation hardening effect. We will discuss filtering effects in more detail in Sect. 4.2.3.

An additional contribution of hot low-mass evolved stars (central stars of planetary nebulae or white dwarfs) has been discussed, for example, by Sokolowski & Bland-Hawthorn (1991) and Flores-Fajardo et al. (2011) to explain the fact that in some galaxies the $[\text{O III}]/[\text{O II}]$ ratio increases for larger distances from the disk. Such objects can occur at larger distances from the plane of the star-forming galactic disk due to their older ages compared to hot massive main-sequence or supergiant stars.

A possible source for additional heating of the DIG is the dissipation of a part of the (macroscopic) mechanical energy of the gas. There have been several approaches for the explanation of the underlying mechanisms. One of them is shocks that can, for example, be produced by supernova explosions or strong stellar winds from massive OB associations (Collins & Rand 2001a). Another possibility for providing the DIG with energy is via magnetic reconnection processes as described by Hoffmann et al. (2012), who have analyzed the contributions of photoionization and magnetic reconnection by computing synthetic spectra for purely photoionized or purely thermally (by magnetic reconnection) excited gas as well as for gas where both mechanisms are present. They find that while the total energy input provided by magnetic reconnection alone may be sufficient to keep the DIG ionized at large heights above the galactic plane, the observed spectra can be explained best by a mixture of both photoionization and thermal excitation.

Here, however, we will concentrate on the ability of hot massive stars close to the mid-plane of the galactic disk to ionize the DIG. Not much is known about the ionizing fluxes of these objects through direct observation. For this reason we employ realistic SEDs from state-of-the-art non-LTE atmospheric models that include the effects of stellar winds and line blocking and blanketing. The SEDs from our group have had a consistently good track record as ionizing sources in models of $H\text{ II}$ regions (Sellmaier et al. 1996; Giveon et al. 2002; Rubin et al. 2007, 2008, 2016). The use of such SEDs becomes even more important as we model gas and stars at different metallicities, where

even fewer detailed direct and indirect observational constraints can be obtained from our nearer environment.

In this paper we systematically explore a plausible subset of the (rather large) parameter space in metallicity, stellar effective temperature, and filtering through surrounding H II regions, to show how observable characteristics of the DIG vary quantitatively with these parameters. As a parameter study, none of the models in our current paper is intended as a detailed description of the DIG in any particular galaxy, and neither is it expected that each particular parameter combination will be realized by nature somewhere in our immediate surroundings. We expect, however, that the large set of theoretical predictions that we present here will serve as a future guide in exploring more detailed quantitative models.

In Sect. 4.2 we study the properties of the DIG as a function of both the temperature- and metallicity-dependent SEDs of the ionizing sources – based on the model stars presented by Weber et al. (2015) – and the escape fractions from the H II regions surrounding the ionizing stars, using the spherically symmetric method described by Hoffmann et al. (2012) and Weber et al. (2015). Together, our study comprises emission line ratios for a grid of 60 spherically symmetric DIG models.

A spherically symmetric approach is suitable for systematically examining the differential variations of the emission line spectrum in dependence of a certain input parameter, such as the spectral energy distribution of the ionizing source. There are, however, two drawbacks regarding simulations of the diffuse ionized gas. First, star-forming galaxies usually contain numerous H II regions whose stars may act as sources of ionization for more distant gas. Second, the density distribution of the absorbing gas is usually not spherically symmetric, and thus the attenuation of the radiation field is anisotropic. In Sect. 4.3 we present a set of simulations whose geometry corresponds to a galactic region above a star-forming spiral arm, in order to account for these effects of the three-dimensional structure of the interstellar gas. We also show how, even for the same mean density and average filling factor, the ionization structure of the DIG is affected by its porosity, which is a function of the size and the spatial distribution of the overdense “clumps”.

4.2 Spherically symmetric simulations of dilute ionized gas surrounding leaky H II regions

In this section we describe a grid of H II region and DIG models in which we vary the effective temperatures and the metallicities of the ionizing stars, as well the escape fraction of ionizing photons from the H II regions surrounding the stars into the DIG.⁴ Our approach corresponds to that of Hoopes & Walterbos (2003), but our study is based on stellar SEDs from non-LTE atmospheric models taking into account the effects of stellar winds and line-blocking in the EUV, namely the model grid of Weber et al. (2015) at 0.1, 0.4, and 1.0 solar metallicities. We will first describe our numerical approach to accurately model the atmospheres of O-type stars that act as sources of ionization. Such detailed modelling is crucial for the determination of the radiation field in the ionizing spectral range above 1 Ryd, which in turn determines the temperature and ionization structure of the gas affected by the stellar radiation. Then we outline the method used to describe the processes in the ionized nebulae. After an explanation of the simulation setup used, we will discuss the effects of the filtering on the ionizing radiation field by the gas in the stellar environment and its effect on the emission line spectrum of both the H II regions in the stellar environment and the diffuse ionized gas. Finally we will compare our results with observations and discuss the implications of the comparison.

⁴If not stated otherwise, we use the term “escape fraction” for the escape fraction of all photons emitted by the source whose energy lies above the ionization threshold of hydrogen.

4.2.1 The general concept for calculating synthetic spectra and SEDs of massive stars

Our approach to modeling the expanding atmospheres of hot, massive stars has been described in detail in a series of previous papers (Pauldrach 1987, Pauldrach et al. 1990, 1993; Pauldrach et al. 1994, Taresch et al. 1997, Haser et al. 1998, Pauldrach et al. 1998, 2001, 2004, 2012), and we summarize the salient points here. Our method is based on the concept of homogeneous, stationary, and spherically symmetric radiation-driven atmospheres. Although this is an approximation to some extent, it is sufficient to reproduce all important characteristics of the expanding atmospheres in some detail.

A complete model atmosphere calculation consists of (a) a solution of the hydrodynamics describing velocity and density structures of the outflow, based on radiative acceleration by line, continuum, and Thomson absorption and scattering – an essential aspect of the model, because the expansion of the atmosphere alters the emergent flux considerably compared to a hydrostatic atmosphere; (b) the computation of the occupation numbers from a solution of the rate equations containing all important radiative and collisional processes, using sophisticated model atoms and corresponding line lists⁵; (c) a calculation of the radiation field from a detailed radiative transfer solution taking into account the Doppler-shifted line opacities and emissivities along with the continuum radiative transfer⁶; and (d) a computation of the temperature from the requirement of radiative (absorption/emission) and thermal (heating/cooling) balance. An accelerated Lambda iteration (ALImI, explained in detail in Pauldrach et al. 2014) procedure⁷ is used to achieve consistency of occupation numbers, radiative transfer, and temperature. If required, an updated radiative acceleration can be computed from the converged model, and the process repeated.

In addition, secondary effects such as the production of EUV and X-ray radiation in the cooling zones of shocks embedded in the wind and arising from the nonstationary, unstable behavior of

⁵In total 149 ionization stages of the 26 most abundant elements (H to Zn, apart from Li, Be, B, and Sc) are considered; a detailed description of the atomic models used is given in Sect. 3 and Table 1 of Pauldrach et al. 2001, and in Sect. 2 of Pauldrach et al. 1994 where several tables and figures that explain the overall procedure are shown. Low-temperature dielectronic recombination is included.

⁶If different spectral lines get shifted across the same observer's frame frequency by the velocity field in the envelope, line overlap, which is responsible for multiple-scattering events, takes place. The method used to solve this problem is an integral formulation of the transfer equation using an adaptive stepping technique on every ray (in p, z geometry) in which the radiation transfer in each micro-interval is treated as a weighted sum on the microgrid,

$$I(\tau_0(p, z)) = I(\tau_n) e^{-(\tau_n - \tau_0)} + \sum_{i=0}^{n-1} \left(e^{-(\tau_i - \tau_0)} \int_{\tau_i}^{\tau_{i+1}} S(\tau) e^{-(\tau - \tau_i)} d\tau(p, z) \right),$$

where I is the specific intensity, S is the source function and τ is the optical depth. To accurately account for the variation of the line opacities and emissivities due to the Doppler shift, all line profile functions are evaluated correctly for the current microgrid-coordinates on the ray, thus effectively resolving individual line profiles (cf. Pauldrach et al. 2001); thus, the effects of line overlap and multiple scattering are naturally included. On the basis of this procedure, the application of the Sobolev technique yields for the radiative line acceleration

$$g_{\text{lines}}(r) = \frac{2\pi}{c} \frac{1}{\rho(r)} \sum_{\text{lines}} \chi_{\text{line}}(r) \int_{-1}^{+1} I_{\nu_0}(r, \mu) \frac{1 - e^{-\tau_s(r, \mu)}}{\tau_s(r, \mu)} \mu d\mu,$$

where

$$\tau_s(r, \mu) = \chi_{\text{line}}(r) \frac{c}{\nu_0} \left[(1 - \mu^2) \frac{v(r)}{r} + \mu^2 \frac{dv(r)}{dr} \right]^{-1}$$

is the Sobolev optical depth and ν_0 is the frequency at the center of each line ($\chi_{\text{line}}(r)$ is the local line absorption coefficient, μ is the cosine of the angle between the ray direction and the outward normal on the spherical surface element, $v(r)$ is the local velocity, and c is the speed of light). A comparison of the line acceleration of strong and weak lines evaluated with the comoving-frame method and the Sobolev technique disregarding continuum interaction is presented in Fig. 5 of Pauldrach et al. (1986), and a comparison of the comoving-frame method and the Sobolev-with-continuum technique is shown in Fig. 3 of Puls & Hummer (1988), demonstrating the excellent agreement of the two methods.

⁷For the latest update of the general method, see Pauldrach et al. (2014).

radiation-driven winds can, together with K-shell absorption, be optionally considered (based on a parametrization of the shock jump velocity; cf. Pauldrach et al. 1994, 2001). However, they have not been included in the stellar models used to describe the ionizing sources here, since they affect only high ionization stages like O vi which are not relevant for the analysis of emission line spectra of H II regions.

Of course, it needs to be clarified whether the spectral energy distributions calculated by our method are realistic enough to be used in diagnostic modeling of H II regions. Although the radiation in the ionizing spectral range cannot be directly observed, the predicted SEDs can be verified indirectly by a comparison of observed emission line strengths and those calculated by nebular models (cf. Giveon et al. 2002; Rubin et al. 2007, 2008, 2016; Sellmaier et al. 1996). A more stringent test can be provided by a comparison of the synthetic and observed UV spectra of individual massive stars, which involves hundreds of spectral signatures of various ionization stages with different ionization thresholds, and covering a large frequency range: because almost all of the ionization thresholds lie in the spectral range shortward of the hydrogen Lyman edge (cf. Pauldrach et al. 2012), and the ionization balances of all elements depend sensitively on the ionizing radiation throughout the entire wind, the ionization balance can be traced reliably through the strength and structure of the wind lines formed throughout the atmosphere. In this way a successful comparison of observed and synthetic UV spectra (Pauldrach et al. 1994, 2001, 2004, 2012) ascertains the quality of the ionization balance and thus of the SEDs.

4.2.2 Numerical modelling of the H II regions

For the computation of spherically symmetric models of gaseous nebulae we have adapted the stellar atmosphere code discussed above (Pauldrach et al. 2001, 2012) to the dilute radiation fields and low gas densities in H II regions (Hoffmann et al. 2012, Weber et al. 2015). The results of this approach describe steady-state H II regions in which ionization and recombination, as well as heating and cooling are in equilibrium at each radius point.

In the stationary state, the ionization fractions of an element are given by the solution \mathbf{n}^∞ of the equation

$$\mathbf{G} \cdot \mathbf{n}^\infty = \mathbf{0}, \quad (4.1)$$

where \mathbf{G} is a matrix formed from the ionization and recombination rate coefficients⁸, and the components of the vector \mathbf{n}^∞ are the number densities of successive ionization stages of the elements considered. Because the rate coefficients in general depend on the radiation field and the temperature (themselves in turn dependent on the ionization ratios), the system is solved iteratively together with the radiation field and the temperature until convergence is reached.

In our spherically symmetric models we compute the radiative transfer along a series of rays with different impact parameters to the central source, yielding the radiative intensity I_ν at every point along each ray. At any given radius shell r , each ray intersecting that shell corresponds to a different angle ϑ with respect to the outward normal, and the mean intensity $J_\nu(r)$ that enters into the radiative rates (photoionization and photoheating) is then obtained as $J_\nu(r) = \frac{1}{2} \int_{-1}^1 I_\nu(r, \mu) d\mu$, with $\mu = \cos \vartheta$. The symmetry allows taking into account the diffuse radiation field (ionizing radiation created in the gas itself via direct recombination to the ground level) without incurring additional computational cost, and thus does not necessitate the use of simplifying approximations such as “on the spot” or “outward only”.

⁸The elements of \mathbf{G} are $G_{ij} = \mathcal{P}_{ji}$ for $i \neq j$ and $G_{ii} = -\sum_{j \neq i} \mathcal{P}_{ij}$, where \mathcal{P}_{ij} is the rate coefficient for the transition from ionization stage i to stage j . The redundant system of equations is closed by replacing one of the rows by the requirement of particle conservation, $\sum_i n_i = n_{\text{tot}}$.

Table 4.1: Emission of the diagnostically important collisionally excited lines [N II] $\lambda\lambda 6584, 6548$, [O II] $\lambda\lambda 3726, 3729$, [O III] $\lambda\lambda 5007, 4959$ and [S II] $\lambda\lambda 6716, 6731$ relative to the corresponding H β emission for matter-bounded (leaky) H II regions and the surrounding DIG. The SEDs of the ionizing sources are from Weber et al. (2015) with metallicities of $0.1 Z_{\odot}$, $0.4 Z_{\odot}$, and $1.0 Z_{\odot}$. The H II regions have densities of $n_{\text{H}} = 10 \text{ cm}^{-3}$ and their outer radii adjusted to allow 70%...5% of the ionizing photons to escape. These are used as ionizing fluxes for the DIG ($n_{\text{H}} = 0.1 \text{ cm}^{-3}$), scaled to 10^{50} ionizing photons/s for easier comparison. For the picket-fence cases the unaltered stellar SEDs are used as the ionizing flux for the (now radiation-bounded) H II regions as well as for the DIG (again scaled to 10^{50} ionizing photons/s). (Continued in Table 4.2.)

T_{eff} (K)	Z (Z_{\odot})	$f_{\text{esc,H}}$	H II regions				DIG				
			[N II]	[O II]	[O III]	[S II]	[N II]	[O II]	[O III]	[S II]	
(in units of H β)											
30 000	0.1	picket fence	0.92	2.1	0.00	0.38	0.92	2.0	0.00	0.33	
		70%	0.95	2.3	0.00	0.21	0.95	2.1	0.00	0.38	
		50%	0.93	2.2	0.00	0.27	1.0	2.6	0.00	0.25	
		30%	0.92	2.1	0.00	0.31	1.0	2.4	0.00	0.35	
		10%	0.91	2.1	0.00	0.35	1.0	2.5	0.00	0.27	
		5%	0.93	2.1	0.00	0.37	0.97	2.4	0.00	0.22	
		0.4	picket fence	1.7	2.2	0.00	0.84	1.7	2.0	0.00	0.82
	70%		1.5	1.8	0.01	0.41	1.8	2.3	0.00	0.88	
	50%		1.5	1.8	0.01	0.51	1.9	2.6	0.00	0.88	
	30%		1.5	1.8	0.00	0.62	2.0	3.0	0.00	0.85	
	10%		1.6	2.1	0.00	0.75	2.2	3.5	0.00	0.71	
	5%		1.6	2.1	0.00	0.79	2.2	3.7	0.00	0.65	
	1.0	picket fence	1.7	1.1	0.00	1.1	1.7	1.1	0.00	0.72	
		70%	1.3	0.79	0.00	0.64	1.9	1.3	0.00	0.97	
		50%	1.3	0.77	0.00	0.73	2.0	1.5	0.00	1.0	
		30%	1.4	0.83	0.00	0.83	2.2	1.8	0.00	1.0	
		10%	1.5	1.0	0.00	1.0	2.5	2.3	0.00	0.92	
		5%	1.6	1.1	0.00	1.1	2.3	2.2	0.00	0.77	
	35 000	0.1	picket fence	0.48	1.9	1.9	0.16	0.55	2.0	1.3	0.25
			70%	0.12	1.1	4.0	0.04	0.63	2.1	1.2	0.26
			50%	0.19	1.4	3.3	0.06	0.71	2.2	1.1	0.27
30%			0.29	1.8	2.7	0.09	0.92	2.6	0.74	0.16	
10%			0.44	1.9	2.2	0.14	1.2	3.2	0.01	0.21	
5%			0.40	1.9	2.0	0.15	1.2	3.4	0.01	0.19	
0.4			picket fence	1.2	3.0	1.9	0.41	1.3	3.2	1.3	0.65
		70%	0.14	1.1	4.4	0.05	1.5	3.5	1.2	0.69	
		50%	0.37	1.9	3.2	0.12	1.9	4.0	1.1	0.72	
		30%	0.60	2.4	2.7	0.19	2.4	4.6	0.70	0.71	
		10%	1.0	2.9	2.2	0.32	3.2	6.2	0.01	0.64	
		5%	1.1	3.0	2.1	0.36	3.4	6.9	0.00	0.58	
1.0		picket fence	1.4	2.1	0.83	0.55	1.4	1.5	0.93	0.62	
		70%	0.19	0.66	1.6	0.06	1.6	1.8	0.71	0.68	
		50%	0.38	1.0	1.4	0.13	1.7	2.3	0.67	0.67	
		30%	0.65	1.5	1.2	0.22	1.6	2.3	0.31	0.69	
		10%	1.1	1.8	0.94	0.38	2.5	2.9	0.00	0.48	
		5%	1.3	2.0	0.88	0.46	1.9	2.5	0.00	0.29	

Table 4.2: As Table 4.1, but for the 40 000 K and 50 000 K model stars as ionizing sources.

T_{eff} (K)	Z (Z_{\odot})	$f_{\text{esc,H}}$	H II regions				DIG				
			[N II]	[O II]	[O III]	[S II]	[N II]	[O II]	[O III]	[S II]	
(in units of $H\beta$)											
40 000	0.1	picket fence	0.1	0.50	5.0	0.09	0.20	0.85	3.9	0.15	
		70%	0.03	0.24	6.6	0.02	0.19	0.80	3.8	0.17	
		50%	0.04	0.32	6.2	0.02	0.18	0.72	4.0	0.18	
		30%	0.06	0.41	5.8	0.04	0.15	0.59	4.9	0.18	
		10%	0.08	0.48	5.4	0.05	0.11	0.38	5.0	0.19	
		5%	0.08	0.49	5.2	0.07	0.10	0.29	5.1	0.20	
	0.4	picket fence	0.32	1.1	6.7	0.22	0.71	2.2	5.2	0.48	
		70%	0.06	0.27	6.5	0.03	0.71	2.2	5.7	0.49	
		50%	0.09	0.40	6.3	0.04	0.67	2.1	6.6	0.49	
		30%	0.14	0.60	6.5	0.07	0.61	2.0	8.2	0.50	
		10%	0.27	0.95	6.8	0.12	0.46	1.5	11	0.53	
		5%	0.26	1.1	6.8	0.15	0.41	1.3	13	0.57	
	1.0	picket fence	0.32	0.64	3.9	0.27	0.78	1.4	3.7	0.61	
		70%	0.03	0.07	2.0	0.02	0.83	1.5	4.1	0.63	
		50%	0.05	0.09	2.0	0.03	0.81	1.6	5.2	0.66	
		30%	0.09	0.16	2.5	0.05	0.77	1.5	7.1	0.70	
		10%	0.18	0.37	3.4	0.11	0.67	1.5	12	0.87	
		5%	0.23	0.50	3.7	0.15	0.62	1.4	15	0.97	
	50 000	0.1	picket fence	0.04	0.22	6.4	0.07	0.14	0.56	4.2	0.18
			70%	0.01	0.10	8.0	0.01	0.13	0.53	4.4	0.18
			50%	0.02	0.13	7.5	0.01	0.12	0.46	4.7	0.19
30%			0.02	0.17	7.2	0.02	0.11	0.38	5.0	0.19	
10%			0.03	0.29	6.7	0.03	0.09	0.27	5.2	0.23	
5%			0.03	0.32	7.5	0.04	0.06	0.17	5.6	0.20	
0.4		picket fence	0.11	0.45	10	0.16	0.43	1.4	9.0	0.34	
		70%	0.02	0.18	9.2	0.01	0.42	1.4	9.9	0.54	
		50%	0.03	0.15	9.4	0.02	0.39	1.4	11	0.56	
		30%	0.04	0.23	10	0.04	0.37	1.2	13	0.60	
		10%	0.07	0.36	11	0.07	0.33	0.96	17	0.73	
		5%	0.08	0.41	11	0.09	0.32	0.85	18	0.84	
1.0		picket fence	0.16	0.48	7.2	0.24	0.60	1.5	6.9	0.71	
		70%	0.01	0.05	3.3	0.01	0.61	1.6	8.1	0.75	
		50%	0.02	0.07	3.5	0.02	0.60	1.6	10	0.80	
		30%	0.04	0.11	4.4	0.03	0.60	1.6	13	0.90	
		10%	0.07	0.24	6.1	0.07	0.58	1.6	21	1.2	
		5%	0.09	0.32	6.8	0.10	0.58	1.6	21	1.2	

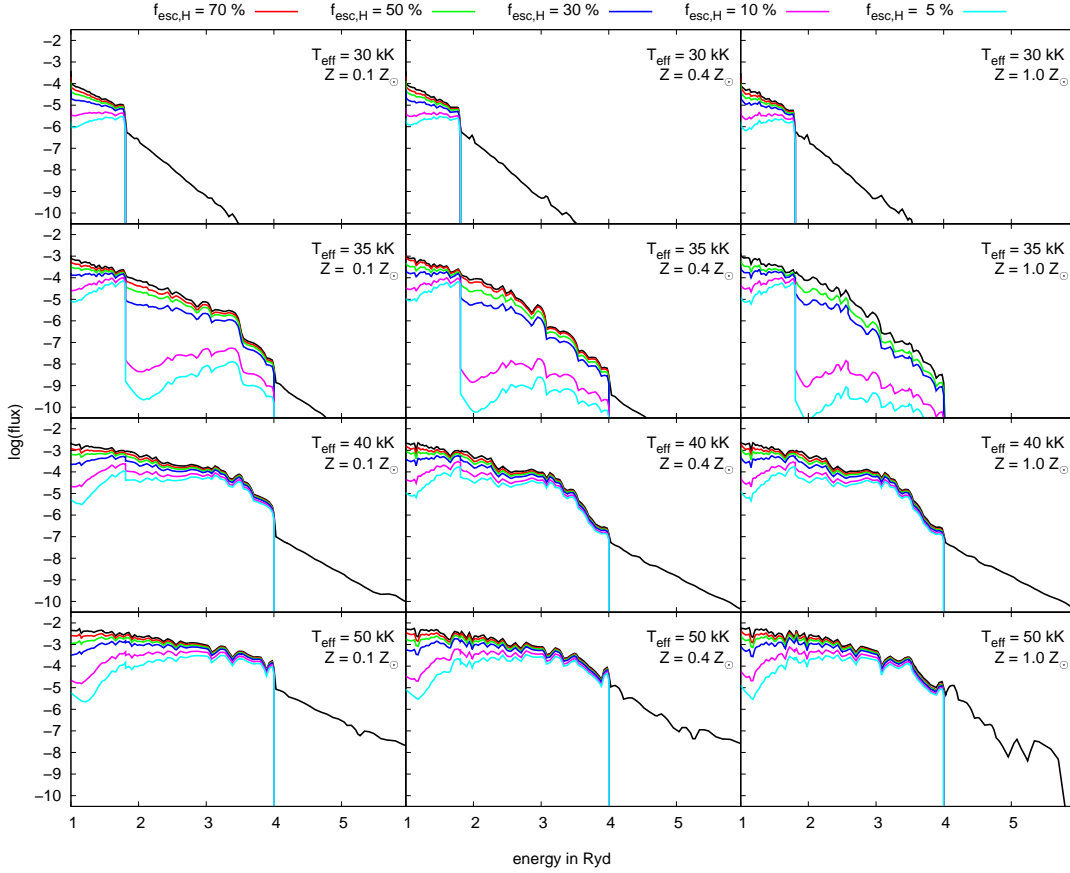


Figure 4.1: Computed stellar SEDs (black lines) modified by homogeneous matter-bounded H II regions ($n_{\text{H}} = 10 \text{ cm}^{-3}$) for different escape fractions (colored lines as labeled). As sources we have used the main-sequence spectra from the hot star model grid by Weber et al. (2015). The chemical composition of the H II regions is assumed to be the same as that of the corresponding stellar atmospheres. Shown are the Eddington fluxes normalized to the stellar radius.

The emission spectrum of the gas depends on both its ionization structure and its temperature, since the recombination and collisional excitation rates are temperature-dependent. Interpretation of the spectra of ionized gas thus also requires considering the microphysical processes that heat and cool the gas and thereby determine its temperature structure. In H II regions, the main heating source is the ionization of H I and He I, which increases the kinetic energy of the gas by $\Delta E = h(\nu - \nu_0)$ per ionization process (ν is the frequency of the ionizing photon and $h\nu_0$ the ionization energy). Cooling of the gas happens via recombination processes (which radiate away the kinetic energy of the electron and the ionization energy of the resulting ion, usually in several steps when recombination occurs to an excited state), radiative de-excitation of collisionally excited states, and free-free radiation (bremsstrahlung).

In H II regions, a large part of the energy of the absorbed ionizing photons is transformed into line emission in the UV, the visible, and the infrared wavelength range. These lines are either recombination lines like the Balmer lines of hydrogen, or collisionally excited lines such as the “nebulium” lines of O III at 4959 Å and 5007 Å. To compute the emission in these lines, the bound-bound tran-

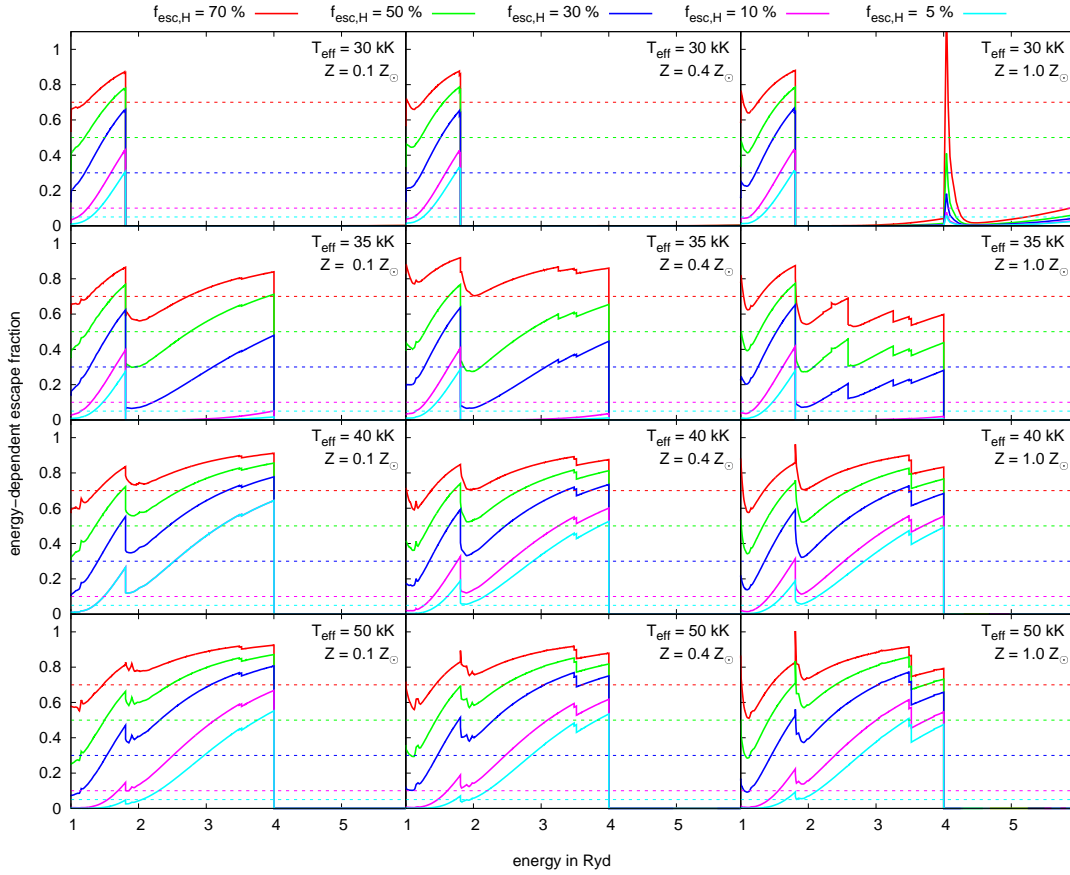


Figure 4.2: Energy-dependent escape fractions $F(\nu)/F_{\star}(\nu)$ of photons above the ionization threshold of hydrogen for the fluxes shown in Fig. 4.1. In general, the escape fraction rises above each of the strong ionization edges due to the decreasing absorption cross sections for higher photon energies. The He II-ionizing photons are almost completely absorbed within the H II regions for all considered stellar sources; for $T_{\text{eff}} = 30\,000\text{ K}$ almost no He I-ionizing radiation can escape from the H II region either. For higher metallicities, in addition to the prominent ionization edges of H I, He I, and He II, there is also notable absorption by metal ions, especially of O II, Ne II, N III, and C III with ionization energies of 2.59 Ryd, 3.35 Ryd, 3.49 Ryd, and 3.52 Ryd, respectively. The dashed lines indicate the corresponding angle-averaged escape fractions for the case of extremely clumpy H II regions that would allow radiation to escape unhindered in some directions while being completely opaque to all wavelengths in others (“picket-fence” case). The spike in the escape fractions of the upper right panel is a result of the extremely low stellar He II-ionizing photon flux, which is approximately 12 orders of magnitude lower than the corresponding hydrogen-ionizing flux. Thus, even very little emission of photons by the H II region in that energy range is sufficient to exceed the flux emitted by the stellar atmosphere.

sition rates among the different excitation states within the ionization stage must be calculated. Our numerical approach for computing these rates is described in detail by Hoffmann et al. (2012) and Weber et al. (2015).

4.2.3 Properties of the filtered stellar radiation

In our first set of simulations we study the emission spectrum of diffuse gas ionized by hot stars surrounded by an H II region of denser gas that attenuates and filters the stellar radiation. For this we use spherically symmetric models and assume a constant density in each of the two gas regions considered ($n_{\text{H}} = 10 \text{ cm}^{-3}$ for the H II region and $n_{\text{H}} = 0.1 \text{ cm}^{-3}$ for the DIG). Our model grid comprises stellar effective temperatures of 30, 35, 40, and 50 kK and uses the spectral energy distributions of the dwarf (i.e., main sequence) star models from Weber et al. (2015) with metallicities of 0.1, 0.4, and $1.0 Z_{\odot}$.⁹ We adjust the radii of the filtering H II regions, which we assume to be ionized by a single model star each, iteratively until a given fraction (70%, 50%, 30%, 10%, and 5%) of the total hydrogen-ionizing photon flux of the stars is able to escape from the matter-bounded H II region into the DIG.

In our models we do not currently consider the effects of dust absorption. While dust is present in H II regions, Mathis & Wood (2005) find the absorption of silicate-based dust to be weak and – in the frequency range of ionizing radiation – almost wavelength-independent. They also call attention to the fact that while carbon-based dust, composed of graphite particles or polycyclic hydrocarbons, has an absorption feature that peaks at 17 eV and could therefore alter the spectral energy distribution of the ionizing radiation field, observations showing that there is almost no C-depletion from the gaseous phase indicate that the carbon-based dust in H II regions has been mostly vaporized. At present we also do not account for the different depletion of individual types of metals from the gaseous phase, as discussed, for instance, by Shields & Kennicutt (1995).

In Fig. 4.1 we plot the SEDs of the ionizing sources, $F_{\star}(\nu)$, as well as the fluxes escaping from the leaky (matter-bounded) H II regions around these sources, $F(\nu)$, as a function of effective temperature, chemical composition, and the total fraction of escaping hydrogen-ionizing photons. Fig. 4.2 shows the spectral shape of the escape fraction $f_{\text{esc}}(\nu) = F(\nu)/F_{\star}(\nu)$, i.e., the “filter functions” of the H II regions.

In the energy range between the ionization edges of hydrogen and (neutral) helium, the escape fraction increases for higher photon energies because the absorption cross-section of hydrogen decreases roughly proportional to ν^{-3} . However, in matter-bounded H II regions diffuse radiation from recombination processes within the gas is also emitted from the H II region into the surrounding gas. The total emission from the H II region results from the sum of the unabsorbed photons from the star and the diffuse radiation that is able to escape from the gas and is responsible for the increased emission in the energy range directly above the ionization threshold of hydrogen.

At the He I ionization edge ($h\nu_0 = 1.81 \text{ Ryd}$) helium becomes an important additional absorber, so that the escape fraction again drops significantly. In the case of the 30 000 K stars, practically no ionizing radiation above the ionization edge of neutral helium can escape from the H II region. This is because the total He-ionizing photon emission rate of these stars is very small (approximately 2.5 dex smaller than the hydrogen-ionizing flux, cf. Weber et al. 2015), and thus the helium within the H II region is sufficient to absorb almost the entire available He-ionizing radiation.

For the 35 000 K stars and escape fractions of 5% and 10% of hydrogen-ionizing photons, the helium-ionizing photons are also nearly completely absorbed in the H II regions, whereas for the larger escape fractions a part of the He I-ionizing radiation can escape into the surrounding DIG. For higher stellar temperatures, the effect of the additional absorption by neutral helium becomes less important because the emission rate of helium-ionizing photons by the star grows in relation to that of hydrogen-ionizing photons. Thus, a smaller fraction of the emitted helium-ionizing photons is consumed to keep the helium in the H II regions ionized.

⁹The abundances representing solar metallicity have been taken from Asplund et al. (2009); for our models with sub-solar metallicities we have uniformly scaled the abundances of all metals with the same factor.

In the energy range above the ionization edge of He I, the escape fraction rises again as a result of ionization cross sections of both hydrogen and helium decreasing for larger frequencies. In this energy range there is also a noticeable contribution of metal ions to the absorption of the stellar radiation. The most important absorbing metal ions are O II ($h\nu_0 = 2.59$ Ryd), Ne II (3.25 Ryd), N III (3.49 Ryd), and C III (3.52 Ryd). The effect is more pronounced for larger metallicities, and for $T_{\text{eff}} = 40\,000$ K only the latter two ions are relevant as absorbers in our model H II regions.

In none of our nebular models does a significant amount of He II-ionizing radiation ($h\nu \geq 4$ Ryd) escape, which is a consequence of the even lower stellar photon emission rates in this energy range, which are several orders of magnitude lower than the corresponding H and He I-ionizing fluxes. Even in the case of the 50 kK model star with a metallicity of $0.1 Z_{\odot}$, which is the strongest emitter of He II-ionizing radiation of the stars considered here, the emission rate of He I-ionizing photons exceeds that of He II-ionizing photons by a factor of approximately 1500.

Another factor influencing the frequency-dependence of the escape fraction in real H II regions is the density structure of the filtering gas. While radiation hardening effects such as those described above are pronounced in homogeneous H II regions, the attenuation would become independent of wavelength (though strongly varying with angle) if all of the radiation were completely blocked in some directions by discrete, completely opaque clumps, and no absorbing matter at all intervened in other directions (“picket-fence” case). This latter scenario (wavelength-independent absorption by opaque clumps) and the former one (filtering of the radiation by homogeneous H II regions) represent hypothetical limiting cases. Actual H II regions (and the DIG) show a more complex density structure, with characteristics of both cases. For instance, Wood et al. (2005) have modeled fractal density structures, where overdense regions exist at different size scales, which are, however, not necessarily optically thick. We will examine the influence of different density distributions in the context of our 3D simulations in Sect. 4.3 below.

In a second step, we use the filtered stellar radiation from the above models to then illuminate homogeneous regions of much thinner gas ($n_{\text{H}} = 10^{-1} \text{ cm}^{-3}$) representing the DIG. For easier comparison, we scale the ionizing fluxes escaping from the H II regions such that the number of hydrogen-ionizing photons is 10^{50} s^{-1} in all cases (i.e., we compare sources with equal photon-number rates but different spectral shapes). We furthermore assume the metallicity of the DIG to be the same as that of the inner H II regions. We approximate the “picket-fence” case by increasing the radii of the H II regions until they become radiation-bounded, while also using the unfiltered SEDs of the model stars as the ionizing fluxes for the DIG (again scaled to 10^{50} ionizing photons per second).

4.2.4 Line ratios in the matter-bounded (leaky) H II regions

In Tables 4.1 and 4.2 we show the predicted luminosities of collisionally excited line radiation (relative to $\text{H}\beta$) both of the matter-bounded H II regions and of the DIG irradiated by the ionizing fluxes escaping from such H II regions.

Concerning the matter-bounded H II regions, we find that the ratio of the lines emitted by the singly ionized atoms of N, O, and S relative to the $\text{H}\beta$ emission increases for lower escape fractions. The reason for this behavior is that these ions occur predominantly in those parts of the H II regions where the optical depth to the emitting source is large, i.e., near the Strömgen radius of a radiation-bounded region. The increase is only small in the case of H II regions ionized by the 30 000 K model stars, because due to their relatively low temperature, these objects emit only a very small number of photons capable of creating doubly ionized states of those elements (cf. Table 4 of Weber et al. 2015). Thus for the 30 000 K stars the singly ionized atoms are abundant even in the inner parts of the H II regions. The $[\text{O III}]/\text{H}\beta$ ratio as a function of the escape fraction strongly depends on

the effective temperature of the ionizing sources. For the 30 000 K stars, this ratio is $\leq 10^{-3}$ for all metallicities and all escape fractions. For an effective temperature of 35 000 K the $[\text{O III}]/\text{H}\beta$ ratio drops for lower escape fractions, as the presence of O III ions is limited to a smaller volume around the source compared to ionized hydrogen responsible for the $\text{H}\beta$ recombination radiation. For the model stars with 40 000 K and 50 000 K the $[\text{O III}]/\text{H}\beta$ ratio as a function of the escape fraction is metallicity dependent. The ratio decreases for lower escape fractions in the case of (nebular) metallicity of $0.1 Z_{\odot}$ whereas it increases for the metallicities of $0.4 Z_{\odot}$ and $1.0 Z_{\odot}$. This is caused by the different radius-dependence of the temperature in the H II region. The temperature – and consequently the excitation of optical O III lines – increases with radius due to the radiation hardening for the metallicities of $0.4 Z_{\odot}$ and $1.0 Z_{\odot}$. In contrast, the temperature (slightly) decreases at larger radii for $Z = 0.1 Z_{\odot}$, which is caused by the cooling by collisionally excited neutral hydrogen, which is more abundant at larger optical depths in the outer parts of the ionized region.¹⁰ The outermost parts of radiation-bounded H II regions are characterized by the highest optical depths with respect to the source of ionization, and therefore the strongest radiation hardening. Consequently, the emission of the collisionally excited lines (relative to $\text{H}\beta$) of those ions still present near the Strömberg radius is enhanced in comparison to that of matter-bounded H II regions. For a stellar effective temperature of $T_{\text{eff}} \leq 35\,000\text{ K}$ this includes the lines of singly ionized nitrogen, oxygen, and sulfur, whereas the line emission $[\text{O III}]$ is only enhanced for the radiation-bounded models at solar metallicity and for effective temperatures of the ionizing model star of at least 40 000 K.

4.2.5 Line ratios in the DIG

For the DIG regions we find that the strength of the $[\text{N II}]$ and $[\text{O II}]$ emission lines increases relative to $\text{H}\beta$ for decreasing escape fractions where the effective temperature of the source is 30 000 K or 35 000 K and the metallicity is $0.4 Z_{\odot}$ or $1.0 Z_{\odot}$. This is caused by the larger temperatures due to the radiation hardening effect. In contrast, the $[\text{S II}]/\text{H}\beta$ emission line ratio overall tends to decrease for DIG ionized by radiation escaping from the optically thicker H II regions, but the line ratio as a function of the escape fraction is often non-monotonic and reaches its highest values not in the picket-fence case, but for DIG irradiated by radiation passing through H II regions with escape fractions of 30 % to 50 %. This is due to two opposing effects on the abundance of singly ionized sulfur in the ionized volume. Since the ionization energy of singly ionized sulfur (23.3 eV) is slightly lower than that of neutral helium (24.6 eV), the fraction of radiation in the interval between these ionization energies relative to the total hydrogen-ionizing radiation rises as a result of radiation hardening and can lead to a reduction of the number of S II ions in the DIG ionized by the filtered radiation. On the other hand, lower escape fractions in H II regions around the model stars with $T_{\text{eff}} \leq 35\,000\text{ K}$ also lead to a more pronounced He I/He II absorption edge, and consequently fewer photons with energies above the corresponding ionization threshold are available to ionize the remaining S II. The latter effect is mainly relevant for the 35 000 K model stars, as the emission of He I-ionizing radiation from the 30 000 K model stars is very low, so that the contribution of radiation in that wavelength range to the total S II-ionizing radiation is negligible.

For the radiation sources with effective temperatures of 30 000 K, almost no O II-ionizing radiation can escape from the H II regions, so that there is no $[\text{O III}]$ line radiation from the DIG. The same is true for the H II regions around the 35 000 K model stars with small escape fractions of 10% or 5%.

¹⁰Due to the less efficient cooling by metal ions for low values of Z , the temperature of the ionized gas is higher for lower metallicities. The higher temperature in turn increases the probability of collisional excitation processes of neutral hydrogen atoms, where the energy gap between the ground state and the lowest excited level is considerably larger than for the metal ions mentioned above (cf. the discussion by Weber et al. 2015).

For larger escape fractions the $[\text{O III}]/\text{H}\beta$ ratio in the DIG rises quickly, with the largest ratio reached for the largest escape fractions.

In contrast, for the higher stellar temperatures of 40 000 K and 50 000 K the $[\text{O III}]/\text{H}\beta$ ratio increases for decreasing escape fractions, as for these sources O II-ionizing photons can leave the H II regions even for small escape fractions of 10% or 5%. Actually, the fraction of O II-ionizing photons of all hydrogen-ionizing photons that can escape from the H II region is larger than the corresponding fraction of ionizing photons originally emitted by the sources, and the ratio increases for smaller escape fractions due to radiation hardening. For instance, we find an increase of approximately 0.6 dex for model stars with an effective temperature of 40 000 K and an escape fraction of 10%. Additionally, the radiation hardening leads to increased temperatures in the DIG. The radiation hardening also leads to decreasing $[\text{N II}]$ and $[\text{O II}]$ emission in the DIG around H II regions with small escape fractions for stellar temperatures of $T_{\text{eff}} \geq 40\,000$ K. In this case the effect of the larger fraction of photons able to strip a further electron from these ions is more important than the temperature increase due to radiation hardening.

The situation is different for S II, where the emission increases for lower escape fractions. The ionization energy for neutral sulfur is below the ionization threshold of hydrogen and the threshold to generate doubly ionized sulfur lies below the ionization threshold of neutral helium. Around hot O stars with strong He I-ionizing fluxes, S II ions therefore exist predominantly in the neutral phase of the medium. At the same time, electrons are required for collisional excitation processes. Most of the S II emission therefore takes place at the interface region between the ionized and the surrounding neutral phase, which is broadened by the radiation hardening as higher photon energies lead to reduced ionization cross-sections, allowing the photons to penetrate deeper into the neutral medium near the Strömgren radius.

In addition to the DIG models where the spectral energy distribution of the ionizing radiation is modified by dense H II regions in the stellar environment, we have also modeled the case where the shape of the ionizing spectrum remains unchanged, and which corresponds to either of the following two scenarios: (a) as a limit case for very high escape fractions, and (b) in situations where the only absorbers are dense clumps that completely absorb the entire ionizing radiation and coexist with “channels” devoid of gas through which photons can escape unhindered from the star (see above). The results of these simulations are presented in Tables 4.1 and 4.2 as the “picket fence” case. In general, the simulated line ratios in the “picket-fence” case continue the trend of the line ratios for higher escape fractions into the DIG at the respective temperature and metallicity. Even if the stellar radiation from the $T_{\text{eff}} = 30\,000$ K model stars is not filtered, the production of photons above the ionization edge of O II is too low to cause a significant amount of $[\text{O III}]$ emission from the DIG. For the models with $T_{\text{eff}} = 35\,000$ K sources, the emission lines from N II and O II are weaker than for the filtered spectra, which is caused by the lack of radiation hardening and the resulting cooler temperatures of the gas. The O III line, in contrast, is stronger than with filtered radiation, where for $T_{\text{eff}} = 35\,000$ K a large fraction of the photons above the He I-ionization edge are consumed within the H II regions.

In the stellar temperature range of $T_{\text{eff}} \geq 40\,000$ K the trend we have observed for increasing escape fractions in the “filtering” case (i.e., weaker absorption), namely a reduced emission of the O III line, continues. There is, however, no further significant increase in the emission from singly ionized nitrogen and oxygen.

4.2.6 Comparison with observations

As noted in the introduction, observations of the diffuse ionized gas in the Milky Way indicate a

softer ionizing spectrum in the DIG compared to typical H II regions. For example, measurements by Madsen et al. (2006) of the H α and He I λ 5876 recombination lines as well as the collisionally excited lines [N II] λ 6583, [N II] λ 5755, [O III] λ 5007, and [S II] λ 6716 emitted by the warm ionized medium of the Milky Way (in the direction of the Orion-Eridanus Bubble) show line ratios (in terms of energy) of [O III]/H α < 0.15.¹¹ In combination with the weak He I λ 5876 recombination line emission (He I/H α \leq 0.015) and the strong emission of [N II] and [S II] ([N II]/H α \sim 0.16...0.43; [S II]/H α \sim 0.13...0.29) this shows that there is only a small fraction of ions that need photons above the ionization edge of He I to be formed, indicating that the DIG is ionized by a soft radiation field. A comparison with Tables 4.1 and 4.2 shows that such conditions can be attained by ionizing radiation that is predominantly emitted by relatively cool O stars ($T_{\text{eff}} < 40\,000$ K). For comparison with the DIG, Madsen et al. (2006) have also observed “classical” H II regions around hot stars, where they have found strongly varying [O III]/H α ratios ranging from 0.025 to 0.45, i.e., the highest ratios found in the sample of H II regions exceed the highest values found in the sample of DIG subregions by a factor of approximately four.¹²

A relatively weak emission of doubly ionized oxygen ([O III]/H α \sim 0.20) has also been found in the diffuse ionized gas of M 31 by Greenawalt et al. (1997), although there the discrepancy in the [O III] emission (normalized to the recombination lines) between DIG and H II regions is smaller than in the Milky Way. These line ratios shows the best agreement with our model DIG around the 35 000 K stars, but indicate a slightly harder ionizing spectrum than found in the nearby DIG of the Milky Way. We note that, as can be seen from Tables 4.1 and 4.2, even a slight variation in the effective temperatures of the ionizing sources or the escape fraction may drastically change the [O III] emission.

In contrast, an ionizing spectrum dominated by stars with effective temperatures of $T_{\text{eff}} = 40\,000$ K or above would cause O III to become the strongest emission line in the optical wavelength range. The radiation hardening and the resulting higher temperatures in the DIG would lead to enhanced [O III] ratios compared to the dense H II regions directly surrounding the ionizing stars, which contradicts the observational results obtained by Greenawalt et al. (1997) and Madsen et al. (2006).

However, the dominance of soft ionizing sources is not consistent with observations that show that at least in some galaxies the [O III]/H β ratio rises in the dilute gas at larger distances from the hot stars near the galactic disk (Otte et al. 2001, Collins & Rand 2001a), because for scenarios with radiation-bounded H II regions around O stars with effective temperatures of $T_{\text{eff}} \lesssim 35\,000$ K the harder radiation above the helium ionization threshold is restricted to the inner parts of the ionized volume, as can be seen from the results in Table 4.1. The situation may be different if not only the H II regions surrounding the stars, but also the DIG is matter-bounded, so that even for a softer spectral energy distribution of the ionizing sources radiation hardening may outweigh the absorption of photons above the He I ionization threshold.

Alternatively, these observational results could be explained by additional sources with high effective temperatures that are not as concentrated towards the galactic disk as massive O stars, for example the evolved stars (central stars of planetary nebulae and white dwarfs) proposed by Sokolowski & Bland-Hawthorn (1991) and Flores-Fajardo et al. (2011). Integral field observations by Lacerda et al. (2018), who find the DIG in galaxies with low current star formation rates to have higher [O III]/H β ratios, support the idea that evolved stars may play an important role in the ionization of the more dilute parts of the DIG. In view of these results it appears unlikely that the rising

¹¹The H α /H β ratio is approximately 2.9 and changes only weakly as a function of temperature and electron density (cf. Hummer & Storey 1987, Osterbrock & Ferland 2006). Thus, in these regions, the strength of the [O III] emission is less than half of the H β emission we use as a reference in Tables 4.1 and 4.2.

¹²For an H II region of gas ionized by a much hotter DO white dwarf (whose temperature was determined to be around $T_{\text{eff}} \approx 120$ kK by Mahsereci et al. 2012) they found a much larger ratio of [O III]/H α \sim 2.6.

$[\text{O III}]/\text{H}\beta$ ratios are mainly the result of hardening of the radiation of hot massive stars. Our results in the previous sections, which are quantified in Table 4.2, show that for stellar effective temperatures of $T_{\text{eff}} \gtrsim 40\,000$ K, He I-ionizing photons are able to leave the inner H II regions even for low escape fractions of the total ionizing radiation, so that the effect of radiation hardening in the energy range between the ionization thresholds of He I and He II leads to an enhanced $[\text{O III}]/[\text{O II}]$ ratio in the DIG. But hot massive stars are extremely rare in early-type galaxies (ellipticals and gas-depleted S0 disk galaxies with little ongoing star formation), while there still exists a population of evolved low-mass hot stars. So an ionization by these objects appears to be more plausible.

4.3 Simulations of the diffuse ionized gas in 3D

In star-forming galaxies there are typically multiple regions containing hot stars that may contribute to the ionization of the DIG. Simulations of the DIG should therefore be able to simultaneously account for several sources located at different positions and embedded in an inhomogeneous interstellar gas. To realize this aim we have applied our 3D radiative transfer code to model the DIG above a spiral arm. The underlying methods of this code are described in detail by Weber et al. (2013) (geometrical aspects of the ray tracing, computation of the ionization structure of hydrogen and helium) and Weber et al. (2015) (ionization structure of metals, computation of the temperature structure of the gas, and computation of the line emission). As in the spherically symmetric models, we assume the ionized gas to exist in two forms, H II regions in the immediate environment of the stars (unresolved in these simulations) and the dilute and extended DIG.

It is not our aim here to exactly reproduce the line ratios of any particular spiral galaxy. Instead, we want to know how varying the inhomogeneity in the DIG affects the ionization structure and the line emission of the diffuse gas. Our approach is complementary to that of Wood et al. (2004, 2005), who concentrated on simulating the escape of ionizing radiation from H II regions in the stellar environment, whereas we focus on inhomogeneities within the diffuse ionized gas itself. Here our approach is similar to that of Wood et al. (2010) and Barnes et al. (2015), who performed photoionization simulations of the DIG based on a density structure obtained from hydrodynamical simulations, or, in the latter case, a fractal density structure as well, while we choose a simpler description, but study how the clumpiness of the DIG affects its observable properties.

4.3.1 Method: 3-dimensional radiative transfer based on ray tracing

The difficulty in modelling the DIG is related to the inherent lack of symmetry of the problem; the presence of multiple ionization sources coupled with the inhomogeneous gas distribution can create a complex 3-dimensional pattern in the radiation field. To compute that pattern numerically a suitable discretization scheme is required. The simplest but still fully general such method is to divide up the simulation volume into a Cartesian grid of cells, where the gas density may vary from cell to cell but the ionization structure and density within each cell is taken to be homogeneous. The accuracy and detail level of the simulation may be then chosen by selecting an appropriate cell size.

Because the spatial extent of the ionized region exceeds stellar radii by typically more than six orders of magnitude, the sources of ionizing radiation can be considered to be point-like, and the radiative transfer can be computed along rays emanating from these points. Limiting the placement of the sources to the centers of cells results in no significant further loss of detail beyond the already effected discretization of the volume into cells, but allows conserving computational resources in calculating the radiation field, because then the intersections of the rays with the cell boundaries

relative to the source are the same for all sources and need to be computed only once; the results are stored and then accessed via a lookup table. The rays themselves are distributed evenly in all directions around a source (using the tessellation scheme of Górski et al. 2005), each ray representing a fixed solid angle $\Delta\Omega = 4\pi/N_{\text{rays}}$ and thereby a given fraction $L_{\text{ray}} = L/N_{\text{rays}}$ of the source's luminosity L . The geometric dilution of the radiation field is automatically provided for by the decreasing number of rays intersecting each cell with increasing distance from the source.

Each source may have a different luminosity and spectral energy distribution, and the radiative transfer is computed for a number of frequency points (typically 100...1000) sufficient to describe the energy distribution of the ionizing flux. We account for the diffuse radiation field by applying the case-B approximation for hydrogen and helium, i.e., the assumption that the photons emitted by recombination directly into the ground state are re-absorbed locally. (In the context of our 3D radiative transfer this approximation is quantitatively discussed by Weber et al. 2013.)

As a further step in our simulation procedure the time-dependent ionization fractions $n \equiv n(\mathbf{r}, t)$ of all ionization stages i of the elements considered are calculated on the basis of the time-dependent rate equation system

$$\frac{d}{dt}n_i(t) = \sum_{j \neq i} \mathcal{P}_{ji}n_j(t) - \sum_{j \neq i} \mathcal{P}_{ij}n_i(t), \quad (4.2)$$

which describes the rate of change of the number density of all ionization stages i . The rate coefficients \mathcal{P}_{ij} are the sums of the radiative (\mathcal{R}_{ij}) and the collisional (\mathcal{C}_{ij}) transition rates. Because the strengths of emission lines depends on the temperature, the heating and cooling processes that determine the temperature structure of the gas must also be accounted for.

In the present work we restrict ourselves to the computation of the stationary state for the temperature and ionization structure.

To determine this equilibrium, it is necessary to compute the ionization and recombination rates. The photoionization rates $\mathcal{R}_{ij}(m)$ from a lower stage i to an upper stage j are calculated for a grid cell m as

$$\mathcal{R}_{ij}(m) = \int_{\nu_{ij}}^{\infty} \frac{4\pi a_{ij}(\nu)}{h\nu} J_{\nu}(m) d\nu, \quad (4.3)$$

where $J_{\nu}(m)$ is the mean intensity in the cell, ν_{ij} the threshold frequency for the corresponding ionization edge, and $a_{ij}(\nu)$ the frequency-dependent ionization cross-section. The mean intensity can be computed by making use of the fact that the number of ionization processes within a grid cell must equal the number of ionizing photons absorbed in the grid cell. This leads to the expression

$$J_{\nu}(m) = \frac{1}{4\pi V(m)} \sum_{\substack{\text{ray} \\ \text{segments}}} \frac{L_{\text{ray},\nu}^{\text{inc}}(1 - e^{-\tau_{\nu}})}{\chi_{\nu}(m)}, \quad (4.4)$$

where $V(m)$ is the volume of the cell, $L_{\text{ray},\nu}^{\text{inc}}(m)$ the frequency-dependent incident luminosity of a ray entering the cell, $\tau_{\nu}(m)$ the optical depth of the ray segment in the cell and $\chi_{\nu}(m)$ the opacity of the material. To obtain the mean intensity, the contributions of all rays crossing the grid cell are added up.

The recombination rates in grid cell m are $\mathcal{R}_{ji}(m) = \alpha_j(T(m)) n_e(m)$, where n_e and T are the electron density and temperature in the cell and $\alpha_j(T)$ is interpolated from tabulated, temperature-dependent recombination rate coefficients containing both radiative and dielectronic contributions. For hydrogen and helium we use the tables of Hummer (1994) and Hummer & Storey (1998); for the metal ions we use the fit functions given by Aldrovandi & Pequignot (1973), Aldrovandi & Pequignot

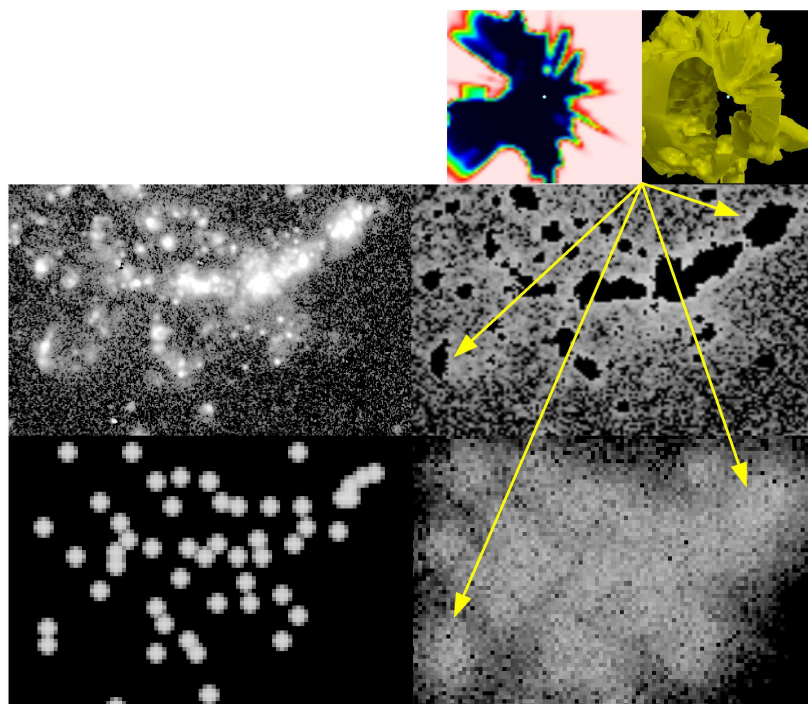


Figure 4.3: Comparison between $H\alpha$ observations of $H\text{ II}$ regions and the DIG in the face-on galaxy M81 by Greenawalt et al. (1998) (middle row) and our simulation results (bottom row) of the ionization of the DIG by radiation escaping from the $H\text{ II}$ regions in the environment of the radiation sources. We find a reasonable qualitative agreement regarding both the dense and relatively intense $H\text{ II}$ regions around the star-forming regions on the left-hand side of the image and the diffuse ionized gas on the right-hand side of the image. (The simulation results presented in this image have been computed for a combination of microclumping and macroclumping with a clumping factor of $f_{\text{cl}} = 5$ each.) The brightness values in these images as well as in Fig. 4.4 represent an emission measure range between 1 and 750 pc cm^{-6} (logarithmic scaling). Observational images: ©AAS. Reproduced with permission.

(1976), Shull & van Steenberg (1982), Nussbaumer & Storey (1983), and Arnaud & Rothenflug (1985), as compiled by D. A. Verner.¹³

To compute the temperature, we consider ionization heating and recombination cooling by hydrogen and helium, as well as free-free cooling and cooling via collisional excitation and radiative de-excitation of bound states. The latter includes cooling through the collisionally excited optical lines of N II, N III, O II, O III, O IV, Ne III, S II, and S III and the fine-structure lines of N II, N III, O III, O IV, Ne II, Ne III, S III, and S IV.

4.3.2 Simulations of the DIG around a spiral arm

With our 3D simulations, we study the ionization ratios in the DIG above and below a section of the galactic disk corresponding to a spiral arm.

In each of our simulations, the stellar population that emits the ionizing radiation is represented by 50 sources, whose positions roughly resemble the distribution of luminous $H\alpha$ emitters in a spiral arm of M81 observed by Greenawalt et al. (1998). The distribution of distances of the sources from

¹³<http://www.pa.uky.edu/~verner/rec.html>

the galactic plane follows an exponential law with a scale height of 90 pc (Bahcall & Soneira 1984). The hydrogen-ionizing flux emitted by each of the sources in the simulation is 7.1×10^{50} photons per second, the emission of photons able to ionize He I and He II is $1.1 \times 10^{50} \text{ s}^{-1}$ and $2.1 \times 10^{46} \text{ s}^{-1}$, respectively.¹⁴ These values were obtained by assuming a star-forming disk galaxy with a continuous star formation rate of approximately $1 M_{\odot} \text{ yr}^{-1}$ like the Milky Way (Robitaille & Whitney 2010) or M 81 (Gordon et al. 2004) and a scale length of the disk of approximately 2 kpc (Porcel et al. 1998), which for a Kroupa IMF with an upper mass limit of $100 M_{\odot}$ in total emits 1.5×10^{53} hydrogen-ionizing photons per second, and multiplying the values with 10 as we assume an enhanced star formation rate in a spiral arm of a star-forming galaxy. This star formation rate was then used as an input to the population synthesis code Starburst99 (Leitherer et al. 1999, Leitherer et al. 2010, Leitherer et al. 2014, Vazquez et al. 2005), where we have chosen the recent Geneva 2012 stellar evolutionary tracks (Ekström et al. 2012, models without rotation) and a slightly subsolar metallicity of $Z \sim 0.014$.

The ionizing flux was then adapted to a simulated volume¹⁵ of $(5 \text{ kpc})^3$, assuming that the center of the simulated volume has a distance of 7.5 kpc from the galactic center (similar to the distance between the galactic center and the position of the sun). This corresponds to a star formation rate of $\sim 0.017 M_{\odot}/\text{yr}$ within the simulated volume.

In the first simulation we assume that the entire radiation is absorbed by H II regions with a hydrogen number density of 2 cm^{-3} . Even with this (in the context of H II regions) comparatively low density, the radii of the ionized regions do not exceed 100 pc. These H II regions are shown in the bottom left panel of Fig. 4.3, where we compare our results for both the H II regions (left-hand side) and the DIG (right-hand side) with an observation by Greenawalt et al. (1998). Among our simulations we find the best agreement to the observations in a model that combines clumping at various scales (see below).

To study the effects of clumping and porosity on the ionization structure of the extraplanar gas, we perform a series of five simulations of the ionization of the DIG for a hydrogen number density that is similar to the values found in the diffuse ionized gas of the Milky Way. For all models, the mean density of the gas in the galactic plane is $n_{\text{H}} = 0.1 \text{ cm}^{-3}$ and its scale height is 1 kpc (Haffner et al. 2009 and references therein). The spectral energy distribution of the flux ionizing the DIG corresponds to that of radiation escaping from a homogeneous H II region having a hydrogen number density of 10 cm^{-3} that absorbs 90% of the hydrogen-ionizing radiation of a source whose energy distribution is that of the synthetic stellar population described above and whose luminosity is 1/50th of that computed for the entire region. We note that this assumption is simplified, because, as shown in Sect. 4.2.3, the filtering of the ionizing radiation depends on the extent of the H II regions and the included stellar population. This means that the spectrum of the radiation that would escape if each of the stellar sources were individually surrounded by an H II region with a given escape fraction is not the same as the spectrum of the radiation escaping from a H II region surrounding a large association of stars. Compared to the energy distribution of the sources, the emergent spectrum is mainly modified by radiation hardening. Whereas for the sources themselves the number ratio between photons able to form He II and those able to form H II is $Q_{\text{HeI}}/Q_{\text{HI}} = 1 : 6.5$, it rises to $1 : 3.75$ for the escaping radiation.

We consider five different scenarios for the density fluctuations in the gas:

1. In the first simulation, the density structure of the gas is smooth, i.e., apart from the exponential drop of the hydrogen density for increasing heights above the galactic plane there are no

¹⁴We currently do not consider a luminosity function of H II regions as described, for instance, by Kennicutt et al. (1989), Oey & Clarke (1998), and Liu et al. (2013).

¹⁵In our simulation, the volume is subdivided into 101^3 grid cells with a volume of $(49.5 \text{ pc})^3$ each.

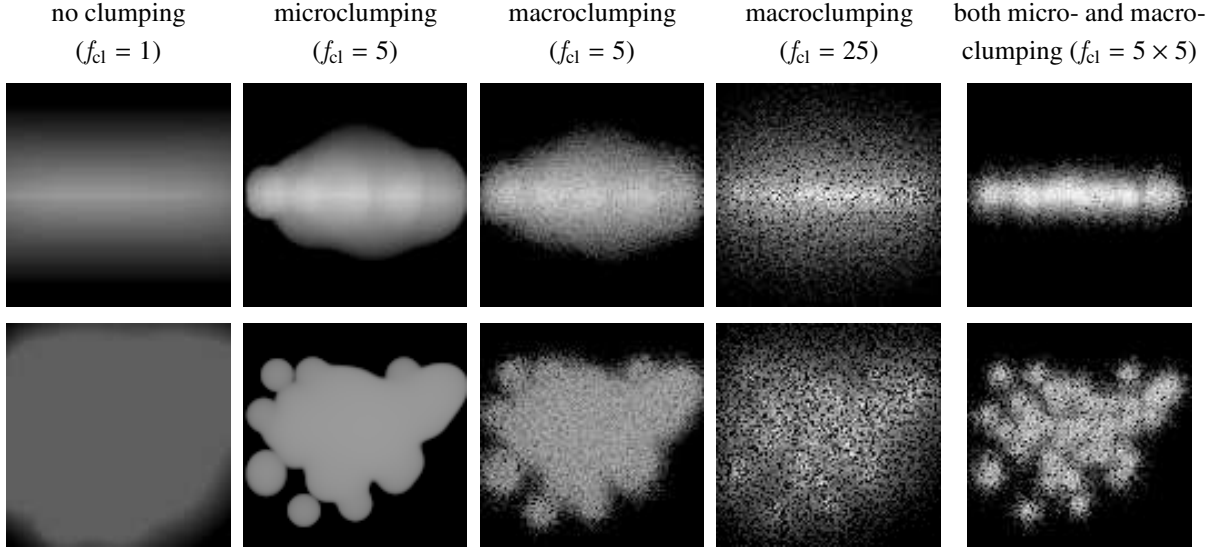


Figure 4.4: Edge-on and face-on emission measure maps for the different simulated clumping scenarios (see text). In each case we have assumed a mean hydrogen number density of $n_{\text{H}}(h) = 0.1 \text{ cm}^{-3} \cdot e^{-|h|/h_0}$, where $|h|$ is the distance from the galactic plane and $h_0 = 1 \text{ kpc}$ is the scale height of the gas. The simulations also share the same distribution and luminosities of the ionizing sources. The edge lengths of the maps are 5 kpc. The macroclumping case with $f_{\text{cl}} = 5$ appears generally very similar to the microclumping case with the same clumping factor, as is expected for sufficiently fine grid resolution. For $f_{\text{cl}} = 25$, the macroclumping becomes very porous at the used grid resolution, opening up channels devoid of gas that allow radiation to escape from the immediate environment of the sources without being absorbed. The combined micro- and macroclumping case with $f_{\text{cl}} = 5 \times 5$ is very different from the macroclumping case with $f_{\text{cl}} = 25$, giving an overall appearance resembling that of the cases with $f_{\text{cl}} = 5$, but with the emission in each of the ionized bubbles more concentrated, somewhat analogous again to the transition from $f_{\text{cl}} = 1$ to $f_{\text{cl}} = 5$.

inhomogeneities.

2. In the second simulation, the gas has a clumping factor of $f_{\text{cl}} = \langle n_{\text{H}}^2 \rangle / \langle n_{\text{H}} \rangle^2 = 5$, a value similar to the one found in the observations by Reynolds (1991). We assume that 20 % of the volume is filled with gas with a hydrogen number density of 0.5 cm^{-3} , whereas the rest of the volume is empty. Here we use the “microclumping” approach, where the clumps are assumed to be optically thin and much smaller than the resolution elements of our simulation. The microclumping case is simulated numerically by multiplying the rate coefficients for the processes involving ion-electron interactions, namely recombination, collisional excitation, and thermal free-free radiation, by the clumping factor, as for otherwise constant conditions the electron number densities in the filled parts of the gas scale with the clumping factor.
3. In the third simulation, we replace the microclumping approach by the assumption of larger-scale inhomogeneities. This is realized by filling only 20% of the grid cells, selected randomly and independently of each other (so that in our simulations the typical length scale of the inhomogeneities corresponds roughly to the cell size of 50 pc), with gas with a density of $n_{\text{H}} = 0.5 \text{ cm}^{-3}$, leaving the rest of the cells empty. While we are certainly aware that this is not necessarily a realistic characterization of the actual statistical distribution of densities in a nonsmooth DIG, we have chosen this description here for two good reasons. First, it is a natural

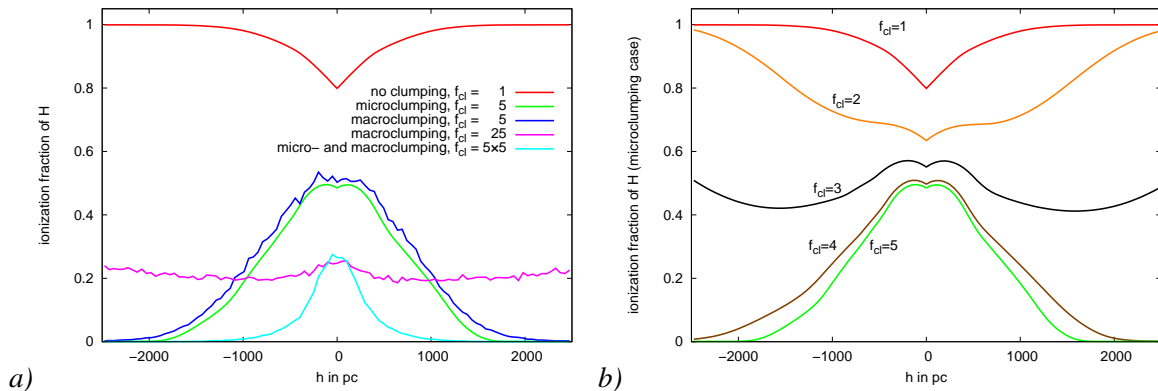


Figure 4.5: *Left:* Ionization fractions of hydrogen as a function of the height above the galactic plane for the different clumping scenarios presented in Fig. 4.4. For the homogeneous density distribution, the gas is predominantly ionized throughout the simulation volume and the ionization fraction rises with increasing galactic heights due to the lower gas densities, which results in decreasing recombination rates and opacities. Both the microclumping case and the macroclumping case with $f_{cl} = 5$ are characterized a similar height dependence, reaching approximately 0.5 near the galactic plane and dropping to 0.1 at a height of about 1.2 kpc. In contrast, in the macroclumping scenario with $f_{cl} = 25$ the ionization fraction varies only slightly throughout the simulation volume. The combination of micro- and macroclumping shows the lowest ionization fraction of all the scenarios, due to the increased recombination rates in the filled cells. While the total clumping factor equals that of the $f_{cl} = 25$ macroclumping case, there are fewer extended empty regions through which radiation can penetrate to greater distances from the galactic plane, where less ionizing radiation is required to maintain the same fraction of ionized hydrogen due to the lower gas densities.

Right: As before, but for a parameter study varying the microclumping factor between 1 and 5. The ionization fraction rises at larger galactic heights in the case of low clumping, whereas it decreases and the gas eventually becomes neutral for high clumping factors. For immediate clumping factors, which for our geometry and density are around $f_{cl} \sim 3$, the ionization fraction as a function of height behaves in a non-monotonic way, first dropping to a minimum and then rising again.

extension of the unresolved (subgrid) microclumping model to a spatially resolved description, as both assume a two-phase medium consisting of swept-up matter and voids. Second, it is the most extreme clumping for a given spatial clumpiness scale. This and the smooth model represent the corner cases between which a more graduated description with intermediate density values would lie.

4. For comparison, we have also performed a simulation where we increased the (macro)clumping factor to $f_{cl} = 25$, i.e., only one out of 25 cells is filled with gas having a hydrogen number density of $n_H = 2.5 \text{ cm}^{-3}$ (in the galactic plane), while the rest of the cells remain empty.
5. Finally, we have simulated a combination of micro- and macroclumping, where both the total amount of gas within each of the grid cells corresponds to the macroclumping case with a clumping factor of $f_{cl} = 5$ and the internal structure of the gas within the single cells is characterized by an additional microclumping factor of 5.

We show both face-on and edge-on emission measure maps¹⁶ of the simulation results in Fig. 4.4 and the ionization fractions of hydrogen as functions of the height above the galactic plane in Fig. 4.5. In the case of the homogeneous gas, ionized hydrogen exists within entire simulation volume, which

¹⁶See Weber et al. (2015) for details on the creation of these maps.

reaches up to 2.5 kpc above the galactic plane. The ionization fraction actually rises at larger heights above the galactic plane due to the lower hydrogen densities, which lead both to lower recombination rates and to a lower opacity of the gas and therefore larger mean free paths of the ionizing photons.

The increased recombination rates in the denser clumps lead to a smaller ionized volume in both the microclumping and the macroclumping case with $f_{cl} = 5$. We find that in these cases the ionization fraction drops to approximately 10% (20% of the maximal value we obtain near the galactic plane) at a height of 1.2 kpc with only small differences between both cases. While clumping increases the recombination rates it also increases the fraction of the volume with below-average densities. Thus, channels may form¹⁷ that allow the ionizing radiation to reach larger distances from its source. This causes the gas to have an ionization fraction of approximately 25% even at large heights above the galactic plane for the $f_{cl} = 25$ case.

The combined micro- and macroclumping case is characterized by the lowest ionization fractions among the simulations. The recombination rates in the filled parts of the volume are equal to the $f_{cl} = 25$ case described above, but due to the larger number of filled cells there are less channels for the radiation to leak out to large distances from the galactic plane.

Fig. 4.5 also visualizes the results of a further parameter study where we have assumed the microclumping scenario and varied the clumping factor between 1 (the unclumped case) and 5 (the microclumping case presented before). The mean densities and ionizing sources are the same as in the previous simulations. In the parameter study the ionization fraction of the gas as a function of the galactic height strongly depends on the clumping factor of the gas. For higher clumping factors, the ionization fraction decreases for larger galactic heights until the gas becomes neutral. In contrast, for low clumping factors the ionization fraction at large galactic heights is larger than within the galactic plane and the ionized region becomes matter-bounded, i.e., ionizing radiation can escape into the intergalactic space. For intermediate clumping factors, the ionization fraction drops until a minimum is reached and then rises again for larger distances from the central plane. The height-dependence of the ionization fraction results from several competing effects. On the one hand, photons have to penetrate the denser, more opaque, layers of gas to ionize high-altitude gas, so that the number of available ionizing photons decreases with increasing height. On the other hand, the recombination rate is lower in the thinner gas above the galactic plane. This increases the equilibrium value for the ionization fraction at higher altitudes. Furthermore, the opacity of the thin gas at large galactic height is lower than the opacity near the galactic plane. A comparison between the results for a clumping factor of 3 and for a clumping factor of 4 shows that the transition between clearly matter-bounded and clearly radiation-bounded ionized gas occurs within a relatively small range for the clumping factor. It can be expected that the ionization structure of the gas at large galactic heights is also strongly affected by slight variations of parameters of the gas that influence the recombination rates, such as the mean density or the temperature, or by a small variation of the amount of ionizing radiation. We note that the numerical values shown in the plots represent lower limits for the ionization fractions, as we assume open boundary conditions, thus neglecting photons entering the volume from the sides.

For the simulations with a clumping factor of $f_{cl} = 5$ and the simulation with combined micro- and macroclumping, we show line ratio maps of the diagnostically important optical lines [N II], [O II], and [O III] relative to $H\beta$ in the face-on view in Fig. 4.6 and in the edge-on view in Fig. 4.7.¹⁸

¹⁷Note that this only happens if the spatial scale on which the medium is clumpy approaches the scale on which the medium becomes optically thick (i.e., the Strömberg radius) (cf. Wood et al. 2005, Owocki et al. 2004). As can be seen by the similarity of the microclumping and macroclumping models with $f_{cl} = 5$, and the subsequent dissimilarity to the $f_{cl} = 25$ macroclumping model, our grid resolution is sufficient to model the onset of this effect. Clumpiness on smaller scales can be adequately represented by microclumping.

¹⁸Because we have not simulated an entire galactic disk, but only a part of it, the *absolute* values of the projected line

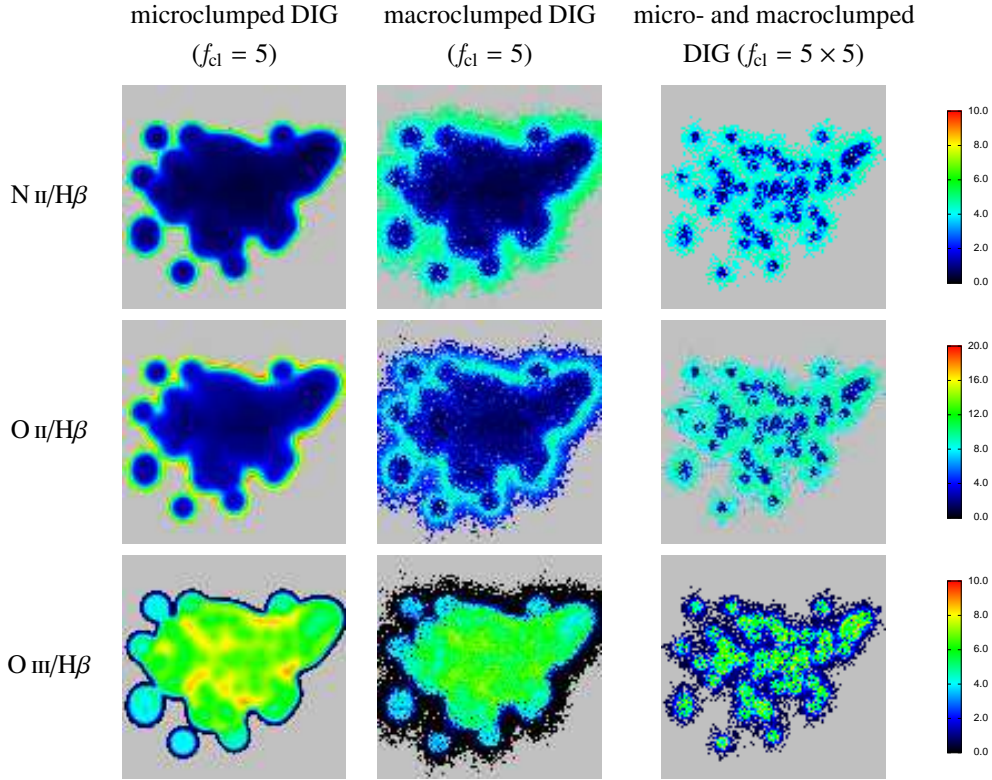


Figure 4.6: Line ratio maps of several collisionally excited lines relative to $H\beta$ in the face-on view of the simulated spiral arm for different density structures of the gas. The gray color indicates emission measures less than 1 pc cm^{-6} .

For the reasons discussed in Sect. 4.2, higher temperatures due to radiation hardening and a larger fraction of singly ionized nitrogen and oxygen, the $[N \text{ II}]/H\beta$ and $[O \text{ II}]/H\beta$ line ratios reach their maximal value in the outer regions of the ionized gas. The $[O \text{ III}]/H\beta$ ratio rises from the galactic plane to its maximal value at heights of up to 800 pc. For larger distances from the galactic plane the $[O \text{ III}]/H\beta$ ratio decreases again. The outermost parts of the ionized gas do not emit $[O \text{ III}]$ line radiation. The overall $[O \text{ III}]/H\beta$ ratios obtained by our 3D simulations are too high to be consistent with the low abundance of ions requiring photons above the ionization threshold of neutral helium to be generated as found, for instance by Reynolds (1985) and Madsen et al. (2006). This could be explained by a lower escape fraction from the galactic plane and a significant contribution of other heat sources, like magnetic reconnection or shocks (cf. Sect. 4.1) or by higher escape fractions of ionizing radiation from $H \text{ II}$ regions around relatively cool ionizing sources (as discussed by Reynolds & Tufté 1995). Furthermore the contribution of the most massive and therefore hottest stars may be lower than assumed in our simulation. This could be either caused by a lower number of stars at the high-mass end of the mass function (for our simulations we assumed a Kroupa IMF with a mass cutoff of $100 M_{\odot}$) or these massive stars may form in larger regions of overdense gas reducing the fraction of radiation being able to escape into the diffuse ionized gas.

intensities in the edge-on views are only a small contribution to the intensity that can be expected from an entire galaxy with the given star formation rate. We furthermore do not account for possible absorption effects by interstellar dust or molecules.

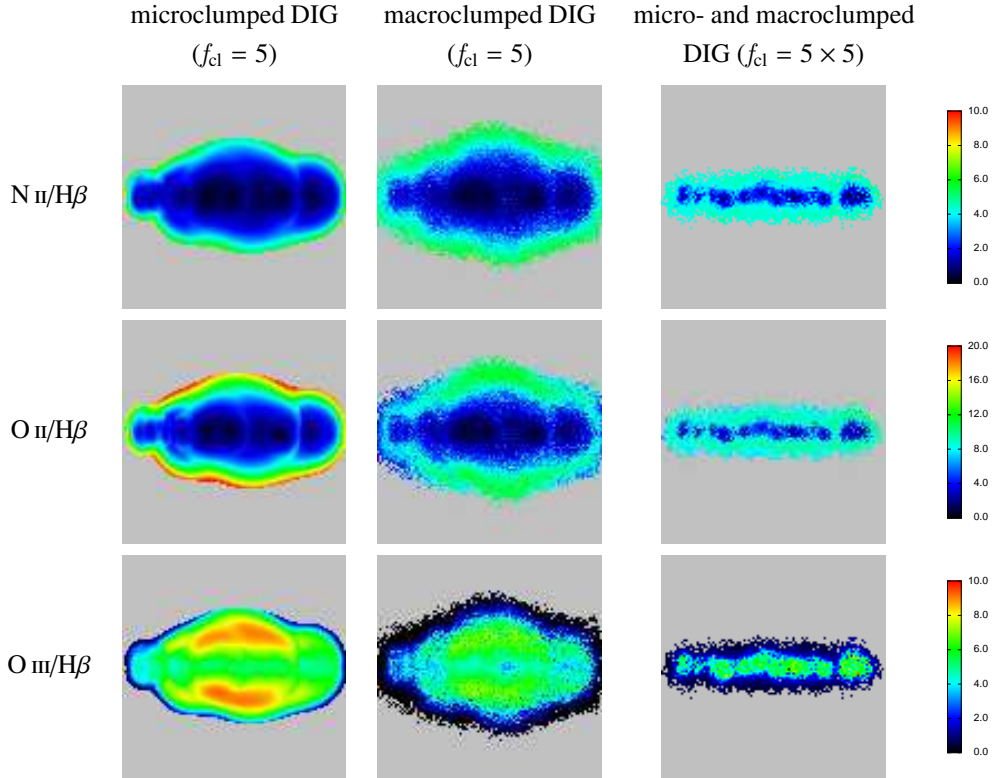


Figure 4.7: As Fig. 4.6, but an edge-on view. Oxygen and nitrogen are predominantly doubly ionized close to the ionizing sources, and singly ionized only in the outer part of the ionized region. Thus, and because of radiation hardening and therefore higher temperatures, the maximum of the line ratios $[N II]/H\beta$ and $[O II]/H\beta$ occurs at larger heights above the galactic plane. For the cases with a clumping factor of $f_{cl} = 5$ the $[O III]/H\beta$ ratio rises up to a height of approximately 700 pc above the galactic plane and drops again at larger distances.

In our simulations we also do not find an increase of the $[O III]/H\beta$ ratio at very large heights above the galactic plane as observed in edge-on galaxies by Otte et al. 2001 and Collins & Rand 2001a, so that additional sources of ionization at larger distances from the galactic plane, such as central stars of planetary nebulae or white dwarfs as proposed by Sokolowski & Bland-Hawthorn (1991) and Flores-Fajardo et al. (2011) and supported by the observational results for galaxies with low star-formation by Lacerda et al. (2018) might need to be considered.

In the simulation with the homogeneous density (not shown in Figs. 4.6 and 4.7) the gas is almost fully ionized and optically thin, so that the effects of photons entering the volume from the sides can not be disregarded. Since we have used open boundary conditions in our simulations these photons are not considered, possibly leading to different results for the ionization structure of metals and consequently for the line emission. In the simulation with $f_{cl} = 25$, on the other hand, most of the grid cells containing gas are optically thick for the ionizing radiation, so that the ionization structure and the properties of the radiation field would in reality vary significantly within the volume of a cell. Because a grid-based approach such as ours assumes that the temperature and ionization structure as well as the radiation field within each cell is constant, this could lead to inaccurate values for the computed emission line ratios.

4.3.3 Comparison with an analytical model for the ionization of the DIG

In this section we compute the height of the layer of ionized gas analytically and compare with the results from the numerical solutions presented above. Hereby we assume a microclumped gas whose mean density declines exponentially as a function of the height above the galactic plane and a purely plane-parallel geometry of the radiation field, without discrete sources, but with a homogeneous flow of ionizing photons emerging from the central plane. For simplicity, we further assume that the gas consists of pure hydrogen with a constant temperature (7500 K) in the ionized volume. For computing the ionization structure we use the Strömberg volume approximation that the gas is either fully neutral or fully ionized.

Under these assumptions we can analytically compute the height z_{\max} of the ionized layer of gas. In equilibrium, the emission rate \dot{N} of ionizing photons equals the number of recombination processes per unit time. Normalized by surface area of the disk the equilibrium can be expressed as

$$\begin{aligned}
 \frac{\dot{N}}{A} &= \int_{-z_{\max}}^{z_{\max}} \alpha_{\text{B}} n_{\text{H II}}(z) n_{\text{e}}(z) f_{\text{cl}} \, dz \\
 &= \int_{-z_{\max}}^{z_{\max}} \alpha_{\text{B}} n_{\text{H II}}(0) e^{-|z|/h} n_{\text{e}}(0) e^{-|z|/h} f_{\text{cl}} \, dz \\
 &= 2\alpha_{\text{B}} n_{\text{H II}}^2(0) f_{\text{cl}} \int_0^{z_{\max}} e^{-2|z|/h} \, dz \\
 &= \alpha_{\text{B}} n_{\text{H II}}^2(0) f_{\text{cl}} h \left(1 - e^{-2z_{\max}/h}\right)
 \end{aligned} \tag{4.5}$$

where α_{B} is the (case-B) recombination coefficient, $n_{\text{H II}}$ the number density of ionized hydrogen and electrons, f_{cl} the clumping factor, and h the scale height of the gas. Equation 4.5 can now be solved for z_{\max} :

$$z_{\max} = -\frac{h}{2} \ln \left(1 - \frac{\dot{N}/A}{n_{\text{H II}}^2(0) f_{\text{cl}} h} \right) \tag{4.6}$$

which becomes infinite for

$$\dot{N}/A \geq \alpha_{\text{B}} n_{\text{H II}}^2(0) f_{\text{cl}} h, \tag{4.7}$$

in which case the ionized gas layer around the disk is no longer radiation-bounded and ionizing radiation can escape into intergalactic space.

For the parameters used in our numerical simulations, namely an ionizing flux of $\dot{N} = 3.55 \times 10^{51} \text{ s}^{-1}$, a section of the galactic plane of $(5 \text{ kpc})^2$, and a (mean) central hydrogen density of 0.1 cm^{-3} , the resulting height of the ionizing layer is $z_{\max} = 221 \text{ pc}$ when assuming microclumping with $f_{\text{cl}} = 5$ and a recombination coefficient of $\alpha_{\text{B}} = 2.8 \times 10^{-13} \text{ cm}^3 \text{ s}^{-1}$. The clumping factor below which the ionization becomes matter-bounded for otherwise unchanged conditions is $f_{\text{cl}} = 1.73$. A comparison of these values with our simulation results shows that for a purely plane-parallel geometry the maximal height of the ionizing gas is lower than in the numerical models that assume discrete sources (compare Fig. 4.5). The clustering of the ionizing sources in the spiral arm locally causes stronger ionizing fluxes of ionizing radiation than the plane-parallel model, allowing the ionizing radiation to reach larger heights above the galactic plane. Conversely, there are also regions in the galactic plane devoid of ionizing sources in the 3D models, so that the gas in these regions remains unionized due to lack of nearby ionizing sources and the absorption by the denser gas at low galactic heights (cf. Fig. 4.5), which is not the case in the simplified analytic model.

4.4 Summary and outlook

The diffuse ionized gas is the major contributor of warm ionized interstellar matter in disk galaxies, but the mechanisms that keep it ionized and determine its energy and density structure are not yet fully resolved. While a number of different ionization scenarios have been suggested, in this work we have concentrated on the ionization of the diffuse interstellar gas by radiation from massive hot stars. Due to their short lifetimes, these objects are associated with star formation regions and are thus concentrated near the galactic disk, so that their ability to ionize the diffuse gas depends on the ability of the emitted radiation to penetrate through the interstellar gas close to the disk.

When the radiation passes through the denser gas surrounding the sources, its attenuation is a function of the frequency-dependent absorption cross-sections of the atoms and ions contained within that gas. Thus the SED of the radiation that penetrates into the DIG can be significantly different from the SEDs of the stellar content of the traversed H II region. The modification of the SEDs depends on the original SED, the escape fraction, and the density distribution of the gas in the environment of the sources, most notably of hydrogen and helium, but also – to a lesser extent and depending on the metallicity of the gas – of carbon, nitrogen, and oxygen ions.

We have studied the dilution effects using both a sophisticated radiative transfer scheme that assumes the problem to be spherically symmetric, as well as a more simplified 3D-approach that, however, dispenses with the requirement of spherical symmetry. For the spherically symmetric case we have computed model grids of the line emission from the matter-bounded H II regions and from the diffuse gas ionized by radiation escaping from these H II regions. For these grids we have used SEDs from state-of-the-art stellar atmosphere models, similar to those which have already previously shown consistently good results as ionizing sources in numerical models of H II regions that were compared with observations. We vary the effective temperature ($30\,000\text{ K} \leq T_{\text{eff}} \leq 50\,000\text{ K}$) and the metallicity ($0.1 Z_{\odot} \leq Z \leq 1.0 Z_{\odot}$) of the model stars, as well as the escape-fraction ($0.05 \leq f_{\text{esc}} \leq 0.7$) of the ionizing radiation escaping from the H II regions around these stars.

As expected, we find that the attenuation accounts for two – partly opposing – effects that result in differences between the emission line spectra of the H II regions and of the diffuse ionized gas. The first effect is radiation hardening: due to the preferential absorption of photons near the ionization thresholds, the ionizing photons that escape from the H II regions are on average more energetic than the photons absorbed in the environment of the sources. Thus, photoionization heating leads to higher temperatures in the DIG than in H II regions, which in turn results in stronger emission of collisionally excited optical lines like N II, O II, or O III.

Second, for stars with effective temperatures $T_{\text{eff}} \lesssim 35\,000\text{ K}$ the volume in which helium is ionized is smaller than the corresponding volume of hydrogen, so that an H II region ionized by such stars (or by a group of stars whose SED is dominated by such stars) can be matter-bounded with respect to hydrogen, but radiation-bounded with respect to helium. In this case the escape fraction of helium-ionizing photons is significantly lower than the escape fraction of hydrogen-ionizing photons, so that the line emission from ions such as O III that require photon energies above the ionization threshold of He I to be formed is reduced or nonexistent in gas ionized by the filtered radiation.

This allows our model DIG to show similar properties as the diffuse ionized gas in the Milky Way, whose observed spectra indicate that both nitrogen and oxygen are predominantly singly ionized and helium appears to be mostly neutral. Nevertheless, stellar radiation with a low number of He-ionizing photons as the sole source of ionization would not be able to account for an increasing [O III]/H β ratio at large distances from the galactic plane as has been observed in the DIG of some edge-on galaxies.

The DIG itself also acts as a filter for the regions farther away from the ionizing sources. To study the effects of different distributions of inhomogeneities in the DIG, we have performed a series of 3D

simulations representing a section of the galactic disk and the diffuse gas above and below it. The models share a common exponential density distribution of the gas but differ in the degree and type of inhomogeneities. We consider three different scenarios: homogeneous gas, inhomogeneous gas with “microclumping” (i.e. the inhomogeneities are optically thin and not spatially resolved within the simulation), and inhomogeneous gas with macroclumping, where we have chosen the inhomogeneities to be of similar scale as the resolution element of the simulation of approximately 50 pc. For the ionizing sources we have used an SED computed using the stellar population synthesis code Starburst99 corresponding to the current star formation rate of the Milky Way. In our simulation, the ionizing flux is equally distributed among a set of sources that are positioned so that their spatial distribution roughly corresponds to those in a spiral arm, and additionally modified by homogeneous H II regions with an escape fraction of 0.1.

We find that small-scale inhomogeneities, as in microclumping, or in macroclumping where the average distance between clumps is smaller than the mean free path of photons in a homogeneous medium, considerably reduce the ability of ionizing photons to escape from the environment of the galactic disk. However, macroclumping with high clumping factors leads to the formation of channels through which the radiation is able to escape from the environment of the galactic disk without being absorbed.

We also find that the $[\text{O II}]/\text{H}\beta$ and $[\text{N II}]/\text{H}\beta$ line ratios increase for larger heights above the galactic plane. However, we find considerably larger $[\text{O III}]/\text{H}\beta$ ratios than observed in the Milky Way or in M31, which may indicate that although the overall number of photons emitted by the stellar population in a star-forming galaxy would be sufficient to ionize the DIG, the filtering characteristics by the stellar environment of the hot massive stars may be different from those we assumed in this simulation.

To explain the deviations, future work may combine 3D simulations with parameter studies regarding the properties of the stellar populations (metallicity, initial mass function, time-dependent effects like starbursts) and consider possible additional energy sources such as magnetic reconnection or hot evolved stars outside the galactic disk.

Acknowledgments We would like to thank to R. Walterbos and the Astrophysical Journal for granting us permission to reproduce the observational images used in Fig. 4.3. This work was supported by the *Deutsche Forschungsgemeinschaft (DFG)* under grant PA 477/18-1 and PA 477/19-1.

5 Summary and conclusions

The knowledge of the interstellar and intergalactic photoionized gas plays an essential role for the understanding of many astrophysical problems. The spatial extents, and the sources of ionization differ considerably among the different occurrences of photoionized gas, e.g., planetary nebulae, “classical” H II regions around hot massive stars, the diffuse ionized gas, active galactic nuclei, and even the reionized intergalactic space of the universe, but all these objects have in common that they consist of dilute gas that is ionized and heated by one or several emitters of photons above the ionization threshold of hydrogen.

The parameters of the photoionized gas strongly depend on its interaction with the radiation field and therefore also on the spectral energy distributions of these ionizing sources. This close connection between the properties of the ionized gas and the spectral energy distributions of the ionizing sources can be utilized to gain information not only about the gas itself, but also about its energy sources. For example, the optical line spectra of H II regions give evidence about the emission of the embedded hot stars in the extreme ultraviolet, which can not be observed directly due to interstellar absorption.

To understand that connection between the ionizing sources and the gas, an accurate quantitative knowledge about the processes that define the state and the observable properties (e.g., its line emission) of the gas is required. Each of the processes that modifies the physical parameters of the gas thereby also changes the extent to which other processes occur. A numerical treatment of photoionized gas is thus based on a system of differential equations that have to be solved for each of the considered volume elements and points in time.

The computational effort further increases if the simulated system lacks inherent symmetry, due to an inhomogeneous density structure of the gas or the presence of multiple ionizing sources. In this cases a fully three-dimensional numerical treatment of the problem is required.

In the introduction of this work (Chapter 1) we have given an overview of the most important types of photoionized gas, discussed observational approaches to determine their properties, and described the physical processes that establish the ionization and temperature structure of the photoionized gas and the resulting emission spectrum. We have concluded the introduction with a discussion of different approximations for the three-dimensional radiative transfer.

Based on this theoretical framework, we have developed a method that allows us to cover a wide range of astrophysical problems connected to photoionized gas in a time-dependent way and in three dimensions, without assuming any symmetry. This methodology has then been applied to the reionized universe, to the connection between galactic H II regions and the spectral energy distribution of the ionizing stars, and to the diffuse ionized gas in disk galaxies.

Below we summarize our studies both with respect our methods and the physical implications of our results.

Did very massive stars of different metallicities drive the second cosmic reionization? First (Chapter 2) we have studied what types of stellar populations could have driven the reionization of the universe, which was completed at $z \sim 6$ (corresponding to a world age of 0.95 Gyr) in the case of hydrogen, but not before $z \sim 2.8$ (corresponding to a world age of 2.3 Gyr) for the reionization of He II to He III.

An obvious candidate as source for the reionization of the universe is the first generation of stars (population III stars) which has formed from primordial gas devoid of metals, a process that might have started as early as $z \sim 30$ (Wise & Abel 2007), i.e., at a world age of 100 Myr. The lack of metals and dust leads to an inefficient cooling of the gas during the star-formation process and possibly inhibits the formation of small fragments that can then collapse and initiate star formation (cf. Abel et al. 2000, Bromm et al. 2002). Therefore, the IMF of the primordial stars may differ significantly from the IMF at present day with a preference to massive stars (Bromm et al. 2002 give masses of $100 \leq M/M_{\odot} \leq 1000$). However, the initial mass function of population III stars is still subject to ongoing research, where some work indicates that the masses of most of the population III stars could be considerably lower (e.g., Greif et al. 2012, Stacy et al. 2016 Fraser et al. 2017) than those mentioned above.

Furthermore, it is likely that the stellar populations had already changed significantly before the reionization of the universe was completed, as the star-forming clouds during the late phase of this period already contained an amount of metals produced by the earlier stellar populations that has been sufficient to increase the efficiency of cooling in the star formation process. This may have led to a population III star formation rate that contributed only a fraction of 10^{-3} to the total star formation rate as early as at a redshift of $z \sim 11 - 13$ (Maio et al. 2010).

To account for the fact that the formation of population III stars had halted to a wide extent before the completion of the reionization, Cen (2003) suggests that there have been two separate epochs of reionization, a first one driven by population III stars at $z \sim 15$ followed by a phase of partial recombination and a second phase of reionization completed at $z \sim 6$.

To investigate whether such a multi-step scenario can lead to a better understanding of the reionization process, we have developed a 3-dimensional radiative transfer code based on a ray-tracing, in order to model and analyze the advancing large-scale ionization including the eventual overlap of the different ionized regions. The main focus of this code is a comprehensive description of the time-dependent ionization structure with regard to a high spectral resolution of the ionizing spectra in order to accurately quantify the evolution of the ionization structures hydrogen and helium.

The geometrical aspects and the time-dependent behavior have been extensively tested by comparisons to analytical models, the results of radially symmetric calculations, and tests presented by the ‘‘Cosmological Radiative Transfer Comparison Project’’ (Iliev et al. 2006). We found good agreement in all of these cases, showing that the important physical mechanisms which control the temporal expansion of the ionization fronts in homogeneous and inhomogeneous gas structures surrounding numerous sources of ionization have been implemented accurately.

As noted above, a realistic modelling of the ionization process requires the consideration of the spectral energy distributions of the ionizing sources. Thus, based on a sophisticated model atmosphere code (Pauldrach et al. 2001, 2004, 2012) which treats the physics of expanding stellar atmospheres consistently, an accurate simulation of realistic SEDs from population III to population I stars at various metallicities, temperatures, and masses has been an important aspect of our work. Because the ionization strongly depends the spectral energy distributions of these sources, especially the emission of photons above the ionization thresholds of the relevant ions (in this study the ionization energies of hydrogen as well as neutral and singly ionized helium), the application of oversimplified spectra (such as blackbodies) can lead to incorrect or misleading results for the ionization structure of the gas exposed to the radiation. We have quantified such possible systematic errors in the context of hot massive stars via a comparison of blackbody and realistic SEDs we have calculated for different metallicities.

In this context we present calculations for the radial ionization structure of hydrogen and helium surrounding $125M_{\odot}$ stars with an effective temperature of 50 000 K stars with various metallicities

($Z = 10^{-3} Z_{\odot}$ to $Z = Z_{\odot}$) that represent the upper end of a Salpeter IMF. Our results show that the variation of the metallicity of the star does not have a strong effect on the emission of hydrogen-ionizing photons, but a pronounced effect on the emission of photons able to generate doubly ionized helium, where, depending on metallicity, the He II ionizing fluxes differ by four orders of magnitude.

In a next step, analogous computations are performed for very massive stars (VMS) as sources of ionization. Such objects may have formed in runaway merging processes in dense clusters (Pauldrach et al. 2012) and can clearly exceed the upper mass limit of approximately $150 M_{\odot}$ for direct star formation assumed for a chemically evolved stellar population. In our simulations we considered the most massive and hottest of the model stars presented by Pauldrach et al. (2012), with masses of $3000 M_{\odot}$ and an effective temperature of $T_{\text{eff}} = 65\,000$ K, where we have considered a model with a metallicity of $0.05 Z_{\odot}$, a model with Z_{\odot} , and a model with solar metallicity but an increased mass fraction of helium in the stellar atmosphere. Like for the $125 M_{\odot}$ stars we find no strong dependence of the hydrogen-ionizing fluxes on the composition of the stellar atmospheres, but a decreasing emission of He II ionizing photons for the models with higher metallicity.

Overall, the hydrogen-ionizing fluxes of the $3000 M_{\odot}$ stars exceed those of the $125 M_{\odot}$ stars by ~ 1.6 dex, but by a factor of approximately 3 dex with respect to their He II-ionizing fluxes (for solar metallicity the factor is even 7 dex). This means that the He II-ionizing flux per unit of stellar mass of the VMS exceeds the one of the “normal” O stars by a factor of ~ 30 in the case of the metal-poor stars to over 200 000 for solar metallicity. As expected, the radii of the respective H II and He III Strömgen spheres scale for otherwise equal conditions with the third root of the corresponding ionizing fluxes.

In the context of the first stage of the reionization history we have shown results of representative 3D radiative transfer simulations which are based on massive population III stars with effective temperatures of $T_{\text{eff}} \sim 10^5$ K surrounded by a primordial environment reflecting a homogeneous intergalactic cosmological gas at $z \sim 15$ (assuming a star formation rate corresponding to Hernquist & Springel 2003 and stellar masses of $100 M_{\odot}$). The calculations showed that our population III stars were able to reionize H as well as He on a timescale of just $t \sim 50$ Myr (corresponding to $\Delta z \sim 1.5$ at $z = 15$) within our chosen volume of comoving $(5.3 \text{ Mpc})^3$. As we are aware that the assumption of a homogeneous universe is just a rough approximation of the real situation, we have further calculated models based on inhomogeneous density structures, simulating volumes that comprise multiple ionizing sources on smaller scales. The “clumpiness” of the gas (including the star-forming density peaks of the ISM) results in considerably more complex ionization structures than those of models with homogeneous gas distributions, and as a consequence the fraction of ionizing photons which can escape their local environment and reach the intercluster medium can differ significantly. To estimate these escape fractions we have modelled inhomogeneous environments with fractal density structures of different sizes and mean densities ranging from the density of star-forming H II regions to that of the diluted interstellar gas. The result of these simulations is that strong variations of the amount of ionizing radiation able to reach the intergalactic medium can result from even small variations in the amount of the absorbing matter in the immediate environment of the ionizing sources.

Thus, a precise determination of this value would require the knowledge of the statistics of the density distribution in the small-scale environment of the sources (i.e., on the order of parsecs to a few kiloparsecs). Furthermore, for a given density distribution the escape-fractions are a function of the photon energy, and reach their minimum just blueward of the ionization edge of He II. The spectral energy distribution of the ionizing radiation escaping into the IGM may thus be different from the intrinsic SEDs of the stellar sources.

Next we studied whether chemically evolved stellar populations were able to complete the second stage of reionization until a redshift of $z \sim 6$ for H and at a redshift of $z \sim 2.8$ for the ionization of He II to He III.

Based on plausible numbers for a standard population we have approximated in a first step the SED of a cluster with a Salpeter IMF by the SED of its most luminous members, namely $125 M_{\odot}$ stars with effective temperatures of 50 000 K, and normalized the result to the same hydrogen-ionizing flux. Our calculations show that these objects have, for cosmological star formation rates as given by Lineweaver (2001), been able to reionize H again (for our chosen volume the process required a time scale of $\Delta t \sim 500$ Myr, corresponding to the redshift interval between $z \sim 10$ and $z \sim 6$), but not He II, which is not unexpected as, from similar considerations, other investigations (Wyithe & Loeb 2003, Glezer et al. 2005, and McQuinn et al. 2009) have also concluded that the sources for the reionization of hydrogen are different from the sources of the reionization helium to He III.

To investigate whether the appearance of very massive, already metal-enriched population II and population I stars could have contributed to the reionization of He II we replaced the $125 M_{\odot}$ stars by the runaway collision mergers of $M = 3000 M_{\odot}$ and effective temperatures of 65 000 K. The result is striking: In contrast to the case where the stellar populations follow a Salpeter or Kroupa IMF our simulations now show that the helium in the universe could have been fully reionized within approximately 2 Gyr (corresponding to a redshift of $z \sim 2.5$) in an environment where a fraction of 1 % of the mass formed into stars consists of mergers resulting in very massive stars, provided that the merger products are characterized by effective temperatures of $T_{\text{eff}} = 65\,000$ K. We note that this percentage is consistent with the mass ratio obtained for intermediate mass black holes (IMBHs) and supermassive black holes (SMBHs) relative to the stellar mass found in the bulges of active galaxies and globular clusters like ω Centauri, and that such VMSs might be possible progenitors of IMBHs and SMBHs. This result therefore offers an at least complementary scenario for the explanation of the reionization of He II to He III at a time where the metallicity of the universe has already reached a value that prevented the formation of population III stars.

SEDs of massive stars and time-dependent modelling of metals in H II regions. In Chapter 3 we investigate the relationship between the spectral energy distributions of hot massive stars and the ionization and temperature structure as well as the emitted spectrum of the surrounding H II regions.

First we have created a grid of dwarf and supergiant model stars in the temperature range between 30 000 K to 55 000 K and in the metallicity range between $0.1 Z_{\odot}$ and $2.0 Z_{\odot}$. The parameter space has been chosen to cover that of observed O stars in the present-day universe. For each of these models we have computed the photon emission rates above the ionization thresholds of hydrogen as well as neutral and singly ionized helium. We also consider the fluxes above the thresholds for photon energies required for the production (or destruction) of metallic ionic species that are important for the temperature structure and the emitted spectrum of H II regions. Specifically, we have considered the energies for the transitions $\text{S II} + \gamma \rightarrow \text{S III} + e^{-}$, $\text{O II} + \gamma \rightarrow \text{O III} + e^{-}$, and $\text{Ne II} + \gamma \rightarrow \text{Ne III} + e^{-}$.

We find that the fluxes in these energy ranges decrease with increasing stellar metallicities due to the enhanced line blocking in the atmospheres of the stars, whereby the effect becomes more important for higher ionization energies.

Additionally, we have performed the same analysis for the models of very massive stars (first presented by Pauldrach et al. 2012) that might have formed in dense clusters and may considerably exceed the mass range of “normal” O type stars. For these objects we have considered masses from $150 M_{\odot}$ to $3000 M_{\odot}$ and temperatures from 40 000 K to 65 000 K. (The models at the upper limit of the mass and temperature range had already been used in the previous chapter to represent the sources that could have contributed to the reionization process.)

The spectral energy distributions of the model stars have been made publicly available and have also been used by Rubin et al. (2016), where the trend that lower metallicity is associated with higher

ionization stages has been observationally confirmed.

The SEDs of our O star models have then been used to describe the ionizing sources in spherically symmetric photoionization models to gauge the effect of stellar and gas metallicity on the ionization structure of the H II regions. For the spherically symmetric simulations we have used the numerical method also used for the stellar atmosphere models, which has been adapted to the dilute radiation fields and low particle number densities in H II regions (Hoffmann et al. 2012). To achieve a more realistic computation of the cooling rates in the ionized gas – and consequently more realistic values for the line emission line ratios – our spherically symmetric method has been complemented with consideration of cooling by infrared emission, which is caused by transitions from the collisionally excited sublevels of the ground states of N II, N III, O III, O IV, Ne II, Ne III, S III, and S IV.

As expected from the SEDs in our O star model grid, for a given stellar effective temperature the integrated number fractions of the different ionization stages of the metals in the gas strongly depend on the metallicity-dependent SEDs for those species whose ionization energies lie above the ionization edge of He I. Furthermore, even at the same metallicity and temperature, the stronger stellar winds of the supergiant stars lead to different ionizing flux ratios compared to the dwarf models. For example, the volume ratio of ionized helium to ionized hydrogen is larger by a factor of 8 in the case of the H II regions around the supergiant stars with an effective temperature of 30 000 K compared to the dwarf stars of the same temperature.

To judge the effects of an inhomogeneous density distribution of the gas on the nebular line emission we have set up simulations in which a stellar source is embedded in gas with a fractal density distribution. The results of these simulations, which we have performed for the dwarf model stars with an effective temperature of 40 000 K and metallicities of $0.1 Z_{\odot}$ and Z_{\odot} , have then be compared with simulations where we have assumed a homogeneous density distribution, but kept the other simulation parameters (ionizing SED and metallicity in the gas).

To perform this analysis, we have extended our existing 3D approach that had been used to simulate the reionization process before. Now, the first four ionization stages of the abundant metals C, N, O, Ne, and S are considered and the time-dependent temperature structure is computed consistently with these changes. Because of the larger number of volume elements ($\sim 10^6$) that have to be considered in the 3D case compared to the spherically symmetric case, where just about 100 depth points are sufficient, we have performed the 3D simulations using the nebular approximation. This approximation assumes that each recombination, ionization, or collisional excitation process occurs from the ground state of the corresponding atom or ion, a condition which is to a very good degree fulfilled in the dilute gas considered in the simulations performed for this study.

By postprocessing the results of these simulations, we have computed integrated line-of-sight intensities and shown synthetic narrow-band images for the emission the diagnostically important optical lines of [O II] and [O III]. For the inhomogeneous density structure the intensity distribution is characterized the presence of higher peaks of the observable line intensities for a given mean density of the gas. Still, we find no relative changes above 20% in the total emission per line, indicating that simplified assumptions about the density distribution of the gas will still lead to reasonable results concerning the overall emission.

Our simulations have been performed in a time-dependent way, assuming an initially neutral gas and sources of ionization that instantaneously start to emit radiation and do not change their spectral energy distribution during the simulated time. Under these conditions, a notable result with regard to the temporal evolution of the H II regions is the brief “overshooting” of the gas temperatures significantly above the equilibrium value when the gas is passed by the ionization front. However, because of the short timescales until equilibrium is reached (on the order of 10 000 years for a hydrogen density of $n_{\text{H}} = 10 \text{ cm}^{-3}$), and because in reality the ionizing sources themselves evolve, this is unlikely

to be of high practical significance for the analysis of H II regions with current models.

Finally, we have studied the effects of clustering of stars in two limiting cases, a dense cluster where the distances between the stars become irrelevant compared to the extent of the combined H II region, and a loose association where the distances between the stars are of the same order as the Strömgen radii, so that the individual H II regions only partly overlap. Between both cases the considered emission lines (H α , [N II], [O II], and [O III]) differ by less than 10%.

Numerical Models for the Diffuse Ionized Gas in Galaxies. In Chapter 4 we have studied to what extent hot massive stars close the galactic plane are able to ionize the diffuse ionized gas (DIG) and whether the observed line ratios in that component of the interstellar gas can be explained by such an ionization scenario.

In spite of its low density of roughly $n_e = 0.1 \text{ cm}^{-3}$, the total emission of the diffuse ionized gas in a star-forming galaxy is of the same order as the emission from denser H II regions in the immediate environment of the sources of ionization (Zurita et al. 2000), which is a result of its large spatial extension – the diffuse ionized gas has been found up to several kiloparsecs above the galactic planes.

The mechanisms that provide the energy required to maintain that component are still not fully understood. While a number of different ionization scenarios have been suggested that involve, for example, hot evolved stars (Sokolowski & Bland-Hawthorn 1991, Flores-Fajardo et al. 2011), shocks (Collins & Rand 2001a), and magnetic reconnection processes in the ionized interstellar medium (Hoffmann et al. 2012), in this work we have concentrated on the ionization of the diffuse interstellar gas by radiation from massive hot stars that are found in the planes of the galactic disks. Their ability to ionize the diffuse gas depends on the ability of the emitted radiation to escape the interstellar gas close to the disk.

When the radiation passes through the denser gas surrounding the sources, its attenuation is a function of the frequency-dependent absorption cross-sections of the atoms and ions contained within that gas. Thus the SED of the radiation that penetrates into the DIG can be significantly different from the SED of the stellar content of the traversed H II region. The modification of the SEDs depends on the original SED, the escape fraction, and the density distribution of the gas in the environment of the sources, most notably of hydrogen and helium, but also – to a lesser extent and depending on the metallicity of the gas – of carbon, nitrogen, and oxygen ions.

For the numerical simulation of the DIG both in spherical symmetry and in 3D we have used the numerical methods developed for our simulations of the reionization process and properties of the H II regions described above.

For the spherically symmetric case we have computed model grids of the line emission from the matter-bounded homogeneous H II regions and from the diffuse gas ionized by radiation escaping from these H II regions. For these grids we have used a subset of the SEDs of the stellar atmosphere models created for the previous study. We vary the effective temperature ($30\,000 \text{ K} \leq T_{\text{eff}} \leq 50\,000 \text{ K}$) and the metallicity ($0.1 Z_{\odot} \leq Z \leq 1.0 Z_{\odot}$) of the model stars and we assume different the escape-fractions ($0.05 \leq f_{\text{esc}} \leq 0.7$) of the ionizing radiation escaping from the H II regions around these stars. Additionally, we have considered a “picket-fence” case, in which the shape of the ionizing spectrum is not altered. This corresponds to an escape fraction of 1 as well as to a “grey” absorption, where the transmission is independent of the wavelength. The latter situation occurs if the absorption is caused by clumps that are optically thick in each wavelength range, but simultaneously there are channels devoid of material where no absorption occurs at all. Obviously, both the assumption of homogeneous H II regions and the assumption of a “gray” absorption by thick clumps are extreme cases and the real situation lies in between.

As expected, we find that the attenuation accounts for two – partly opposing – effects that result in differences between the emission line spectra of the H II regions and of the diffuse ionized gas. The first effect is radiation hardening, where due to larger absorption cross-sections for photons near the ionization thresholds, the ionizing photons that escape from the H II regions are on average more energetic than the photons absorbed in the environment of the sources. This leads to higher temperatures in the gas ionized by radiation whose spectral distribution has already been modified by the gas closer to the source. The higher temperatures in turn lead to an increased emission of the strongly temperature-dependent collisionally excited optical lines of nitrogen and oxygen.

Second, for stars with effective temperatures $T_{\text{eff}} \lesssim 35\,000$ K the volume in which helium is ionized is smaller than the corresponding volume of hydrogen, so that an H II region ionized by such stars (or by a group of stars whose SED is dominated by such stars) can be matter-bounded with respect to hydrogen, but radiation-bounded with respect to helium. In this case the escape fraction of helium-ionizing photons is significantly lower than the escape fraction of hydrogen-ionizing photons, or practically absent. Consequently, the line emission from ions such as O III that require photon energies above the ionization threshold of He I to be formed is reduced or nonexistent in gas ionized by the filtered radiation.

We find the best agreement between our simulations and the observed line ratios in the Milky Way and in M 31, which indicate a soft ionizing spectrum, if we assume that the ionization of the diffuse ionized gas is mainly driven by such relatively cool O stars.

On the other hand, an ionization scenario dominated by relatively cool O stars near the galactic plane is unable to explain the rising [O III]/H β ratios at large distances from the galactic plane, as has been observed in the DIG of some edge-on galaxies, so that additional energy sources are likely.

The DIG itself also acts as a filter for the regions farther away from the ionizing sources. To study the effects of different distributions of inhomogeneities in the DIG, we have performed a series of 3D simulations representing a section of the galactic disk and the diffuse gas above and below it. The models share a common exponential density distribution of the gas but differ in the degree and type of inhomogeneities. We consider three different scenarios: homogeneous gas, inhomogeneous gas with “microclumping” (i.e., the inhomogeneities are optically thin and not spatially resolved within the simulation), and inhomogeneous gas with macroclumping, where we have chosen the inhomogeneities to be of similar scale as the resolution element of the simulation of approximately 50 pc. For the ionizing sources we have used an SED computed using the stellar population synthesis code Starburst99 by Leitherer et al. (2014) corresponding to the current star formation rate of the Milky Way. In our simulations, the ionizing flux is equally distributed among a set of sources that are positioned such that their spatial distribution resembles those in a spiral arm, and additionally modified by homogeneous H II regions with an escape fraction of 0.1.

We find that small-scale inhomogeneities, where the average distance between clumps along the direction of the photons is smaller than the mean free path of photons in an homogeneous medium, considerably reduce the ability of ionizing photons to escape from the environment of the galactic disk. This is a result in the of the increased recombination rates in the filled parts of the gas.

However, if the distance between the clumps becomes large compared to the mean free path of ionizing photons within the ionized medium, channels form that allow the ionizing radiation to escape from the environment of the galactic disk or even to enter the intergalactic space, contributing to the ionization of the intergalactic matter.

Concerning the line ratios find that [O II]/H β and [N II]/H β increase for larger heights above the galactic plane. However, we find considerably larger [O III]/H β ratios than observed in the Milky Way or in M 31, which may indicate that although the overall number of photons emitted by the stellar population in a star-forming galaxy would be sufficient to ionize the DIG, the filtering characteristics

by the stellar environment of the hot massive stars may be different from those we assumed in this simulation. Like our spherically symmetric models this indicates that either the diffuse radiation field is dominated by relatively cool source of ionization or photoionization is not the only significant energy source for the diffuse ionized gas.

A Computational aspects of our 3D radiative transfer approach

This appendix contains a short description of technical and numerical aspects of the 3D radiative transfer code that has been newly developed in the context of this work. The program that implements the approach is called `occup_3d_ext`.

A.1 The iteration scheme of the simulation runs

The rough structure of the program run is shown in Fig. A.1. First the initial conditions of the simulated system, i.e., the density, ionization, and temperature structure of the gas as well as the positions and spectral energy distributions of the ionizing sources, are set up based on the data provided in the input files (see below). This is followed by the main loop of the program, where for each time step the radiative transfer procedure is performed and the ionization and temperature structure are recomputed. Based on the change of temperature and ionization structure, the length of the next time step is computed (cf. Sect. A.3). The loop is iterated until the chosen simulated time (with respect to the initial state of the simulated system) has been reached. Optionally the program can consider the cosmological expansion of space according to Eq. 2.16 by adjusting the size of the grid cells and reducing the number densities of the gas accordingly after each timestep. During the loop and at the end of the simulation snapshots of the files are written that can be used by post-processing or visualization tools. The numerical methods used for the computations are described in detail in sections 2.2, 2.3, and 3.3.2.1.

A.2 Input to and output from the simulations

Specification of the simulation parameters In the main input file the variables that specify the behavior of the program and the initial conditions of the simulated system are read using a Fortran namelist. As the file is passed to the program via standard input, the name of the file does not matter. The notation of the values corresponds to the notation that is used in Fortran source code. If no value is assigned to a variable in the input file, the default values are used. For some variables there are no default values, which may lead to undefined behavior. However, these variables are only evaluated if certain options are switched on.

The sources of ionization are usually described in a separate file, with the default name `sources.txt`. The structure of the file is as follows:

- The first line of the file can contain an arbitrary text (so that it can be used for comments or explanations) and is not evaluated.
- The second line contains the (integer) number of sources.
- The third line is a comment (or empty) again.

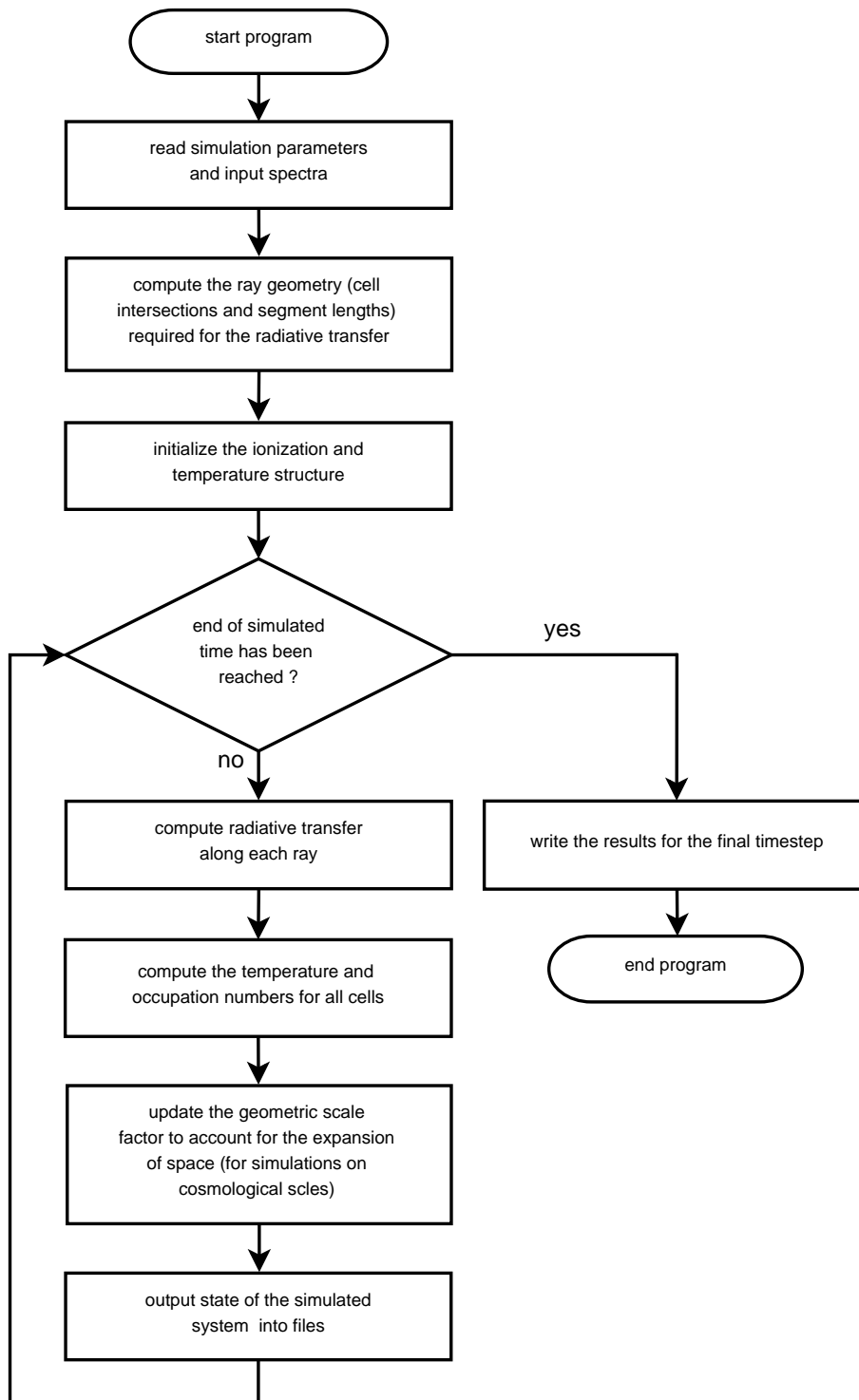


Figure A.1: Flow-chart of the steps performed in during the execution of the 3-dimensional radiative transfer program.

- The fourth line has the structure
 x y z *radius* *spectrum* *start* *stop*
Here the integer values x , y , and z represent the indices of the cell the source is located in¹. *radius* is the radius of the source in units of solar radii. If the source is not a spherical object (such as an entire star cluster, for example), an equivalent radius has to be chosen that yields the desired luminosity. *spectrum* is the name of a file that contains the description of the SED of the ionizing source. `occup_3d_ext` can read files containing the SEDs, whose data format corresponds to that of the files written by the “WM-Basic” method (cf. Pauldrach et al. 2001, 2004, 2012, 2014 and Hoffmann et al. 2012).
- Further sources are described the same way as the first source. The descriptions of two different sources are separated by a comment line.

If the simulated system has an inhomogeneous density structure, the user can specify it in a text file, whose format is compatible to the program package IFRIT². In the first line the dimension of the simulated volume in units of grid cells is set. (Note that the physical size of the simulated volume additionally depends on the grid cell edge length.) Because of the symmetry of the coordinate system – the cell with the coordinates (0, 0, 0) is located in the center of the simulated volume – the first line has the form

$$“2 \times x_{\max} + 1 \quad 2 \times y_{\max} + 1 \quad 2 \times z_{\max} + 1”$$

For example, if $x_{\max} = 20$, $y_{\max} = 30$, and $z_{\max} = 40$, then the first line is “41 61 81”.

The remaining lines contain in their first column the total hydrogen number density and in their second column the number density of neutral hydrogen in units of cm^{-3} at the beginning of the simulation. The file may contain no empty lines or comments and must end with a newline character. The order of the lines is such that first x -coordinate is incremented, then the y -coordinate, and finally the z -coordinate.

Alternatively the program can, read the temperature structure and the ionization structure of each considered element in a format that corresponds to the output data described below (for example, from a previous program run) and use these data as initial conditions for a new program run. This can also be used for resuming a program run in the case of an interruption of the computation, which is important as depending on the simulated system a computing run can require several days.

The structure of the output data. In the files that describe the ionization structure, the first n columns contain the number densities (in units of cm^{-3}) of the ionization stages E^0 (i.e., neutral atoms) to E^{n-1} of the corresponding element (the suffix of the files corresponds to the element symbol). The last column contains the total number density of the atoms/ions belonging to the corresponding element. Currently included are hydrogen (H^0 and H^+), helium (He^0 , He^+ , and He^{2+}), and the ionization stages E^0 to E^{+3} of the elements C, N, O, Ne, S and Ar. Additionally a file (suffix `.e`) is written that contains the electron number density in units of cm^{-3} .

¹The range of the indices x , y , and z is defined by the input parameters x_{\max} , y_{\max} and z_{\max} such that $-x_{\max} \leq x \leq +x_{\max}$, $-y_{\max} \leq y \leq +y_{\max}$, and $-z_{\max} \leq z \leq +z_{\max}$. Thus the cell with the coordinates (0, 0, 0) is always located in the center of the simulated volume.

²IFRIT is a program by N. Gnedin that allows the visualization of ionization fronts and density structures. The free software can be obtained from <https://sites.google.com/site/ifrithome/> and is available for Windows and for Unixes.

In `occup_3d_ext` all files that describe the properties of the individual cells are read or written in a fileformat that can be read by IFRIT.

If the energy balance and the temperature structure are computed, the program also writes output files that describe the temperature structure of the simulated volume at the given time step:

- The file with the suffix `.temp.txt` contains in its first column the temperature of the cells before the past time step in K, in its second column the temperature after the past time step in K, and in its third column the mean value of the temporal derivative of the temperature dT/dt in units of K/yr.
- The file with the suffix `.energy.txt` contains in its only column the value of the thermal energy density in units of erg cm^{-3} .
- The files with the ending `xx.heatcool.txt`, where `xx` is the name of the respective element, contain the heating and the cooling rates per element. In the IFRIT compatible files the first column contains the heating rates, the second column the cooling rates, and the third column the difference between the heating and the cooling rates. The values are given in units of $\text{erg s}^{-1}\text{cm}^{-3}$.

The first column of the file `time.txt` contains the length of the past time step in years, the second column the total simulated time since the start of the simulated process and the third the counter for the time steps. The fourth column is the wall-clock time required per iteration cycle, the fifth column the CPU time per iteration cycle. A comparison of the two latter values indicates how well the code is parallelized (see Sect. A.3). If the simulation parameters are chosen such that the program considers the cosmological expansion of space, the redshift for each of the time steps is inserted as the third column.

Optionally the escape fraction from the volume is written as a function of the wavelength in files with the suffix `.escape.txt`. The escape fraction is computed separately for each of the sources. The first column contains the wavelength in \AA and the second the fraction of escaping photons for that wavelength.

A.3 Performance aspects

Even if the 3D radiative transfer is solved using the approximations as discussed in Sect. 1.6 and Sect. 2.3, it still requires a large computational effort that scales at best linearly with the number of resolution elements, so that, for example, the computational effort to solve a simulation grid with 100^3 grid cells is at least 8 times larger than for the same simulation resolved in only 50^3 grid cells. The factor can be considerably larger if the aim is to trace the temporal evolution of the system, because smaller grid cells are crossed by an ionization front in a shorter time and therefore smaller time-steps have to be chosen (as we will discuss in Sect. A.3.3). To be able to perform reasonably resolved simulations it is therefore essential that the numerical approach is “parallelized”, which means that the computations are distributed among several CPUs located on a single computer and/or several computing nodes. After a discussion of different approaches to parallelization and motivating our choice for OpenMP, we will describe our implementation of the parallelization and show tests of its efficiency.

A.3.1 Overview over different approaches to parallel computing

There exist several approaches to parallelize the processing of large amounts of data (here we mention only the most important ones in the context of scientific programming).

In the case of *automatic parallelization* the compiler tries to detect loops whose instructions can be distributed among several processes³. The main advantage of this approach is that it does, in principle, not require extra source code and is a built-in feature of modern compilers like Intel Fortran or GCC. However, automatic parallelization is likely to fail if the loops contain instructions that may introduce side-effects, such as subroutine calls. Furthermore, automatic parallelization usually only works for shared-memory architectures, i.e., single computers where the processes can directly access the same memory, but not among different computers within a cluster.

By contrast, the basic idea behind the *Message Passing Interface (MPI)* is that the data shared between the parallel processes have to be explicitly sent among them as the processes can not access each others memory directly. While this approach increases the development effort connected with the parallelization, it is very flexible. It can, for instance, be used both on single shared memory machines and among compute clusters, where a network is used to exchange the data. MPI is available for all relevant platforms and can be used to combine different computing architectures. It is therefore the most used solution for computing processes distributed over a very large number of CPUs (super-computing). Examples of MPI implementations of radiative transfer codes are the ones described by Ercolano (2002), Petkova & Springel (2009), and Petkova & Springel (2011)⁴.

The approach of *OpenMP* lies between the automatic parallelization and MPI. In contrast to MPI, the communication between the single processes does not need to be implemented explicitly, but the programmer has to declare which of the variables have to be copied to each process and where a syncing of the processes is required to avoid race conditions⁵. Current OpenMP implementations only work on shared-memory machines and does not support the prallelization of a programming process among different machines communicating via a network. The syntax of OpenMP directives is implemented such that compilers not supporting OpenMP will ignore them. OpenMP-based code can therefore be programmed such that it works correctly as serial programs when built with such compilers. OpenMP is currently (2018) supported by most compilers, so that OpenMP-based code remains portable. Implementations of parallel radiative transfer codes using OpenMP have been described by Gritschneider et al. (2009) and Partl et al. (2011).

Graphic processing units (GPUs, graphics cards) or similar coprocessors are efficient in performing the same mathematical operations on a set of multiple data at the same time (SIMD: single instruction multiple data, an approach similar to the concept of dedicated vector computers), so that considerable performance gains can be achieved for the solution of problems that involve such tasks, as is often the case for vector and matrix operations. These gains vanish for computations that do not involve the simultaneous execution of the same instructions for multiple data. Furthermore, the communication between the main processor and the GPUs can be critical. Heymann & Siebenmorgen (2012) have implemented a 3D radiative transfer code for dust using GPUs to accelerate the computations.

It is possible to combine these methods. For example several computers running OpenMP programs can communicate with each other among a network using MPI.

³In this section we use the expression “process” as a generic term that can refer both to a “full” process (“*task*”) with a memory space separated from the memory spaces of other processes and to a light-weight subprocesses (“*thread*”) that shares the same memory space with other subprocesses.

⁴The latter two code utilize a combination of MPI and OpenMP (see below).

⁵A race condition occurs if several processes try to write to the same variable at the same time. In this case the resulting value of the variable is undefined.

A.3.2 Parallelization of the 3D radiative transfer code used in this work

As we run our simulations on multi-core, shared-memory workstations and our aim was a portable code, we have decided to parallelize our code using OpenMP directives.

We parallelized the radiative transfer routines as well as the solvers that compute the ionization and the temperature structure of the gas.

The radiative transfer has been parallelized such that if there are n processes, each of these performs the radiative transfer for $1/n$ -th of the rays. The rays are distributed among the processes such that the processes that run in parallel compute the radiative transfer for rays with similar directions. This is realized using the HEALPix (nested) numeration scheme for the different ray directions (Górski et al. 2005, cf. also Sect. 1.6.1), which in most cases tends to assign consecutive numbers to neighboring directions. The aim of such a distribution is to minimize the effects of direction-dependent lengths of the rays which occur if a source is not centered in the simulation volume: As the radiative transfer is halted when the border of the simulation volume is reached, the computational effort to trace shorter rays is lower than for longer rays. Thus, distributing the rays such that parallel-running processes compute rays with considerably different lengths lead to different run times of the processes. Consequently the processes tracing the short rays would be idle until the processes tracing the longer rays are finished.

Concerning the computation of the ionization and temperature structure we had initially chosen a parallelization over the different z -indexes of the grid cells as the loop over these indexes is the outermost loop and therefore the computational effort required for the synchronization of the processes is minimized. The disadvantage of this approach is that it does not scale well if the number of processes is no longer small compared to the number of cells along the z -axis. The reason is that the largest number of cells that have to be computed by an individual process is

$$N_{\max_per_process} = N_x \cdot N_y \cdot \left\lceil \frac{N_z}{N_{\text{processes}}} \right\rceil, \quad (\text{A.1})$$

where N_x , N_y , and N_z are the number of cells along the coordinate axes and $N_{\text{processes}}$ is the number of parallel processes. The ceiling symbols ($\lceil \cdot \rceil$) indicate that if the fraction is not equal to an integer, it has to be rounded up to the next larger integer, whereas for an ideal scaling behavior each of the processes would have to process the total number of grid cells divided by the number of processes. We show $N_{\max_per_process}$ as a function of $N_{\text{processes}}$ in Fig A.2. The maximal time required for an individual process corresponds to the total time to complete the computation of the corresponding loop, because no code after the loop can be executed before each of the processes has completed.

To reduce the uneven distribution of the computed cells among the processes, we have finally replaced the parallelization over the z -coordinates by a parallelization over a consecutive number assigned to each grid cell. The grid coordinates of each cell are then computed as a function of its number. In this case the maximal number of grid cells that have to be computed per process is reduced to

$$N_{\max_per_process} = \left\lceil \frac{N_x \cdot N_y \cdot N_z}{N_{\text{processes}}} \right\rceil \quad (\text{A.2})$$

and the number of cells per thread differs by at most one.

We have found the computational effort to perform that transformation to be small compared to the performance gain resulting from the more efficient parallelization. For a system with 41^3 grid cells where 12 parallel processes have been used⁶, the new parallelization scheme has lead to an overall

⁶The number has been chosen to match the number of physical CPU cores on the test machine.

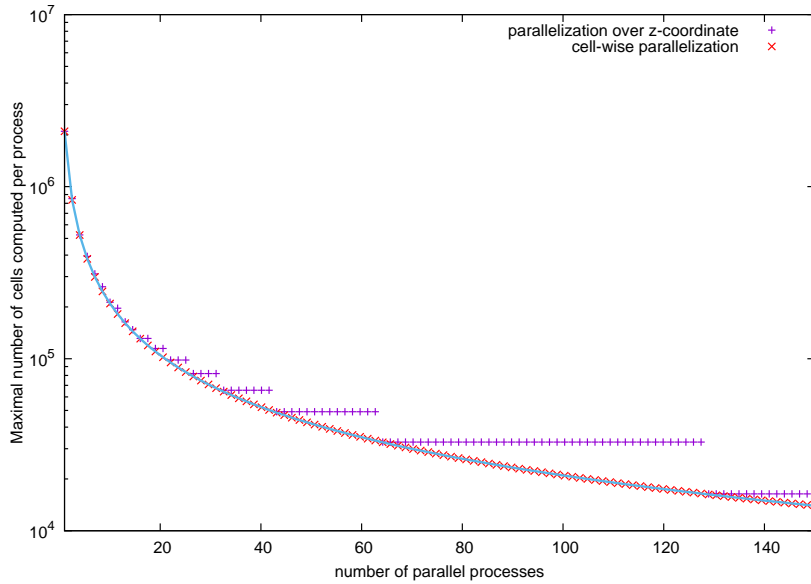


Figure A.2: The position of the purple crosses corresponds to the maximal number of grid cells whose properties have to be computed by an individual process as a function of the number of parallel process for a grid with 128^3 cells if the parallelization is performed over the z -index. As all cells with the same z -index are always computed by the same process, the maximal amount of grid cells that has to be computed by an individual process is no longer the same for each thread. indirectly proportional to the number of parallel processes if the number of parallel processes is not small compared to the number of cells along the z -axis. If the parallelization is performed over a consecutive number assigned to each grid cell, the computational effort can be distributed more evenly (red crosses) so that the number of grid cells that have to be processed by thread varies at most one grid cell and thus almost perfectly resembles the ideal scaling behavior (blue line).

reduction of the required time per iteration cycle of approximately 10%. Depending on the geometry of the simulation volume and the number of parallel processes, the results will differ considerably. The performance measurements described below have been carried out using the more even distribution.

A.3.3 Tests of the scaling behavior

Scaling with the number of parallel threads. To test how the run time of our program scales with the number of parallel processes we have repeated the same simulation with 1 to 12 parallel processes⁷. The test simulation consists of a box with 41^3 cells, a simulated volume of $(30 \text{ pc})^3$, a homogeneous hydrogen number density of 10 cm^{-3} (initially the gas is neutral), and a chemical composition that corresponds to the solar abundances. As ionizing source we have chosen the 40 kK dwarf model with solar metallicity described in Sect. 3.2.2. The radiation field of the stars has been split into 196 608 rays so that there are approximately 10 rays per cell at the outer edge of the simulation volume. The simulation included computation of the temperature structure of the gas and the ionization structure of the metals. The simulated time was 30 000 yrs, after which equilibrium was approximately reached. In Fig. A.3 we show the execution speed of the simulation (in units of iteration cycles per hour of wall-clock time) as a function of the number of processes and compare it with the ideal case of a

⁷The test have been performed on a workstation with 12 physical cores, so we have chosen 12 as the maximal number of parallel processes.

performance that scales linearly with the number of processes. In Fig. A.4 we show the efficiency, i.e., the quotient of the measured and the ideal performance. We find that the efficiency is approximately 95 % when the number of processes is increased from 1 to 2. For 4 processes, the efficiency drops to approximately 80 % and remains above 70 % for up to 10 processes. Between 10 and 12 processes (i.e., the number of processes that corresponds to the number of physical cores) there is a notable loss of efficiency, which might be related to the other programs running on the same machine (e.g., the graphical user interface) that compete with the simulation program for CPU time and memory access.

Note that these values may differ considerably for different simulation parameters and for different compilers⁸ or hardware.

In addition to our test of the efficiency of the parallelization, we have also studied the relationship between number of grid cells and sources and the computational effort required for the simulation. This was realized by simulating the same physical system as described in Sect. A.3.3. The total time needed for the execution of the simulation on the one hand depends on the time for the completion of one time or, more generally, iteration step and on the other hand on the number of steps the simulation has to perform until the required degree of convergence is reached.

For the simulation treated here, the length of the time steps is set to

$$\Delta t_{\text{new}} = \min \left(\max \left(0.15 \times \min_{\text{all cells}} \Delta t_{\text{old}} \frac{n_e}{\Delta n_e}, 0.15 \times \min_{\text{all cells}} \Delta t_{\text{old}} \frac{n_{\text{H I}}}{\Delta n_{\text{H I}}} \right), \max_{\text{all cells}} \Delta t_{\text{old}} \frac{500 \text{ K}}{\Delta T} \right), \quad (\text{A.3})$$

where Δt_{old} is the duration of the previous time step. Δn_e , $\Delta n_{\text{H I}}$ and ΔT are the changes of the electron number density, the number density of neutral hydrogen, and the temperature during the previous time step. (As we now fully consider changes in the temperature structure, we have to add the change the timescale for heating/cooling processes as an additional criterion to the one presented in Sect. 2.2.2.1.) n_e and $n_{\text{H I}}$ are the number densities of electrons and neutral hydrogen atoms after that time step. The simulation starts with the gas being initially neutral, and the source(s) of ionization are switched on at $t = 0$. The simulation stops at $t = 30\,000 \text{ yr}$ when temperature and ionization structure have almost reached their equilibrium values. Our results for resolutions of 21^3 , 41^3 , and 81^3 grid cells are presented in Table A.1.

As expected, the CPU time per iteration is approximately proportional to the number of grid cells within a factor of less than 1.5 for the tested simulations. The deviation from the theoretical linear scaling are likely to be related to the fact that when using the ‘‘HEALPIX’’ scheme the number of simulated rays can only be varied by factors of 4, such that, even if only cubical volumes are considered, the computational effort for the ray-tracing procedure shows strong deviations from a direct proportionality to the number of grid cells.

For the system with 41^3 grid cells, we have additionally switched off the computation of the temperature structure or both inclusion of the metal ions and the temperature structure and compared the the computation time with that for the run that includes both. We find only a modest ($< 5 \%$) reduction of the run time per iteration cycle, if only the computation of the temperature is switched off, but not considering changes in the temperature structure partly allows larger time-steps. Consequently the number of time-steps required until the simulation is completed is reduced (for our test by approximately 30 %). For a fixed temperature, neglecting the metals in the gas does not further reduce the number of time steps, which are mainly controlled by the changes of the temperature structure and the ionization fractions of hydrogen, but reduces the computational effort per time step (for the test case presented here by 30 %).

⁸For the performance testes presented here we have used Version 16 of the Intel Fortran compiler.

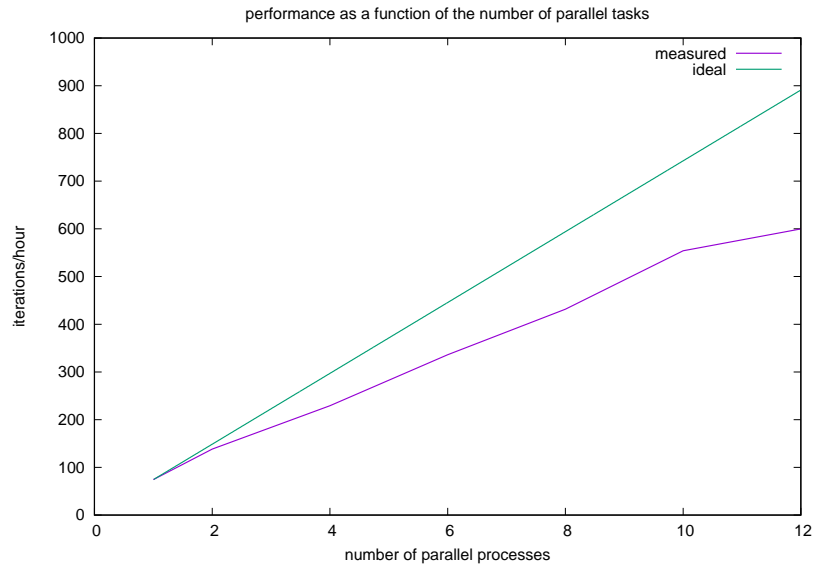


Figure A.3: Performance of the simulation in iteration cycles per hour of wall-clock time as a function of the number of computing processes. The purple line shows the measured values. By comparison, the green line shows a linear scaling of the performance for one process with the number of processes, which would describe the performance for an ideal parallelization.

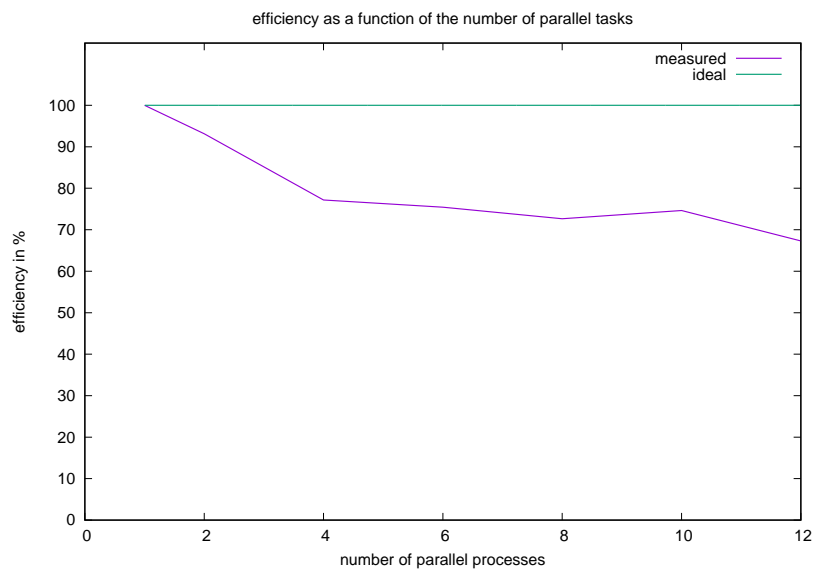


Figure A.4: In our test case, the efficiency, which is defined as the ratio between the required wall-clock time of the program run and the wall-clock time required for run with a single process divided by the number of processes, time of the parallelization drops to approximately 67 % for 12 parallel processes.

Table A.1: Computational effort and memory usage of the simulations in dependence of the number of grid cells N_{cells} , the number of sources N_{sources} , the computation of the temperature structure, and the inclusion of metals. For each of the systems we consider an ionizing radiation source that corresponds to the radiation of a 40 kK main sequence star with 10 solar radii. For the simulation No. 5, we consider 25 sources with $10/\sqrt{10} \approx 3.16$ solar radii at the same position, such that the total emission into the surrounding gas remains the same. The source(s) is/are centered in a cubical box with a volume of $(30 \text{ pc})^3$, which is filled with an initially neutral gas whose hydrogen number density a density of $n_{\text{H}} = 10 \text{ cm}^{-3}$. The simulation traces the first 30 000 years after the source(s) is/are switched on. The composition of the gas corresponds to the solar one, except for the simulation that does not consider metals at all. As each of the simulations is performed with 12 parallel processes, the table shows both the wall clock time for the simulation, i.e., the time between the start and the end of the simulation, and the required CPU time. The relative value always refers to run No. 2, the run with 41^3 grid cells, one source, and consideration of both metals and temperature structure (highlighted in the table by a grey background).

Run no.	1	2	3	4	5	6
N_{cells}	21^3	41^3	81^3	41^3	41^3	41^3
	(9 261)	(68 921)	(531 441)	(68 921)	(68, 921)	(68 921)
relative value	0.13	1.00	7.71	1.00	1.00	1.00
N_{sources}	1	1	1	1	1	10
N_{rays}	49 152	196 608	786 432	196 608	196 608	$10 \times 196 608$
relative value	1/4	1	1	1	1	10
consideration of metals	yes	yes	yes	yes	no	yes
computation of temperature	yes	yes	yes	no	no	yes
iteration cycles	344	631	1 139	432	433	631
relative value	0.55	1.00	1.81	0.68	0.71	1.00
total wallclock time in s	$2.63 \cdot 10^2$	$3.79 \cdot 10^3$	$7.05 \cdot 10^4$	$252 \cdot 10^3$	$1.88 \cdot 10^3$	$3.013 \cdot 10^4$
relative value	0.07	1.00	18.6	0.66	0.50	7.95
total CPU time in s	$3.15 \cdot 10^3$	$4.42 \cdot 10^4$	$8.25 \cdot 10^5$	$2.93 \cdot 10^4$	$2.20 \cdot 10^4$	$3.46 \cdot 10^5$
relative value	0.07	1.00	18.69	0.66	0.50	7.85
wallclock time / iteration in s	0.76	6.00	61.86	5.82	4.35	47.75
relative value	0.13	1.00	10.31	0.97	0.73	7.96
CPU time / iteration in s	9.15	69.97	724.42	67.88	50.78	548.98
relative value	0.13	1.00	10.35	0.97	0.73	7.85
CPU time / wallclock time	11.97	11.66	11.71	11.66	11.67	11.50
RAM usage in MB	39	252	1809	251	235	252
relative value	0.15	1.00	7.17	1.00	0.93	1.00

For the same simulated physical system a higher resolution requires a larger number of time-steps, because the ionization state (and temperature) of the volume represented by a smaller cell changes quicker when it is crossed by an ionization front than the larger volume represented by a cell in a low-resolution simulation.

The computational effort for the ray-tracing procedure to determine the mean intensity within the grid cells is approximately proportional to the number of sources for otherwise identical simulation parameters. By contrast, the computation time required to set up and solve the rate equation systems and to consider the heating and cooling processes is independent of the number of sources. To study the influence of multiple sources on the total time required by a simulation run we have performed a test run (with 51^3 grid cells, and the consideration of metals and heating/cooling processes) where we have replaced the source with a radius of $R = 10 R_{\odot}$ by 25 sources with radii of $R = 10 R_{\odot} / \sqrt{25} = 2 R_{\odot}$. These sources are located in the center of the simulated volume such that the total radiation field corresponds to the simulation with a single cell. In this case the time required per iteration step is increased by a factor of approximately 16 for the simulation that includes 25 sources. This means that for the given simulation parameters approximately 60 % of the computation time are used for the computation of the radiative transfer.

A.4 Outlook and future work

The expected future increase of computational resources will allow extending the current capabilities of the presented method. This refers both to improvements of the numerical approach and to a better coverage of the relevant parameter space concerning the properties of the ionizing sources and the simulated gas. Among these improvements we consider:

Increasing the spatial resolution. In various problems concerning the photoionized gas, the relevant length scales differ by several orders of magnitude. Examples are the ionization of the extended warm ionized medium by radiation leaking from porous H II regions in the environment of hot stars, or the reionization of the universe. For a grid of equally-sized grid cells it would therefore cause a prohibitive computational effort to simultaneously simulate the small-scale and the large-scale processes. There are several approaches to overcome the problem. In this work we have chosen to first simulate the smaller scales and inserting the results (or approximations to the results, for example the escape fractions of ionizing photons from H II regions) as input parameters for the simulations of the larger scale processes (e.g., the ionization of the diffuse interstellar or the intergalactic medium). The use of adaptive mesh-refinement techniques (like in O’Shea et al. 2004, Petkova & Springel 2011, or in Hubber et al. 2016), where the size of the grid cells can be adapted to the respectively relevant length scales could enable the consideration of processes that occur at the various scales within a single simulation run.

Extension of the considered atomic data. The architecture of the developed program allows a straightforward integration of new chemical elements, additional ionization stages, or improved models for the already included atoms or ions. These can be added when required for the study of the corresponding radiative transfer problem. The full consideration of the excited states, as it has been implemented in the spherically symmetric method used in this work can, in principle, also be combined with our three-dimensional radiative transfer scheme. Especially denser environments, that no longer fulfill the conditions required for the nebular approximation, might be more accurately described by such an approach. Combining a complex chemical network with a large

number of grid cells leads, however, to very large demand of both CPU time and memory. Therefore such a combined method would require developing a strategy concerning the distribution of the computations among a larger number of nodes in an effective way.

Inclusion of dust and molecules. The abundance ratios between metal species can differ significantly between the gas phases of H II regions and stellar atmospheres. For example, the abundance of sulfur compared to neon appears to be significantly lower in both galactic and extragalactic H II regions than in the solar atmosphere (Rubin et al. 2008). The discrepancy can be explained by the different depletion of various elements from the gas phase onto dust grains. Dust depletion and the interaction between dust particles and the radiation field might also be responsible for the absence of observations of very cool H II regions even for gas with supersolar metallicity (Shields & Kennicutt 1995). Thus the quality of the results, especially in metal-rich regions, could be enhanced by the consideration of the dust depletion factors and the dust-radiation interaction.

Like other stars, the O stars that act as sources of ionization are formed within clouds consisting of molecular gas and dust. Due to their short lifetimes of a few million years their presence remains strongly correlated with these clouds, as can be seen, for example, in Fig. 1.2. The molecular clouds interact with the stellar radiation by acting as absorbers on the one hand and being modified with respect to their molecular content on the other hand. For example, the mass function of the first stars and the possible formation of primordial supermassive black holes strongly depends on the dissociation of molecular hydrogen due to Lyman-Werner photons ($h\nu \geq 11.2 \text{ eV}$) by stellar radiation (such systems have, for example, been studied by Petkova & Maio 2012 and Maio et al. 2016). The complexity of the molecular networks – especially in the case of the present-day universe where metal compounds like CO are present – requires, however, a trade-off between a comprehensive coverage of the relevant chemical processes and the computing requirements.

Inclusion of hydrodynamics. So far, the described 3D code considers the temporal evolution of the ionization structure under the assumption that the total mass of the gas in each grid cell remains constant. However, hot massive stars are able to alter the density structure of the gas in their environment by their radiation pressure, their stellar winds, and finally by supernovae explosions. Therefore we aim to combine the existing code with hydrodynamical methods.

Bibliography

- Abel T., Norman M. L., & Madau P.: *Photon-conserving Radiative Transfer around Point Sources in Multidimensional Numerical Cosmology*. *ApJ* **523**, 66 (1999)
- Abel T., Bryan G. L., & Norman M. L.: *The Formation and Fragmentation of Primordial Molecular Clouds*. *ApJ* **540**, 39 (2000)
- Abel T. & Wandelt B. D.: *Adaptive ray tracing for radiative transfer around point sources*. *MNRAS* **330**, L53 (2002)
- Aldrovandi S. M. V. & Pequignot D.: *Radiative and Dielectronic Recombination Coefficients for Complex Ions*. *A&A* **25**, 137 (1973)
- Aldrovandi S. M. V. & Pequignot D.: *Erratum; Radiative and Dielectronic Recombination Coefficients for COM plex Ions*. *A&A* **47**, 321 (1976)
- Aller L. H., Ufford C. W., & van Vleck J. H.: *Multiplet Intensities for the Nebular Lines $\lambda^4S - \lambda^2D$ of O II*. *ApJ* **109**, 42 (1949)
- Alvarez M. A., Bromm V., & Shapiro P. R.: *The H II Region of the First Star*. *ApJ* **639**, 621 (2006)
- Anderson H., Ballance C. P., Badnell N. R., & Summers H. P.: *An R -matrix with pseudostates approach to the electron-impact excitation of H I for diagnostic applications in fusion plasmas*. *Journal of Physics B: Atomic, Molecular and Optical Physics* **33**, 1255 (2000)
- Arnaud M. & Rothenflug R.: *An updated evaluation of recombination and ionization rates*. *A&AS* **60**, 425 (1985)
- Asplund M.: *New Light on Stellar Abundance Analyses: Departures from LTE and Homogeneity*. *ARA&A* **43**, 481 (2005)
- Asplund M., Grevesse N., Sauval A. J., & Scott P.: *The Chemical Composition of the Sun*. *ARA&A* **47**, 481 (2009)
- Bahcall J. N. & Soneira R. M.: *Comparisons of a standard galaxy model with stellar observations in five fields*. *ApJS* **55**, 67 (1984)
- Baker J. G. & Menzel D. H.: *Physical Processes in Gaseous Nebulae. III. The Balmer Decrement*. *ApJ* **88**, 52 (1938)
- Balsler D. S., Rood R. T., Bania T. M., & Anderson L. D.: *H II Region Metallicity Distribution in the Milky Way Disk*. *ApJ* **738**, 27 (2011)
- Barger A. J., Cowie L. L., & Richards E. A.: *Mapping the Evolution of High-Redshift Dusty Galaxies with Submillimeter Observations of a Radio-selected Sample*. *AJ* **119**, 2092 (2000)

- Barnes J. E., Wood K., Hill A. S., & Haffner L. M.: *Models of diffuse H α in the interstellar medium: the relative contributions from in situ ionization and dust scattering*. *MNRAS* **447**, 559 (2015)
- Becker R. H., Fan X., White R. L., Strauss M. A., Narayanan V. K., Lupton R. H., Gunn J. E., Annis J., Bahcall N. A., Brinkmann J., et al.: *Evidence for Reionization at $z \sim 6$: Detection of a Gunn-Peterson Trough in a $z = 6.28$ Quasar*. *AJ* **122**, 2850 (2001)
- Belkus H., Van Bever J., & Vanbeveren D.: *The Evolution of Very Massive Stars*. *ApJ* **659**, 1576 (2007)
- Bennert N., Jungwiert B., Komossa S., Haas M., & Chini R.: *Size and properties of the narrow-line region in Seyfert-1 galaxies from spatially-resolved optical spectroscopy*. *A&A* **459**, 55 (2006)
- Bennert V. N., Auger M. W., Treu T., Woo J.-H., & Malkan M. A.: *The Relation between Black Hole Mass and Host Spheroidal Stellar Mass Out to $z \sim 2$* . *ApJ* **742**, 107 (2011)
- Bisbas T. G., Wünsch R., Whitworth A. P., Hubber D. A., & Walch S.: *Radiation-driven Implosion and Triggered Star Formation*. *ApJ* **736**, 142 (2011)
- Blum R. D. & Pradhan A. K.: *Rate coefficients for the excitation of infrared and ultraviolet lines in C II, N III, and O IV*. *ApJS* **80**, 425 (1992)
- Bresolin F. & Kennicutt R. C., Jr.: *Optical Spectroscopy of Metal-rich H II Regions and Circumnuclear Hot Spots in M83 and NGC 3351*. *ApJ* **572**, 838 (2002)
- Bromm V., Coppi P. S., & Larson R. B.: *The Formation of the First Stars. I. The Primordial Star-forming Cloud*. *ApJ* **564**, 23 (2002)
- Brown A. G. A., Dekker G., & de Zeeuw P. T.: *Kinematic ages of OB associations*. *MNRAS* **285**, 479 (1997)
- Burgess A.: *Delectronic Recombination and the Temperature of the Solar Corona*. *ApJ* **139**, 776 (1964)
- Butler K. & Zeippen C. J.: *Atomic data from the IRON Project. V. Effective collision strengths for transitions in the ground configuration of oxygen-like ions*. *A&AS* **108**, 1 (1994)
- Caffau E., Bonifacio P., François P., Spite M., Spite F., Zaggia S., Ludwig H.-G., Steffen M., Mashonkina L., Monaco L., et al.: *A primordial star in the heart of the Lion*. *A&A* **542**, A51 (2012)
- Carroll B. W. & Ostlie D. A.: *An introduction to modern astrophysics and cosmology*. (2006)
- Cedr s B., Cepa J., Bongiovanni  ., Casta neda H., S nchez-Portal M., & Tomita A.: *Two-dimensional metallicity distribution of the ionized gas in NGC 628 and NGC 6946*. *A&A* **545**, A43 (2012)
- Cen R.: *The Universe Was Reionized Twice*. *ApJ* **591**, 12 (2003)
- Chluba J. & Sunyaev R. A.: *Two-photon transitions in hydrogen and cosmological recombination*. *A&A* **480**, 629 (2008)
- Ciardi B., Ferrara A., Marri S., & Raimondo G.: *Cosmological reionization around the first stars: Monte Carlo radiative transfer*. *MNRAS* **324**, 381 (2001)

- Clark P. C., Glover S. C. O., Smith R. J., Greif T. H., Klessen R. S., & Bromm V.: *The Formation and Fragmentation of Disks Around Primordial Protostars*. *Science* **331**, 1040 (2011)
- Cocato L., Gerhard O., Arnaboldi M., Das P., Douglas N. G., Kuijken K., Merrifield M. R., Napolitano N. R., Noordermeer E., Romanowsky A. J., et al.: *Kinematic properties of early-type galaxy haloes using planetary nebulae*. *MNRAS* **394**, 1249 (2009)
- Collins J. A. & Rand R. J.: *Ionization Sources and Physical Conditions in the Diffuse Ionized Gas Halos of Four Edge-On Galaxies*. *ApJ* **551**, 57 (2001a)
- Collins J. A. & Rand R. J.: *Shocks as a Secondary Source of Ionization in Diffuse Ionized Gas Halos*. In: Hibbard J. E., Rupen M., & van Gorkom J. H. (eds.): *Gas and Galaxy Evolution*. *Astronomical Society of the Pacific Conference Series* **240**, 392 (2001b)
- Converse J. M. & Stahler S. W.: *The dynamical evolution of the Pleiades*. *MNRAS* **405**, 666 (2010)
- Cowie L. L. & Songaila A.: *High-resolution optical and ultraviolet absorption-line studies of interstellar gas*. *ARA&A* **24**, 499 (1986)
- Crowther P. A., Schnurr O., Hirschi R., Yusof N., Parker R. J., Goodwin S. P., & Kassim H. A.: *The R136 star cluster hosts several stars whose individual masses greatly exceed the accepted 150 M_{solar} stellar mass limit*. *MNRAS* **408**, 731 (2010)
- Dale J. E. & Bonnell I.: *Ionizing feedback from massive stars in massive clusters: fake bubbles and untriggered star formation*. *MNRAS* **414**, 321 (2011)
- Dale J. E., Ercolano B., & Bonnell I. A.: *Ionizing feedback from massive stars in massive clusters - III. Disruption of partially unbound clouds*. *MNRAS*, 587 (2013)
- Dinerstein H. L., Lester D. F., & Werner M. W.: *Far-infrared line observations of planetary nebulae. I - The forbidden O III spectrum*. *ApJ* **291**, 561 (1985)
- Dufour R. J., Talbot R. J., Jr., Jensen E. B., & Shields G. A.: *M83 II: Spectral characteristics and chemical abundances of H II regions*. *ApJ* **236**, 119 (1980)
- Dufour R. J.: *The composition of H II regions in the Magellanic Clouds*. In: van den Bergh S. & de Boer K. S. D. (eds.): *Structure and Evolution of the Magellanic Clouds*. *IAU Symposium* **108**, 353 (1984)
- Ebisuzaki T., Makino J., Tsuru T. G., Funato Y., Portegies Zwart S., Hut P., McMillan S., Matsushita S., Matsumoto H., & Kawabe R.: *Missing Link Found? The "Runaway" Path to Supermassive Black Holes*. *ApJ* **562**, L19 (2001)
- Ekström S., Georgy C., Eggenberger P., Meynet G., Mowlavi N., Wyttenbach A., Granada A., Decressin T., Hirschi R., Frischknecht U., et al.: *Grids of stellar models with rotation. I. Models from 0.8 to 120 M_{\odot} at solar metallicity ($Z = 0.014$)*. *A&A* **537**, A146 (2012)
- El Eid M. F., Fricke K. J., & Ober W. W.: *Evolution of massive pregalactic stars. I - Hydrogen and helium burning. II - Nucleosynthesis in pair creation supernovae and pregalactic enrichment*. *A&A* **119**, 54 (1983)
- Elmegreen B. G. & Falgarone E.: *A Fractal Origin for the Mass Spectrum of Interstellar Clouds*. *ApJ* **471**, 816 (1996)

- Ercolano B.: *Three Dimensional Monte Carlo Simulations of Ionized Nebulae*. University College London (2002)
- Ercolano B., Barlow M. J., Storey P. J., & Liu X.-W.: *MOCASSIN: a fully three-dimensional Monte Carlo photoionization code*. *MNRAS* **340**, 1136 (2003)
- Ercolano B., Barlow M. J., & Storey P. J.: *The dusty MOCASSIN: fully self-consistent 3D photoionization and dust radiative transfer models*. *MNRAS* **362**, 1038 (2005)
- Ercolano B., Bastian N., & Stasińska G.: *The effects of spatially distributed ionization sources on the temperature structure of HII regions*. *MNRAS* **379**, 945 (2007)
- Ercolano B., Young P. R., Drake J. J., & Raymond J. C.: *X-Ray Enabled MOCASSIN: A Three-dimensional Code for Photoionized Media*. *ApJS* **175**, 534 (2008)
- Fan X., Narayanan V. K., Lupton R. H., Strauss M. A., Knapp G. R., Becker R. H., White R. L., Pentericci L., Leggett S. K., Haiman Z., et al.: *A Survey of $z > 5.8$ Quasars in the Sloan Digital Sky Survey. I. Discovery of Three New Quasars and the Spatial Density of Luminous Quasars at $z \sim 6$* . *AJ* **122**, 2833 (2001)
- Fan X., Carilli C. L., & Keating B.: *Observational Constraints on Cosmic Reionization*. *ARA&A* **44**, 415 (2006a)
- Fan X., Carilli C. L., & Keating B.: *Observational Constraints on Cosmic Reionization*. *ARA&A* **44**, 415 (2006b)
- Ferland G. J., Porter R. L., van Hoof P. A. M., Williams R. J. R., Abel N. P., Lykins M. L., Shaw G., Henney W. J., & Stancil P. C.: *The 2013 Release of Cloudy*. *Rev. Mexicana Astron. Astrofis.* **49**, 137 (2013)
- Flores-Fajardo N., Morisset C., Stasińska G., & Binette L.: *Ionization of the diffuse gas in galaxies: hot low-mass evolved stars at work*. *MNRAS* **415**, 2182 (2011)
- Ford H., Peng E., & Freeman K.: *Extragalactic Planetary Nebulae*. In: Da Costa G. S., Sadler E. M., & Jerjen H. (eds.): *The Dynamics, Structure & History of Galaxies: A Workshop in Honour of Professor Ken Freeman*. *Astronomical Society of the Pacific Conference Series* **273**, 41 (2002)
- François P., Matteucci F., Cayrel R., Spite M., Spite F., & Chiappini C.: *The evolution of the Milky Way from its earliest phases: Constraints on stellar nucleosynthesis*. *A&A* **421**, 613 (2004)
- Fraser M., Casey A. R., Gilmore G., Heger A., & Chan C.: *The mass distribution of Population III stars*. *MNRAS* **468**, 418 (2017)
- Freitag M., Gürkan M. A., & Rasio F. A.: *Runaway collisions in young star clusters - II. Numerical results*. *MNRAS* **368**, 141 (2006)
- Furlanetto S. R. & Loeb A.: *Is Double Reionization Physically Plausible?* *ApJ* **634**, 1 (2005)
- Furlanetto S. R.: *Fluctuations in the Ionizing Background During and After Helium Reionization*. *ApJ* **703**, 702 (2009)

- Gal-Yam A., Mazzali P., Ofek E. O., Nugent P. E., Kulkarni S. R., Kasliwal M. M., Quimby R. M., Filippenko A. V., Cenko S. B., Chornock R., et al.: *Supernova 2007bi as a pair-instability explosion*. **Nature** **462**, 624 (2009)
- Garnett D. R., Shields G. A., Skillman E. D., Sagan S. P., & Dufour R. J.: *Interstellar Abundance Gradients in NGC 2403: Comparison to M33*. **ApJ** **489**, 63 (1997)
- Giveon U., Sternberg A., Lutz D., Feuchtgruber H., & Pauldrach A. W. A.: *The Excitation and Metallicity of Galactic H II Regions from Infrared Space Observatory SWS Observations of Mid-Infrared Fine-Structure Lines*. **ApJ** **566**, 880 (2002)
- Gleser L., Nusser A., Benson A. J., Ohno H., & Sugiyama N.: *Patchy He II reionization and the physical state of the intergalactic medium*. **MNRAS** **361**, 1399 (2005)
- Gnedin N. Y. & Bertschinger E.: *Building a Cosmological Hydrodynamic Code: Consistency Condition, Moving Mesh Gravity, and SLH-P 3M*. **ApJ** **470**, 115 (1996)
- Gnedin N. Y. & Ostriker J. P.: *Reionization of the Universe and the Early Production of Metals*. **ApJ** **486**, 581 (1997)
- Gnedin N. Y.: *Cosmological Reionization by Stellar Sources*. **ApJ** **535**, 530 (2000)
- Gnedin N. Y. & Abel T.: *Multi-dimensional cosmological radiative transfer with a Variable Eddington Tensor formalism*. **New Astronomy** **6**, 437 (2001)
- Gordon K. D., Pérez-González P. G., Misselt K. A., Murphy E. J., Bendo G. J., Walter F., Thornley M. D., Kennicutt R. C., Jr., Rieke G. H., Engelbracht C. W., et al.: *Spatially Resolved Ultraviolet, H α , Infrared, and Radio Star Formation in M81*. **ApJS** **154**, 215 (2004)
- Górski K. M., Hivon E., Banday A. J., Wandelt B. D., Hansen F. K., Reinecke M., & Bartelmann M.: *HEALPix: A Framework for High-Resolution Discretization and Fast Analysis of Data Distributed on the Sphere*. **ApJ** **622**, 759 (2005)
- Graziani L., Maselli A., & Ciardi B.: *CRASH3: cosmological radiative transfer through metals*. **MNRAS** **431**, 722 (2013)
- Greenawalt B., Walterbos R. A. M., & Braun R.: *Optical Spectroscopy of Diffuse Ionized Gas in M31*. **ApJ** **483**, 666 (1997)
- Greenawalt B., Walterbos R. A. M., Thilker D., & Hoopes C. G.: *Diffuse Ionized Gas in M51/NGC 5195 and M81*. **ApJ** **506**, 135 (1998)
- Greif T. H., Bromm V., Clark P. C., Glover S. C. O., Smith R. J., Klessen R. S., Yoshida N., & Springel V.: *Formation and evolution of primordial protostellar systems*. **MNRAS** **424**, 399 (2012)
- Grevesse N. & Sauval A.: *The Contribution of Field OB Stars to the Ionization of the Diffuse Ionized Gas in M33*. **Space Science Reviews** **85**, 161 (1998)
- Gritschneider M., Naab T., Burkert A., Walch S., Heitsch F., & Wetzstein M.: *iVINE - Ionization in the parallel TREE/SPH code VINE: first results on the observed age-spread around O-stars*. **MNRAS** **393**, 21 (2009)

- Gunn J. E. & Peterson B. A.: *On the Density of Neutral Hydrogen in Intergalactic Space*. *ApJ* **142**, 1633 (1965)
- Gürkan M. A., Freitag M., & Rasio F. A.: *Formation of Massive Black Holes in Dense Star Clusters. I. Mass Segregation and Core Collapse*. *ApJ* **604**, 632 (2004)
- Gurzadyan G. A.: *The Physics and Dynamics of Planetary Nebulae*. (1997)
- Haffner L. M., Reynolds R. J., & Tufte S. L.: *WHAM Observations of H α , [S II], and [N II] toward the Orion and Perseus Arms: Probing the Physical Conditions of the Warm Ionized Medium*. *ApJ* **523**, 223 (1999)
- Haffner L. M., Dettmar R.-J., Beckman J. E., Wood K., Slavin J. D., Giammanco C., Madsen G. J., Zurita A., & Reynolds R. J.: *The warm ionized medium in spiral galaxies*. *Reviews of Modern Physics* **81**, 969 (2009)
- Harayama Y., Eisenhauer F., & Martins F.: *The Initial Mass Function of the Massive Star-forming Region NGC 3603 from Near-Infrared Adaptive Optics Observations*. *ApJ* **675**, 1319 (2008)
- Harris H. C., Dahn C. C., Monet D. G., & Pier J. R.: *Trigonometric parallaxes of Planetary Nebulae (Invited Review)*. In: Habing H. J. & Lamers H. J. G. L. M. (eds.): *Planetary Nebulae*. *IAU Symposium* **180**, 40 (1997)
- Haser S. M., Pauldrach A. W. A., Lennon D. J., Kudritzki R. P., Lennon M., Puls J., & Voels S. A.: *Quantitative UV spectroscopy of early O stars in the Magellanic Clouds. The determination of the stellar metallicities*. *A&A* **330**, 285 (1998)
- Hasinger G., Burg R., Giacconi R., Hartner G., Schmidt M., Trumper J., & Zamorani G.: *A Deep X-Ray Survey in the Lockman-Hole and the Soft X-Ray N-Log*. *A&A* **275**, 1 (1993)
- Hasinger G.: *The Extragalactic X-Ray Background: ROSAT Observations*. In: Wamsteker W., Longair M. S., & Kondo Y. (eds.): *Frontiers of Space and Ground-Based Astronomy*. *Astrophysics and Space Science Library* **187**, 381 (1994)
- Hernquist L. & Springel V.: *An analytical model for the history of cosmic star formation*. *MNRAS* **341**, 1253 (2003)
- Heydari-Malayeri M., Charmandaris V., Deharveng L., Rosa M. R., Schaerer D., & Zinnecker H.: *HST observations of the LMC compact HII region N 11A*. *A&A* **372**, 527 (2001)
- Heymann F. & Siebenmorgen R.: *GPU-based Monte Carlo Dust Radiative Transfer Scheme Applied to Active Galactic Nuclei*. *ApJ* **751**, 27 (2012)
- Hirschmann M., Naab T., Davé R., Oppenheimer B. D., Ostriker J. P., Somerville R. S., Oser L., Genzel R., Tacconi L. J., Förster-Schreiber N. M., et al.: *The effect of metal enrichment and galactic winds on galaxy formation in cosmological zoom simulations*. *MNRAS* **436**, 2929 (2013)
- Hoffmann T. L., Lieb S., Pauldrach A. W. A., Lesch H., Hultzsch P. J. N., & Birk G. T.: *Numerical models for the diffuse ionized gas in galaxies. I. Synthetic spectra of thermally excited gas with turbulent magnetic reconnection as energy source*. *A&A* **544**, A57 (2012)
- Hoopes C. G. & Walterbos R. A. M.: *Optical Spectroscopy and Ionization Models of the Diffuse Ionized Gas in M33, M51/NGC 5195, and M81*. *ApJ* **586**, 902 (2003)

- Hoyle F. & Ellis G. R. A.: *On the Existence of an Ionized Layer about the Galactic Plane*. *Australian Journal of Physics* **16**, 1 (1963)
- Hubber D. A., Ercolano B., & Dale J.: *Observing gas and dust in simulations of star formation with Monte Carlo radiation transport on Voronoi meshes*. *MNRAS* **456**, 756 (2016)
- Hummer D. G. & Storey P. J.: *Recombination-line intensities for hydrogenic ions. I - Case B calculations for H I and He II*. *MNRAS* **224**, 801 (1987)
- Hummer D. G.: *A fast and accurate method for evaluating the nonrelativistic free-free Gaunt factor for hydrogenic ions*. *ApJ* **327**, 477 (1988)
- Hummer D. G.: *Total Recombination and Energy Loss Coefficients for Hydrogenic Ions at Low Density for $10 \leq T_e/Z^2 \leq 10^7$ K*. *MNRAS* **268**, 109 (1994)
- Hummer D. G. & Storey P. J.: *Recombination of helium-like ions - I. Photoionization cross-sections and total recombination and cooling coefficients for atomic helium*. *MNRAS* **297**, 1073 (1998)
- Iben I., Jr. & Tutukov A. V.: *Model stars with degenerate dwarf cores and helium-burning shells - A stationary-burning approximation*. *ApJ* **342**, 430 (1989)
- Iliev I. T., Ciardi B., Alvarez M. A., Maselli A., Ferrara A., Gnedin N. Y., Mellema G., Nakamoto T., Norman M. L., Razoumov A. O., et al.: *Cosmological radiative transfer codes comparison project - I. The static density field tests*. *MNRAS* **371**, 1057 (2006)
- Iliev I. T., Whalen D., Mellema G., Ahn K., Baek S., Gnedin N. Y., Kravtsov A. V., Norman M., Raicevic M., Reynolds D. R., et al.: *Cosmological radiative transfer comparison project - II. The radiation-hydrodynamic tests*. *MNRAS* **400**, 1283 (2009)
- Jelic V.: *Cosmological 21cm experiments: Searching for a needle in a haystack*. Kapteyn Astronomical Institute, University of Groningen, vjelic@astro.rug.nl (2010)
- Jones T. A., Ellis R. S., Schenker M. A., & Stark D. P.: *Keck Spectroscopy of Gravitationally Lensed $z \sim 4$ Galaxies: Improved Constraints on the Escape Fraction of Ionizing Photons*. *ApJ* **779**, 52 (2013)
- Kannan R., Vogelsberger M., Marinacci F., McKinnon R., Pakmor R., & Springel V.: *AREPO-RT: Radiation hydrodynamics on a moving mesh*. *ArXiv e-prints* **1804.01987** (2018)
- Kashikawa N.: *The End of the Reionization Epoch Probed by Ly α Emitters at $z = 6.5$* . In: Afonso J., Ferguson H. C., Mobasher B., & Norris R. (eds.): *Deepest Astronomical Surveys*. *Astronomical Society of the Pacific Conference Series* **380**, 11 (2007)
- Kennicutt R. C., Jr., Edgar B. K., & Hodge P. W.: *Properties of H II region populations in galaxies. II - The H II region luminosity function*. *ApJ* **337**, 761 (1989)
- Kennicutt R. C., Jr., Bresolin F., & Garnett D. R.: *The Composition Gradient in M101 Revisited. II. Electron Temperatures and Implications for the Nebular Abundance Scale*. *ApJ* **591**, 801 (2003)
- Kewley L. J. & Ellison S. L.: *Metallicity Calibrations and the Mass-Metallicity Relation for Star-forming Galaxies*. *ApJ* **681**, 1183 (2008)

- Khangulyan D. V., Barkov M. V., Bosch-Ramon V., Aharonian F. A., & Dorodnitsyn A. V.: *Star-Jet Interactions and Gamma-Ray Outbursts from 3C454.3*. *ApJ* **774**, 113 (2013)
- Kingdon J. B. & Ferland G. J.: *Grains in Ionized Nebulae. II. Heavy-Element Depletion*. *ApJ* **477**, 732 (1997)
- Kingsburgh R. L. & Barlow M. J.: *Distances for galactic planetary nebulae using mean forbidden O II doublet ratio electron densities*. *MNRAS* **257**, 317 (1992)
- Kippenhahn R.: *On the core mass luminosity relation*. *A&A* **102**, 293 (1981)
- Klessen R. S., Glover S. C. O., & Clark P. C.: *On the formation of very metal poor stars: the case of SDSS J1029151+172927*. *MNRAS* **421**, 3217 (2012)
- Kramida A., Ralchenko Y., Reader J., & NIST ASD Team: *NIST Atomic Spectra Database (version 5.5.6)*. <https://physics.nist.gov/asd> (2018)
- Kriss G. A., Shull J. M., Oegerle W., Zheng W., Davidsen A. F., Songaila A., Tumlinson J., Cowie L. L., Deharveng J., Friedman S. D., et al.: *Resolving the Structure of Ionized Helium in the Intergalactic Medium with the Far Ultraviolet Spectroscopic Explorer*. *Science* **293**, 1112 (2001)
- Kroupa P.: *On the variation of the initial mass function*. *MNRAS* **322**, 231 (2001)
- Kudritzki R. P., Pauldrach A., & Puls J.: *Radiation driven winds of hot luminous stars. II - Wind models for O-stars in the Magellanic Clouds*. *A&A* **173**, 293 (1987)
- Lacerda E. A. D., Cid Fernandes R., Couto G. S., Stasińska G., García-Benito R., Vale Asari N., Pérez E., González Delgado R. M., Sánchez S. F., & de Amorim A. L.: *Diffuse ionized gas in galaxies across the Hubble sequence at the CALIFA resolution*. *MNRAS* **474**, 3727 (2018)
- Lada C. J. & Lada E. A.: *Embedded Clusters in Molecular Clouds*. *ARA&A* **41**, 57 (2003)
- Langer N., Hamann W.-R., Lennon M., Najarro F., Pauldrach A. W. A., & Puls J.: *Towards an understanding of very massive stars. A new evolutionary scenario relating O stars, LBVs and Wolf-Rayet stars*. *A&A* **290**, 819 (1994)
- Leitherer C. & Heckman T. M.: *Synthetic properties of starburst galaxies*. *ApJS* **96**, 9 (1995)
- Leitherer C., Schaerer D., Goldader J. D., González Delgado R. M., Robert C., Kune D. F., de Mello D. F., Devost D., & Heckman T. M.: *Starburst99: Synthesis Models for Galaxies with Active Star Formation*. *ApJS* **123**, 3 (1999)
- Leitherer C., Ortiz Otálvaro P. A., Bresolin F., Kudritzki R., Lo Faro B., Pauldrach A. W. A., Pettini M., & Rix S. A.: *A Library of Theoretical Ultraviolet Spectra of Massive, Hot Stars for Evolutionary Synthesis*. *ApJS* **189**, 309 (2010)
- Leitherer C., Ekström S., Meynet G., Schaerer D., Agienko K. B., & Levesque E. M.: *The Effects of Stellar Rotation. II. A Comprehensive Set of Starburst99 Models*. *ApJS* **212**, 14 (2014)
- Lennon D. J. & Burke V. M.: *Atomic data from the IRON project. II. Effective collision strength S for infrared transitions in carbon-like ions*. *A&AS* **103**, 273 (1994)

- Lineweaver C. H.: *An Estimate of the Age Distribution of Terrestrial Planets in the Universe: Quantifying Metallicity as a Selection Effect*. *Icarus* **151**, 307 (2001)
- Liu G., Calzetti D., Kennicutt R. C., Jr., Schinnerer E., Sofue Y., Komugi S., Egusa F., & Scoville N. Z.: *The Pa α Luminosity Function of H II Regions in Nearby Galaxies from HST/NICMOS*. *ApJ* **772**, 27 (2013)
- Luridiana V., Pérez E., & Cerviño M.: *Physical Conditions in the O⁺⁺ Zone from ISO and HST Data: NGC 6543 Revisited*. *AJ* **125**, 3196 (2003)
- Lutz D., Kunze D., Spoon H. W. W., & Thornley M. D.: *Faint [O iv] emission from starburst galaxies*. *A&A* **333**, L75 (1998)
- Ly C., Malkan M. A., Nagao T., Kashikawa N., Shimasaku K., & Hayashi M.: *"Direct" Gas-phase Metallicities, Stellar Properties, and Local Environments of Emission-line Galaxies at Redshifts below 0.90*. *ApJ* **780**, 122 (2014)
- Madsen G. J., Reynolds R. J., & Haffner L. M.: *A Multiwavelength Optical Emission Line Survey of Warm Ionized Gas in the Galaxy*. *ApJ* **652**, 401 (2006)
- Magorrian J., Tremaine S., Richstone D., Bender R., Bower G., Dressler A., Faber S. M., Gebhardt K., Green R., Grillmair C., et al.: *The Demography of Massive Dark Objects in Galaxy Centers*. *AJ* **115**, 2285 (1998)
- Mahabal A., Stern D., Bogosavljević M., Djorgovski S. G., & Thompson D.: *Discovery of an Optically Faint Quasar at $z = 5.70$ and Implications for the Faint End of the Quasar Luminosity Function*. *ApJ* **634**, L9 (2005)
- Mahsereci M., Ringat E., Rauch T., Werner K., & Kruk J. W.: *Spectral analysis of PG 1034+001, the exciting star of Hewett 1*. In: *IAU Symposium* **283**, 426 (2012)
- Maio U., Ciardi B., Yoshida N., Dolag K., & Tornatore L.: *The onset of star formation in primordial haloes*. *A&A* **503**, 25 (2009)
- Maio U., Ciardi B., Dolag K., Tornatore L., & Khochfar S.: *The transition from population III to population II-I star formation*. *MNRAS* **407**, 1003 (2010)
- Maio U., Petkova M., De Lucia G., & Borgani S.: *Radiative feedback and cosmic molecular gas: the role of different radiative sources*. *MNRAS* **460**, 3733 (2016)
- Márquez I., Masegosa J., Moles M., Varela J., Bettoni D., & Galletta G.: *Rotation curves and metallicity gradients from HII regions in spiral galaxies*. *A&A* **393**, 389 (2002)
- Marten H.: *Zeitabhängige Effekte in der entwicklung Plaetarischer Nebel und deren Bedeutung für die Interpretation von Beobachtungen*. Christaian-Albrechts-Universität zu Kiel (1993)
- Maselli A., Ferrara A., & Ciardi B.: *CRASH: a radiative transfer scheme*. *MNRAS* **345**, 379 (2003)
- Mathis J. S. & Wood K.: *The effects of clumping on derived abundances in HII regions*. *MNRAS* **360**, 227 (2005)
- McQuinn M., Lidz A., Zahn O., Dutta S., Hernquist L., & Zaldarriaga M.: *The morphology of HII regions during reionization*. *MNRAS* **377**, 1043 (2007)

- McQuinn M., Lidz A., Zaldarriaga M., Hernquist L., Hopkins P. F., Dutta S., & Faucher-Giguère C.: *He II Reionization and its Effect on the Intergalactic Medium*. *ApJ* **694**, 842 (2009)
- Meatheringham S. J., Wood P. R., & Faulkner D. J.: *A study of some southern planetary nebulae*. *ApJ* **334**, 862 (1988)
- Mellema G., Iliev I. T., Alvarez M. A., & Shapiro P. R.: *C²-ray: A new method for photon-conserving transport of ionizing radiation*. *New Astronomy* **11**, 374 (2006)
- Melnick J.: *On the core-halo structure of NGC604*. *A&A* **86**, 304 (1980)
- Menten K. M., Reid M. J., Forbrich J., & Brunthaler A.: *The distance to the Orion Nebula*. *A&A* **474**, 515 (2007)
- Menzel D. H., Aller L. H., & Hebb M. H.: *Physical Processes in Gaseous Nebulae. XIII*. *ApJ* **93**, 230 (1941)
- Mihalas D.: *Stellar atmospheres /2nd edition/*. (1978)
- Mihalas D. & Mihalas B. W.: *Foundations of radiation hydrodynamics*. (1984)
- Milne E. A.: *XVIII. Statistical equilibrium in relation to the photo-electric effect, and its application to the determination of absorption coefficients*. *Philosophical Magazine* **47**, 209 (1924)
- Miralda-Escudé J., Haehnelt M., & Rees M. J.: *Reionization of the Inhomogeneous Universe*. *ApJ* **530**, 1 (2000)
- Miszalski B., Acker A., Ochsenbein F., & Parker Q. A.: *A consolidated online database of Galactic planetary nebulae*. In: *IAU Symposium* **283**, 442 (2012)
- Morisset C., Stasińska G., & Peña M.: *Modelling of aspherical nebulae - I. A quick pseudo-3D photoionization code*. *MNRAS* **360**, 499 (2005)
- Morisset C.: *Cloudy_3D, a new pseudo-3D photoionization code*. In: Barlow M. J. & Méndez R. H. (eds.): *Planetary Nebulae in our Galaxy and Beyond*. *IAU Symposium* **234**, 467 (2006)
- Moy E., Rocca-Volmerange B., & Fioc M.: *Evolution of photoionization and star formation in starbursts and ion HII galaxies*. *A&A* **365**, 347 (2001)
- Muench A., Getman K., Hillenbrand L., & Preibisch T.: *Star Formation in the Orion Nebula I: Stellar Content*. In: Reipurth B. (ed.): *Handbook of Star Forming Regions, Volume I*. 483 (2008)
- Murray N.: *Star Formation Efficiencies and Lifetimes of Giant Molecular Clouds in the Milky Way*. *ApJ* **729**, 133 (2011)
- Nakamoto T., Umemura M., & Susa H.: *The effects of radiative transfer on the reionization of an inhomogeneous universe*. *MNRAS* **321**, 593 (2001)
- Nanni A., Bressan A., Marigo P., & Girardi L.: *Evolution of thermally pulsing asymptotic giant branch stars - II. Dust production at varying metallicity*. *MNRAS* **434**, 2390 (2013)
- Norman M. L.: *Pop III Stellar Masses and IMF*. In: D. J. Whalen, V. Bromm, & N. Yoshida (ed.). *American Institute of Physics Conference Series* **1294**, 17 (2010)

- Noyola E., Gebhardt K., Kissler-Patig M., Lützgendorf N., Jalali B., de Zeeuw P. T., & Baumgardt H.: *Very Large Telescope Kinematics for Omega Centauri: Further Support for a Central Black Hole.* *ApJ* **719**, L60 (2010)
- Nussbaumer H. & Storey P. J.: *Dielectronic recombination at low temperatures.* *A&A* **126**, 75 (1983)
- O'Dell C. R., Sabbadin F., & Henney W. J.: *The Three-Dimensional Ionization Structure and Evolution of NGC 6720, The Ring Nebula.* *AJ* **134**, 1679 (2007)
- Oey M. S. & Massey P.: *Triggered Star Formation and the Dynamics of a Superbubble in the LMC: The OB Association LH 47/48 in DEM 152.* *ApJ* **452**, 210 (1995)
- Oey M. S. & Clarke C. J.: *On the Form of the H II Region Luminosity Function.* *AJ* **115**, 1543 (1998)
- O'Shea B. W., Bryan G., Bordner J., Norman M. L., Abel T., Harkness R., & Kritsuk A.: *Introducing Enzo, an AMR Cosmology Application.* *ArXiv Astrophysics e-prints* (2004)
- Osterbrock D. E., Tran H. D., & Veilleux S.: *Faint emission lines in the spectrum of the Orion Nebula and the abundances of some of the rarer elements.* *ApJ* **389**, 305 (1992)
- Osterbrock D. E. & Ferland G. J.: *Astrophysics of gaseous nebulae and active galactic nuclei.* (2006)
- Osterbrock D. & Flather E.: *Electron Densities in the Orion Nebula. II.* *ApJ* **129**, 26 (1959)
- Otte B., Reynolds R. J., Gallagher J. S., III, & Ferguson A. M. N.: *Searching for Additional Heating: [O II] Emission in the Diffuse Ionized Gas of NGC 891, NGC 4631, and NGC 3079.* *ApJ* **560**, 207 (2001)
- Owocki S. P., Gayley K. G., & Shaviv N. J.: *A Porosity-Length Formalism for Photon-Tiring-limited Mass Loss from Stars above the Eddington Limit.* *ApJ* **616**, 525 (2004)
- Paczynski B.: *Evolution of Single Stars. I. Stellar Evolution from Main Sequence to White Dwarf or Carbon Ignition.* *Acta Astron.* **20**, 47 (1970)
- Partl A. M., Maselli A., Ciardi B., Ferrara A., & Müller V.: *Enabling parallel computing in CRASH.* *MNRAS* **414**, 428 (2011)
- Pauldrach A. W. A., Kudritzki R. P., Puls J., & Butler K.: *Radiation driven winds of hot luminous stars. VII - The evolution of massive stars and the morphology of stellar wind spectra.* *A&A* **228**, 125 (1990)
- Pauldrach A. W. A., Feldmeier A., Puls J., & Kudritzki R. P.: *Radiation driven winds of hot stars: theory of O-star atmospheres as a spectral tool.* *Space Science Reviews* **66**, 105 (1993)
- Pauldrach A. W. A., Kudritzki R. P., Puls J., Butler K., & Hunsinger J.: *Radiation-driven winds of hot luminous stars. 12: A first step towards detailed UV-line diagnostics of O-stars.* *A&A* **283**, 525 (1994)
- Pauldrach A. W. A., Lennon M., Hoffmann T. L., Sellmaier F., Kudritzki R. P., & Puls J.: *Realistic Models for Expanding Atmospheres.* In: *Boulder-Munich II: Properties of Hot, Luminous Stars, edited by Ian Howarth.* *ASP Conf. Ser.* **131**, 258 (1998)

- Pauldrach A. W. A., Hoffmann T. L., & Lennon M.: *Radiation-driven winds of hot luminous stars. XIII. A description of NLTE line blocking and blanketing towards realistic models for expanding atmospheres.* **A&A** **375**, 161 (2001)
- Pauldrach A. W. A.: *Hot Stars: Old-Fashioned or Trendy? (With 24 Figures).* In: R. E. Schielicke (ed.). **Reviews in Modern Astronomy** **16**, 133 (2003)
- Pauldrach A. W. A., Hoffmann T. L., & Méndez R. H.: *Radiation-driven winds of hot luminous stars. XV. Constraints on the mass-luminosity relation of central stars of planetary nebulae.* **A&A** **419**, 1111 (2004)
- Pauldrach A. W. A., Vanbeveren D., & Hoffmann T. L.: *Radiation-driven winds of hot luminous stars XVI. Expanding atmospheres of massive and very massive stars and the evolution of dense stellar clusters.* **A&A** **538**, A75 (2012)
- Pauldrach A. W. A., Hoffmann T. L., & Hultsch P. J. N.: *Non-LTE models for synthetic spectra of type Ia supernovae. III. An accelerated lambda-iteration procedure for the mutual interaction of strong spectral lines in SN Ia models with and without energy deposition.* **A&A** **569**, A61 (2014)
- Pauldrach A. W. A.: *Radiative Processes and the Physics of Gaseous Nebulae (lecture notes).* <http://www.usm.uni-muenchen.de/~adi/lect-gn.htm> (2016)
- Pauldrach A., Puls J., & Kudritzki R. P.: *Radiation-driven winds of hot luminous stars - Improvements of the theory and first results.* **A&A** **164**, 86 (1986)
- Pauldrach A., Puls J., & Kudritzki R. P.: *Radiation-driven winds of hot luminous stars - Improvements of the theory and first results.* **A&A** **164**, 86 (1986)
- Pauldrach A.: *Radiation driven winds of hot luminous stars. III - Detailed statistical equilibrium calculations for hydrogen to zinc.* **A&A** **183**, 295 (1987)
- Pauli W.: *Über das H-theorem vom Anwachsen der Entropie vom Standpunkt der neueren Quantenmechanik.* In: Debye P. (ed.): *Probleme der modernen Physik. Arnold Sommerfeld zum 60. Geburtstag gewidmet.* 30 (1928)
- Petkova M. & Springel V.: *An implementation of radiative transfer in the cosmological simulation code GADGET.* **MNRAS** **396**, 1383 (2009)
- Petkova M. & Springel V.: *A novel approach for accurate radiative transfer in cosmological hydrodynamic simulations.* **MNRAS** **415**, 3731 (2011)
- Petkova M. & Maio U.: *Radiative feedback and cosmic molecular gas: numerical method.* **MNRAS** **422**, 3067 (2012)
- Pettini M., Steidel C. C., Adelberger K. L., Dickinson M., & Giavalisco M.: *The Ultraviolet Spectrum of MS 1512-CB58: An Insight into Lyman-Break Galaxies.* **ApJ** **528**, 96 (2000)
- Pilyugin L. S., Lara-López M. A., Grebel E. K., Kehrig C., Zinchenko I. A., López-Sánchez Á. R., Vílchez J. M., & Mattsson L.: *The metallicity-redshift relations for emission-line SDSS galaxies: examination of the dependence on the star formation rate.* **MNRAS** **432**, 1217 (2013)
- Porcel C., Garzon F., Jimenez-Vicente J., & Battaner E.: *The radial scale length of the Milky Way.* **A&A** **330**, 136 (1998)

- Portegies Zwart S. F., Makino J., McMillan S. L. W., & Hut P.: *Star cluster ecology. III. Runaway collisions in young compact star clusters*. *A&A* **348**, 117 (1999)
- Portegies Zwart S. F. & McMillan S. L. W.: *The Runaway Growth of Intermediate-Mass Black Holes in Dense Star Clusters*. *ApJ* **576**, 899 (2002)
- Portegies Zwart S. F., Dewi J., & Maccarone T.: *Intermediate mass black holes in accreting binaries: formation, evolution and observational appearance*. *MNRAS* **355**, 413 (2004)
- Pradhan A. K.: *Collision strengths for O II and S II*. *MNRAS* **177**, 31 (1976)
- Preibisch T. & Zinnecker H.: *Sequentially triggered star formation in OB associations*. In: Elmegreen B. G. & Palous J. (eds.). *IAU Symposium* **237**, 270 (2007)
- Press W. H., Teukolsky S. A., Vetterling W. T., & Flannery B. P.: *Numerical recipes in FORTRAN. The art of scientific computing*. Cambridge: University Press, —c1992, 2nd ed. (1992)
- Puls J. & Hummer D. G.: *The Sobolev approximation for the line force and line source function in a spherically-symmetrical stellar wind with continuum opacity*. *A&A* **191**, 87 (1988)
- Rand R. J., Wood K., Benjamin R. A., & Meidt S. E.: *Infrared Spectroscopy of the Diffuse Ionized Halos of Edge-on Galaxies*. *ApJ* **728**, 163 (2011)
- Razoumov A. O. & Cardall C. Y.: *Fully threaded transport engine: new method for multi-scale radiative transfer*. *MNRAS* **362**, 1413 (2005)
- Reimers D., Kohler S., Wisotzki L., Groote D., Rodriguez-Pascual P., & Wamsteker W.: *Patchy intergalactic He II absorption in HE 2347-4342. II. The possible discovery of the epoch of He-reionization*. *A&A* **327**, 890 (1997)
- Reynolds D. R., Hayes J. C., Paschos P., & Norman M. L.: *Self-consistent solution of cosmological radiation-hydrodynamics and chemical ionization*. *Journal of Computational Physics* **228**, 6833 (2009)
- Reynolds R. J.: *Detection of the forbidden O III lambda 5007 emission line in the Galactic background*. *ApJ* **298**, L27 (1985)
- Reynolds R. J.: *Line integrals of N_E and n_E -squared at high Galactic latitude*. *ApJ* **372**, L17 (1991)
- Reynolds R. J. & Tufté S. L.: *A search for the He I lambda 5876 recombination line from the diffuse interstellar medium*. *ApJ* **439**, L17 (1995)
- Reynolds R. J., Sterling N. C., Haffner L. M., & Tufté S. L.: *Detection of [N II] lambda 5755 Emission from Low-Density Ionized Interstellar Gas*. *ApJ* **548**, L221 (2001)
- Ritzerveld J., Icke V., & Rijkhorst E.-J.: *Triangulating Radiation: Radiative Transfer on Unstructured Grids*. *ArXiv Astrophysics e-prints* (2003)
- Robitaille T. P. & Whitney B. A.: *The Present-Day Star Formation Rate of the Milky Way Determined from Spitzer-Detected Young Stellar Objects*. *ApJ* **710**, L11 (2010)
- Roennback J. & Bergvall N.: *Blue low surface-brightness galaxies. II. Spectroscopy and chemical abundances*. *A&A* **302**, 353 (1995)

- Rosolowsky E. & Simon J. D.: *The M33 Metallicity Project: Resolving the Abundance Gradient Discrepancies in M33*. *ApJ* **675**, 1213 (2008)
- Rossa J. & Dettmar R.-J.: *Extraplanar diffuse ionized gas in a small sample of nearby edge-on galaxies*. *A&A* **359**, 433 (2000)
- Rubin R. H., Simpson J. P., Haas M. R., & Erickson E. F.: *Axisymmetric model of the ionized gas in the Orion Nebula*. *ApJ* **374**, 564 (1991a)
- Rubin R. H., Simpson J. P., Haas M. R., & Erickson E. F.: *Modeling the Orion nebula as an axisymmetric blister*. *PASP* **103**, 834 (1991b)
- Rubin R. H., Simpson J. P., Colgan S. W. J., Dufour R. J., Ray K. L., Wakefield B. F., Key D. B., Erickson E. F., Haas M. R., & Pauldrach A. W. A.: *Spitzer Observations of M83 and the Hot Star, H II Region Connection*. In: Barlow M. J. & MÃ©ndez R. H. (eds.): *Planetary Nebulae in our Galaxy and Beyond*. **234**, 495 (2006)
- Rubin R. H., Simpson J. P., Colgan S. W. J., Dufour R. J., Ray K. L., Erickson E. F., Haas M. R., Pauldrach A. W. A., & Citron R. I.: *Spitzer observations of M83 and the hot star, HII region connection*. *MNRAS* **377**, 1407 (2007)
- Rubin R. H., Simpson J. P., Colgan S. W. J., Dufour R. J., Brunner G., McNabb I. A., Pauldrach A. W. A., Erickson E. F., Haas M. R., & Citron R. I.: *Spitzer observations of M33 and the hot star, HII region connection*. *MNRAS* **387**, 45 (2008)
- Rubin R. H., McNabb I. A., Simpson J. P., Dufour R. J., Pauldrach A. W. A., Colgan S. W. J., Craven T. W., Gitterman E. D., & Lo C. C.: *Spitzer finds cosmic neon's and sulfur's sweet spot: part III, NGC 6822*. In: Cunha K., Spite M., & Barbay B. (eds.). *IAU Symposium* **265**, 249 (2010)
- Rubin R. H., Kader J. A., Sivaraja V., Simpson J. P., Pauldrach A. W. A., Dufour R. J., Colgan S. W. J., McNabb I. A., Zhuge S. Y., & Kalyanasundaram V.: *Spitzer Observations of H II Regions in NGC 6822 and the Hot Star - H II Region Connection*. In: *American Astronomical Society Meeting Abstracts 220*. *American Astronomical Society Meeting Abstracts* **220**, 106.05 (2012)
- Rubin R. H., Simpson J. P., Colgan S. W. J., Dufour R. J., Kader J., McNabb I. A., Pauldrach A. W. A., & Weber J. A.: *Spitzer observations of extragalactic H II regions - III. NGC 6822 and the hot star, H II region connection*. *MNRAS* **459**, 1875 (2016)
- Rudolph A. L., Fich M., Bell G. R., Norsen T., Simpson J. P., Haas M. R., & Erickson E. F.: *Abundance Gradients in the Galaxy*. *ApJS* **162**, 346 (2006)
- Ryu D., Ostriker J. P., Kang H., & Cen R.: *A cosmological hydrodynamic code based on the total variation diminishing scheme*. *ApJ* **414**, 1 (1993)
- Sandford M. T., II, Whitaker R. W., & Klein R. I.: *Radiation-driven implosions in molecular clouds*. *ApJ* **260**, 183 (1982)
- Santos M. G., Silva M. B., Pritchard J. R., Cen R., & Cooray A.: *Probing the first galaxies with the Square Kilometer Array*. *A&A* **527**, A93 (2011)
- Schaerer D. & Stasińska G.: *On the origin of [O IV] emission in Wolf-Rayet galaxies*. *A&A* **345**, L17 (1999)

- Schaerer D.: *On the properties of massive Population III stars and metal-free stellar populations.* **A&A** **382**, 28 (2002)
- Schaller G., Schaerer D., Meynet G., & Maeder A.: *New grids of stellar models from 0.8 to 120 solar masses at $Z = 0.020$ and $Z = 0.001$.* **A&AS** **96**, 269 (1992)
- Scheuer P. A. G.: *The absorption coefficient of a plasma at radio frequencies.* **MNRAS** **120**, 231 (1960)
- Schmidt-Voigt M. & Koeppen J.: *Influence of stellar evolution on the evolution of planetary nebulae. I - Numerical method and hydrodynamical structures. II - Confrontation of models with observations.* **A&A** **174**, 211 (1987)
- Schneider R., Omukai K., Limongi M., Ferrara A., Salvaterra R., Chieffi A., & Bianchi S.: *The formation of the extremely primitive star SDSS J102915+172927 relies on dust.* **MNRAS** **423**, L60 (2012)
- Schwabl F.: *Quantenmechanik (QM I)*. Springer (2002)
- Seaton M. J. & Osterbrock D. E.: *Relative [O II] Intensities in Gaseous Nebulae.* **ApJ** **125**, 66 (1957)
- Seaton M. J.: *Thermal Inelastic Collision Processes.* **Reviews of Modern Physics** **30**, 979 (1958)
- Seaton M. J.: *Radiative recombination of hydrogenic ions.* **MNRAS** **119**, 81 (1959)
- Seaton M. J.: *Atomic and molecular processes.* In: Bates D. R. (ed.). Academic Press (1962)
- Sellmaier F. H., Yamamoto T., Pauldrach A. W. A., & Rubin R. H.: *A possible solution for the [Ne III] problem in HII regions.* **A&A** **305**, L37 (1996)
- Shaver P. A.: *Electron Temperatures of HII Regions.* **Astrophys. Lett.** **5**, 167 (1970)
- Shaver P. A., McGee R. X., Newton L. M., Danks A. C., & Pottasch S. R.: *The galactic abundance gradient.* **MNRAS** **204**, 53 (1983)
- Shields J. C. & Kennicutt R. C., Jr.: *Consequences of Dust in Metal-rich H II Regions.* **ApJ** **454**, 807 (1995)
- Shull J. M. & van Steenberg M.: *The ionization equilibrium of astrophysically abundant elements.* **ApJS** **48**, 95 (1982)
- Shull J. M., Stevans M., & Danforth C. W.: *HST-COS Observations of AGNs. I. Ultraviolet Composite Spectra of the Ionizing Continuum and Emission Lines.* **ApJ** **752**, 162 (2012)
- Simpson J. P., Witteborn F. C., Price S. D., & Cohen M.: *Midcourse Space Experiment Spectra of the Orion Nebula and the Implications for Abundances in the Interstellar Medium.* **ApJ** **508**, 268 (1998)
- Smith N., Egan M. P., Carey S., Price S. D., Morse J. A., & Price P. A.: *Large-Scale Structure of the Carina Nebula.* **ApJ** **532**, L145 (2000)
- Smith N.: *A census of the Carina Nebula - I. Cumulative energy input from massive stars.* **MNRAS** **367**, 763 (2006)

- Sokolowski J. & Bland-Hawthorn J.: *Photoionization of high-latitude gas in NGC 891*. **PASP** **103**, 911 (1991)
- Spitzer L.: *Physical processes in the interstellar medium*. (1978)
- Spitzer L.: *Physical Processes in the Interstellar Medium*. Physical Processes in the Interstellar Medium, by Lyman Spitzer, pp. 335. ISBN 0-471-29335-0. Wiley-VCH, May 1998. (1998)
- Stacy A., Bromm V., & Lee A. T.: *Building up the Population III initial mass function from cosmological initial conditions*. **MNRAS** **462**, 1307 (2016)
- Stanghellini L., Magrini L., Villaver E., & Galli D.: *The population of planetary nebulae and H II regions in M 81. A study of radial metallicity gradients and chemical evolution*. **A&A** **521**, A3 (2010)
- Stasińska G. & Leitherer C.: *H II Galaxies versus Photoionization Models for Evolving Starbursts*. **ApJS** **107**, 661 (1996)
- Steidel C. C., Giavalisco M., Pettini M., Dickinson M., & Adelberger K. L.: *Spectroscopic Confirmation of a Population of Normal Star-forming Galaxies at Redshifts $Z > 3$* . **ApJ** **462**, L17 (1996)
- Sternberg A., Hoffmann T. L., & Pauldrach A. W. A.: *Ionizing Photon Emission Rates from O- and Early B-Type Stars and Clusters*. **ApJ** **599**, 1333 (2003)
- Storey P. J.: *Recombination processes*. In: Flower D. R. (ed.): *Planetary Nebulae*. **IAU Symposium** **103**, 199 (1983)
- Struve O. & Elvey C. T.: *Emission Nebulosity in Cygnus and Cepheus*. **ApJ** **88**, 364 (1938)
- Subrahmanyan R.: *330-MHz radio continuum observations of the H II regions M42 and M43*. **MNRAS** **254**, 291 (1992)
- Subrahmanyan R., Goss W. M., & Malin D. F.: *Radio Continuum Structure of the Orion Nebula*. **AJ** **121**, 399 (2001)
- Suzuki T. K., Nakasato N., Baumgardt H., Ibukiyama A., Makino J., & Ebisuzaki T.: *Evolution of Collisionally Merged Massive Stars*. **ApJ** **668**, 435 (2007)
- Syphers D., Anderson S. F., Zheng W., Smith B., Pieri M., Kriss G. A., Meiksin A., Schneider D. P., Shull J. M., & York D. G.: *He II Ly β Gunn-Peterson Absorption: New HST Observations, and Theoretical Expectations*. **ArXiv e-prints** **1108.4727** (2011)
- Syphers D., Anderson S. F., Zheng W., Meiksin A., Schneider D. P., & York D. G.: *HST/COS Observations of Thirteen New He II Quasars*. **AJ** **143**, 100 (2012)
- Takáts K. & Vinkó J.: *Distance estimate and progenitor characteristics of SN 2005cs in M51*. **MNRAS** **372**, 1735 (2006)
- Taresch G., Kudritzki R. P., Hurwitz M., Bowyer S., Pauldrach A. W. A., Puls J., Butler K., Lennon D. J., & Haser S. M.: *Quantitative analysis of the FUV, UV and optical spectrum of the O3 star HD 93129A*. **A&A** **321**, 531 (1997)

- Targett T. A., Dunlop J. S., & McLure R. J.: *The host galaxies and black hole-to-galaxy mass ratios of luminous quasars at $z \sim 4$* . **MNRAS** **420**, 3621 (2012)
- Tayal S. S. & Gupta G. P.: *Collision Strengths for Electron Collision Excitation of Fine-Structure Levels in S III*. **ApJ** **526**, 544 (1999)
- Telfer R. C., Zheng W., Kriss G. A., & Davidsen A. F.: *The Rest-Frame Extreme-Ultraviolet Spectral Properties of Quasi-stellar Objects*. **ApJ** **565**, 773 (2002)
- Trac H. & Cen R.: *Radiative Transfer Simulations of Cosmic Reionization. I. Methodology and Initial Results*. **ApJ** **671**, 1 (2007)
- Tremonti C. A., Heckman T. M., Kauffmann G., Brinchmann J., Charlot S., White S. D. M., Seibert M., Peng E. W., Schlegel D. J., Uomoto A., et al.: *The Origin of the Mass-Metallicity Relation: Insights from 53,000 Star-forming Galaxies in the Sloan Digital Sky Survey*. **ApJ** **613**, 898 (2004)
- Tüllmann R. & Dettmar R.-J.: *Spectroscopy of diffuse ionized gas in halos of selected edge-on galaxies*. **A&A** **362**, 119 (2000)
- Tully R. B.: *Nearby galaxies catalog*. (1988)
- Vazquez G. A., Leitherer C., & Geneva Group Collaboration: *Evolutionary Synthesis Models with Stellar Rotation for Young Populations*. In: *American Astronomical Society Meeting Abstracts #206. Bulletin of the American Astronomical Society* **37**, 464 (2005)
- Volonteri M. & Gnedin N. Y.: *Relative Role of Stars and Quasars in Cosmic Reionization*. **ApJ** **703**, 2113 (2009)
- Walch S. K., Whitworth A. P., Bisbas T., Wunsch R., & Hubber D.: *Dispersal of molecular clouds by ionizing radiation*. **MNRAS** **427**, 625 (2012)
- Weber J. A., Pauldrach A. W. A., Knogl J. S., & Hoffmann T. L.: *Three-dimensional modeling of ionized gas. I. Did very massive stars of different metallicities drive the second cosmic reionization?* **A&A** **555**, A35 (2013)
- Weber J. A., Pauldrach A. W. A., & Hoffmann T. L.: *Three-dimensional modeling of ionized gas. II. Spectral energy distributions of massive and very massive stars in stationary and time-dependent modeling of the ionization of metals in HII regions*. **ArXiv e-prints** **1501.05264** (2015)
- Weedman D. W.: *Electron Densities in Planetary Nebulae from [S II]*. **PASP** **80**, 314 (1968)
- White R. L., Becker R. H., Fan X., & Strauss M. A.: *Probing the Ionization State of the Universe at $z > 6$* . **AJ** **126**, 1 (2003)
- Willott C. J., Delfosse X., Forveille T., Delorme P., & Gwyn S. D. J.: *First Results from the Canada-France High- z Quasar Survey: Constraints on the $z = 6$ Quasar Luminosity Function and the Quasar Contribution to Reionization*. In: **633**, 630 (2005)
- Wise J. H. & Abel T.: *How Very Massive Metal Free Stars Start Cosmological Reionization*. **ArXiv e-prints** **710** (2007)
- Wise J. H. & Abel T.: *ENZO+MORAY: radiation hydrodynamics adaptive mesh refinement simulations with adaptive ray tracing*. **MNRAS** **414**, 3458 (2011)

- Wood K. & Mathis J. S.: *Monte Carlo photoionization simulations of diffuse ionized gas*. *MNRAS* **353**, 1126 (2004)
- Wood K., Mathis J. S., & Ercolano B.: *A three-dimensional Monte Carlo photoionization code for modelling diffuse ionized gas*. *MNRAS* **348**, 1337 (2004)
- Wood K., Haffner L. M., Reynolds R. J., Mathis J. S., & Madsen G.: *Estimating the Porosity of the Interstellar Medium from Three-dimensional Photoionization Modeling of H II Regions*. *ApJ* **633**, 295 (2005)
- Wood K., Hill A. S., Joung M. R., Mac Low M.-M., Benjamin R. A., Haffner L. M., Reynolds R. J., & Madsen G. J.: *Photoionization of High-altitude Gas in a Supernova-driven Turbulent Interstellar Medium*. *ApJ* **721**, 1397 (2010)
- Wood K., Barnes J. E., Ercolano B., Haffner L. M., Reynolds R. J., & Dale J.: *Three-dimensional Geometries and the Analysis of H II Regions*. *ApJ* **770**, 152 (2013)
- Woosley S. E. & Weaver T. A.: *The Evolution and Explosion of Massive Stars. II. Explosive Hydrodynamics and Nucleosynthesis*. *ApJS* **101**, 181 (1995)
- Wright E. L.: *A Cosmology Calculator for the World Wide Web*. *PASP* **118**, 1711 (2006)
- Wu X.-B., Wang F., Fan X., Yi W., Zuo W., Bian F., Jiang L., McGreer I. D., Wang R., Yang J., et al.: *An ultraluminous quasar with a twelve-billion-solar-mass black hole at redshift 6.30*. *Nature* **518**, 512 (2015)
- Wyithe J. S. B. & Loeb A.: *Reionization of Hydrogen and Helium by Early Stars and Quasars*. *ApJ* **586**, 693 (2003)
- Yoshida N., Bromm V., & Hernquist L.: *The Era of Massive Population III Stars: Cosmological Implications and Self-Termination*. *ApJ* **605**, 579 (2004)
- Zanstra H.: *Untersuchungen über planetarische Nebel. Erster Teil: Der Leuchtprozeßplanetarischer Nebel und die Temperatur der Zentralsterne. Mit 4 Abbildungen*. *ZAp* **2**, 1 (1931)
- Zaritsky D., Kennicutt R. C., Jr., & Huchra J. P.: *H II regions and the abundance properties of spiral galaxies*. *ApJ* **420**, 87 (1994)
- Zeippen C. J.: *Improved radiative transition probabilities for O II forbidden lines*. *A&A* **173**, 410 (1987)
- Zhang Y., Liu X.-W., Wesson R., Storey P. J., Liu Y., & Danziger I. J.: *Electron temperatures and densities of planetary nebulae determined from the nebular hydrogen recombination spectrum and temperature and density variations*. *MNRAS* **351**, 935 (2004)
- Zurita A., Rozas M., & Beckman J. E.: *The origin of the ionization of the diffuse interstellar medium in spiral galaxies. I. Photometric measurements*. *A&A* **363**, 9 (2000)
- Zurita A., Beckman J. E., Rozas M., & Ryder S.: *The origin of the ionization of the diffuse ionized gas in spirals. II. Modelling the distribution of ionizing radiation in NGC 157*. *A&A* **386**, 801 (2002)

Danksagung

Im Laufe meiner Zeit an der Sternwarte bin ich vielen Menschen begegnet, denen ich an dieser Stelle „Danke“ sagen will.

Zuerst geht mein Dank an PROF. DR. ADALBERT PAULDRACH für das Stellen des Themas und die ausführlichen Diskussionen zur zugehörigen Physik und zu sonstigen Fragestellungen, welche die Anfertigung der Doktorarbeit mit sich brachte. Vielen Dank auch für einige wichtige Hilfestellungen, die über das, was unmittelbar mit der Doktorarbeit zusammenhängt, hinausgehen. Auch bei PD Dr. Klaus Dolag, der sich gleich dazu bereit erklärt hat, der Zweitgutachter meiner Arbeit zu werden, möchte ich mich herzlich bedanken.

DR. TADZIU HOFFMANN hatte in seiner Doppelfunktion als Mitarbeiter unserer Arbeitsgruppe und als Systemadministrator immer ein offenes Ohr bei den verschiedensten Arten von Problemen, ob es nun knifflige Fragestellungen physikalischer Natur, beispielsweise den Strahlungstransport betreffend, oder aber Computerprobleme vom Typ „Ich glaube, ich habe mein Passwort vergessen...“ waren. (Ein Dank geht an dieser Stelle auch an Lisa Schneiders für ihre beständige Toleranz bezüglich der Unruhe, die ich und meine Kollegen manchmal in ihr und Tadzius Büro bringen.) Vielen Dank auch für das Korrekturlesen.

DR. KEITH BUTLER und DR. MARGARITA PETKOVA halfen mir durch Diskussionen über die atomaren Daten beziehungsweise den Strahlungstransport in einem expandierenden Universum sowie für Hinweise auf weiterführende Literaturquellen.

Des weiteren möchte ich mich bei allen Kollegen, mit denen ich in den vergangenen Jahren mein Büro geteilt habe, für das angenehme Arbeitsklima bedanken. Dies sind in alphabetischer Reihenfolge – sollte ich jemanden vergessen haben, so möge er oder sie sich in gleicher Weise angesprochen fühlen: CHRISTIAN ALIG, ALEXANDER ARTH, MICHAEL AUMER, ALEXANDER BECK, ANNA BRUCALASSI, MAX BRUNNER, MARIA-ROSA CIONI, CLAIRE DOBBS, KATHARINA FIERLINGER, MATTHIAS GEORGII, CAROLINE HEBINCK, STEFAN HEIGL, DAVID HUBBER, MAXIMILIAN IMGUND, VERONIKA JUNK, CORNELIUS KASCHINSKI, MADHURA KILLEDAR, CHRISTINE KÖPFERL, MICHAEL KOPP, RALF KOSYRA, SABINE KRETSCHMANN, FLORIAN LANG-BARDL, GUANG-XING LI, YUJUAN LIU, LEILA MIRZAGHOLI, MAX MEHLHORN, JUDITH NGOMOU, EVANGELIA NTORMOUSI, CHRISTAN OBERMEIER, HENRIKE OHLENDORF, MICHAEL OPITSCH, BEATA PASTERNAK, STEFANIE PEKRUHL, MARGARITA PETKOVA, LENNARD REB, STEFAN REISSL, FEDERICO STASYSZYN, CORVIN STERN, RAMONA STROBL, CARSTEN STRÜBIG, PETER ZEIDLER und MARTIN ZINTL.

Die Zusammenarbeit mit SEBASTIAN KNOGL im Rahmen unserer Diplomarbeiten legte den Grundstein für meine Beschäftigung mit dem dreidimensionalen Strahlungstransport und somit auch für die hier vorliegende Arbeit. Ein Dank geht auch die Teilnehmer der morgendlichen Kaffeerrunde, bei der regelmäßig verschiedenste (nicht nur) physikalische Themen besprochen worden sind, also an FRAUKE ALEXANDER, NATASCHA GREISEL, REBEKA GRELLMANN, TADZIU HOFFMANN, HENRIKE OHLENDORF, STEFANIE PEKRUHL, THORSTEN RATZKA und RHEA-SILVIA REMUS.

Eine Besonderheit hier an der Sternwarte ist, dass wir unser Mittagessen bei UFOs bestellen können. Gemeint ist natürlich das USM Food Ordering System, das das Werk von JOHANNES KOPPENHÖFER ist. Auch dem Rest der Essensgruppe sei für die mittäglichen Diskussionen über alles mögliche gedankt.

Ferner möchte ich mich noch bei meinen Studienkollegen und Freunden JOHANNES ERDMANN, JOHANNES SCHMELZL, FLORIAN SEILMEIER, und JOHNAS WILL für gelegentliche Besuche de Münchner Gastronomie, für Grillabende und Bergtouren bedanken.

Ein Dank geht auch an meine Schulfreunde WERNER BAUMANN, CHRISTOPH BROSDA, ARMIN FERASCHIN, MICHAEL HECHT, PETER LEONHARDT, ANDREAS PROKOP sowie GEORG und MARTIN SCHWARZENBÖCK.

Zu guter Letzt möchte ich mich bei meiner Familie für die fortwährende Unterstützung in jederlei Hinsicht bedanken, deren Bedeutung an dieser Stelle nicht in Worte gefasst werden kann.